SUBSTITUTED IRON PHTHALOCYANINES: ELECTROCATALYTIC ACTIVITY TOWARDS O_2 REDUCTION IN A PROTON EXCHANGE MEMBRANE FUEL CELL CATHODE ENVIRONMENT AS A FUNCTION OF TEMPERATURE

by

RYAN CHRISTOPHER COLIN BAKER

B.Sc. (Chemistry Co-op), The University of Victoria, 2000

A THESIS SUBMITTED IN PARTIAL FULFILLMENT OF
THE REQUIREMENTS FOR THE DEGREE OF

MASTER OF APPLIED SCIENCE

in

THE FACULTY OF GRADUATE STUDIES
(CHEMICAL AND BIOLOGICAL ENGINEERING)

THE UNIVERSITY OF BRITISH COLUMBIA
(Vancouver)

October 2008

Abstract

In this thesis five iron phthalocyanines (FePc's), four of which having different electron withdrawing or electron donating substituents, were evaluated as O_2 reduction reaction (ORR) catalysts. The experimental approach simulated a PEM fuel cell environment using both ex-situ electrochemical techniques and in situ fuel cell testing.

The kinetic ORR parameters for the FePc species each adsorbed on a pyrolytic graphite WE were evaluated at four temperatures (20, 40, 60, 80°C) in a novel half cell using cyclic voltammetry (CV) and rotating disk electrode (RDE) voltammetry. Kinetic ORR parameters included the overall ORR electron transfer number, reaction rate constants, cathodic Tafel slopes, electron transfer numbers in the rate determining step, and electron transfer co-efficients. An increase in temperature from 60°C to 80°C showed a decrease in the overall electron transfer number observed for all four substituted FePc species. A mechanism was also proposed based on the experimental results.

The RDE results were confirmed using a rotating ring disk electrode (RRDE). From these RRDE results, the fraction of H_2O_2 produced (X_{H2O2}) at the disk during the ORR was calculated. These X_{H2O2} values agreed with the overall ORR electron transfer numbers from the RDE results obtained under the same conditions.

Iron(II) 1,2,3,4,8,9,10,11,15,16,17,18,22,23,24,25 – hexadecachloro-29H,31H-phthalocyanine ($FePcCl_{16}$) was down selected for further investigation

as the most stable and active substituted FePc species for the ORR. Both $FePcCl_{16}$ and the unsubstituted FePc, were supported on carbon and made into catalyst inks for carbon fibre paper (CFP) electrode testing, and then evaluated using CV in the N_2 purged, followed by the air saturated, electrolytes, respectively.

Finally, MEA's for fuel cell testing were made using FePc species catalyst ink cathodes, and commercial Pt/C anodes. The MEA's were tested using custom designed and built fuel cell hardware. Open circuit voltages, polarization curves, and power curves were recorded. Initial results indicated the $FePcCl_{16}$ MEA's showed superior stability, higher open circuit voltages, as well as better polarization and power curves when compared to the unsubstituted FePc species.

It was found that FePc species with strongly electron withdrawing substituents, such as $FePcCl_{16}$, showed the highest stability and greatest ORR activity. FePc species, including pyrolized FeN_X/C analogues, show much promise as alternatives to Pt in PEMFC's, as well as dye sensitized solar cells (DSSC's).

Table of Contents

List of Tables

List of Figures

Nomenclature

A	active surface area of bare working electrode (cm^{-2})
b	Tafel slope ($mV\ decade^{-1}$)
b_a	anodic Tafel slope ($mV\ decade^{-1}$)
b_c	cathodic Tafel slope ($mV\ decade^{-1}$)
C_{DL}	interfacial double layer capacitance ($C\ V^{-1}$)
C_i	ionic capacitance ($C\ V^{-1}$)
C_{O2}	concentration of dissolved O_2 in the electrolyte ($mol\ L^{-1}$ or M)
D_{O2}	dissolved O_2 diffusion coefficient ($cm^2\ s^{-1}$)
E_e	equilibrium potential (V)
E^o	standard potential for the redox reaction at 298°K and 1 atm (V)
E_a	reaction activation energy ($kJ\ mol^{-1}$)
E_f	formal potential (V)
E_i	initial potential (V)
E_p	peak potential (V)
F	Faraday's constant (96485.4 $C\ mol^{-1}$)
i_{Tot}	disk current for RDE (A)
I_D	disk current for RRDE (A)
i_{Lev}	Levich, or diffusion, or mass transfer limited, current (A)
i_{kin}	kinetic current (A)
I_R	ring current for RRDE (A)
i_p	peak current (A)

j	current density (A cm^{-2})
j_a	partial anodic, or positive oxidation, current density (A cm^{-2})
j_c	partial cathodic, or negative reduction, current density (A cm^{-2})
j_o	exchange current density (A cm^{-2})
j_o^o	absolute exchange current density (A cm^{-2})
k_s	rate constant from the Arrhenius equation
k_s^o	pre exponential factor from the Arrhenius equation
k_{O2}	kinetic rate constant for the ORR (cm^3 mol^{-1} s^{-1})
k_{O2}^o	kinetic rate constant for the ORR at T = ∞ (cm^3 mol^{-1} s^{-1})
L_{ads}	inductance due to redox of an adsorbed intermediate (Wb A^{-1})
n	number of electrons
n_α	electron transfer number
N	RRDE ring collection efficiency
OCP	open circuit potential for a three electrode cell (V)
OCV	open circuit voltage for a two electrode cell (V)
Ox	oxidant, reactant species to undergo reduction
R	universal gas constant (8.314 j mol^{-1} K^{-1})
R_{ads}	intermediate adsorbate resistance (Ω cm^{-2})
R_{CT}	charge transfer resistance (Ω cm^{-2})
R_i	ionic ohmic resistance (Ω cm^{-2})
Red	reductant, reactant species to undergo oxidation
RH	relative humidity (%)

R_s	ohmic resistance of the solution electrolyte (Ω cm^{-2})
t	time (s, hr)
T	temperature, in degrees Kelvin (K) or degrees Celsius (°C)
X_{H2O2}	fraction of H_2O_2 produced at the disk of an RRDE
Z'	real part of complex impedance from EIS spectra (Ω cm^{-2})
Z''	imaginary part of complex impedance from EIS spectra (Ω cm^{-2})

Greek symbols

α	electron transfer co-efficient
α_a	anodic electron transfer co-efficient
α_c	cathodic electron transfer co-efficient
γ	kinematic viscosity of the electrolyte solution (cm^2 s^{-1})
Γ_{cal}	theoretically calculated surface concentration (mol cm^{-2})
Γ_{exp}	experimentally determined surface concentration (mol cm^{-2})
Γ_{FePc}	surface concentration of adsorbed FePc species (mol cm^{-2})
η	overpotential (V)
η_a	anodic overpotential (V)
η_c	cathodic overpotential (V)
υ	scan rate (V s^{-1})
ω	rotation rate (rpm)

Selected macrocycle nomenclature

FeN_x/C	pyrolyzed 1 iron : 2 nitrogen / 1 iron : 4 nitrogen, carbon macrocyclic structures
FeNpPc	iron naphthalocyanine (preceeded by 1,2 or 2,3 for the respective isomer)
$FeNpPc(tBu)_4$	Iron(II) 2,11,20,29-Tetra-*tert*-butyl-2,3-naphthalocyanine
FePc	Iron(III) phthalocyanine chloride
$FePcCl_{16}$	Iron(II) 1,2,3,4,8,9,10,11,15,16,17,18,22,23,24,25 – hexadecachloro-29H,31H-phthalocyanine
$FePc(SO_3H)_4$	Iron(III) phthalocyanine-4,4′,4″,4‴-tetrasulfonic acid
$FePc(tBu)_4$	Iron(II) 2,9,16,23-Tetra-*tert*-butyl-phthalocyanine
Pc	phthalocyanine
Por	porphyrin
TM	transition metal
TPP	tetra phenyl porphyrin

General nomenclature

BPPG	basal plane pyrolytic graphite
CFP	carbon fibre paper
CME	chemically modified electrode
DFT	density functional theory
DMSO	dimethyl sulfoxide
ECA	catalyst electrochemical surface area (ex-situ, cm^2 Pt g^{-1} Pt)

EPPG	edge plane pyrolytic graphite
EPSA	catalyst effective platinum surface area (in situ, dimensionless)
GDL	gas diffusion layer
HOMO	highest occupied molecular orbital
IPA	isopropanol, or 2-propanol
LUMO	lowest unoccupied molecular orbital
MEA	membrane electrode assembly
MPL	micro porous layer
N,N-DMF	dimethylformamide
ORR	oxygen (O_2) reduction reaction
PEMFC	proton exchange, or polymer electrolyte membrane fuel cell
PFA	perfluroalkoxy
PTFE	poly(tetrafluoroethylene)
SS	stainless steel

Spectroscopy

UV-Vis	ultraviolet and visible
MALDI-TOF	matrix assisted laser desorption ionization – time of flight

Electrochemical techniques

CV	cyclic voltammetry
ECM	equivalent circuit model
EIS	electrochemical impedance spectroscopy
RDE	rotating disk electrode
RRDE	rotating ring disk electrode

Reference electrodes

NHE	normal hydrogen electrode
SCE	standard calomel electrode
RHE	regular hydrogen electrode

Acknowledgements

I would like to thank both of my thesis supervisors, Dr. David P. Wilkinson and Dr. Jiujun Zhang for giving me the opportunity to perform this research as a joint project between the University of British Columbia's Department of Chemical and Biological Engineering (UBC-CHBE) and the National Research Council of Canada's Institute for Fuel Cell Innovation (NRC-IFCI). The opportunity to study and work at the same time is a rewarding challenge and a great privilege. Under their leadership, and through our teamwork, we were able to accomplish far more than I imagined.

The encouragement of Maja Veljkovic to pursue this program, and especially the guidance from both Lori Law and Sabrina Henry to make the most of this work-study opportunity, were invaluable.

Involved discussions with friends and colleagues in both Dr. Zhang's team and Dr. Wilkinson's group were essential in helping perfect my experimental technique as well as data analysis. In particular, input from Dr. Kunchan Lee, Dr. Hansan Liu and Dr. Jianlu Zhang are greatly appreciated.

The patience, help and attention to detail demonstrated by NRC-IFCI's machine shop staff was critical in almost every aspect of the hardware used.

I would like to thank my family for their encouragement, support, and for believing in me.

Finally, the financial support from the National Sciences and Engineering Council of Canada (NSERC) as well as NRC-IFCI are greatly appreciated.

Chapter 1

1.0 Introduction

Versions of some of the chapters presented in this thesis have either been submitted for publication, or published [1]. Further details, along with other related co-authored publications, can be found in Appendix XVI [2,3]. Proton exchange membrane (PEM) fuel cells have the potential for higher energy efficiency and lower emissions than traditional power generation methods, such as internal combustion engines [4]. However, the high cost of PEM fuel cells has hindered their commercialization, mostly due to the use of expensive noble metal electrocatalyst materials such as platinum (Pt) [4]. Therefore, research and development on novel, inexpensive catalyst materials is essential to reduce PEM fuel cell cost. The main approach is to synthesize, evaluate, and then down select candidate catalysts in a manner that enables the transfer of these successful candidates from the laboratory, and into a cost-effective commercial product.

As an alternative to Pt group based electrocatalysts, more commercially viable electrocatalysts, such as substituted iron phthalocyanines (FePc's) and pyrolized iron macrocyclic structures (FeN_X/C), have been actively researched as possible solutions [5-7]. With respect to the oxygen reduction reaction (ORR), the rate determining reaction in a hydrogen / air fuel cell, not only can the metal center play an important role in the catalytic activity of these aforementioned transition metal (TM) macrocyclic catalysts, but the type of macrocyclic ligands

can also significantly affect their activity and stability as well. In addition, different substituents on the same TM macrocyclic ligand, or conjugated heteroatomic ring structure, can also strongly affect the corresponding coordination complexes between the TM and: functional groups of a substrate / support, such as pyrolytic graphite; reactants such as O_2; or even other TM macrocycles [5,7,8]. To obtain a more fundamental understanding of the substituent effect to be used in the design of new catalysts, a systematic study using both experimental and theoretical approaches is necessary.

In this thesis, the substituent effect was investigated by choosing four FePc's with different substituents to investigate their stabilities and catalytic ORR activities using an unsubstituted FePc as the baseline, for comparison. The stabilities and catalytic ORR activities were also studied at different temperatures in order to obtain kinetic information on the catalyzed ORR mechanisms as well as to simulate operating PEM fuel cell conditions. Among these five FePc catalysts, three of them were commercially available, and the other two were synthesized in our laboratory.

With respect to the evaluation of the as bought and in house synthesized FePc's, electrochemical methods such cyclic voltammetry (CV), rotating disk electrode (RDE) as well as rotating ring-disk electrode (RRDE) voltammetry, electrochemical impedance spectroscopy (EIS), and fuel cell testing were performed under various experimental conditions. The whole process for evaluating catalysts such as FePc species involved the following experimental conditions: electrode preparation of the catalyst alone; catalyst ink and catalyst

layer formation to make catalyst ink electrodes; as well as the fabrication of the membrane electrode assemblies (MEA's) using the catalyst. Spectroscopic methods such as UV-Vis, as well as matrix assisted laser desorption ionization time of flight (MALDI-TOF) mass spectrometry were also used to characterize the structure of the newly synthesized FePc's.

Electrochemical evaluation of the FePc species alone, and the FePc species catalyst ink coated electrode for PEM fuel cell catalyst evaluation, respectively, was achieved using the novel half-cell described in Chapter 2. The corresponding electrode design for evaluating the FePc species alone is shown in Appendix VII, and that for the FePc species catalyst ink coated electrode is shown in Chapter 5. The objective was to validate both the novel half cell and the in situ catalyst ink coated modified working electrode (WE) at four different temperatures (20, 40, 60, 80°C) in a PEM fuel cell like environment using ex situ techniques [2].

In Chapter 2, as two of the substituted FePc species selected were not commercially available, they were synthesized in house, characterized, and then tested for ORR activity. A simple synthesis method, similar to that reported by Nemykin and co-workers [9], was employed to insert the Fe centre into commercially available Pc ligands. To characterize catalyst structure and activity, spectroscopic methods such as UV-Vis, and MALDI-TOF mass spec, as well as electrochemical methods were used [10], [11-15]. For the first time, the synthesis of two FePc species with de-activating substituents as well as their preliminary ORR activities were reported, and compared, at 20°C in Chapter 2.

In Chapter 3, all five unsupported FePc species, adsorbed on a pyrolytic graphite electrode, were evaluated in the novel half-cell designed for this thesis at four different temperatures (20, 40, 60, 80°C) using conventional electrochemistry techniques such as CV and RDE. The FePc species' redox couples (surface waves), surface concentrations on the pyrolytic graphite electrode, and their corresponding ORR activities, which included kinetic parameters, were described along with substituent and temperature effects. The best substituted FePc in terms of stability and ORR activity was then down selected.

In Chapter 4, the results reported in Chapter 3 were verified using RRDE voltammetry and the same novel half cell. The fraction of H_2O_2 produced (X_{H2O2}) as a by-product of the ORR (an undesirable reaction intermediate) was reported for each of the five FePc species and then compared to the respective observed number of electrons transferred for the ORR (n) reported in Chapter 3.

In Chapter 5, both the down selected FePc from Chapter 3 as well as the baseline FePc were used to make FePc catalyst ink coated electrodes. Their activities were evaluated in the same novel half cell and then compared to those for the respective unsubstituted FePc species from Chapter 3. Both FePc's were then used as cathode catalysts in MEA fabrication. Preliminary fuel cell performance data for these FePc MEA's, evaluated in a custom in house fuel cell, was also described in Chapter 5.

In summary, five FePc species were evaluated as a function of substitution and temperature as PEM fuel cell ORR electrocatalysts using three successive

approaches. These three approaches evaluated the unsupported FePc species, the supported FePc species in a catalyst ink coated CFP, and finally the FePc species cathode in a MEA inside an operating PEM fuel cell. The ORR mechanisms catalyzed by these FePc species, as well as the effect of substituents and temperature on their stabilities and reaction kinetics, were explored in this thesis. The results obtained here gave insight into the FePc species electrocatalyzed ORR from in terms of fundamental understanding as well as potential applications in PEM fuel cells.

1.1 Research objectives and approach

Non-noble metal catalysts, such as TM macrocycles are actively researched in contemporary scientific journal papers for a broad range of useful applications, including PEM fuel cells [7,8]. The most common TM macrocyles studied are porphyrins (Por) and their analogues. To date, the most promising TM macrocyles are the porphyrin analogues tetra phenyl porphyrin (TPP) and phthalocyanine (Pc). The focus of this thesis was the latter, specifically, substituted Iron (Fe) phthalocyanines (FePc's).

Objectives

The objectives were: (1) to compare the cathodic electrocatalytic activity of FePc's having different electron withdrawing and donating substituents for the oxygen reduction reaction (ORR) at different temperatures in a cathodic PEM fuel cell environment, (2) based on the performance of the best substituted, or down selected FePc species, evaluate its' performance as a potential PEM fuel cathode catalyst in a real fuel cell environment, and (3) to gain a more fundamental understanding how structure relates to reactivity in order to further improve both catalyst stability and activity, as well as new catalyst design.

Approach

This thesis focused on the electrocatalytic activity of substituted FePc's, including a trend of electron withdrawing and donating substituents as a function of temperature, as PEM fuel cell cathode catalysts for the ORR. Electron withdrawing or acceptor (de-activating) substituents increased, and electron donating (activating) substituents decreased, catalytic activity, respectively [16].

Additionally, activity as a function of temperature, as a function of increasingly electron donating or withdrawing substituents, or even in a cathodic PEM fuel cell environment has not yet been experimentally examined. This thesis is novel in that substituted FePc's are tested using conventional electrochemical techniques in an environment closer to that of the PEM fuel cell cathode. To date, literature on testing TM macrocycles as electrocatalysts in a PEM fuel cell environment is limited [17-22]. Therefore, this research will make a valuable contribution towards the evaluation of TM macrocycles for PEM fuel cell applications.

As all of the desired Pc's were difficult to find commercially, two substituted FePc's were custom synthesized for evaluation. Once the five FePc catalyst species had been obtained, and/or synthesized, they were evaluated: unsupported on a pyrolytic graphite electrode; supported in a catalyst layer electrode; and as the cathode catalyst layer in an MEA, all using conventional electrochemical techniques and fuel cell performance testing. Using a novel half-cell design, the catalytic ORR activities of these substituted FePc's were evaluated at temperatures of 20, 40, 60 and 80°C in an acidic aqueous electrolyte. The electrochemical data obtained was used for kinetic studies.

From the experimental results and data analysis, two trends were observed: one showing the relative increase or decrease in activity of substituted relative to unsubstituted FePc's, and the other showing the effect of temperature on each separate FePc.

Finally, the best substituted FePc was down selected and used to make a catalyst ink which was spray coated onto carbon fiber paper (CFP). A small section of the catalyst ink coated CFP was used first to make electrodes to test the activity of the two FePc catalyst inks. The remaining sections were used to make two sets of FePc cathode MEA's. The FePc catalyst ink CFP electrodes were evaluated in the same novel half cell and the FePc cathode MEA's were evaluated in an in-house designed and fabricated fuel cell.

1.2 Literature review

TM macrocycles are one of the many different non-noble metal catalyst routes that are actively researched both in fundamental studies and in practical applications [7,8]. The most common TM macrocycles studied are TM porphyrins and their analogues: TM tetraphenyl porphyrins (TM TPP's) and TM phthalocyanines (TM Pc's). These types of TM macrocycles have been investigated mainly as cathodic ORR catalysts, as the largest overpotential of the two electrochemical reactions occurring in a hydrogen (H_2) PEM fuel cell is exhibited by the ORR [23]. Indeed, it is the cathode polarization at all current densities as well as mass transport limitations at high current densities that influence all PEM fuel cell performance [24]. A significant amount of work has been done in the field of the TM macrocyclic catalyzed ORR [5,6,25-27], but little in the environment of an operating PEM fuel cell, or as a function of temperature and substitution in an acidic electrolyte ($pH \leq 4$) adsorbed on pyrolytic graphite.

In general, the reduction of O_2 to water is a four electron ($4e^-$) process [23,28] that can proceed via different pathways as shown in Figure 1.1 [23,29,30]:

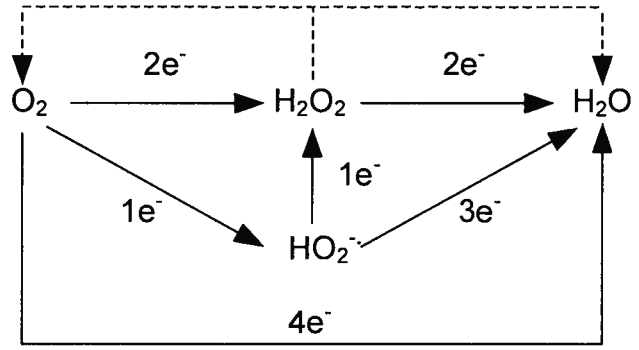

Fig. 1.1. Oxygen reduction reaction pathways (solid lines) and peroxide chemical decomposition (dashed lines) in an acidic aqueous electrolyte.

The first, and most preferable path is the $4e^-$ reduction directly to water. The second, and more common path is the $2e^-$ reduction to hydrogen peroxide (H_2O_2) with a further $2e^-$ reduction that converts H_2O_2 to water. With the formation of H_2O_2, there also exists the possibility of a chemical decomposition, or disproportionation, to form O_2 and water. The third, and least preferable path is the $1e^-$ reduction to the hydroperoxyl radical ($HO_2^{\cdot}$) in acidic media or to the superoxide (O_2^-) in basic media. The one electron ORR product is unstable, and thus seldom observed as a free species in basic electrolytes (pH > 10) [31,32]. Otherwise it rapidly decomposes upon formation. Using a TM Pc ($CoPcF_{16}$) catalyst, a stable superoxide species was observed, but in basic solution [32]. Under normal conditions at an otherwise inert electrode (e.g., Pt or Gold (Au)), the one electron pathway is highly unfavourable relative to the four and two electron pathways [30]. In fuel cell applications, the most favorable ORR pathway is the direct $4e^-$ reduction pathway. The formation of hydrogen peroxide and/or hydroperoxyl / superoxide is undesirable due to their detrimental effects on the fuel cell membrane and catalyst layers. Some catalysts, such as FePc,

promote this decomposition / disproportionation reaction. This type of chemical catalytic activity is known as catalase activity [29,33]. It is therefore desirable to have cost-effective catalysts that can selectively catalyze the four-electron reduction of O_2 directly to water with low overpotential, as well as low H_2O_2 and $HO_2^{-\cdot}$ / O_2^{-} production [34].

This need for a more economic alternative to noble metal catalysts has led current research to the following most promising options [28]:

1. Low loading Pt catalysts supported on high surface area of carbon black.
2. Transition metal chalcogenides.
3. Poly-nuclear metal compounds.
4. Transition metal macrocycles.

Because the ORR involves multiple electron-transfer steps, and in turn, a high activation barrier to initiate the reaction, current non-Pt based electrocatalysts require significant improvement [35]. In this regard, TM macrocyclic electrocatalysts show much promise.

Starting with work by Jasinski [36] and later Jahnke [37], the ability of TM porphyrins and phthalocyanines to reduce diatomic, π-bonded gases, including O_2, has led to significant research in the ORR field, particularly as possible PEM fuel cell electrocatalysts.

The basic structure of a TM macrocycle constists of a metal centre (TM), that has redox couple capability, and a large planar conjugated ring structure which binds the metal center via four nitrogen (N) moities [37]. In order of decreasing

catalytic activity, the most active TM macrocycle compounds towards the ORR in acidic solution are [29,33]:

1. Fe > Co > Cu phthalocyanine (Pc)
2. Co > Fe > Cu tetra phenyl porphyrin (TPP)

Structure and numbering of positions for both porphyrin based macrocyle compounds are shown (without metal centres) in Figure 1.2. Of the two aforementioned macrocycles, TM Por and TM TPP show higher activity than TMPc's towards O_2 reduction [38]. TM TPP's are more active than TM Por's due to the effect of the four phenyl groups on the aromatic porphyrin ring. However, electrocatalyst stability is difficult to realize in an acidic environment, with constant temperature changes [24].

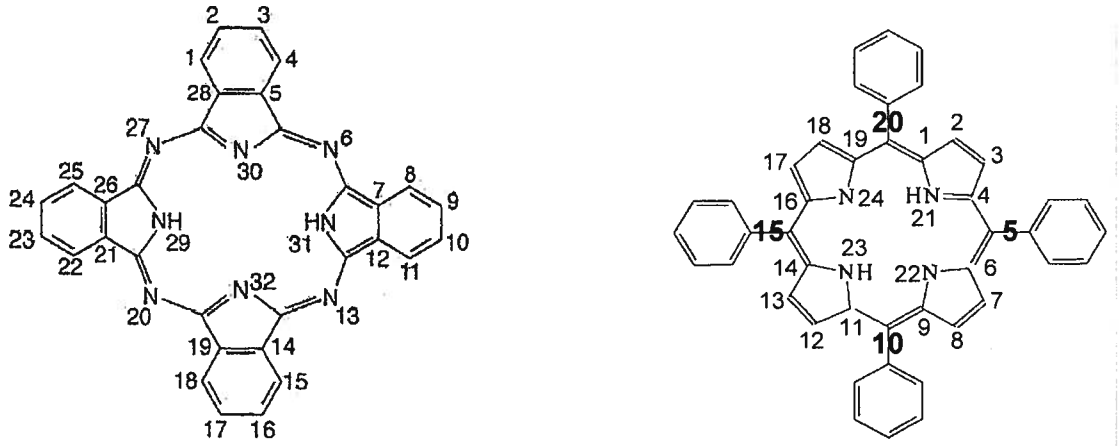

(a) (b)

Fig. 1.2. Numbering of positions for (a) Pc [39], and (b) TPP [17,30].

TM Pc's are studied as possible PEM fuel cell ORR electrocatalysts because the added tetra aza nitrogens give them greater thermal stability and lower susceptibility to oxidation when compared to porphyrins, including TPP [39,40]. Relative to TM Pors and TM TPP's, TM Pc's are generally easier to synthesize and more cost effective to produce [10]. In this manner, even though TM TPP's may be better electrocatalysts for the ORR [29,41], they are not as stable as Pc's in a PEM fuel cell environment, and lose their catalytic activity over time more quickly.

It has been recognized that adding functional groups, or substituents, to a TM macrocycle plays a critical role in its' chemical as well as electrochemical properties and functionalities [7,10,16,41-48]. It appears that the selectivity of TM macrocycles towards a chemical and/or electrochemical reaction is "set" by the TM centre, and the activity is then "tuned" by the peripheral substituents [7,8]. The number and position of these substituents both on the macrocyle and on one or both of the metal centre's axial sites can significantly change both its' electro-catalytic and purely chemical catalytic activity, as well as the associated reaction mechanisms [7,8,16,29,39,41,44,46,48-50]. Conversely, strongly electron donating substituents at the para position on all four meso (5, 10, 15, 20) phenyls in TM TPP increases catalytic activity [29,48,49]. In addition, even the site of electrocatalytic activity can be changed from the metal centre to sites on the organic ring structure [45]. For TM Pcs, strongly electron withdrawing substituents at all available sites (e.g., fully halogenated (X) at positions 1,2,3,4,8,9,10,11,15,16,17,18,22,23,24,25 or PcX_{16}) on the four fused phenyl

rings increases catalytic activity towards the ORR [7,8,29,39]. Symmetrically substituted de-activating, or electron withdrawing substituents with inductive effects (e.g., SO_3H and Cl) have the strongest influence in increasing TM Pc catalytic activity if, and only if, they are incapable of forming π-bonds directly with the macrocycle. Any π-bonds formed directly to the Pc ring likely create unstable resonance structures, relative to the unsubstituted Pc. Symmetrically substituted activating, or electron donating, substituents at these positions (e.g. $(tBu)_4$) would be expected to decrease TM Pc catalytic activity [7,8,29,39]. This can be explained in terms of using global and local hard soft acid base (HSAB) theory where a local hard acid (Fe^{II}) attracts a local hard base (O_2) [45]. Indeed, the central metal ion gains Lewis acid character when FePc is hexa deca substituted with chlorine [16]. It is thus important, relative to Fe, to decrease the basicity of the electron rich Pc. It is this relative change in acidity of the Fe centre that has the most pronounced effect on electrocatalyst activity, as long as the associated decrease in electron density does not significantly affect the Fe centre to the point that it is unable to back bond with the adsorbed O_2, and affect the transfer of electron density into O_2's anti-bonding orbitals. It is this relative change in acidity that has the most significant effect on electrocatalyst activity. However, the effect of fully halogenating FePc could modify the chemical or catalase activity and not the electrochemical activity [45]. Also, these substituents increase the FePc's maximum net charge, that can also be a good indicator for the preferred reaction site [45]. In addition to increasing catalytic activity, the effect of fully substituting TM Pc's with de-activiating substituents with inductive

effects increases the ionization potential of the macrocycle, thus protecting it from oxidative destruction or decomposition [46].

Another explanation is that substituents change the energy level(s) of the TM Pc's electronic orbitals. The electronic transitions in among the TM Pc's orbitals as well as those to and from a reactant's orbitals (with sufficient overlap) determine the stability of the TM Pc and the reactivity between the TM Pc and the reactant(s), respectively [8,26]. The energy gap between the TM Pc's highest occupied molecular orbital (HOMO) and lowest unoccupied molecular orbital (LUMO) have a significant effect on its' stability. The smaller the gap, the more facile the electronic transitions to and from the HOMO to the LUMO. If the LUMO is an anti bonding orbital, which is the case for the FePc species shown here, then any electronic transitions into the LUMO de-stabilize the molecule. Conversely, the larger the gap, the more stable the molecule. For TM Pc's, electron withdrawing substituents decrease the energy of the HOMO, increasing the gap between the HOMO and LUMO, thus stabilizing the TM Pc. The converse is true for electron donating substituents. To experimentally elucidate these changes in TM Pc energy levels, UV-Vis spectroscopy has been shown to be a good method to determine the energy levels of the HOMO, referred to as the Q band (600-750 nm), and of the LUMO, referred to as the Soret band (300-450 nm) [5,8].

Zagal and co-workers have shown that molecular hardness is a good measure of both the stability of TM Pc's as well as their activities towards the ORR [5,26,27,45]. Hardness is defined as roughly one half the difference

between the energy of the TM Pc's HOMO and LUMO. The larger the gap, the greater the hardness and the more stable the TM Pc. The converse is true as this gap decreases.

To better understand the effect of substitution on TM Pc's towards ORR activity, Zagal and co workers [5] described the donor acceptor hardness of the donor-acceptor pair, where the TM Pc is defined as the electron donor, and O_2 is defined as the electron acceptor. The donor-acceptor hardness is defined as one half the difference between the energy of the LUMO of the acceptor, and the energy of the HOMO of the donor. Stated previously, symmetric electron withdrawing substituents reduce the energy level of the donor TM Pc's HOMO, making the gap between its' LUMO and HOMO larger, increasing the TM Pc's hardness and hence making it more stable. However, the energy of the acceptor O_2' s LUMO remains unchanged and lower than that of both the TM Pc's LUMO and HOMO. Therefore, as the TM Pc's hardness increases as a result of the electron withdrawing substitutents, the donor acceptor hardness is actually decreasing, making the energy gap between the TM Pc's HOMO and O_2's LUMO smaller, decreasing their combined hardness and hence increasing their reactivity. Conversely, electron donating substituents, such as tetra *tert* butyl groups increase the TM Pc's HOMO making it both more unstable on its' own as well as less reactive towards the ORR in comparison to both the unsubstituted FePc as well as FePc's with electron withdrawing substitutents.

Finally, the type of support or substrate to which the TM Por or macrocycle electrocatalyst is bound to, or deposited on, also has a significant effect on

catalytic activity. For example, TM Por and porphyrin analogues (TM Pc, TM TPP, etc.) electrocatalysts supported on basal and edge plane pyrolytic graphite (BPPG and EPPG, respectively) electrodes give the best catalytic activity, whereas those supported on glassy carbon show relatively little activity [30,51]. This might be because polishing of the BPPG or EPPG electrodes introduces functional groups on the exposed graphite planes that could act as anchors for the adsorbed complexes [51]. Such supported catalyst electrodes are termed Chemically Modified Electrodes (CME's) [7,33,48,51].

It should be noted that since the work of Bagotzky [52], it has been known that the heat treatment of TM macrocycles in an inert (anoxic) atmosphere at temperatures of several hundred degrees Celsius significantly increases their stability and catalytic activity [53,54]. Further studies have shown pyrolizing a mixture of the TM, an organic precursor and a source of nitrogen in an inert atmosphere produces similar results [6,18-21,55,56]. However, the structures are not defined well enough for a true quantitative study and the exact ratio of Fe/N at the active catalytic sites is difficult to determine [21]. Additionally, both FeN_2/C as well as FeN_4/C have been shown to be catalytically active species for the ORR [18]. Even though the catalytic results may be more promising than those for the non-pyrolized macrocycles, the structure(s) and mechanism(s) need to be known in order to quantify what makes the most active and stable pyrolyzed TM catalyst. For this reason, studying well-defined TM macrocycles, such as different FePc species, offer the opportunity to study model systems and quantify the link between structure and reactivity, possibly allowing comparison to, and

insight into their more active, stable and less expensive pyrolyzed analogues. A full study of the pyrolized FeN_x/C analogues is beyond the scope of this thesis.

Of the five FePc species selected, three of them were commercially available from Sigma Aldrich. These three FePc species are shown in Figure 1.3. The other two were not commercially available, but their Pc ligands were available from Sigma Aldrich as well. These two substituted Pc ligands are shown in Figure 1.4. After reviewing the literature, a synthesis method was used [9] to successfully insert the Fe metal centre into the substituted Pc ligands using the laboratory facilities at NRC-IFCI.

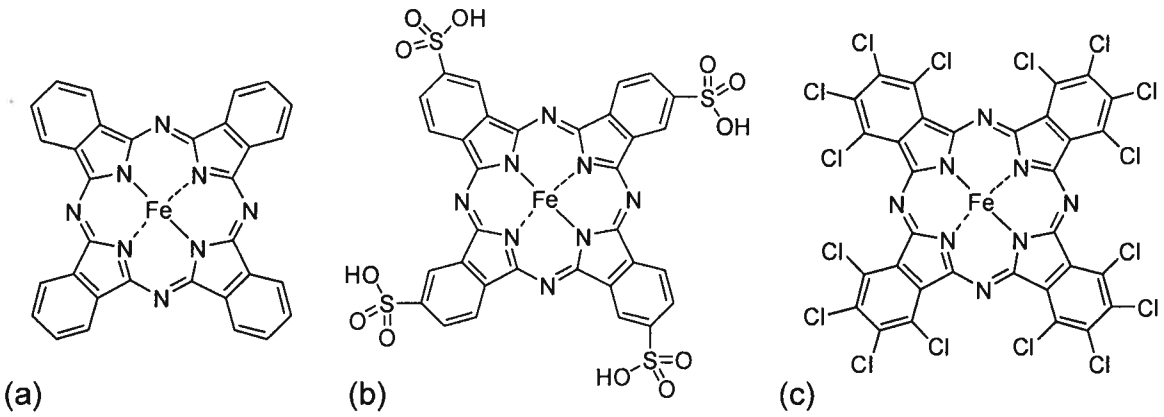

Fig. 1.3. (a) Iron(III) phthalocyanine chloride (Aldrich catalogue number: 37,957-3), (b) Iron(III) phthalocyanine-4,4′,4″,4‴-tetrasulfonic acid (Aldrich catalogue number: 45,252-1), and (c) Iron(II) 1,2,3,4,8,9,10,11,15,16,17,18,22,23,24,25-hexadecachloro-29H,31H-phthalocyanine (Aldrich catalogue number: 44,804-4).

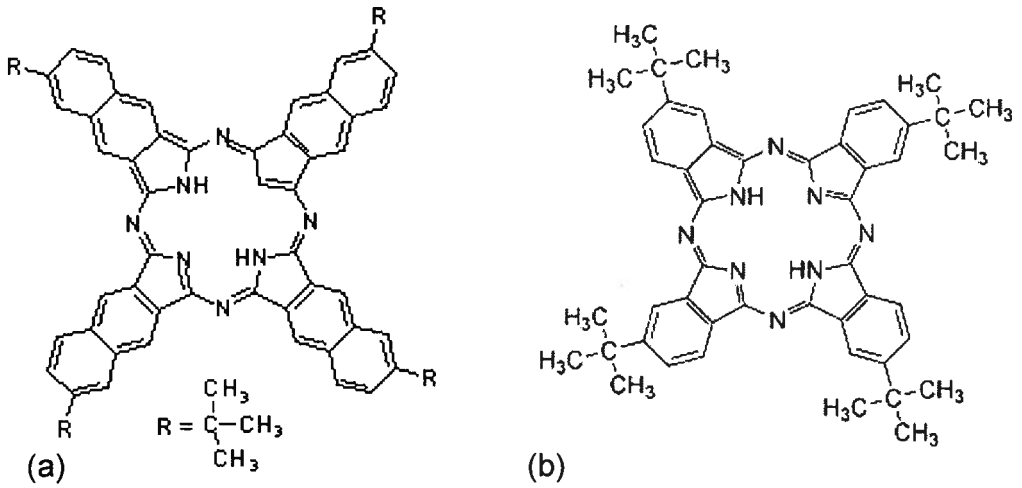

Fig. 1.4. (a) 2,11,20,29-Tetra-tert-butyl-2,3-naphthalocyanine (Aldrich catalogue number: 42,527-3), and (b) 2,9,16,23-Tetra-tert-butyl-29H,31H-phthalocyanine (Aldrich catalogue number: 42,315-7).

Electrochemical testing was performed using CV's, RDE, RRDE, and possibly EIS measurement techniques and analysis methods. All equipment and laboratory facilities described herein were in place and operational at NRC-IFCI.

FePc's on both pyrolytic graphite, and CFP, electrodes were constructed according to established procedures [2,3]. The electrolyte throughout all experiments was 0.1 M H_2SO_4. The novel half-cell used for electrochemical measurements is shown in Chapter 2. CV's were run using a Solartron 1287A or 1480A Potentiostat and EIS were run using the same 1287A or 1480A Potentiostat coupled to a Solartron 1260B or 1255B frequency response analyzer (FRA), respectively. The associated Scribner software was used for data logging and analysis. RDE and RRDE experiments were performed using an ARS or MSR rotator, respectively (Pine Instruments). The RRDE experiments were operated using Pine's AFCBP1 computer controlled Bipotentiostat.

For electrode adsorption studies, surface waves from cyclic voltammograms were observed on a FePc modified pyrolytic graphite electrode. From the surface wave CV's the actual surface concentration and orientation of adsorbed FePc's were obtained. The number of electrons involved in each step, the pH dependence, and the number of protons involved could be calculated as future work.

For ORR activity measurements, the bare, followed by the adsorbed FePc species electrode were both scanned in N_2 saturated 0.1 M H_2SO_4 until a stable surface CV was obtained. Then the solution was bubbled with air to make an O_2 saturated electrolyte. Using this catalyzed electrode, the ORR CV was then

recorded. This process was repeated at different temperatures. Using Figure 1.5(i) and $Co^{II}PcF_{16}$ as an example, the following CV's were run: (a) bare electrode in the presence of O_2; (b) $Co^{II}PcF_{16}$ adsorbed electrode in the presence of O_2; (c) $Co^{II}PcF_{16}$ adsorbed electrode in the absence of O_2; (d) $Co^{II}PcF_{16}$ adsorbed electrode in the presence of H_2O_2; (e) bare electrode in the presence of H_2O_2. It was important to run CV's of FePc's in the presence of H_2O_2 (at the same concentration as the dissolved O_2) and in the N_2 purged electrolyte, to see if the TM Pc was active for H_2O_2 reduction. The aforementioned procedure was repeated for each of the five FePc species at each of the four temperatures. The conditions for the CV shown in Figure 1.5(i)(f), the $Co^{II}PcF_{16}$ adsorbed electrode in the presence of O_2 and 1.0 M methanol, were not tested for this thesis.

Quantitative kinetic parameters for the FePc species catalyzed ORR were evaluated through RDE voltammetry at different rates of rotation and at each of the four temperatures (Figure 1.5(ii)). The RDE data was first used to roughly estimate kinetic parameters for the ORR. This was done using a simplified cathodic Butler-Volmer equation, or Tafel equation, from which the Tafel slopes were obtained from the kinetic region of the RDE scans at each of the four temperatures. The Tafel plot allowed kinetic parameters such as b, and αn_α to be obtained, where b is the Tafel slope, and $n_\alpha \alpha_c$ is the cathodic transfer co-efficient, for the TM Pc catalyzed ORR. The reciprocal of the limiting current (plateau currents in Figure 1.5(ii)) was then plotted against the reciprocal of the square root of the rate of rotation alongside a plot calculated according to Koutecky-Levich theory. From the Koutecky-Levich plot, the observed number of

electrons transferred (n), the kinetic rate constant for the ORR (k_{O2}), the kinetic rate constant at infinite temperature (k_{O2}^{O}) and the ORR activation energy (E_a) were also obtained. A more detailed discussion of k_{O2}, k_{O2}^{O} and E_a can be found in Appendix XIII. Based on the information obtained as well as information from the literature, FePc electrocatalytic O_2 reduction mechanisms were proposed. RRDE voltammetry was then used to confirm the RDE results and quantify the amount of H_2O_2 produced by the FePc species catalyzed ORR.

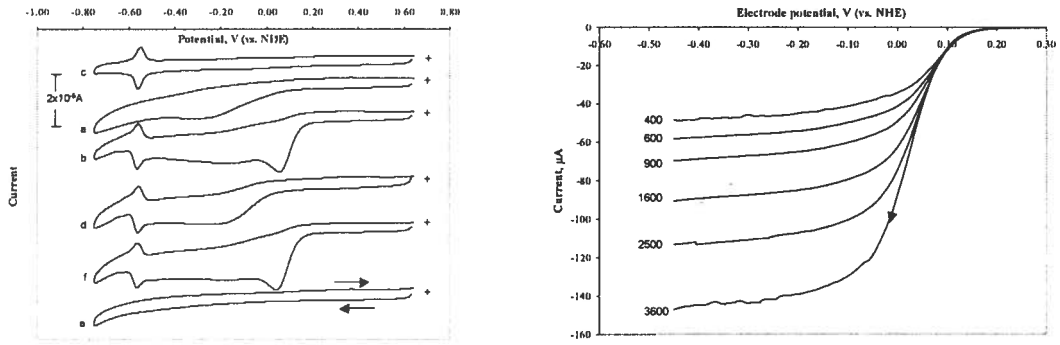

(i) (ii)

Fig. 1.5. (i) CV's of $Co^{II}PcF_{16}$ on EPPG [3], (ii) RDE current-potential curves, both in 0.1 M $NaHSO_4$, pH = 6.0, 1 atm, at 20°C [3].

The Tafel method described (vide supra) only yielded limited information about the reaction mechanism. For other reaction parameters that occur within the catalyst layer, such as mass transfer resistance, ionic conductivity, etc., EIS, or specifically AC impedance spectroscopy, was used to quantitatively obtain such parameters. A modified equivalent circuit model (ECM) was developed to obtain model fuel cell reaction kinetic parameters using Z-Plot's complex non-linear least squares-fitting program to fit the ECM curve to the EIS experimental data, or Nyquist plots [2]. Kinetic parameters included: ohmic resistance of solution electrolyte, ionic resistance and capacitance, charge transfer resistance, etc., depending on the reaction to be studied.

The EIS and ECM techniques described yielded useful data for a model fuel cell reaction used to validate the half cell and calalyst ink coated electrode [2]. However, when the same techniques were applied to the FePc cathode catalyst MEA's later in this thesis, the initial results were inconclusive. This is further discussed in Chapter 5.

As a final experiment, the best substituted and unsubstituted FePc's were used as cathode catalysts to make test MEA's that were evaluated in an in-house designed and built fuel cell using one of NRC-IFCI's FC test stations. A view of the fuel cell to be used is shown in Figure 1.6.

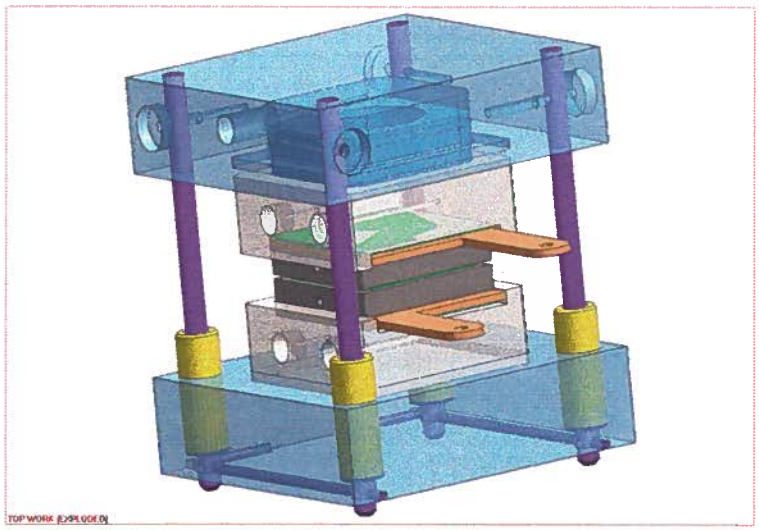

Fig. 1.6. In-house designed and built fuel cell (see Chapter 5 and Appendix IV for further details).

The FePc cathode MEA's were made by spray coating commercial gas diffusion layers (GDL's) [20,57,58]. A Fideris FCTS test station, gas humidifier, and software was used with the fuel cell shown in Figure 1.6. The fuel cell was operated at 80^0C, 30 psig back pressure, as well as a bladder pressure of 50 psig, with H_2 and O_2 flow rates of 0.03 and 0.09 L min^{-1} at 100% RH, respectively.

1.3 Research significance and ultimate impact

TM macrocycles, such as FePc's, are promising low cost alternatives to platinum (Pt). Developing a low cost PEM fuel cell catalyst is a key driver to make fuel cells commercially viable. Much work is still needed in the field of non-noble metal catalysis, including TM macrocylces such as FePc. $FePcCl_{16}$ has been shown to be a promising non-noble metal catalyst [7,59,60]. Studying the effect of different electron withdrawing and donating substituents as a function of temperature is novel and, could give more details on the ORR mechanism and parameters that affect pyrolyzed FeN_x/C analogues.

Insight into the reaction mechanism as a function of temperature and different electron withdrawing and donating substituents has added knowledge in the field of non-noble metal catalysis through publications [1-3]. In addition, this project added to the core competency of the National Research Council of Canada's Institute for Fuel Cell Innovation (NRC-IFCI), and built stronger links with the University of British Columbia (U.B.C.), specifically the chemical and biological engineering department and clean energy research centre.

Chapter 2

Facile Synthesis, Spectroscopy and Electrochemical Activity of Two Substituted Iron Phthalocyanines as Oxygen Reduction Catalysts in a Fuel Cell Environment

2.0 Objective

Two substituted FePc macrocycles were synthesized and their activity as oxygen reduction electrocatalysts were demonstrated in a PEM fuel cell environment. The non-noble, TM macrocycles Iron(II) 2,9,16,23-Tetra-*tert*-butyl-phthalocyanine ($FePc(tBu)_4$), and Iron(II) 2,11,20,29-Tetra-*tert*-butyl-2,3-naphthalocyanine ($FeNpPc(tBu)_4$) were made via a facile synthesis. Successful synthesis was confirmed using UV-Vis spectroscopy as well as matrix-assisted laser desorption/ionization time of flight (MALDI-TOF) mass spectroscopy. These two substituted FePcs were characterized using CV and their electrocatalytic activities towards the oxygen reduction reaction (ORR) were demonstrated using CV techniques.

2.1 Description

In selecting and testing substituted FePc candidates, the advantange of a simple synthesis method allows the insertion of Fe into a wide variety of commercially available substituted Pc ligands. Such a method was employed in this chapter using a portion of the synthesis reported by Nemykin and co-workers

[9]. Elsewhere in the literature synthesis, spectroscopic characterization, and electrochemical stability of Cobalt(II) 2,11,20,29-Tetra-*tert*-butyl-2,3-naphthalocyanine ($CoNpPc(tBu)_4$), and Cobalt(II) 2,9,16,23-Tetra-*tert*-butyl-phthalocyanine ($CoPc(tBu)_4$) have been reported [10], as has the synthesis, and ORR activity, of FePc as well as FeNpPc [11-15].

For the first time, the synthesis, spectra, and preliminary ORR activities of $FePc(tBu)_4$ as well as $FeNpPc(tBu)_4$ are reported, and compared. The effect of de-activating substituents on two Fe phthalocyanines is demonstrated. These FePc species were irreversibly adsorbed onto a pyrolytic graphite electrode and electrochemically evaluated in a PEM fuel cell-like environment of 0.1M H_2SO_4, at room temperature, and 1 atm. The initial results presented show stability and ORR activity comparisons can be made between the unsubstituted, and tetra tert butyl substituted, FePc and FeNpPc electrocatalysts. UV-Vis spectra demonstrates a decrease in stability and ORR activity for $FeNpPc(tBu)_4$ compared to $FePc(tBu)_4$, which is confirmed by preliminary ORR CV data.

2.2 Experimental

2.2.1 Chemicals

2,11,20,29-Tetra-*tert*-butyl-2,3-naphthalocyanine (Sigma cat. no. 425273, lot no. 05012CA), 2,11,20,29-Tetra-*tert*-butyl-phthalocyanine (Sigma cat. no. 423157, lot no. 13506DC), (abbreviated as $NpPc(tBu)_4$, and $Pc(tBu)_4$ respectively), and Iron(II)chloride tetrahydrate (Sigma cat. no. 220299, batch no. 11001BH) were all purchased from Sigma Aldrich and used as received. Potassium chloride, potassium ferricyanide, N,N-dimethylformamide, pyridine,

sulfuric acid, acetone, ethanol (100% reagent alcohol), and dimethyl sulfoxide (certified A.C.S. spectranalyzed) were all purchased from Fisher, certified A.C.S. reagent grade, unless otherwise marked in brackets, and used as received. Aqueous solutions were prepared using de-ionized (DI) water, 18.2 MΩ cm^{-1}, from a Millipore MilliQ purification system. Nitrogen gas (99.999%), UHP 5.0 from Praxair, was first bubbled through a gas sparger (Sandfire Scientific Ltd.) filled with DI H_2O before being bubbled through the electrolyte to remove O_2. Air (filtered, oil-free, -40°C dewpoint) was bubbled in the same fashion as N_2 to saturate the electrolyte with O_2. Gasses were bubbled for at least 45 minutes at the desired temperature before performing any experiments.

2.2.2 Synthesis of iron(II) 2,11,20,29-tetra-tert-butyl-2,3-naphthalocyanine

Iron(II) 2,11,20,29-Tetra-*tert*-butyl-2,3-naphthalocyanine ($FeNpPc(tBu)_4$) was synthesized under 99.9999% argon (6.0 research grade, Praxair) in a one step reaction between the as-bought $NpPc(tBu)_4$ and Iron(II) chloride tetrahydrate according to the method of Nemkyn et. al. [9]. A labelled photo of the synthesis set up is shown in Appendix II.

Glassware (round bottom flask, stoppers and adaptors) that was in contact with synthesis reagents were thoroughly washed and then submerged in a hot mix of 50/50 H_2SO_4 and HNO_3, followed by rinsing in DI H_2O. Other glassware was first rinsed with Ethanol, followed by Acetone, and then rinsed, washed, and rinsed again in DI H_2O. All glassware was finally dried in an oven at 90°C.

0.5253 g of $NpPc(tBu)_4$ and 0.2124 g of Iron (II) chloride tetrahydrate were weighed out using a Denver Instruments Pinnacle Series PI-214 analytical balance and quickly transferred to a 500 ml three neck round bottom flask containing a magnetic poly(tetrafluoroethylene) (PTFE) stir bar. 68 ml of dimethyl sulfoxide (DMSO) (Fisher cat. no. D136-1, lot no. 040295) was added followed by insertion of a Hg thermometer and a glass pasteur pipette, both submerged in the reactant mixture, through the respective adaptors. Argon was connected to the pipette and a reflux condenser with an outlet drying tube was attached to the round bottom flask. All connections were sealed with Dow Corning silicone vacuum grease. The mixture was left to stir, bubbling under Argon for three hours at room temperature to ensure the synthesis environment was fully purged of air and water.

The synthesis apparatus was then submerged in an insulated mineral oil bath and heated to 180 - 185°C. The mixture refluxed under Argon for 45 minutes, after which it was removed from the oil bath and left to cool to room temperature while stirring and still under Argon.

The synthesis mixture was transferred to a vacuum flask mounted Buchner funnel and filtered at room temperature (Whatman no. 42, 125 mm diameter, cat. no. 1442125). The filtrate was poured into a 250 ml solution of hot, saturated KCl in DI H_2O. The resulting slurry was filtered again and rinsed several times with DI H_2O. The resulting filtrate was disposed. The solid product was dried at 75°C under vacuum (–30 inches Hg) for 5 hours.

The final product yield was 0.2587 g. The reactant $NpPc(tBu)_4$ was grass green in colour, and the product was an olive brown colour. Assuming 1:1 stoichiometry, with pure $NpPc(tBu)_4$ as the limiting reagent, a pure product, and that the reaction goes to completion, the final yield was 46.5%. This compares well to Nemykin and co-worker's final yield of 49.5% [9].

As an initial test to see if the synthesis product was ORR active, a simple CV test scan was performed (vide infra) which yielded a similar result to those for the as-bought FePc's. Spectroscopy was then used to confirm successful synthesis.

2.2.3 Synthesis of iron(II) 2,11,20,29-tetra-tert-butyl-phthalocyanine

Iron(II) 2,11,20,29-Tetra-*tert*-butyl-phthalocyanine ($FePc(tBu)_4$) was synthesized under 99.9999% argon (6.0 research grade, Praxair) in a one step reaction between the as-bought $Pc(tBu)_4$ and Iron(II) chloride tetrahydrate, also according to the method of Nemkyn et. al. [9]. Again, a labelled photo of the synthesis set up is shown in Appendix II.

Glassware was cleaned and prepared according to section 2.2.2. 0.5209 g of $Pc(tBu)_4$ and 0.3030 g of Iron (II) chloride tetrahydrate were weighed out using a Denver Instruments Pinnacle Series PI-214 analytical balance and quickly transferred to a 500 ml three neck round bottom flask containing a magnetic PTFE stir bar. 68 ml of DMSO (See section 2.2.2) was added to the round bottom. The same synthesis steps as described in section 2.2.2 were then followed.

The reactant $Pc(tBu)_4$ was sky or Nordic blue in colour, and the product $FePc(tBu)_4$ was a blue green colour. The final product yield was 0.4846 g.

Assuming 1:1 stoichiometry, with pure $Pc(tBu)_4$ as the limiting reagent, a pure product, and that the reaction goes to completion, the final yield was 86.5%. This is significantly higher than Nemykin and co-worker's final yield of 49.5% [9]. Possible reasons for the difference in yield could be that the literature results are for Lanthanide derivatives of Tetra-*tert*-butyl-2,3-naphthalocyanine, while the synthesis above is for Tetra-*tert*-butyl-2,3-phthalocyanine. The difference in ligands may also afford a higher yield for $FePc(tBu)_4$. Spectroscopy did indicate the possibility of a μ-oxo dimer for $FePc(tBu)_4$ (vide infra), which would increase the mass of the product, and hence increase the yield. However, the additional mass of the oxygen atom alone could not increase the yield enough to be considered the only factor. Impurities could also increase the yield, but the rigorous experimental set up and synthesis was designed to eliminate impurities. Impurities as a result of side reactions are possible but were ruled out using spectroscopy (vide infra).

Again, an initial test was performed to see if the synthesis product was ORR active. A simple CV test scan was performed (vide infra) which yielded a similar result to those for the as-bought FePc's.

2.2.4 Spectroscopy

Successful synthesis of both $FePc(tBu)_4$ and $FeNpPc(tBu)_4$ was confirmed using spectroscopy. UV-Vis (Cary 300, quartz cuvettes) results of the $Pc(tBu)_4$ and $NpPc(tBu)_4$ reactant as well as $FePc(tBu)_4$ and $FeNpPc(tBu)_4$ product peaks are compared to those reported by Kobayashi et al. [10] for the Co analogue in section 2.3.1.1. The solvents (50/50 IPA / DI H_2O, N,N-DMF as well as Pyridine)

were chosen to match the solvents used to make the 10^{-4} M solutions of each FePc species, in addition to the solvent used in the literature, respectively. These solvents were used to see if they had an effect on the UV-Vis spectra of both synthesized FePc species, which could then affect the mode of adsorption onto the pyrolytic graphite WE. The results (not shown) were inconclusive in comparing spectra obtained with different solvents.

Matrix-assisted laser desorption/ionization time of flight (MALDI TOF) mass spectroscopy (Voyager-DE STR) using sinapinic acid (SA) as the matrix of the $Pc(tBu)_4$ and $NpPc(tBu)_4$ reactant as well as $FePc(tBu)_4$ and $FeNpPc(tBu)_4$ products are further discussed in section 2.3.1.2.

2.2.5 Working electrode preparation

The WE was comprised of a brass RDE modified to house a BPPG tip, with silver epoxy connecting the two of them. The entire shaft was sealed using heat shrink polyolefin tubing. A detailed description of RDE WE design, modification, and calibration check is found in Appendix VII. The graphite electrodes had a geometric area of 0.13 cm^2 and were mounted such that the basal planes were exposed on the face of the disk. Due to the nature of the BPPG used, the polishing procedure could result in some edge plane exposure. A 1.00×10^{-3} mol dm^{-3} solution of $K_3[Fe(CN)_6]$ was used to electrochemically determine the active electrode area of 0.12 cm^2 (Appendix IX).

To polish the electrodes, 0.3 μm alumina was used and a PTFE disc was used to hold the electrode perpendicular to the polishing pad during the process. The electrodes were cleaned by submerging and sonicating them in: DI water,

followed by ethanol, and then acetone, for no more than 10 s in each solvent, and with DI water rinsing between each solvent. The electrodes were then immediately placed either in the FePc species solution, or bare, in the electrochemical cell (vide infra) to avoid oxidizing the graphite surface [61].

2.2.6 Surface attachment

Solutions of each FePc species were made to an approximate concentration of $1.0x10^{-4}$ M. N,N-DMF (10mL) was used to dissolve $FePc(tBu)_4$ and $FeNpPc(tBu)_4$. Both FePc species solutions were sonicated for 5 min to ensure complete dissolution. Because some FePc species solutions are known to form adducts with O_2, as well as undergo side reactions if left for long periods of time, all such solutions were kept sealed when not in use, and made fresh every day. To adsorb the FePc species onto the graphite electrode, the polished and cleaned graphite electrode (vide supra) was immersed in the FePc species solution for no more than 30 s and then rinsed with DI water before immediately being transferred to the electrochemical cell containing only the supporting electrolyte. Adsorption was irreversible and not affected by temperature (Appendix XII).

2.2.7 Novel three electrode half cell

Figure 2.1 shows the schematic set-up of the custom, novel half-cell design (fabricated by Sandfire Scientific Ltd.) for catalyst evaluation and fuel cell electrode characterization. The CE reservoir is on the left hand side, the WE and its' holder are placed in the central chamber, the WE glass frit, and an upward oblique salt bridge is connected to the RE chamber, on the right hand side. An

upward oblique, rather than horizontally, orientated reference salt bridge and a glass frit was employed to avoid gas accumulation inside the bridge tube. Experiments showed that this special feature is necessary to prevent gas accumulation and subsequent loss of electrolyte continuity inside the RE bridge. The WE holder has its' back connected to the RE salt bridge glass frit. The front and top of the WE holder is open to the electrolyte. In this manner, the current only passes between the WE and the CE such that no current distribution fields exist between the WE and RE. This way, it is possible to repeatably fix the WE in the same position, if desired, as well as minimize any potential dependence of the RE's position or height in the RE chamber. Separating the CE and RE chambers from the WE chamber via glass frits also reduces the risk of contaminating the WE. This is especially important in non-noble metal catalysis, where even ppm or ppb levels of Pt in the electrolyte will affect results, yielding false positives. The half-cell can then be used for testing FePc, or any non-noble metal based catalyst ink supported on CFP GDE's. The three-way valve ("T" stop-cock) and purge gas tube shown in Figure 2.1 are used for either bubbling gas from the bottom of the half cell, or passing gas over the surface of the electrolyte, or isolating the cell from gas flow altogether.

The whole half-cell was kept in a temperature controlled water bath covered with insulating plastic balls to minimize temperature fluctuation and evaporation.

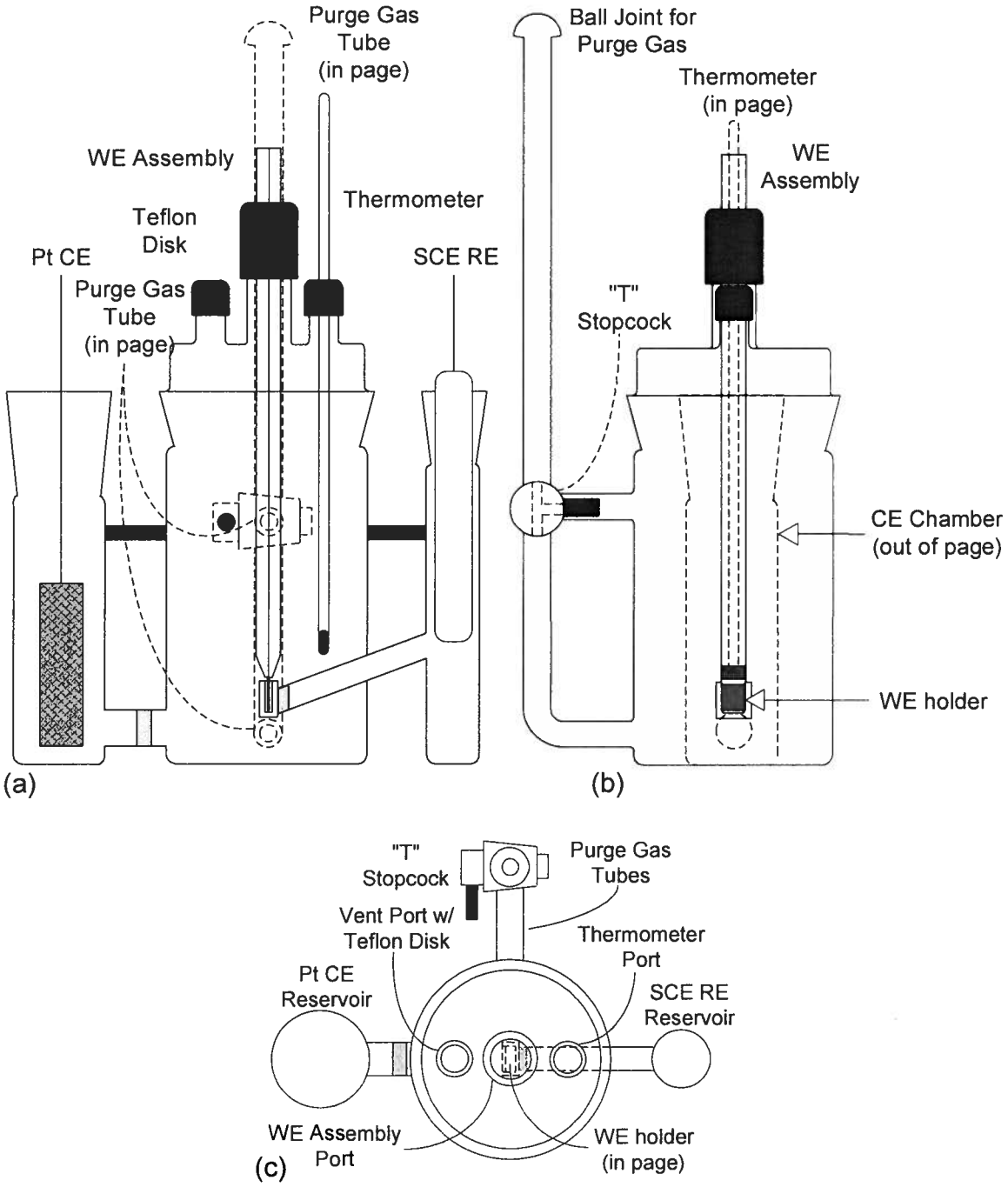

Fig. 2.1. (a) Half-cell design front view. (b) Half-cell design side view. Note the 0.5 cm^2 active geometric area of the CFP WE (Figure 5.1). (c) Top-view of the half-cell assembly.

2.2.8 Electrochemical measurements

All electrochemical measurements were performed using the custom three electrode, three-compartment half-cell described in section 2.2.7. The reference electrode (RE) was a saturated calomel electrode (SCE), and a platinized mesh was used as the auxiliary or counter electrode (CE). Care and calibration checking of the SCE are shown in Appendix V. All potentials reported in this paper were converted from the SCE to the reversible hydrogen electrode (RHE) scale according to the method outlined in Appendix VI. Cyclic voltammetry was performed using a Solartron Multistat 1480, controlled with CorrWare software (Scribner). Rotating disc voltammetry was performed using an ASR rotator (Pine Instrument Co.). A labelled photo of this experimental set up is shown in Appendix III. All experiments were conducted at ambient pressure (1 atm), and at a room temperature of 20 +/- 1°C, with 0.1M H_2SO_4 as the electrolyte.

2.3 Results and discussion

2.3.1 Spectroscopy of synthesized $FeNpPc(tBu)_4$ and $FePc(tBu)_4$

2.3.1.1 UV-Vis Spectroscopy

Peak absorbances for both as bought $Pc(tBu)_4$ and $NpPc(tBu)_4$ reactants agree well with the literature values [10] shown in Table 2.1. The peaks for the synthesized $FePc(tBu)_4$ and $FeNpPc(tBu)_4$ products are also similar to those reported in the literature for their respective Co analogues [10]. Disappearance of the 700.9 nm peak followed by the appearance of the 415.1 nm peak for $FePc(tBu)_4$ seen in Figure 2.2, and disappearance of the 785.0 nm peak followed by the appearance of the 459.0 nm peak for $FeNpPc(tBu)_4$ seen in Figure 2.3,

that indicate successful synthesis. The 415.1 nm and 459.0 nm peaks are associated with metal-to-ligand charge transfers (MLCT) [10].

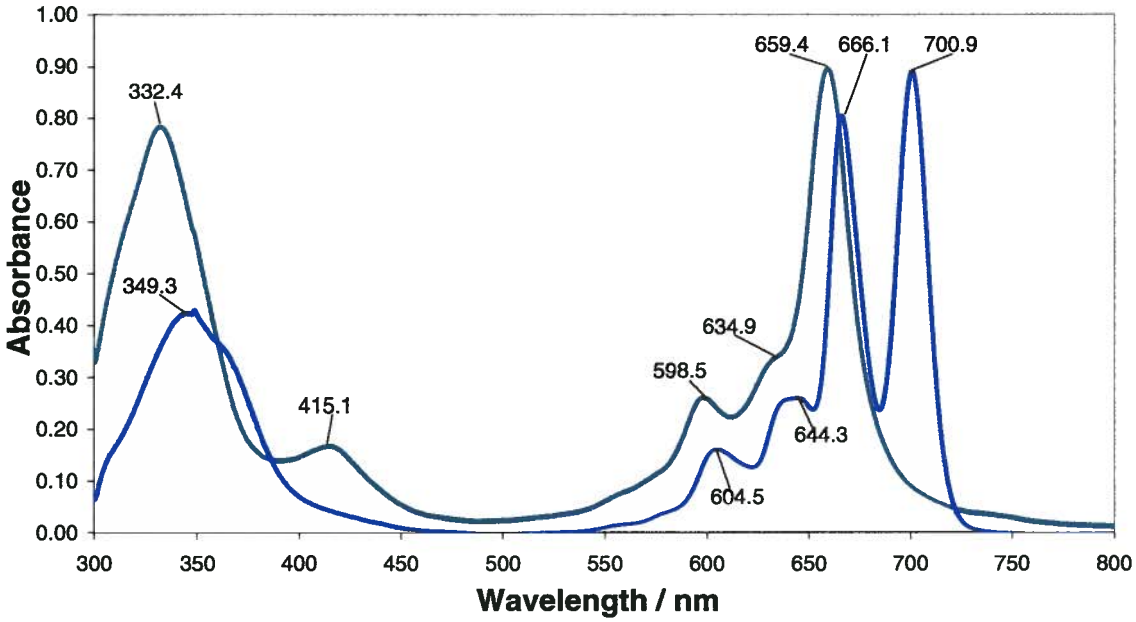

Fig. 2.2. UV-Vis spectra of the as bought $Pc(tBu)_4$ reactant (sky blue trace) and the in house synthesized $FePc(tBu)_4$ product (blue green trace) in pyridine with peak absorbance wavelengths, as marked.

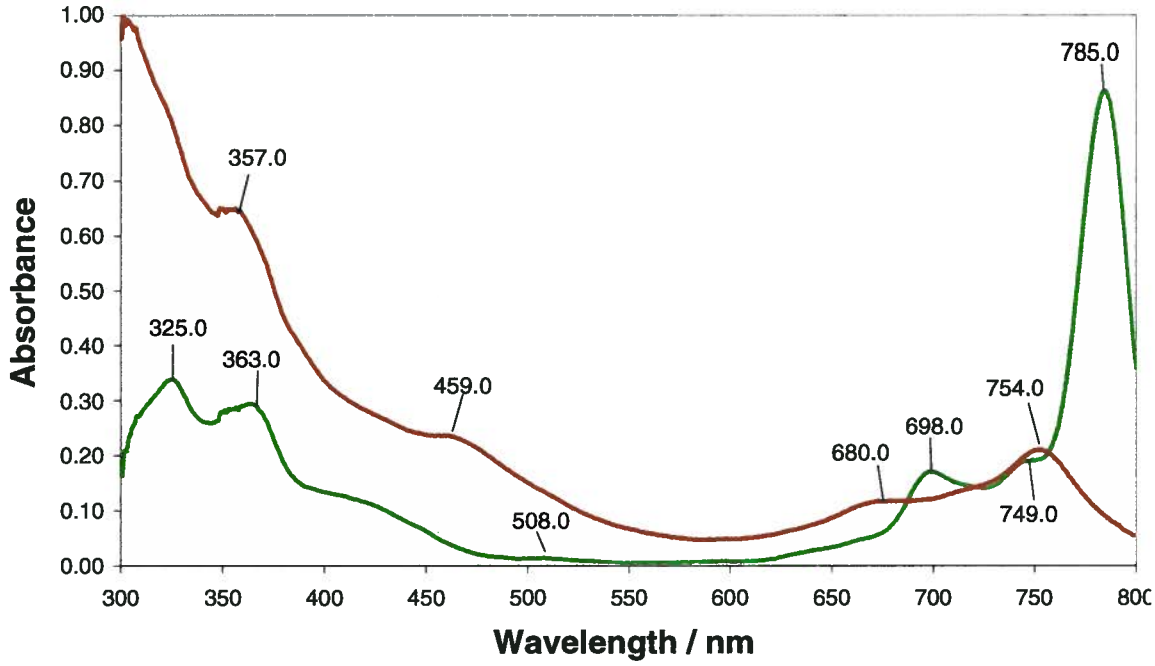

Fig. 2.3. UV-Vis spectra of the as bought $NpPc(tBu)_4$ reactant (grass green trace) and the in house synthesized $FeNpPc(tBu)_4$ product (olive brown trace) in pyridine with peak absorbance wavelengths as marked.

Table 2.1. UV-Vis spectroscopy data for (a) as bought $Pc(tBu)_4$, and synthesized $FePc(tBu)_4$, as well as for (b) as bought $NpPc(tBu)_4$, and synthesized $FeNpPc(tBu)_4$, both with the respective literature values for comparison.

(a)

Phthalocyanine	Data	Peaks / nm					
$Pc(tBu)_4$	Experimental	700.9	666.1	644.3	604.5	n/a	349.3
$Pc(tBu)_4$	Kobayashi [5]	698.0	664.3	640.1	602.0	n/a	344.0
$FePc(tBu)_4$	Experimental	n/a	659.4	634.9 sh	598.5	415.1	332.4
$CoPc(tBu)_4$	Kobayashi [5]	n/a	660.0	n/a	599.0	n/a	332.0

(b)

Phthalocyanine	Data	Peaks / nm						
$NpPc(tBu)_4$	Experimental	785.0	749.0	698.0	508.0	n/a	363.0	325.0
$NpPc(tBu)_4$	Kobayashi [5]	783.6	746.7	697.5	505.6	n/a	362.0	327.3
$FeNpPc(tBu)_4$	Experimental	n/a	754.0	680.0	n/a	459.0	357.0	n/a
$CoNpPc(tBu)_4$	Kobayashi [5]	n/a	752.0	672.5	n/a	n/a	340.0	n/a

As discussed in Chapter 1, UV-Vis spectroscopy is a good indicator for the relative energy levels of a FePc species' molecular orbitals, specifically the HOMO and LUMO. Much of a FePc species' stability can be inferred from its' HOMO – LUMO gap, as well as its' activity by the gap between its' HOMO and the LUMO of a reactant such as O_2. In this way, the effect of different substituents on a FePc species' HOMO energy level can be seen quite readily in the UV-Vis spectra's Q band (600 – 700 nm). De-activating substituents, like tetra *tert* butyl groups and additional conjugated ring structures are expected to increase the energy level of the HOMO, decreasing the energy gap between the HOMO and LUMO and hence moving the peak absorbance of the Q band to longer, or lower energy, wavelengths. This is clearly evident when comparing Figures 2.2 and 2.3 where the Q band has shifted from 659.4 nm in $FePc(tBu)_4$,

to 754.0 nm in $FeNpPc(tBu)_4$. This shift of nearly 100 nm to longer wavelengths confirms a decrease both in the HOMO energy level as well as the associated decreases in stability and ORR activity for $FeNpPc(tBu)_4$. UV-Vis spectra for CoPc and CoNpPc found in the literature agree well with the shift in the Q band shown here [8,10,13].

2.3.1.2 MALDI-TOF Mass Spectrometry

The parent ion m/z peaks for both $Pc(tBu)_4$ and $NpPc(tBu)_4$ reactants shown in Figures 2.4 and 2.5, respectfully, agree well with the calculated values shown in Table 2.2. Small peaks for the dimer form of $NpPc(tBu)_4$ are also observed, which agree with the calculated value as well. However, no dimer form of $Pc(tBu)_4$ was observed. The peaks ca. 1480 Da (not shown) that could correspond to the dimer form of $Pc(tBu)_4$ are obscured by baseline noise. Seeing as the $NpPc(tBu)_4$ dimer peak intensity was approximately 0.2%, any m/z peaks for $Pc(tBu)_4$ of a similar intensity would be very difficult to resolve against a baseline noise of approximately 1%.

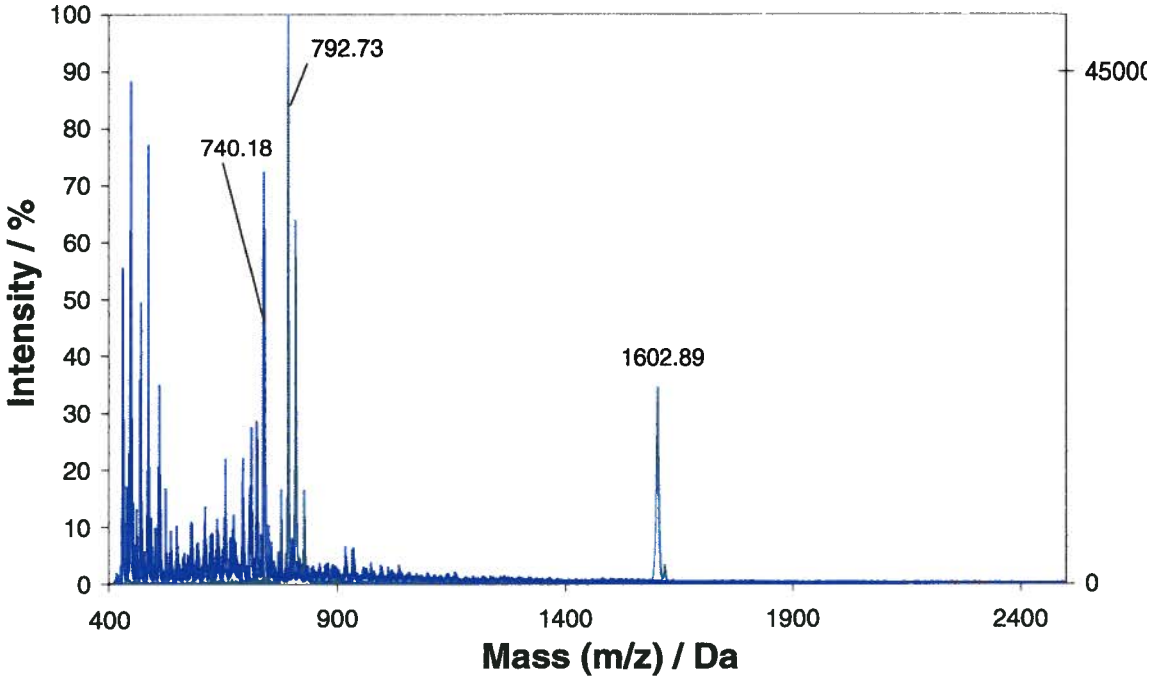

Fig. 2.4. MALDI-TOF mass spectra of the as bought $Pc(tBu)_4$ reactant (sky blue trace) and the in house synthesized $FePc(tBu)_4$ product (blue green trace) in SA as the matrix, with main m/z peaks as marked.

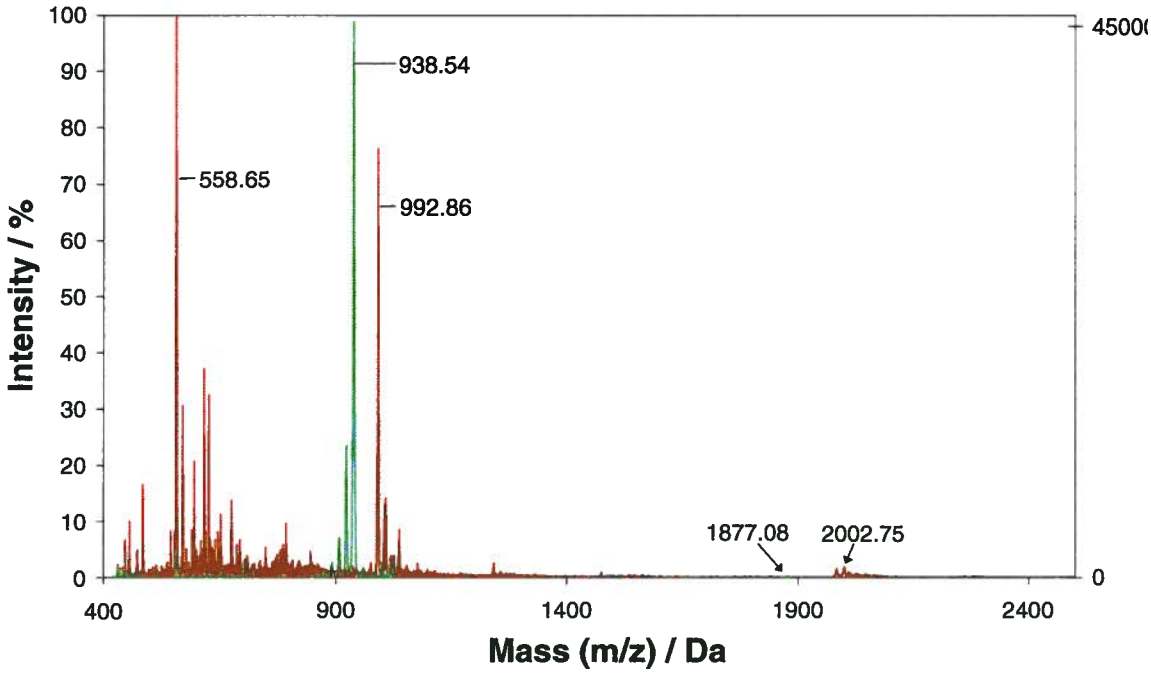

Fig. 2.5. MALDI-TOF mass spectra of the as bought $NpPc(tBu)_4$ reactant (grass green trace) and the in house synthesized $FeNpPc(tBu)_4$ product (olive brown trace) in SA as the matrix, with main m/z peaks as marked.

Table 2.2. MALDI-TOF mass spectra data for the as bought $Pc(tBu)_4$, and $NpPc(tBu)_4$, as well as the synthesized $FePc(tBu)_4$, and $FeNpPc(tBu)_4$, including calculated values and molecular weights.

Species		Source	Experimental m/z Peak / Da	Relative Intensity / %	Calculated m/z Peak / Da	Difference Calc - Exp / Da	Molecular Weight / g mol^{-1}
$Pc(tBu)_4$	Monomer	Aldrich	740.18	82.0	739.99	0.19	738.98
$Pc(tBu)_4$	Dimer	Aldrich	n/a	n/a	1479.98	n/a	1477.96
$FePc(tBu)_4$	Monomer	In-house	792.73	100.0	793.83	-1.10	792.82
$FePc(tBu)_4$	Dimer	In-house	1602.89	34.0	1587.66	15.23	1585.64
$NpPc(tBu)_4$	Monomer	Aldrich	938.54	100.0	940.20	-1.66	939.19
$NpPc(tBu)_4$	Dimer	Aldrich	1877.08	0.2	1880.40	-3.32	1878.38
$FeNpPc(tBu)_4$	Monomer	In-house	992.86	77.0	994.03	-1.17	993.02
$FeNpPc(tBu)_4$	Dimer	In-house	2002.75	2.0	1988.06	14.69	1986.05

For the synthesized $FePc(tBu)_4$ and $FeNpPc(tBu)_4$ products, the m/z peaks agree well with the calculated values based on molecular weight in Table 2.2, confirming removal of two hydrogens and substitution of Fe. This is also seen in Figures 2.4 and 2.5 as a shift of the parent ion peaks to higher m/z values. The multiple m/z peaks below the main parent ion peaks for $FeNpPc(tBu)_4$ may be collision products, and/ or matrix fragments, as a similar case can be seen for the pure $Pc(tBu)_4$ reactant. For example, other MALDI-TOF mass spectra for $Pc(tBu)_4$ in different matrices (not shown) did not contain any such m/z peaks below the parent ion peak. It is interesting to note the re-appearance of dimer peaks, but in contrast to the reactant dimer peak, these product dimer peaks are approximately 15 +/- 1 Da greater than the calculated values. This could be could be a μ-oxo dimer as some FePc species have been shown to exist in this form [62,63]. In particular, the dimer peak for $FePc(tBu)_4$ has a large relative

intensity of 34%, considerably greater than the $FeNpPc(tBu)_4$ dimer's relative intensity of 3%. Future work involving density functional theory (DFT) calculations could be used to confirm the possibility of these dimer forms for $FePc(tBu)_4$ and $FeNpPc(tBu)_4$.

2.3.1.3 Spectroscopy summary

The respective changes in colour from reactant to product and both the UV-Vis spectra as well as MALDI-TOF mass spectrometry all demonstrated the successful synthesis of $FePc(tBu)_4$ and $FeNpPc(tBu)_4$, with little or no carry over of either reactant ligands.

2.3.2 Surface electrochemical response of adsorbed FePc's on a pyrolytic graphite electrode

Molecular structures of the three FePc's studied are shown in Figures 3.1(d) and 3.1(e) of Chapter 3. Figures 3.3(d) and 3.3(e) in Chapter 3 show the cyclic voltammograms (CV's) of these two FePc species adsorbed on a pyrolytic graphite electrode at a scan rate of 100 mV s^{-1} run in a N_2 purged 0.1 M H_2SO_4 electrolyte at room temperature (20°C +/- 1°C) and 1 atm. The CV's shown in Figures 3.3(d) and 3.3(e) confirmed the two successfully synthesized FePc's adsorbed onto the WE surface, and exhibited stable reversible redox behavior. $FeNpPc(tBu)_4$ showed only one reversible redox peak, whereas $FePc(tBu)_4$ showed two such peaks for the conditions used in these experiments.

2.3.3 FePc catalyzed O_2 reduction using cyclic voltammetry

With the reversible redox behaviour of the synthesized FePc's established, CV's were run in the air saturated electrolyte at 20°C to determine if these synthesized FePc's exhibited ORR activity. Figure 2.6 shows initial ORR CV's for both $FePc(tBu)_4$ and $FeNpPc(tBu)_4$.

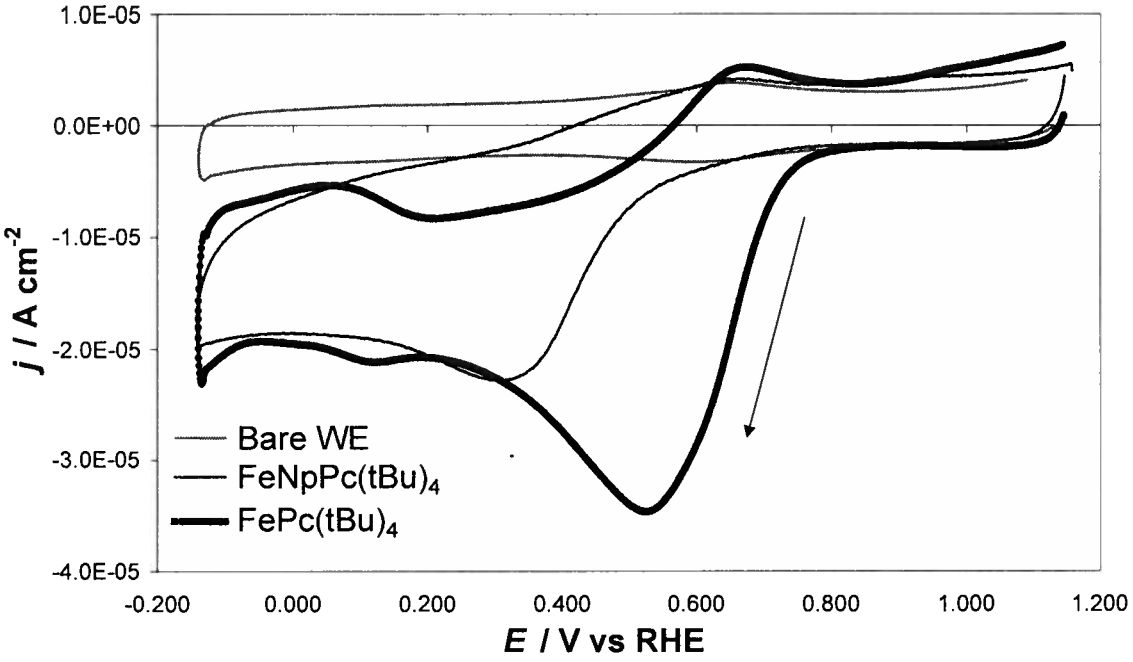

Fig. 2.6. Cyclic voltammograms at a scan rate of 100 mV s^{-1} of the bare pyrolytic graphite electrode, as well as $FeNpPc(tBu)_4$ and $FePc(tBu)_4$ adsorbed on pyrolytic graphite electrodes, in an air-saturated 0.1 M H_2SO_4 solution at 20°C and 1 atm.

Figure 2.6 clearly demonstrated both synthesized FePc's are ORR active. These preliminary results indicated a pronounced substituent effect for $FeNpPc(tBu)_4$ in comparison to $FePc(tBu)_4$, whereby the former's ORR current was roughly one half that of the latter's. This suggested a two electron

mechanism for FeNpPc($tBu)_4$. However, more detailed analysis was required to confirm these results. A thorough electrochemical analysis using CV, RDE and RRDE of the two synthesized FePc's along with the other three as-bought FePc species are described in Chapters 3 and 4.

2.4 Summary

Two novel substituted phthalocyanine macrocycle-based iron complexes were synthesized according to a facile method [9] and then characterized using UV-Vis as well as MALDI-TOF mass spectroscopy. These two complexes, which all irreversibly adsorbed on a pyrolytic graphite electrode, were studied using surface electrochemical techniques (surface voltammetry).

Cyclic Voltammograms run in an N_2 purged electrolyte showed the tetra *tert* butyl substitution of FeNpPc yielded no reversible redox couple near 0.1 V vs RHE, in contrast to FePc($tBu)_4$ which did show this peak. When adsorbed on the electrode surface, both exhibited ORR activity, but as predicted these two synthesized FePc species with de-activating substituents showed reduced catalytic activity when compared to the baseline FePc. Initial tests indicated tetra *tert* butyl substitution of FeNpPc decreased its' ORR activity more than the same substituents on FePc. Further studies involving CV, RDE and RRDE experiments as well as analysis are the subject of Chapters 3 and 4.

Chapter 3

Electrocatalytic Activity and Stability of Substituted Iron Phthalocyanines Towards Oxygen Reduction Evaluated at Different Temperatures

3.0 Objective

The kinetic ORR parameters of five FePc's as a function of different peripheral substituents, were each evaluated at four temperatures (20, 40, 60, 80°C) using cyclic and RDE voltammetry. The results obtained provide insight into the effect of substituents as well as temperature, and the corresponding change in catalyzed ORR mechanisms.

3.1 Description

There has been much work in the field of the TM macrocycle catalyzed ORR, but not in a PEM fuel cell environment. Specifically, adsorbing different substituted FePc species onto a pyrolytic graphite electrode and performing electrochemical experiments in 0.1 M H_2SO_4 as a function of temperature. Despite these harsh conditions, which promote de-activation of the FePc species, experimental data is still obtainable by slightly modifying the experimental procedure. There is the possibility that comparisons can then be made to provide insight into the similarities and differences in the performance of their pyrolized FeN_X/C analogues.

3.2 Experimental

3.2.1 Chemicals

Iron(III) phthalocyanine chloride (Sigma cat. no. 379573, lot no. 06023AC), Iron(III) phthalocyanine-4,4′,4″,4‴-tetrasulfonic acid (Sigma cat. no. 452521, lot no. 10421BD), Iron(II) 1,2,3,4,8,9,10,11,15,16,17,18,22,23,24,25-hexadecachloro-29*H*,31*H*-phthalocyanine (Sigma cat. no. 448044, lot no. 04731JS), (all abbreviated as FePc, $FePc(SO_3H)_4$, and $FePcCl_{16}$, respectively), were all purchased from Sigma Aldrich and used as received. Both $FeNpPc(tBu)_4$ and $FePc(tBu)_4$ were not commercially available and were thus synthesized in house as described in Chapter 2. 3.1% aqueous hydrogen peroxide, and isopropyl alcohol (IPA) were purchased from Fisher, certified A.C.S. reagent grade, and used as received. All other chemicals, aqueous solutions, DI H_2O, and gasses are as described in Chapter 2. Gasses were bubbled for at least 45 minutes at the desired temperature before performing any experiments.

3.2.2 O_2 concentrations, O_2 diffusion coefficients, and water viscosities

Dissolved O_2 concentrations for air in water at 1.0 atm and the desired temperatures were taken from the IUPAC solubility data series [64]. These values were then used to make fresh H_2O_2 solutions of equivalent concentration for each temperature. O_2 diffusion coefficients at 1.0 atm and the desired temperatures were calculated using the correlation developed by Wilke and Chang [65]. Water viscosities at 1.0 atm and the desired temperatures were

taken from the CRC handbook of chemistry and physics [66]. For the experimental conditions, it was assumed the electrolyte used was dilute enough such that these values (dissolved O_2 concentration and viscosity) are similar to those for pure H_2O. These parameters are summarized in Table 3.1.

Table 3.1. Dissolved O_2 concentration (C_{O2}), O_2 diffusion co-efficients (D_{O2}), kinetic viscosities (γ_{H2O}) at various temperatures in an air saturated aqueous solution at 1 atm.

Temperature	/ °C	20	40	60	80
D_{O2}	/ $cm^2\ s^{-1}$	1.97E-05	3.23E-05	4.82E-05	6.72E-05
C_{O2}	/ mol cm^{-3}	2.70E-07	1.88E-07	1.48E-07	1.27E-07
γ_{H2O}	/ $cm^2\ s^{-1}$	1.00E-02	6.58E-03	4.74E-03	3.65E-03

3.2.3 Working electrode preparation

The pyrolytic graphite electrodes were mounted such that the basal planes were exposed on the face of the disk. The active electrode area of 0.12 cm^2 was electrochemically determined with a 1.00 x 10^{-3} M $K_3[Fe(CN)_6]$ solution (Appendix IX). A full description of WE preparation is described in Chapter 2 [1,3,67].

3.2.4 Surface attachment

Irreversible adsorption of the TM macrocycle onto the WE disk surface was achieved by immersion in an approximately 1.0x10^{-4} M solution of the FePc species for no longer than 30 seconds. Full details of this technique are described in Appendix XII and Chapter 2 [1,3,67]. One of the many effects of substitution is that the solubilities for each FePc species can change significantly. A 50/50 mixture of isopropanol (5mL) and DI H_2O (5mL) was used to dissolve

FePc and $FePc(SO_3H)_4$ while N,N-DMF (10mL) was used to dissolve $FePcCl_{16}$, $FeNpPc(tBu)_4$ and $FePc(tBu)_4$. WE compatability in N,N-DMF is described in Appendix VIII.

3.2.5 Electrochemical measurements

All electrochemical measurements were performed with the custom three electrode, three-compartment half-cell (Sandfire Scientific Ltd.) described in Chapter 2. The RE was a double junction saturated calomel electrode (SCE) from Aldrich (Z113115), and a platinized mesh was used as the auxiliary or CE. All potentials reported in this paper were converted from the SCE (Appendix VI) to the reversible hydrogen electrode (RHE) to correct for the SCE's temperature dependence. Experimental data for the SCE vs RHE open circuit voltages (OCV's) at each temperature (Appendix VI) was used for this conversion. Cyclic voltammetry was performed using a Solartron Multistat 1480, controlled with CorrWare software (Scribner). Rotating disc voltammetry was performed using an ASR rotator (Pine Instrument Co.). All experiments were conducted at ambient pressure (1 atm), and the desired temperature, with 0.1M H_2SO_4 as the electrolyte. The whole half-cell was immersed in a temperature controlled water bath (IKA RCT Basic, or Fisher Isotemp 205) covered with insulating plastic balls to minimize temperature fluctuations and evaporation.

3.3 Results and discussion

3.3.1 Surface electrochemical response of adsorbed FePc's on a pyrolytic graphite electrode

Molecular structures of the five FePc's studied are shown in Figure 3.1. The FePc's are large planar conjugated organometallic molecules showing symmetry on two axes. These conjugated π–bonded planar structures are similar to those of graphite, facilitating the irreversible adsorption of the FePc species on the graphite electrode surface. Even FePc species which exhibit high solubilities in aqueous solvents, such as $FePc(SO_3H)_4$, form a strong irreversible adsorption on pyrolytic graphite [7]. This irreversible adsorption on the electrode surface provides a simple method to investigate the surface electrochemical behavior of the adsorbed species. If there are no other reactive species in solution, the irreversible surface adsorption greatly simplifies both the data analysis and exploration of the electrocatalytic mechanisms.

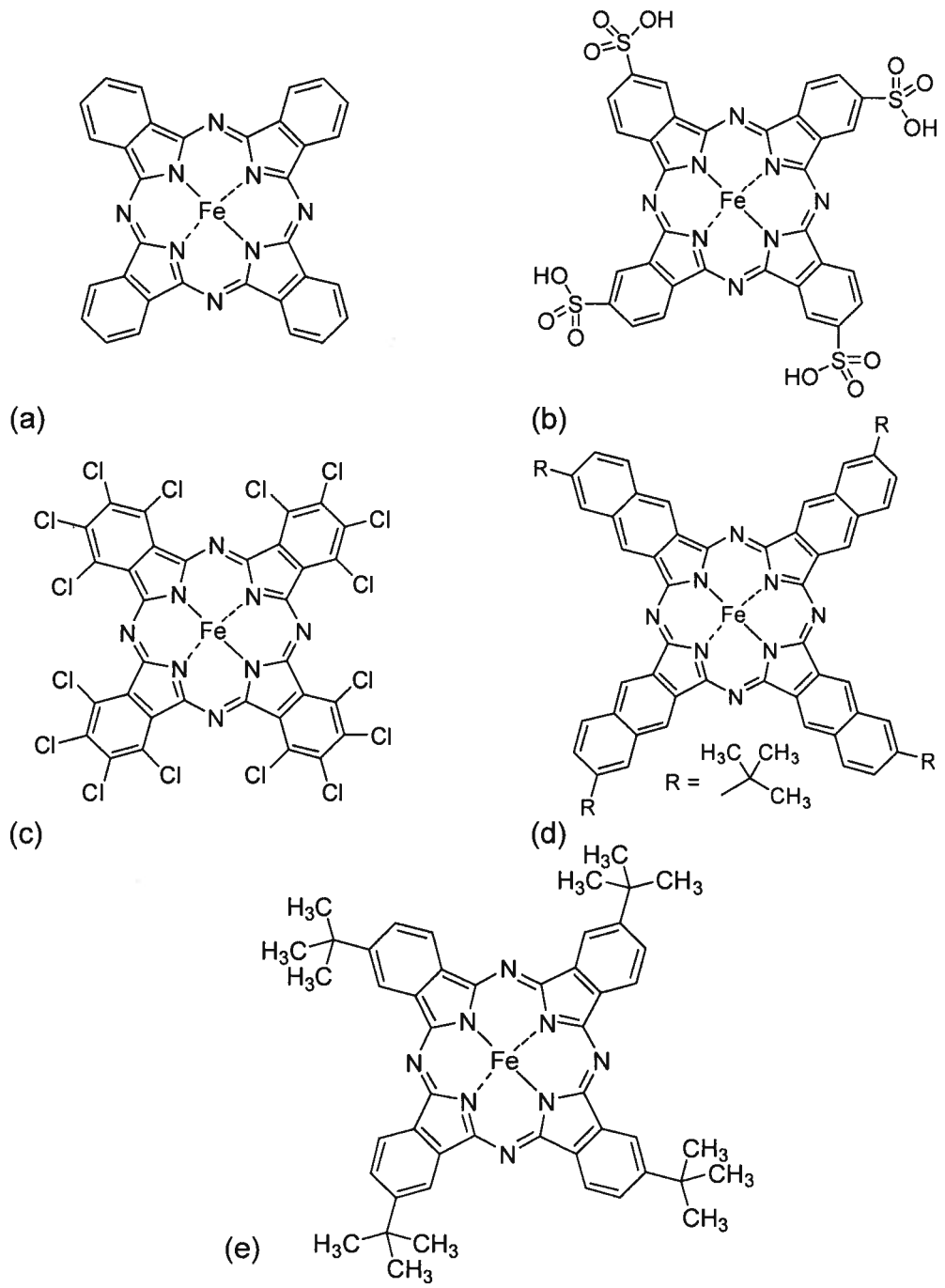

Fig. 3.1. (a) Iron(III) phthalocyanine chloride, (b) Iron(III) phthalocyanine-4,4′,4″,4‴-tetrasulfonic acid, (c) Iron(II) 1,2,3,4,8,9,10,11,15,16,17,18,22,23,24,25 - hexadecachloro-29H,31H-phthalocyanine, (d) Iron(II) 2,11,20,29-Tetra-*tert*-butyl-2,3-naphthalocyanine and (e) Iron(II) 2,9,16,23-Tetra-*tert*-butyl-phthalocyanine.

Figure 3.2 shows the cyclic voltammograms (CV's) of the unsubstituted, or baseline, FePc adsorbed on a pyrolytic graphite electrode at three (100, 500, 1000 mV s^{-1}) of the total six (100, 200, 300, 400, 500, 750, and 1000 mV s^{-1}) different scan rates run in a N_2 purged 0.1 M H_2SO_4 electrolyte at room temperature (20°C +/- 1°C) and 1 atm. In order to make a relevant comparison, the corresponding surface CVs of the bare pyrolytic graphite electrode surface, also plotted in the figure, were run immediately before those of the adsorbed FePc species on the same surface. This is because the redox peaks for both the bare, and FePc species adsorbed, pyrolytic graphite electrodes co-incide [51]. Surface quinone and phenol groups are responsible for the redox waves obtained on the bare pyrolytic graphite electrode surface. The redox waves are in the range of 0.58 to 0.65 V vs RHE for the four FePc adsorbed electrode surfaces corresponding to the redox process for the iron center ($Fe^{III/II}$).

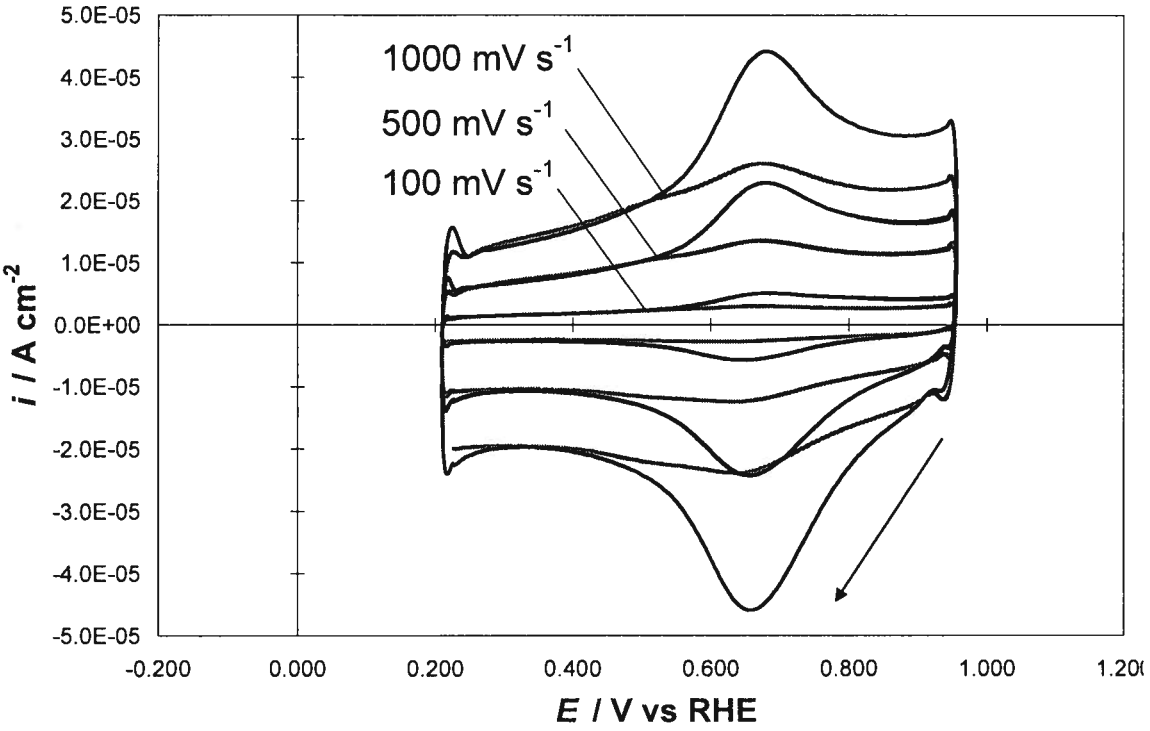

Fig. 3.2. Cyclic voltammograms of both FePc (solid lines) adsorbed on a pyrolytic graphite electrode, as well as those of the bare pyrolytic graphite (dotted lines), each at the indicated scan rates. Scans performed at 20°C, and 1 atm, in a N_2 purged 0.1M H_2SO_4 electrolyte.

The three pairs of surface waves shown in Figure 3.2 clearly indicate that the peak potential (E_p) does not change with scan rate (ν). This establishes that the catalyst redox states can be cycled reversibly and that the redox centre is immobilized on the graphite surface.

Figure 3.3 shows surface CV's under N_2 of the five FePc's studied in this thesis. For each FePc species, a CV of the bare pyrolytic graphite WE, followed by a CV of the adsorbed FePc species on the same bare WE surface, and finally the same adsorbed FePc species at steady state, are shown for comparison. For the conditions used in these experiments, $FeNpPc(tBu)_4$ showed only one redox

peak, FePc, $FePc(SO_3H)_4$ and $FePc(tBu)_4$ showed two peaks, while $FePcCl_{16}$ showed four peaks [7,8,15,16]. In comparing the surface waves near 0.11 V vs RHE for FePc, 0.18 V vs RHE for $FePc(SO_3H)_4$, 0.22 V vs RHE for $FePcCl_{16}$ and 0.08 V vs RHE for $FePc(tBu)_4$, the respective peak currents diminish slightly with successive scans. Those for $FePc(SO_3H)_4$ diminish the most while those for $FePcCl_{16}$ diminish the least. The waves near 0.65 V for FePc, 0.63 V for $FePc(tBu)_4$ 0.62 V for $FePc(SO_3H)_4$, 0.60 V for $FePcCl_{16}$, and 0.58 V for $FeNpPc(tBu)_4$ can all be assigned to the $Fe^{III/II}$ redox process. The associated peak currents showed minimal diminishment relative to those near 0.1 V vs RHE. It is interesting to note the shift in redox peaks for $FePc(SO_3H)_4$ with successive scans, where the peak ca. 0.79 V vs RHE diminishes, while that ca. 0.62 V vs RHE increases. The same pattern is seen for $FePc(SO_3H)_4$'s peaks ca. 0.18 V vs RHE and 0.07 V vs RHE, respectively. This is likely a chemical change from the μ-oxo dimer to the monomer form of the adsorbed $FePc(SO_3H)_4$, and is discussed further in section 3.3.5.4. Other workers, notably Lever et. al., have correlated such Fe redox potentials with Hammett parameters of the substituents [41,48]. Along with DFT analysis, these two topics could be the subject of future work, as discussed in section 3.3.5.4.

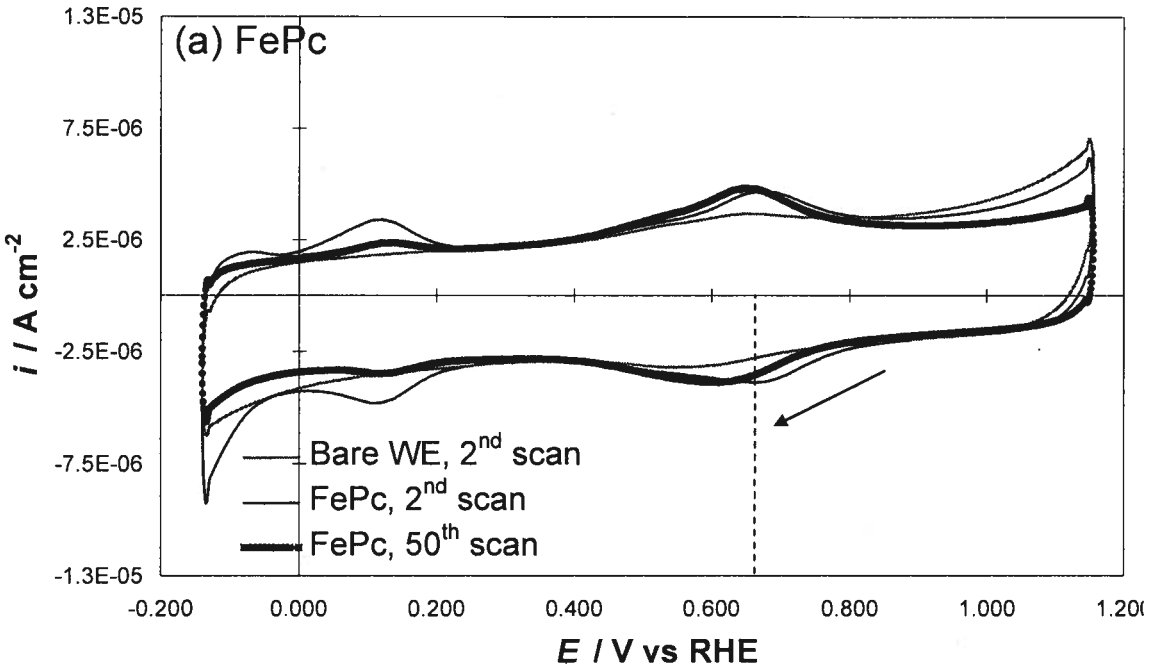

Fig. 3.3. Cyclic voltammograms at a scan rate of 100 mV s^{-1} for: (a) FePc; (b) $FePc(SO_3H)_4$; (c) $FePcCl_{16}$; (d) $FeNpPc(tBu_4)$; and (e) $FePc(tBu_4)$; each adsorbed on a pyrolitic graphite electrode. Second scans of the bare electrode, and adsorbed FePc species, as well as fiftieth scan of the same FePc species electrode as marked. Peak potential for the $Fe^{III/II}$ reduction wave indicated with a dotted line. Scans performed at 20°C and 1 atm in a N_2 purged 0.1 M H_2SO_4 electrolyte.

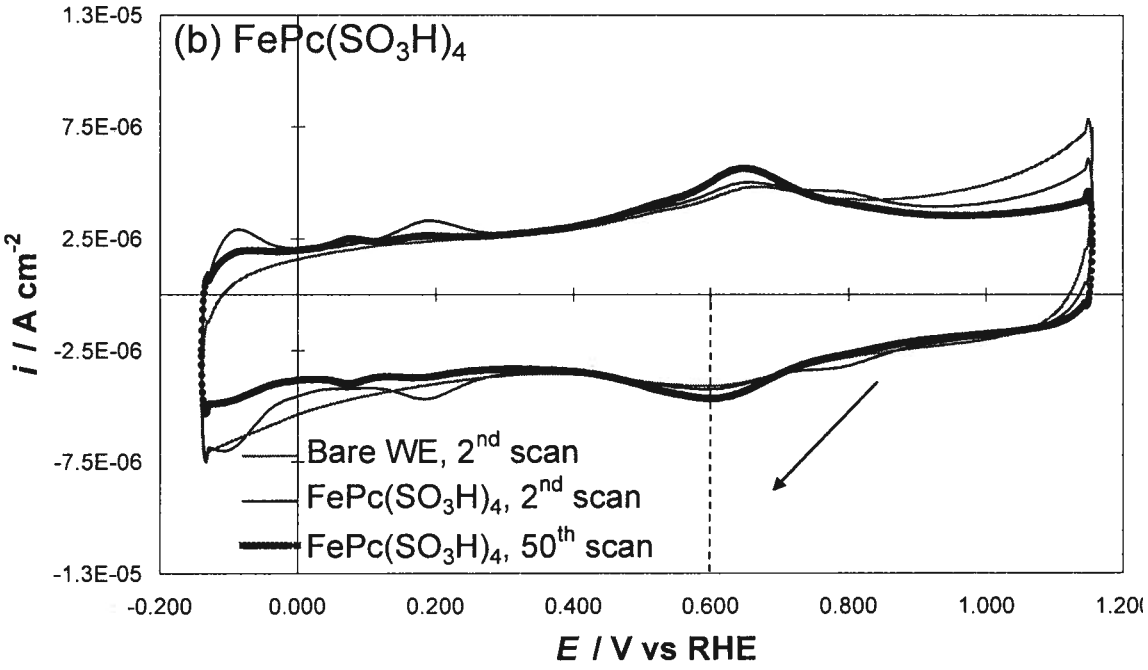
(b) FePc(SO3H)4
1.3E-05
7.5E-06
2.5E-06
-2.5E-06
-7.5E-06
-1.3E-05
i / A cm-2
-0.200
0.000
0.200
0.400
0.600
0.800
1.000
1.20(
Bare WE, 2nd scan
FePc(SO3H)4, 2nd scan
FePc(SO3H)4, 50th scan
E / V vs RHE

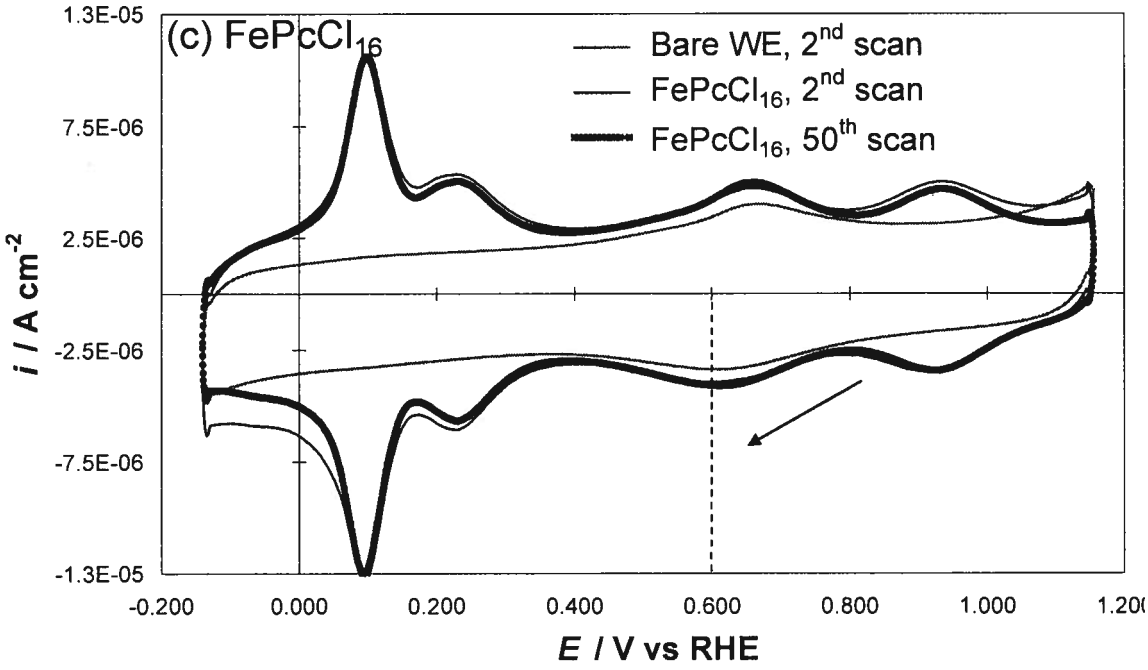
(c) FePcCl16
1.3E-05
7.5E-06
2.5E-06
-2.5E-06
-7.5E-06
-1.3E-05
i / A cm-2
-0.200
0.000
0.200
0.400
0.600
0.800
1.000
1.20(
Bare WE, 2nd scan
FePcCl16, 2nd scan
FePcCl16, 50th scan
E / V vs RHE

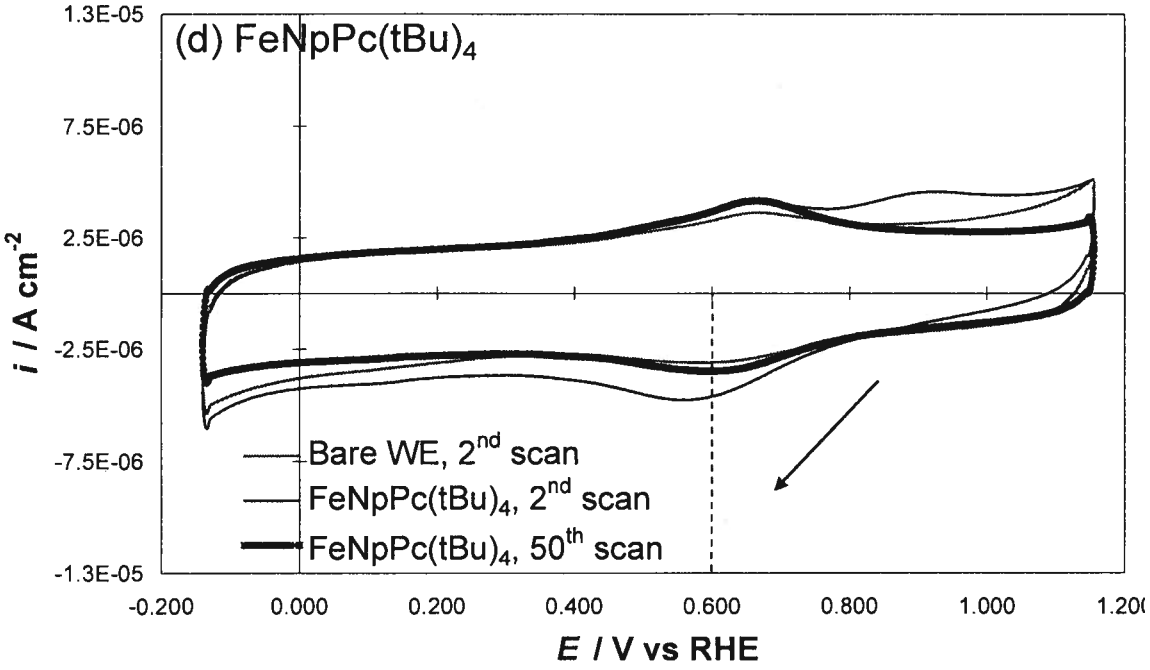
(d) FeNpPc(tBu)4
1.3E-05
7.5E-06
2.5E-06
-2.5E-06
-7.5E-06
-1.3E-05
i / A cm-2
-0.200
0.000
0.200
0.400
0.600
0.800
1.000
1.20(
E / V vs RHE
Bare WE, 2nd scan
FeNpPc(tBu)4, 2nd scan
FeNpPc(tBu)4, 50th scan

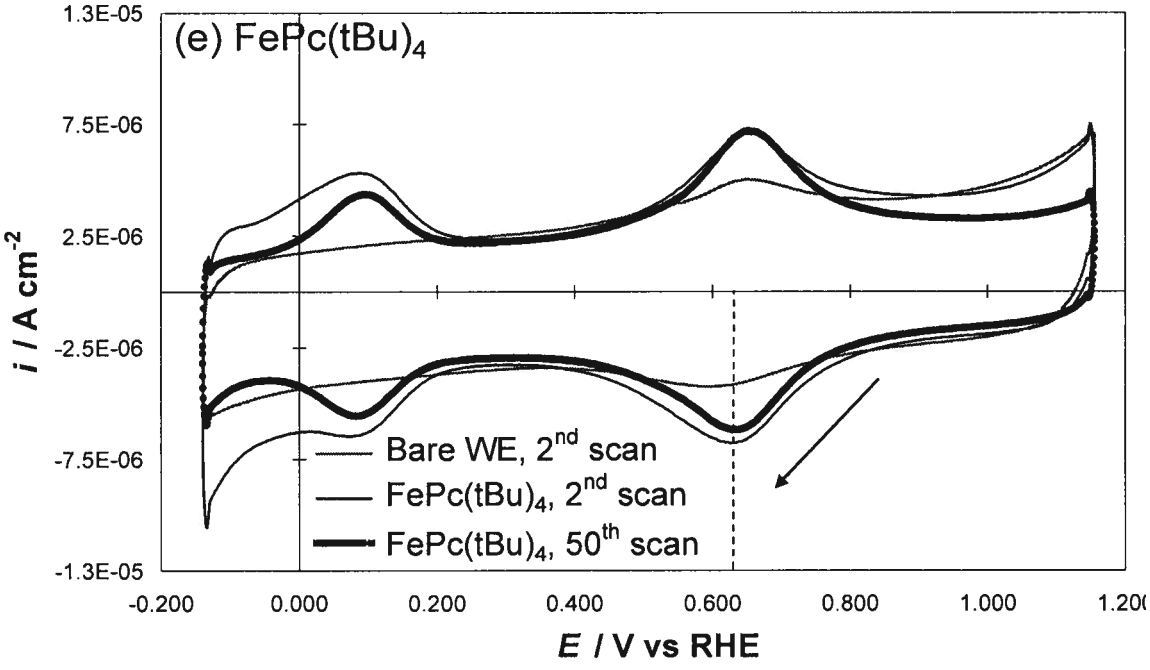
(e) FePc(tBu)4
1.3E-05
7.5E-06
2.5E-06
-2.5E-06
-7.5E-06
-1.3E-05
i / A cm-2
-0.200
0.000
0.200
0.400
0.600
0.800
1.000
1.20(
E / V vs RHE
Bare WE, 2nd scan
FePc(tBu)4, 2nd scan
FePc(tBu)4, 50th scan

All of the $Fe^{III/II}$ peaks shown in Figures 3.2 and 3.3 exhibit linear relationships between peak current and potential scan rate. This linear behavior indicates that the $Fe^{III/II}$ waves are indeed a surface controlled process. The relationship between the peak current and the potential scan rate for a reversible surface electrochemical response can be expressed by the Equation [67,68]:

$$i_p = \frac{n_{FePc}^2 F^2}{4RT} A \upsilon \Gamma_{FePc} \qquad (3.1)$$

where i_p is the reversible redox peak current for a surface adsorbed species, n_{FePc} is the electron transfer number involved in the surface electrochemical reaction of the FePc species, F is Faraday's constant, R is the universal gas constant, T is the temperature, A is the electrode area, ν is the potential scan rate, and Γ_{FePc}, is the surface concentration of the FePc species. The slope obtained from a plot of i_p vs ν, allows either Γ_{FePc} (if n_{FePc} is known) or n_{FePc} (if Γ_{FePc} is known) to be determined. As the redox peaks in the range of 0.58 to 0.65 V vs RHE correspond to the one electron $Fe^{III/II}$ redox couple, n_{FePc} is known and Γ_{FePc} can then be solved for. Such plots are shown in Figure 3.4. In the following sections, the surface concentration of adsorbed FePc species obtained using Eq. (3.1) will be used to evaluate surface orientation as well as to estimate the kinetic ORR rate constant k_{O2} (of the adsorbed FePc's).

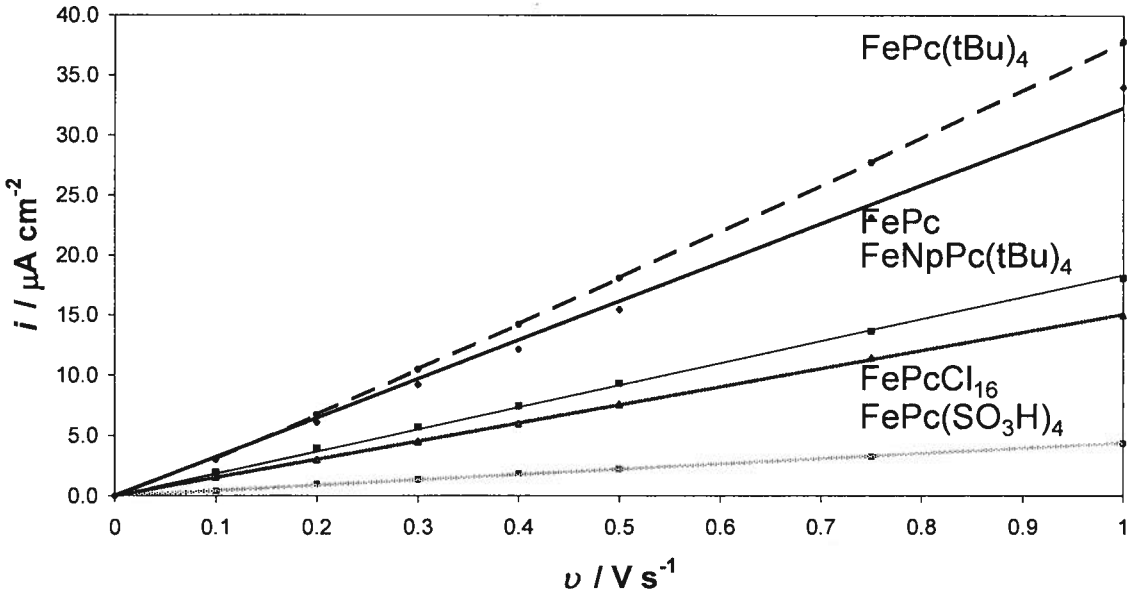

Fig. 3.4. Peak current as a function of potential scan rate. Data taken from Figures 3.2 and 3.3.

3.3.2 Surface layer coverage and orientation of adsorbed FePc's

Assuming n_{FePc} = 1 for the peak in the range of 0.58 to 0.65 V vs RHE, which is associated with the $Fe^{III/II}$ redox couple, experimental Γ_{FePc}'s were calculated from the data shown in Figure 3.3 and are listed in Table 3.2. The scans for both the reduction and oxidation of the $Fe^{III/II}$ peak were averaged for each scan rate and the experiment was repeated five times under the same conditions for each FePc species. The Γ_{exp}'s reported are an average of the five experiments on freshly adsorbed surfaces each time, for each FePc species. A detailed example calculation for $\Gamma_{FePcCl16}$ is described in Appendix X.

Table 3.2. Molecular plane areas (*MPA's*), experimental (Γ_{exp}) and calculated theoretical surface concentrations (Γ_{cal}) and experimental to theoretical surface concentration ratios ($\Gamma_{exp}/\Gamma_{cal}$) for different FePc's.

	MPA / cm^{-2}	Γ_{cal} / mol cm^{-2}	Γ_{exp} / mol cm^{-2}	$\Gamma_{exp}/\Gamma_{cal}$
FePc	1.5E-14	1.1E-10	2.4E-10	2.1
$FePc(SO_3H)_4$	2.5E-14	6.7E-11	5.0E-11	0.8
$FePcCl_{16}$	1.8E-14	9.3E-11	8.0E-11	0.9
$FeNpPc(tBu)_4$	3.6E-14	4.7E-11	1.3E-10	2.7
$FePc(tBu)_4$	2.4E-14	6.9E-11	3.1E-10	4.5

The orientation of the adsorbed FePc species can be deduced by comparing the experimental surface layer coverage, or concentration (Γ_{exp}), to a calculated theoretical value (Γ_{cal}) for flat, monolayer adsorption. Bond lengths and bond angles were used to estimate the molecular plane area (*MPA*) for each FePc species and then calculate Γ_{cal} [3,7,67]. It should be noted that in calculating Γ_{cal} for $FePc(SO_3H)_4$ it was assumed at pH = 1 that all four sulfonate groups are fully protonated thus O^- / O^- charge repulsion between adjacent adsorbed $FePc(SO_3H)_4$'s can be ignored. A ratio of $\Gamma_{exp}/\Gamma_{cal}$ approximately equal to one indicates flat monolayer adsorption. Values larger than one can indicate adsorption of more than one monolayer, agglomeration, adduct formation, edge-on adsorption, or any combinations thereof. Details of these calculation methods for each FePc species are found in Appendix XI. Both $FePcCl_{16}$ and $FePc(SO_3H)_4$ gave values slightly less than one indicating that each forms a monolayer. However, FePc, $FeNpPc(tBu)_4$, and $FePc(tBu)_4$ show values of 2, 3,

and 5, respectively, indicating the possibility of edge-on adsorption or some other surface orientation. It should be noted that several different approaches were used to achieve a monolayer for some of the FePc species all of which still yielded the same $\Gamma_{exp}/\Gamma_{cal}$ ratio.

3.3.3 Electrocatalytic activity of FePc's towards O_2 reduction

To separate the effects of the catalyst redox process alone and the redox process of the supporting electrode, identical CV scans were all run at a scan rate of 100 mV s^{-1} for the bare and FePc species adsorbed pyrolytic graphite electrode in the presence and absence, separately, of O_2 and H_2O_2 [3]. A total of six separate CV experiments were run for each FePc species at every temperature. Figure 3.5 shows a typical set of six such CV's for the baseline FePc at 20°C. The first scan of the bare pyrolytic graphite electrode in N_2 saturated electrolyte showed the redox peak associated with the surface functional groups, but otherwise no activity. The second scan of the FePc adsorbed electrode showed the corresponding surface waves that are seen in Figure 3.5(b). The next scan was performed using the same FePc adsorbed electrode in an air-saturated electrolyte as seen in Figure 3.5(c). An onset potential of approximately 0.75 V vs RHE was observed for the O_2 reduction wave, which coincides with both surface waves associated with the FePc adsorbed and bare graphite electrode. Approximate onset potentials were measured by the method of intersecting tangents on the current potential curves corrected for the pyrolytic graphite baseline in N_2 saturated electrolyte. Immediately after the ORR scan, the electrode was polished, cleaned and a scan

of the bare pyrolytic graphite electrode was run in the air-saturated electrolyte. No apparent activity towards the ORR was observed, showing only the reduction of O_2 to H_2O_2 at an onset potential of around 0.2 V vs RHE, much more negative than that for the FePc catalyzed ORR. The following scan in Figure 3.5(e) used the same bare pyrolytic graphite electrode in a N_2 purged electrolyte containing H_2O_2 in exactly the same concentration as the dissolved O_2 for that temperature. The bare pyrolytic graphite electrode showed no activity towards H_2O_2 reduction. Finally, the same FePc species was adsorbed onto the electrode and a scan in the same N_2 purged electrolyte containing H_2O_2 was subsequently run (Figure 3.5(f)), showing some H_2O_2 reduction activity at a similar onset potential to that of the previous ORR CV.

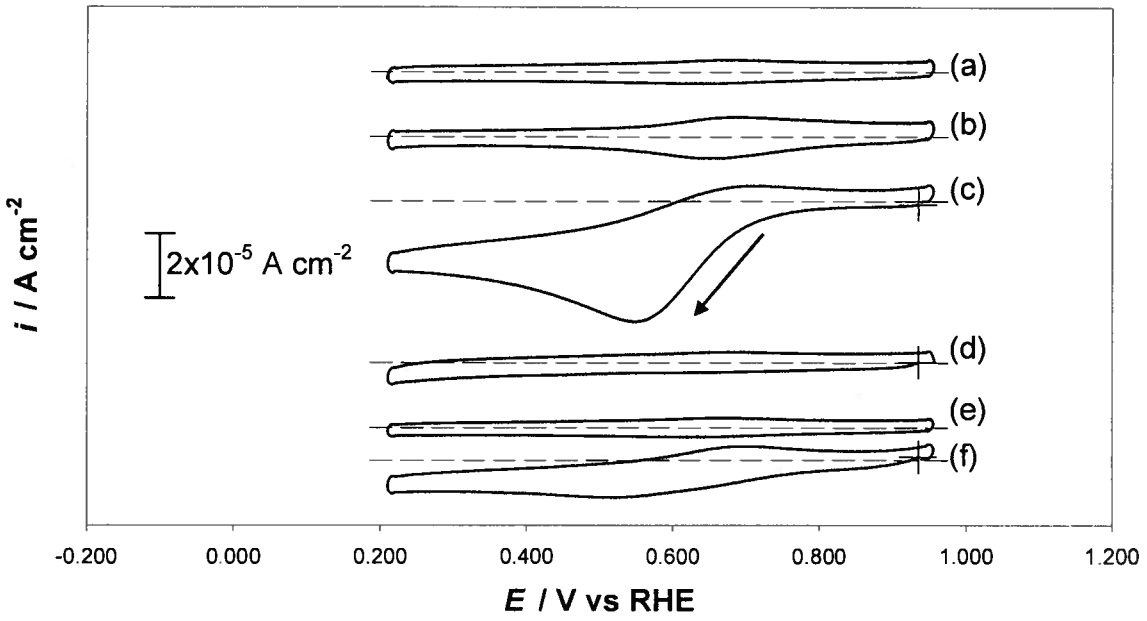

Fig. 3.5. Cyclic voltammetry of FePc adsorbed on a pyrolytic graphite electrode for different cases: (a) bare electrode in a N_2 saturated solution; (b) FePc adsorbed electrode in a N_2 saturated solution; (c) FePc adsorbed electrode in an air saturated solution; (d) bare electrode in an air saturated solution; (e) bare electrode in the presence of a 0.28 mM H_2O_2 solution; (f) FePc adsorbed electrode in the presence of 0.28 mM H_2O_2 solution. Dashed lines represent zero lines. Scans performed at 20°C, 1 atm, in a 0.1M H_2SO_4 electrolyte. Scan rate: 100 mV s^{-1}.

If the O_2 and H_2O_2 reduction reactions are catalysed, it usually occurs at that particular redox couple associated with the electrocatalyst [3,67]. In this manner, all FePc species tested exhibited electrocatalytic activity towards both the O_2 and H_2O_2 reduction reaction, except $FePc(SO_3H)_4$ which showed no activity towards H_2O_2 reduction under these experimental conditions.

It should be noted that in the operating range for these experiments, the dissolved O_2 concentration decreases monotonically with increasing temperature

[64]. Experiments were also performed to see the effect of increasing temperature on Γ_{FePc} in the range of 20°C to 80°C (Appendix XII) which showed that Γ_{FePc} was constant irrespective of both the temperature of, or time in, the electrolyte. Even though Γ_{FePc} is constant, Table 1 shows each FePc species has a different Γ_{FePc}, which in turn will have an effect on *i*.

3.3.4 Effect of temperature on different FePc catalysed O_2 and H_2O_2 reduction

The effect of temperature on O_2 and H_2O_2 reduction for each FePc species can be seen in Figure 3.6. The data in Figure 3.6 has not been corrected for different Γ_{FePc} coverages or for the effect of temperature on dissolved oxygen concentration as it only serves to qualitatively demonstrate the effect of temperature and substitution. These two aforementioned variables will be accounted for in section 3.3.5.4.

The shift in onset potential to more negative values with increasing temperature is a result of the decreasing O_2 concentration. It can be observed that an increase in temperature from 20°C to 60°C increases the current density, after which a further increase to 80°C reduces it. Three effects are at play: the O_2 diffusion coefficient (D_{O2}), the O_2 concentration ($[O_2]$), and the reaction kinetics. In the temperature range of 20°C to 60°C, the effect of an increasing D_{O2} and improved reaction kinetics with increasing temperature outweighs that of a decreasing $[O_2]$, resulting in an overall increase in current density. However, from 60°C to 80°C the effect of a decreasing $[O_2]$ becomes more dominant and hence the current density decreases. Another possibility is that the decrease in

current density is a result of the Fe metal centre being out of plane in the presence of an air saturated electrolyte, an effect known from haeme chemistry. This makes the FePc species more susceptible to demetallation, especially at elevated temperatures where the activity of the protons has increased significantly. To test the effect of the proton's increased activity at elevated temperatures, additional surface layer coverage experiments were performed at 20°C and then at 80°C for all four FePc species. The procedure was the same as outlined in sections 3.3.1 and 3.3.2 above, except after the experiments were run at 20°C, the WE was immediately placed in an identical half cell at 80°C, and the experiment was repeated. The results (not shown) demonstrated for these experimental conditions, and for a length of time greater than the maximum time observed to run the ORR experiments, no significant change in Γ was observed. A separate test to check the stability of the four FePc species with increasing temperature in the presence of dissolved O_2 is described in section 3.3.5.

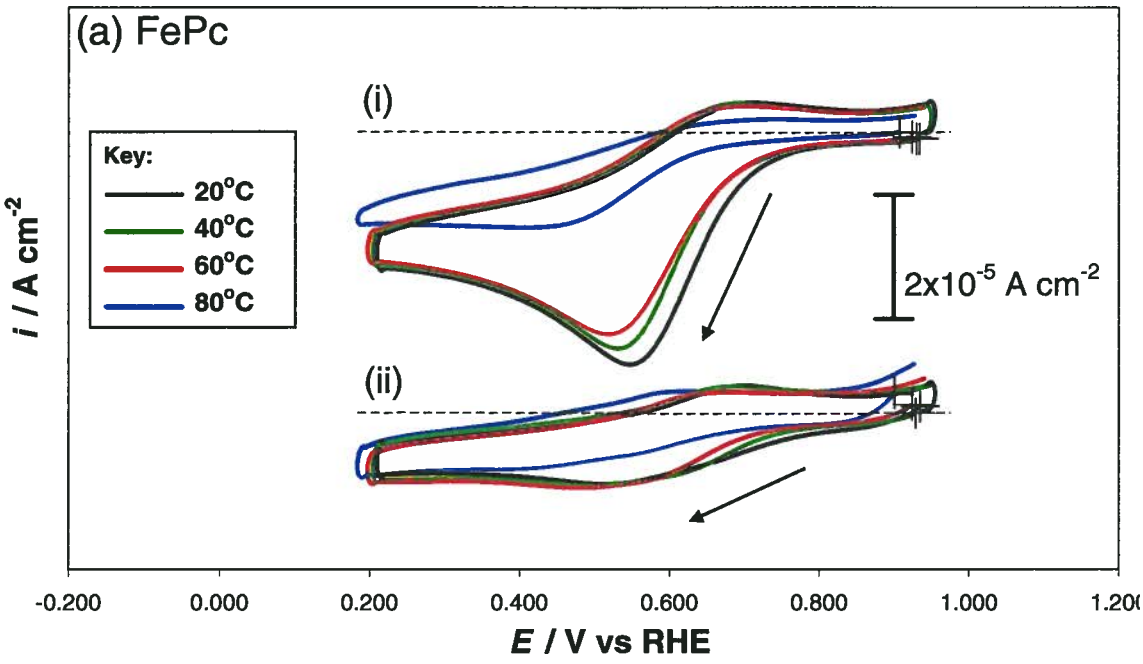

Fig. 3.6. Cyclic voltammograms at a scan rate of 100 mV s^{-1} for: (a) FePc, (b) $FePc(SO_3H)_4$, (c) $FePcCl_{16}$, (d) $FeNpPc(tBu)_4$, (e) $FePc(tBu)_4$, adsorbed on pyrolytic graphite electrodes in: (i) air-saturated solution; (ii) N_2 purged H_2O_2 solution at the same O_2 concentration as in (i), both at the same temperature, and in a 0.1 M H_2SO_4 electrolyte at 1 atm. For each pair (i, ii) temperatures are as marked. Dashed lines represent zero lines.

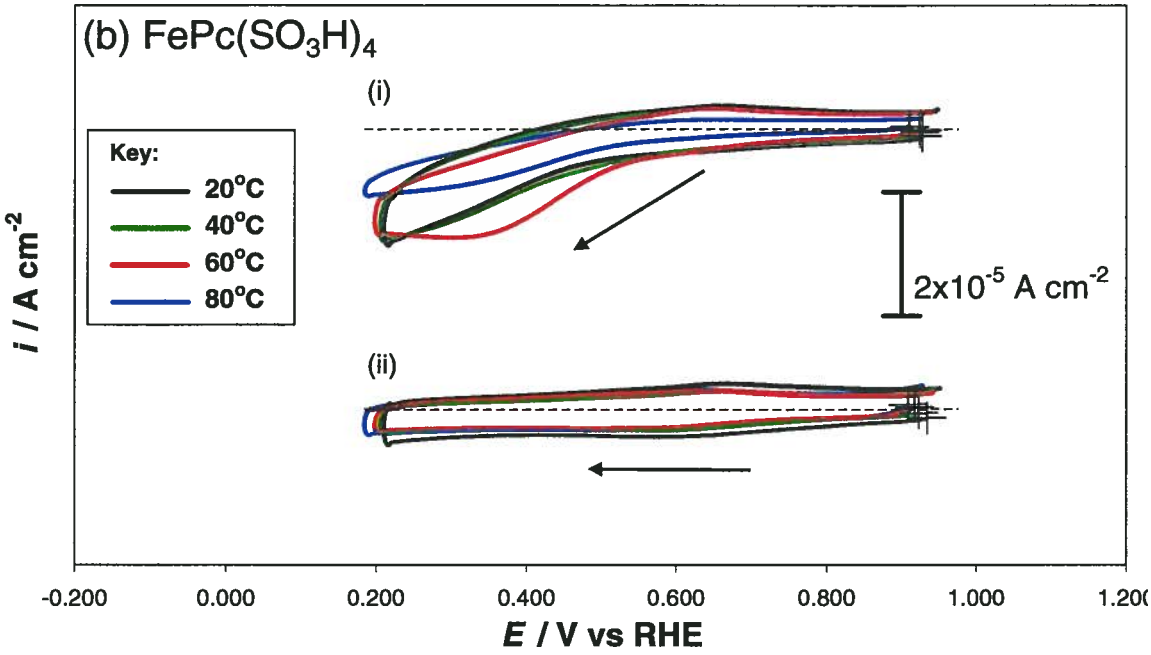
(b) FePc(SO3H)4
(i)
Key:
20°C
40°C
60°C
80°C
2x10-5 A cm-2
(ii)
i / A cm-2
-0.200
0.000
0.200
0.400
0.600
0.800
1.000
E / V vs RHE

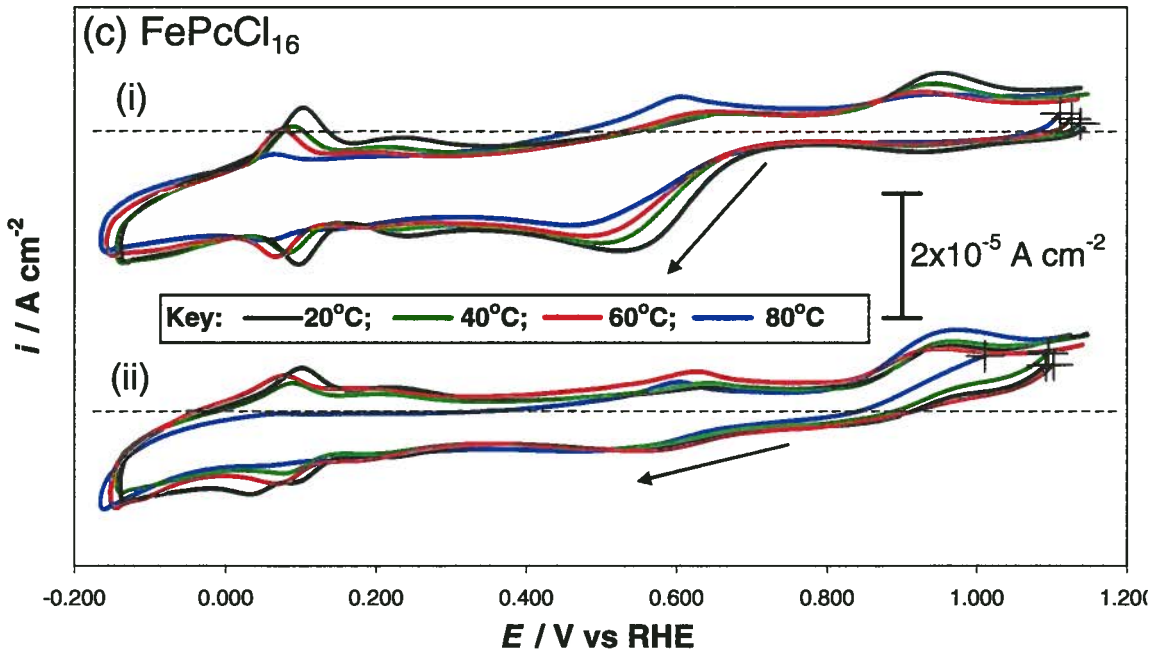
(c) FePcCl16
(i)
2x10-5 A cm-2
Key: 20°C; 40°C; 60°C; 80°C
(ii)
i / A cm-2
-0.200
0.000
0.200
0.400
0.600
0.800
1.000
E / V vs RHE

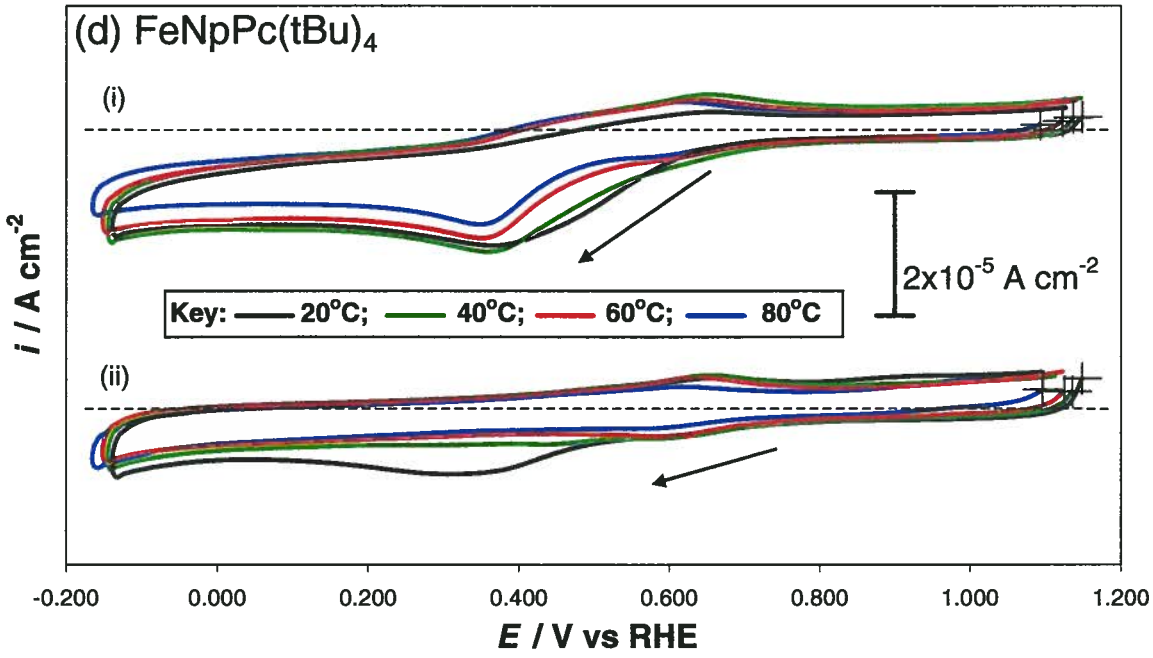
(d) FeNpPc(tBu)4
(i)
(ii)
Key: 20°C; 40°C; 60°C; 80°C
2x10-5 A cm-2
i / A cm-2
-0.200
0.000
0.200
0.400
0.600
0.800
1.000
1.200
E / V vs RHE

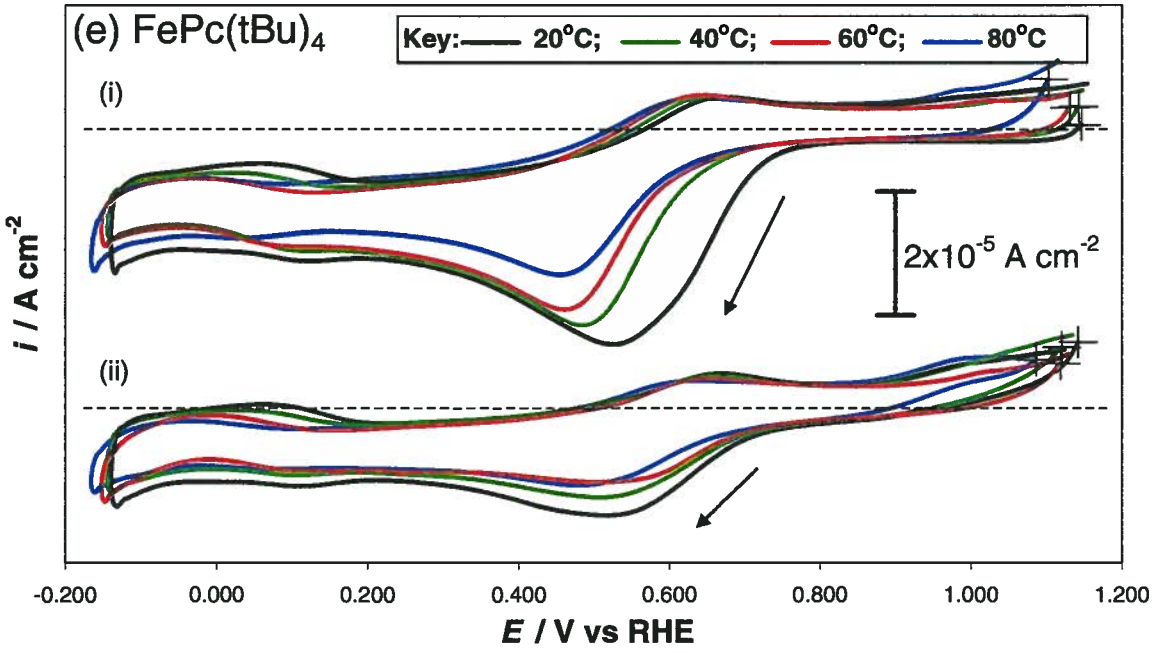
(e) FePc(tBu)4
Key: 20°C; 40°C; 60°C; 80°C
(i)
(ii)
2x10-5 A cm-2
i / A cm-2
-0.200
0.000
0.200
0.400
0.600
0.800
1.000
1.200
E / V vs RHE

Again, all FePc species show both O_2 and H_2O_2 reduction activity at all temperatures, except for $FePc(SO_3H)_4$ (Figure 3.6(b)) which exhibited no apparent H_2O_2 reduction activity. Other workers have reported more anodic onset potentials for FePc catalyzed H_2O_2 reduction [58], but it is difficult to determine if this onset potential is real, or an effect of an earlier onset of the O_2 wave as seen in Figures 3.6 (a), (c), (d) and (e). It is unusual that the shape of both the $FePc(SO_3H)_4$ catalyzed O_2, as well as the $FeNpPc(tBu)_4$ catalyzed O_2 and H_2O_2 reduction curves at 20°C in Figures 3.6(b) and (d) is noticeably different from those at higher temperatures. This is further discussed in section 3.3.5.4.

3.3.5 FePc catalyzed O_2 reduction kinetics evaluated by rotating disk electrode experiments

RDE voltammetry was employed to obtain quantitative reaction parameters such as Tafel slopes (b_c), cathodic transfer co-efficients for the rate limiting step ($n_\alpha \alpha_c$), the observed overall number of electrons involved in the reaction occurring on the disk surface (n), and the kinetic rate constant for the ORR (k_{O2}). Current-potential curves were obtained at different rotation rates using the same FePc species adsorbed pyrolytic graphite electrode. Figure 3.7 shows typical RDE curves for the baseline FePc at different electrode rotation rates, from which the parameters mentioned above can be obtained. The curves display a plateau current when the electrode potential is in the high polarization range, indicating an O_2 diffusion controlled process. However, when the potential is further reduced to less than 0.0 V vs RHE, the plateau current decreases, suggesting a

loss in catalyst activity. This can be attributed to degradation of the catalyst [69] if no other ORR active surface redox processes were observed in this potential window (Plots (a),(b),(c),(e) in Figures 3.3 and 3.6, respectively).

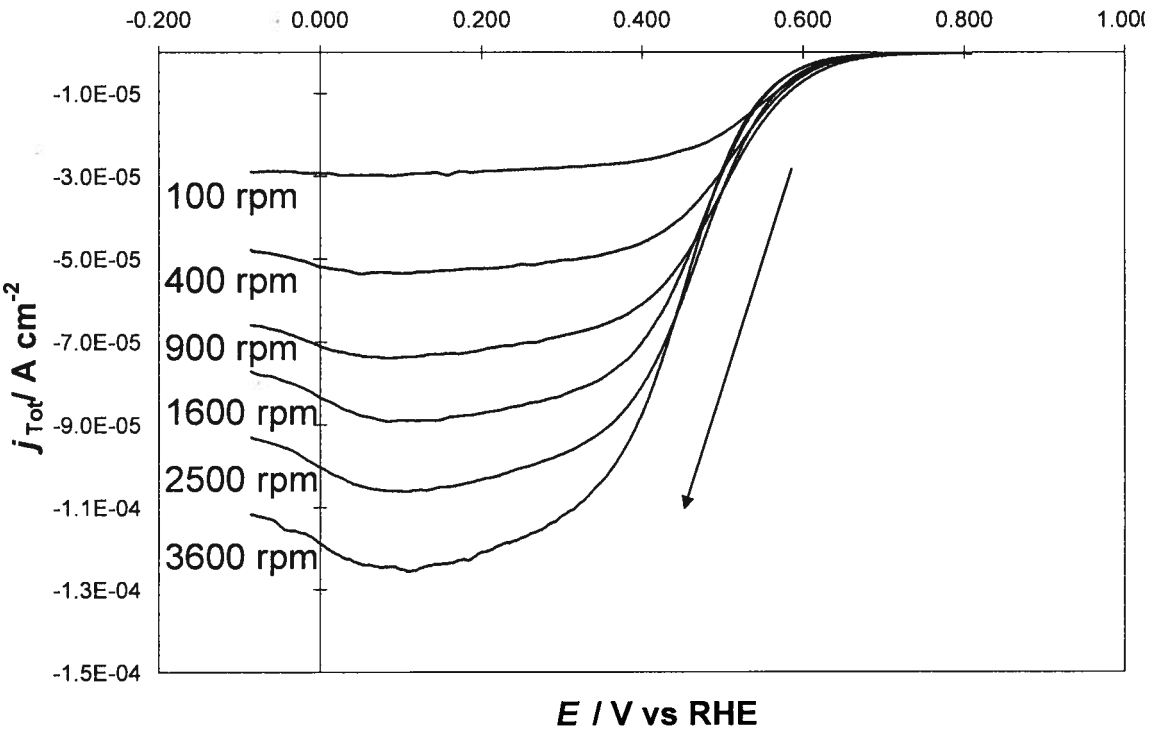

Fig. 3.7. Current-potential curves for FePc adsorbed on a rotating pyrolytic graphite disk electrode at different rates of rotation as marked on each trace, recorded in a 0.1M H_2SO_4 air-saturated solution at 80°C and 1 atm. Scan rate: 10 mV s^{-1}.

The instability of FePc's at low pH and reductive potentials in air-saturated electrolyte is well known [70,71]. When performing the RDE experiments, it was observed that all scans showed a marked reduction in current density with each successive scan, regardless of the order the scans were run in (Appendix XIV). The degradation in catalyst activity due to the FePc species decomposition, for

each subsequent scan for the same FePc species adsorbed on the surface necessitated the use of a freshly adsorbed FePc species surface for each rate of rotation experiment [70]. Coupled with the slight variation of the pyrolytic graphite surface after each polishing, this approach meant the kinetic regions for all rotation rates at each temperature do not overlap perfectly. However, once the potential is sufficiently negative to achieve the diffusion-limited plateau, these differences in the kinetic region seen in Figure 3.7 were assumed to be negligible, and should therefore have little effect on the data obtained from the diffusion-limited regime (i.e., n and k_{O2}).

The possibility of a significant loss in catalytic activity before or during the ORR RDE scan due to demetallation, or due to another mode of decomposition, was examined by comparing experimental data for the open circuit potentials (OCP's) and ORR RDE's (which immediately followed the OCP's) for each FePc species at each of the four temperatures. The OCP data showed that all four FePc species tested held stable potentials before the ORR RDE was run. Six pairs of sequential reduction and oxidation ORR RDE traces for the same fresh surface of each FePc species were run separately at 100, 900, and 3600 rpm. The first and sixth scans for each FePc species at 900 rpm and 80°C are qualitatively compared in Appendix XIV. These sequential ORR RDE scans showed at each temperature, and in the same amount of time, $FeNpPc(tBu)_4$ and $FePc(tBu)_4$ showed the greatest decrease in activity, whereas $FePcCl_{16}$ followed by $FePcSO_3H_4$ showed the smallest decrease in activity. However, during the first reduction scan for each freshly adsorbed FePc species, demetallation or

decomposition was not observed until sufficiently cathodic potentials were reached to decrease the plateau current. In summary, for a freshly adsorbed FePc species surface, decomposition was not observed before the ORR RDE trace was performed, and during the first reductive scan (up to 0.0 V vs RHE).

3.3.5.1. Tafel slopes

RDE curves (Figure 3.7) in the region less than 100 mV negative of the onset potential were assumed to be under purely kinetic control. Data from this region at all electrode rotation rates and for each FePc species as a function of temperature was used to calculate the Tafel slopes. The differences from one adsorbed FePc species surface to the next have a noticeable affect on the Tafel slopes, and in turn, the cathodic transfer coefficient. It was only possible to obtain linear log(i) vs. E plots within 100 mV of the onset potential, from each linear region of the different rpm's that, although they did not overlap perfectly, were parallel to each other. For this reason, the data obtained from the kinetic region (b_c and $n_\alpha\alpha_c$) is a close approximation. Other workers have reported similar challenges in obtaining Tafel slopes for FePc's at low pH values [72]. Table 3.3 lists the Tafel slopes for the ORR obtained at different temperatures for the five different FePc catalyzed electrodes. Although the Tafel slopes for all FePc species do change with temperature (Table 3.3), no drastic changes are observed either for the baseline FePc or for the substituted FePc's. This indicates the rate determining step of the reaction mechanism does not change appreciably with temperature for all the FePc species examined. The values of

$n_\alpha\alpha_c$ obtained are in the range of 0.5 to 0.7, which agree with those widely reported for the ORR [73].

Table 3.3. Tafel slopes (b_c) and cathodic transfer co-efficients ($n_\alpha\alpha_c$), at different temperatures for various FePc's.

Phthalocyanine	Temperature / °C	b_c / mV dec^{-1}	$n_\alpha \alpha_c$
FePc	20	-92	-0.63
	40	-106	-0.58
	60	-102	-0.65
	80	-105	-0.67
$FePc(SO_3H)_4$	20	-116	-0.50
	40	-134	-0.46
	60	-123	-0.54
	80	-124	-0.57
$FePcCl_{16}$	20	-92	-0.63
	40	-93	-0.67
	60	-96	-0.69
	80	-100	-0.70
$FeNpPc(tBu)_4$	20	-106	-0.56
	40	-120	-0.52
	60	-124	-0.53
	80	-139	-0.51
$FePc(tBu)_4$	20	-94	-0.62
	40	-92	-0.67
	60	-110	-0.60
	80	-110	-0.64

3.3.5.2. Effect of temperature

Figure 3.8 shows the effect of temperature on the baseline FePc catalyzed ORR process. It is obvious that the onset potential shifts to more negative values with increasing temperature. As previously discussed, this is mainly due to the decrease in solution $[O_2]$ with increasing temperature. The diffusion limited, or plateau currents increase with temperature in the range of 20°C to 60°C, even though $[O_2]$ is decreasing. Again, this is due to the greater contribution of an increasing D_{O2} and increasing reaction kinetics in this temperature range. The same decrease in current density is seen as in Figure 3.6 when the temperature is increased from 60°C to 80°C, as now the effect of a decreasing $[O_2]$ becomes more dominant. Another cause for this reduction in current density at 80°C could be a change in the reaction mechanisms and the number of electrons involved in the reaction, depending on the particular substituted FePc. It should be stated that the RDE curve only records electrochemical processes occurring at the disk and these processes do not necessarily always go to completion. This will be discussed further in section 3.3.5.4.

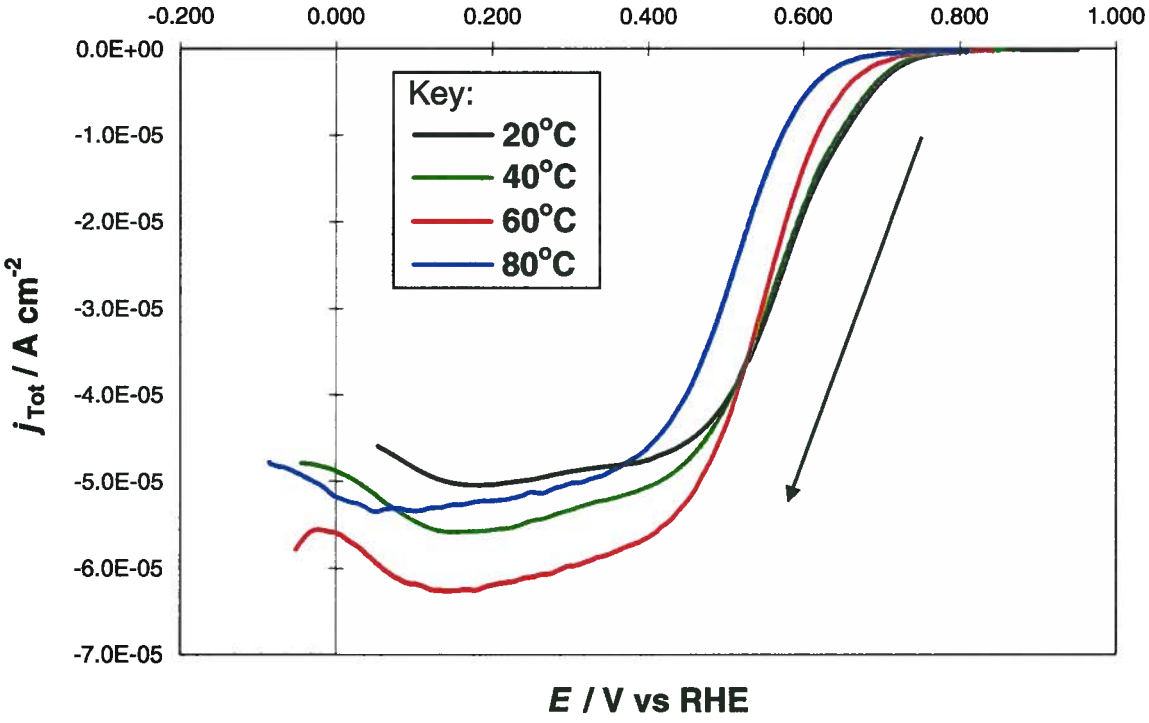

Fig. 3.8. Current-potential curves for FePc adsorbed on a rotating pyrolytic graphite disk electrode at 400 rpm and a scan rate of 10 mV s^{-1}, recorded in a 0.1M H_2SO_4 air-saturated solution and 1 atm, at different temperatures as marked.

3.3.5.3. Substituent effect

The effect of different substituents at 20°C and 80°C is shown in Figures 3.9 and 3.10, respectively. Of the five substituted FePc's, $FePcCl_{16}$ shows the greatest stability, as well as the best performance in terms of lowest kinetic overpotential and greatest diffusion limited current density, after the baseline FePc. The relative stabilities of each FePc species are further described in Appendix XIV. The kinetic overpotential for $FePcCl_{16}$ is essentially the same as that for FePc. $FePc(tBu)_4$ shows similar, but slightly lesser onset potentials and

diffusion limited plateaus, than FePc. $FePc(SO_3H)_4$ and $FeNpPc(tBu)_4$ have similar performances to each other. This is unexpected as the difference in electron withdrawing and donating substitutents between $FePc(SO_3H)_4$ and $FeNpPc(tBu)_4$, respectively, should give better performance for $FePc(SO_3H)_4$. As $FePc(SO_3H)_4$ is known to form adducts with O_2, the increase in overpotential could be a result of the reduction of the adduct before the catalyst can participate in the ORR. The trace for $FeNpPc(tBu)_4$ shows a quasi diffusion limited plateau, or linear region , between two monotonically increasing mixed reducing current regions, all at significantly diminished currents compared to $FePc(tBu)_4$ and FePc. This is unusual as all three aforementioned FePc species have surface concentrations that are similar to each other, and quite large in comparison to those for $FePc(SO_3H)_4$ and $FePcCl_{16}$. Compared to the baseline FePc, all substituted FePc's show significantly reduced diffusion limited current densities. This does not necessarily indicate a reduction in ORR activity due to substitution. A change in the plateau current can reflect a change in *n* and possibly the ORR mechanism.

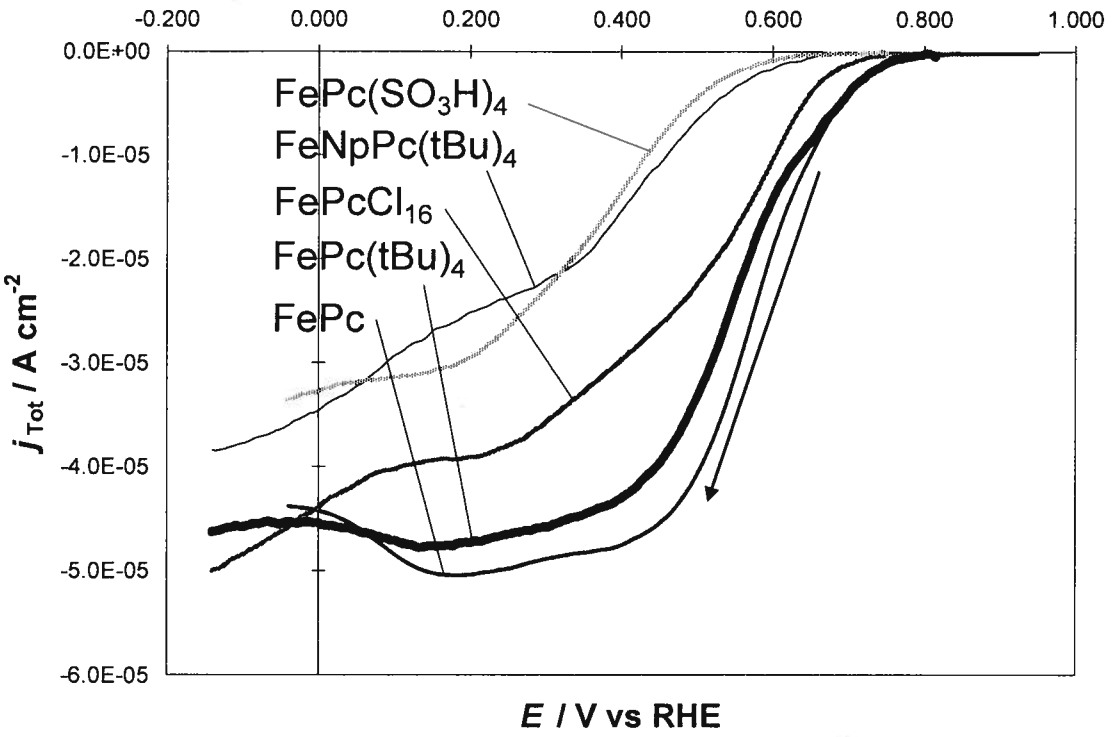

Fig. 3.9. Current-potential curves for different FePc's, as marked on each trace, adsorbed on a rotating pyrolytic graphite disk electrode at 400 rpm and a scan rate of 10 mV s^{-1}, recorded in a 0.1M H_2SO_4 air-saturated solution at 20°C and 1 atm.

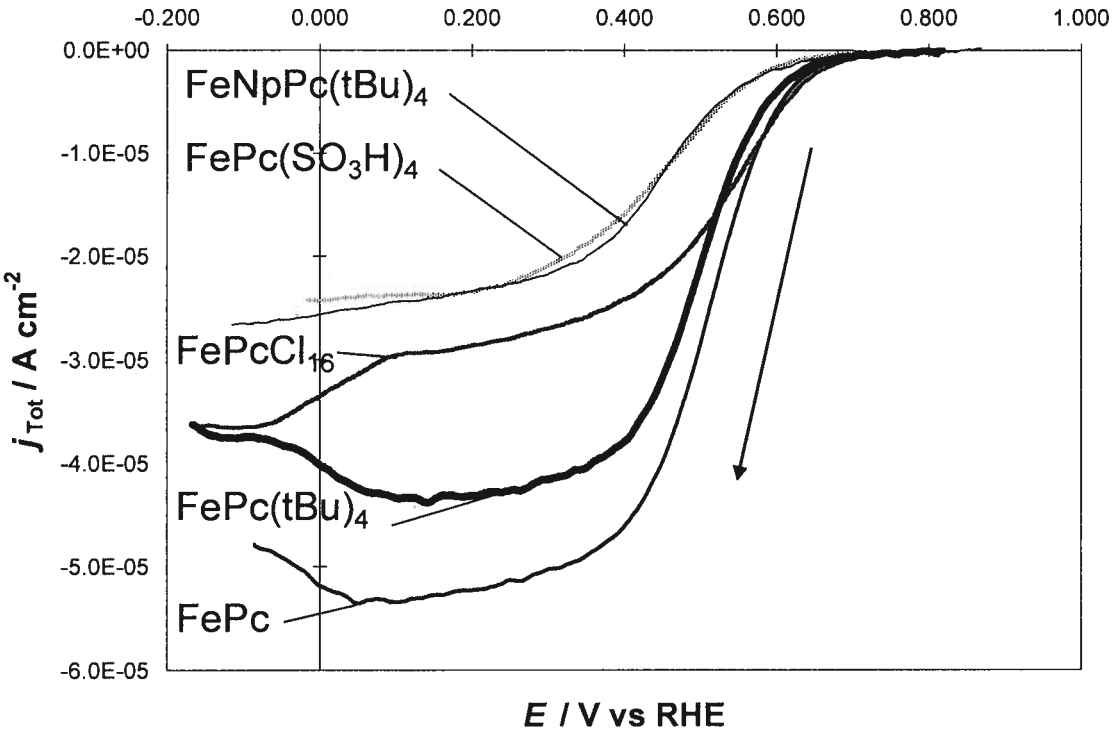

Fig. 3.10. Current-potential curves for different FePc's, as marked on each trace, adsorbed on a rotating pyrolytic graphite disk electrode at 400 rpm and a scan rate of 10 mV s^{-1}, recorded in a 0.1M H_2SO_4 air-saturated solution at 80°C and 1 atm.

3.3.5.4. Kinetic parameters obtained through the Koutecky-Levich approach

The RDE current (i_{disk}, or i_{Tot}) is related to the diffusion limited current (i_{diff}) and the kinetic current (i_{kin}), according to the Koutecky-Levich Equation [74]:

$$\frac{1}{i_{Tot}} = \frac{1}{i_{diff}} + \frac{1}{i_{kin}} \qquad (3.2)$$

where i_{diff} is also known as the Levich current (i_{Lev}), governed by the Equation [74]:

$$i_{Lev} = 0.201 nFAC_{O_2} D_{O_2}^{2/3} \gamma^{-1/6} \omega^{1/2} \quad (3.3)$$

where n is the overall electron transfer number, F is Faraday's constant, A is the geometric electrode area, D_{O2} is the diffusion coefficient of O_2, C_{O2} is the dissolved O_2 concentration in the electrolyte solution, γ is the kinematic viscosity of the electrolyte solution and ω is the rotation rate in rpm. The disk current in the plateau region is dominated by the levich current (i_{Lev}). So if all other parameters in the Levich Equation (3.3) are constant during the RDE scan (such as D_{O2}, C_{O2}, γ, and ω) and if the values are known at the scan temperature, then a change in plateau current will reflect a change in n. Therefore, a decrease in i_{Lev} would likely indicate a decrease in n for the FePc catalyzed ORR. The i_{kin} term in Eq. 3.2 can be expressed as the Equation [74]:

$$i_{kin} = nFAk_{O_2} C_{O_2} \Gamma_{FePc} \quad (3.4)$$

where k_{O2} is the kinetic rate constant for the catalyzed ORR, Γ_{FePc} is the surface concentration of the adsorbed FePc species, and all other variables are as described in Eq. 3.3. This kinetic constant is dependant on the electrode potential before the plateau current is reached. The diffusion controlled ORR could be limited by a chemical reaction between O_2 and the catalyst sites [22].

Eq. 3.3 automatically takes into account the change in $[O_2]$ with respect to temperature, as does Eq. 3.4. As Eq. 3.3 only depends on the electrode area, it is independent of Γ_{FePc}. The different Γ_{FePc}'s for each species are however taken into account in Eq. 3.4.

In order to quantitatively evaluate the FePc species catalyzed ORR, Koutecky-Levich plots of i_{Tot}^{-1} as a function of $\omega^{-1/2}$, according to Eq.'s 3.2 and 3.3, were generated for each FePc species as shown in Figure 3.11. It can be seen that the Koutecky-Levich plots yielded approximately linear relationships, indicating the reaction order with respect to O_2 was unity for all four FePc species tested at all four temperatures. Two dashed lines representing the theoretical $2e^-$ and $4e^-$ processes, calculated according to Eq. 3.3, are also plotted in each corresponding figure in order to compare the experimental data to expected theoretical values. Calculations based on Eq. 3.3 and 3.4 are still necessary, however, in order to get an accurate overall electron transfer number and kinetic rate constant.

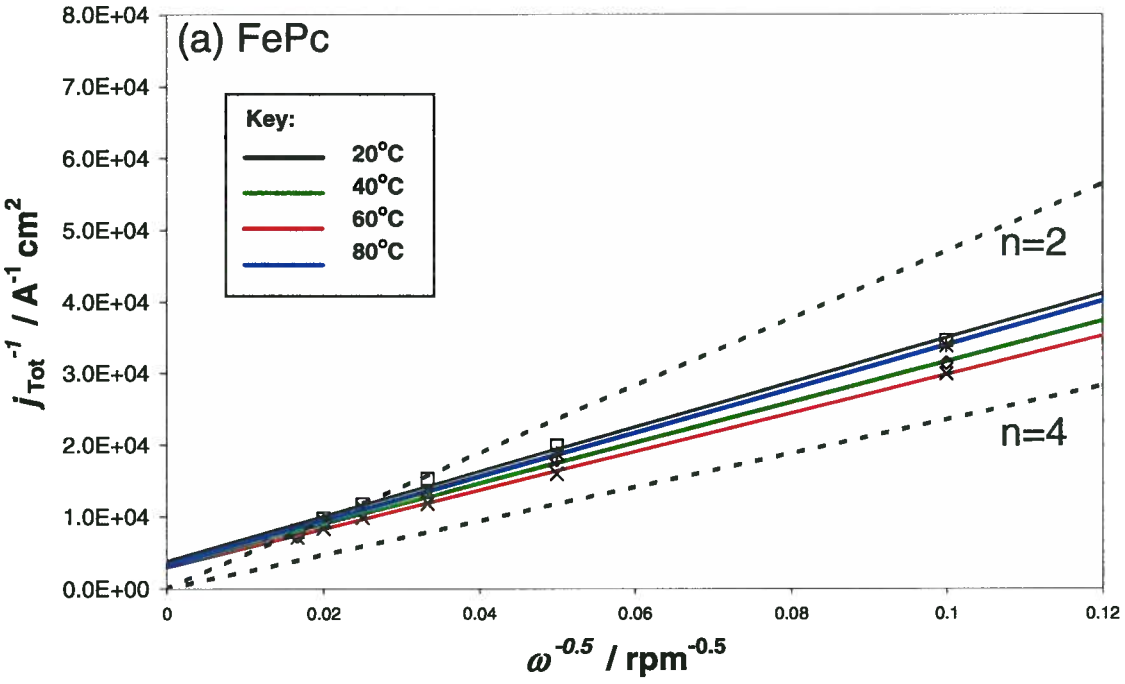

Fig. 3.11. Koutecky-Levich plots of (a) FePc, (b) $FePc(SO_3H)_4$, (c) $FePcCl_{16}$, (d) $FeNpPc(tBu)_4$, (e) $FePc(tBu)_4$, adsorbed on a pyrolytic graphite electrode, at different temperatures as marked. Theoretical lines for the two, and four, electron O_2 reduction process are as marked.

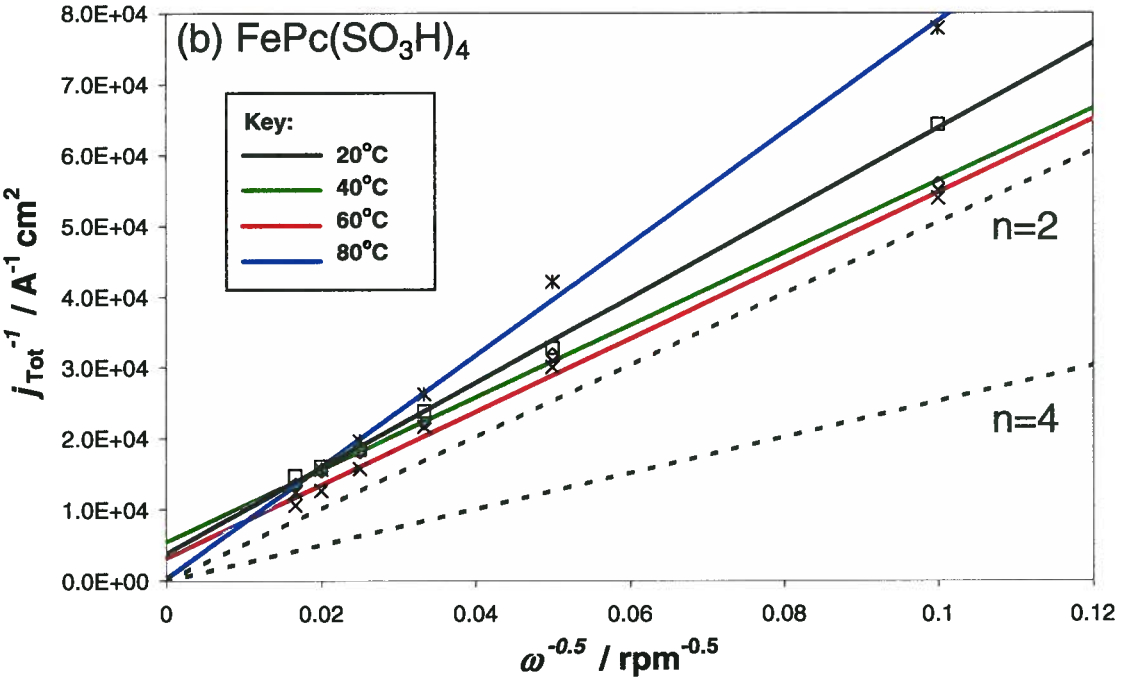
(b) FePc(SO3H)4
Key:
20°C
40°C
60°C
80°C
n=2
n=4
8.0E+04
7.0E+04
6.0E+04
5.0E+04
4.0E+04
3.0E+04
2.0E+04
1.0E+04
0.0E+00
0
0.02
0.04
0.06
0.08
0.1
0.12
j Tot -1 / A-1 cm2
ω-0.5 / rpm-0.5

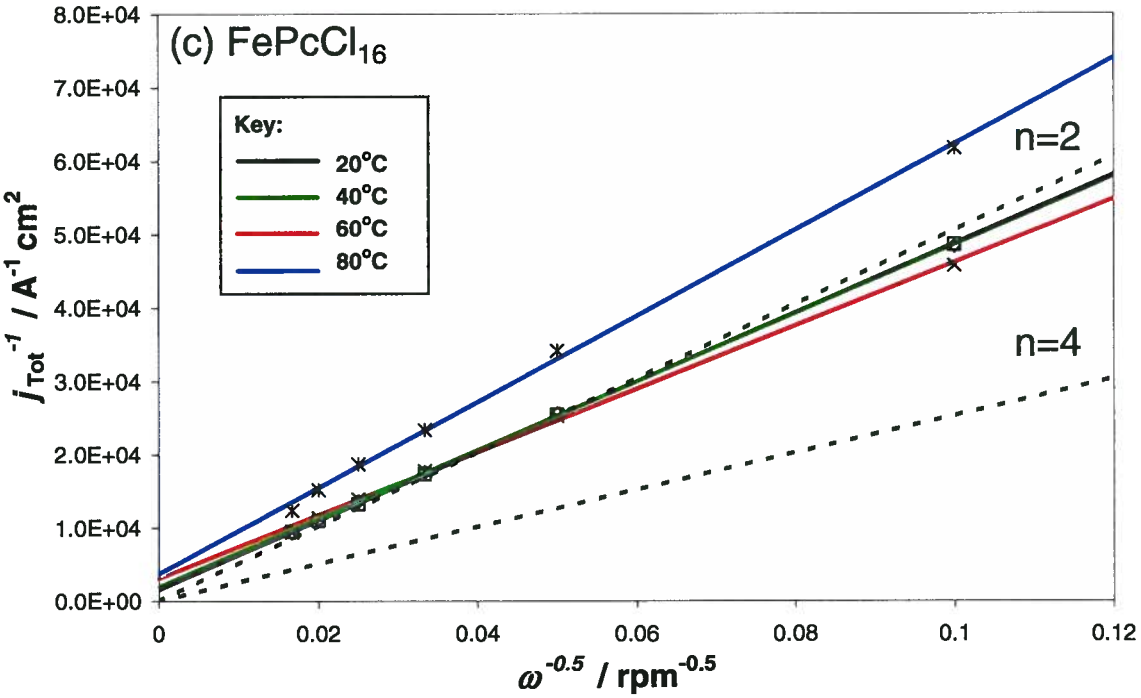
(c) FePcCl16
Key:
20°C
40°C
60°C
80°C
n=2
n=4
8.0E+04
7.0E+04
6.0E+04
5.0E+04
4.0E+04
3.0E+04
2.0E+04
1.0E+04
0.0E+00
0
0.02
0.04
0.06
0.08
0.1
0.12
j Tot -1 / A-1 cm2
ω-0.5 / rpm-0.5

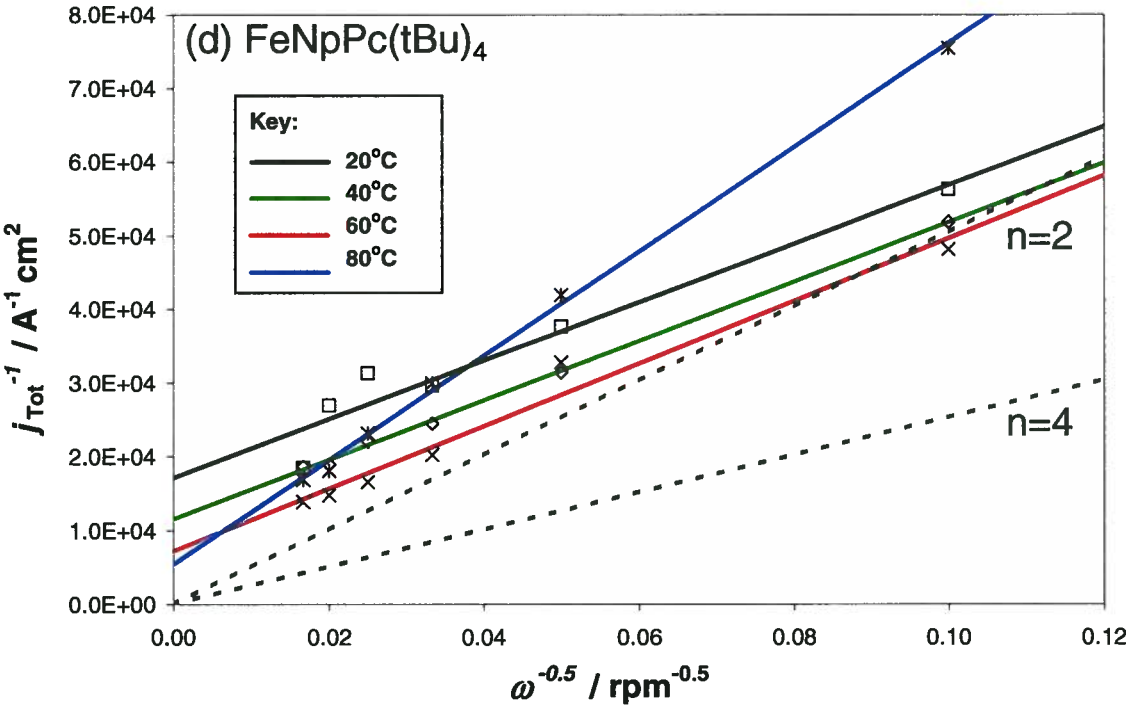
(d) FeNpPc(tBu)4
Key:
20°C
40°C
60°C
80°C
n=2
n=4
8.0E+04
7.0E+04
6.0E+04
5.0E+04
4.0E+04
3.0E+04
2.0E+04
1.0E+04
0.0E+00
0.00
0.02
0.04
0.06
0.08
0.10
0.12
jTot-1 / A-1 cm2
ω-0.5 / rpm-0.5

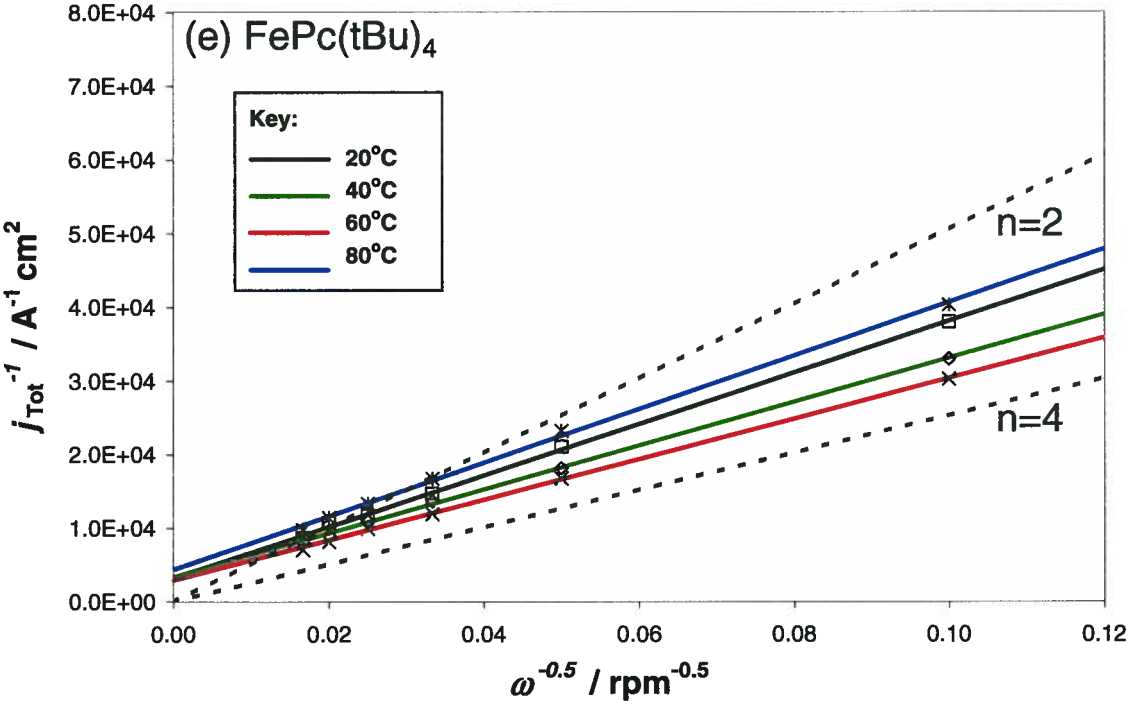
(e) FePc(tBu)4
Key:
20°C
40°C
60°C
80°C
n=2
n=4
8.0E+04
7.0E+04
6.0E+04
5.0E+04
4.0E+04
3.0E+04
2.0E+04
1.0E+04
0.0E+00
0.00
0.02
0.04
0.06
0.08
0.10
0.12
jTot-1 / A-1 cm2
ω-0.5 / rpm-0.5

The results for the overall electron transfer number, n, and the kinetic rate constant, k_{O2}, obtained for the different FePc species in the temperature range of 20°C to 80°C, are listed in Table 3.4.

Table 3.4. Number of electrons consumed (n) and kinetic rate constant (k_{O2}) at different temperatures for various FePc's taken at potentials as marked.

Phthalocyanine	Potential / V vs RHE	Temperature / °C	n	k_{O2} / $cm^3\ mol^{-1}\ s^{-1}$
FePc	0.165	20	3.3	1.06E+08
		40	3.4	1.70E+08
		60	3.3	2.54E+08
		80	2.6	3.24E+08
$FePc(SO_3H)_4$	0.165	20	1.7	9.72E+08
		40	1.9	8.90E+08
		60	1.7	2.18E+09
		80	1.0	5.29E+10
$FePcCl_{16}$	0.315	20	2.1	1.86E+09
		40	2.1	2.47E+09
		60	2.1	1.93E+09
		80	1.4	2.76E+09
$FeNpPc(tBu)_4$	0.165	20	2.5	5.78E+07
		40	2.4	1.31E+08
		60	2.1	3.12E+08
		80	1.1	8.91E+08
$FePc(tBu)_4$	0.315	20	2.9	8.00E+07
		40	3.3	1.07E+08
		60	3.3	1.61E+08
		80	2.2	1.86E+08

For the baseline FePc (Figure 3.11 (a)), the electron transfer number obtained at all temperatures is 3.3, which is typical for a mixed two- and four-electron process [75]. For $FePc(SO_3H)_4$ (Figure 3.11 (b)), the electron transfer number is 1.7 – 1.9 in the temperature range of 20°C to 60°C. However, at 80°C, the overall electron transfer number becomes 1.0. For $FePcCl_{16}$ (Figure 3.11 (c)), the electron transfer number is 2.1 in the temperature range of 20°C to 60°C, the exception being at 80°C, where it is 1.1. For $FeNpPc(tBu)_4$ (Figure 3.11 (d)), the electron transfer number is 2.5 at 20°C, 2.4 – 2.1 at both 40°C and 60°C, and again 1.1 at 80°C, respectively. Lastly for $FePc(tBu)_4$ (Figure 3.11 (e)), the electron transfer number is 2.9 at 20°C, 3.3 at both 40°C and 60°C, and again 2.2 at 80°C, respectively. The differences in overall electron transfer number likely reflect the effect of the different substituents and temperature on the FePc species catalytic mechanisms. It is quite challenging to fully understand why different substituent groups can change the catalyzed ORR mechanism to such an extent. DFT modeling is currently being carried out in our group in order to obtain a deeper understanding of the effect of temperature and substituents on the FePc species and in particular on the electron density of the metal centre [76,77]. DFT analysis could be combined with Hammett parameter studies on existing and additional substituted FePc species [41,48]. More experimental work is required to elucidate the effect of temperature and substituents on the overall electron transfer number. The C_{O2}, D_{O2}, and γ values used to calculate n were extensively checked using different accepted literature values as well as calculation methods to see if there was a significant affect. These re-calculations

on average decreased the value of n in the third and sometimes second decimal place, and were thus insignificant. An experiment according to the method of Winlove and co-workers [78,79] was also performed to simultaneously determine in situ values for C_{O2} and D_{O2} at 80°C. The current experimental set up prevented accurate, repeatable measurements at the nA level and thus was inconclusive.

As FePc, $FePc(SO_3H)_4$, $FePcCl_{16}$ and $FePc(tBu)_4$ all show more than one surface redox process (Figures 3.3 (a), (b), (c) and (e), respectively), current densities for Koutecky-Levich plots were taken at a potential where all FePc's displayed diffusion limited ORR plateaus, but before any secondary ORR active redox processes took place. This potential was 0.165 V vs RHE for FePc, $FePc(SO_3H)_4$, $FeNpPc(tBu)_4$ and 0.315 V vs RHE for $FePc(tBu)_4$ and $FePcCl_{16}$ at all four temperatures. Wherever possible, Koutecky-Levich plots for data taken at other potentials (0.015, and either 0.165 or 0.315 V vs RHE, respectively) were also made to see if there was any effect on kinetic parameters (not shown). If no secondary redox processes were occurring at either of these potentials, the change in n was insignificant, and the change in k_{O2} was small. These k_{O2} values were plotted as a function of temperature for each FePc species according to the Arrhenius theory described in Appendix I, to determine the energy of activation for the observed reaction (E_a) as well as the kinetic rate constant for the FePc catalysed ORR at infinite temperature (k_{O2}°). Because $n < 4$, and these n values then decreased with increasing temperature, the E_a and k_{O2}° values reported in Appendix XIII were not indicative of a complete ORR and thus not accurate.

However, the relative differences in k_{O2} values as a function of substitution and temperature did show interesting trends. These trends are also described in Appendix XIII.

Two of the tetra-substituted FePc's ($FePc(SO_3H)_4$ and $FeNpPc(tBu)_4$) each exhibited two different RDE curve shapes at 20°C which in turn yielded non-linear Koutecky-Levich data (Figure 3.11(d) for $FeNpPc(tBu)_4$, but not shown for $FePc(SO_3H)_4$). As discussed in section 3.3.2, FePc's can have different modes of adsorption onto the pyrolytic graphite surface, including interactions with each other as well as with other species in the electrolyte solution. With further experimentation, it was possible to control the state of the adsorbed $FePc(SO_3H)_4$ surface such that the resulting Koutecky–Levich plot for this temperature was linear. This was accomplished by running a potentiostatic experiment on the freshly adsorbed $FePc(SO_3H)_4$ surface at 1.0 V vs RHE in a N_2 purged electrolyte for two minutes, immediately before transferring the electrode to an air saturated electrolyte for a ten minute open circuit potential experiment, followed by the ORR RDE scan. The different types of curves exhibited by $FeNpPc(tBu)_4$, however, could not be controlled in the same manner. Two RDE curve shapes were separately seen (Figure 3.11(d)) for 100 to 900 rpm and for 1600 to 3600 rpm, the former showing linear Koutecky-Levich behaviour. Both the inclusion and exclusion of this non linear data for the two FePc's discussed did not have a significant effect on the values n and k_{O2} obtained at 20°C. At 40°C and above, both $FePc(SO_3H)_4$ and $FeNpPc(tBu)_4$ showed only one type of curve which yielded linear Koutecky-Levich plots.

It is well known that adding symmetrically substituted electron donating and withdrawing substituents on the periphery of a TM macrocycle ring can change its' mode of adsorption, its' electrochemical and chemical activity along with its' stability by affecting the electron density of both the ring and in particular the metal centre [7,10,16,41-48,77]. In addition, the reaction mechanisms may change, and in turn, the electrochemical as well as chemical activities can be affected. The reduction from n=3 for the baseline FePc to n=2 for the substituted FePc's in the temperature range of 40°C to 60°C could indicate the ORR mechanism has changed such that the two electron reduction to H_2O_2 is favoured over the direct four electron reduction. It is also possible that the additional two-electron step to reduce H_2O_2 to H_2O has become more rate limiting so that the overall four electron mechanism is not seen. As well, the rate for the purely chemical pathway for the decomposition of H_2O_2 could increase to the point that it is now overtaking the rate of H_2O_2 electrochemical reduction and the peroxide is being decomposed back into O_2 and H_2O before it has time to further reduce. Another explanation could be that the different modes of adsorption of the FePc species onto the pyrolytic graphite surface have an effect on n observed [57]. This holds true if the adsorption mode allows macrocycle to macrocycle, metal centre to metal centre, and/or macrocycle to metal centre electron transfers for neighbouring TM macrocycle species [8,30]. Although the adsorption mode could have an effect on the mechanism and hence n observed, it likely is not the dominant factor in this case as FePc, $FeNpPc(tBu)_4$ and $FePc(tBu)_4$ have greater surface concentrations, but relative to FePc, both $FeNpPc(tBu)_4$ and $FePc(tBu)_4$

still show a decrease in *n* with increasing temperature, similar to $FePc(SO_3H)_4$ and $FePcCl_{16}$.

Other authors have reported on the synthesis and ORR activity of FeNpPc as well as CoNpPc [11-15], where FeNpPc was shown to proceed via 4 electron, and CoNpPc was shown to proceed via 2 electron, reduction mechanism. It is unusual that the tetra-*tert*-butyl substitution of FePc has a minimal effect on its' ORR mechanism, but the same substituents on FeNpPc appear to have a significant effect on the $FeNpPc(tBu)_4$ ORR mechanism. This is even more so considering $FeNpPc(tBu)_4$'s surface concentration is similar to those of FePc as well as $FePc(tBu)_4$, and greater than those of $FePc(SO_3H)_4$ and $FePcCl_{16}$.

In Chapter, 4, RRDE experiments at 20°C and under the same conditions are performed to confirm the RDE results presented in this chapter. As part of our future work, further RRDE experiments will be run in air saturated 0.1M H_2SO_4 electrolyte both at 20°C and 80°C and 1 atm using established procedures to separately quantify the electrochemical reduction of O_2 to H_2O_2 and the chemical decomposition of H_2O_2 to O_2 and H_2O [75].

The apparent change from a two to one electron ORR mechanism at 80°C for all five substituted FePc's at 80°C needs to be clarified. Although the one electron pathway is possible, it is highly unfavourable as it proceeds at –0.046 V vs NHE at an otherwise inert (Pt or Au) electrode [30]. Given the type of CME used in this work is not the same as a well defined Pt or Au electrode, it is possible the one electron pathway could proceed at potentials significantly positive of –0.046 V vs NHE. The possibility of the one electron pathway at 80°C

would have to be either confirmed or ruled out experimentally. The existence of a reversible one electron ORR product to the superoxide species (O_2^-) is reported in the literature, but for a hexadeca fluoro-substituted cobalt phthalocyanine ($CoPcF_{16}$) at a pH of 14 (1M NaOH) [32]. For this work, similar ORR CV experiments were performed at various scan rates (1, 10, 50, 100, 500, 1000 mV s^{-1}) using $FePcCl_{16}$, an analogue to $CoPcF_{16}$, and the baseline FePc, both in 0.1M H_2SO_4 and in 1M NaOH at 20°C and 80°C. Although the one electron product is highly unstable in acidic media, tests at a pH of 1 were performed to duplicate the experimental ORR RDE conditions. Results did not show a reversible one electron product at any of the scan rates used for either FePc or $FePcCl_{16}$ in both acidic and basic media at 20°C and 80°C. Even if the existence of a one electron product is established, this does not necessarily indicate a change to the one electron reaction mechanism. Other groups have established $HO_2^{-\cdot}$ could be an adsorbed intermediate as part of the two electron reaction mechanism forming H_2O_2 [80]. As the aforementioned ORR CV result is inconclusive, RRDE experiments at 60°C and 80°C would be beneficial.

The possibility of demetallation also exists (vide supra), but does not appear to be significant for these experimental conditions. No correlation was found between a decrease in stability of the FePc species and a decrease in *n*. The opposite is observed where the substituted FePc's, which show a decrease in *n* with increasing temperature, have a greater stabililty and hence a lower rate of demetallation, relative to the baseline FePc.

Another explanation could be either the reactants and/or intermediates are removed from the disk before the electrochemical reaction goes to completion, or the reactant and/or intermediates are too unstable and spontaneously decompose. Considering the instability of the $HO_2^{\cdot}$ species, the latter is more likely than the former given the relative time scales for convection as well as diffusion when compared to decomposition. This becomes more plausible when the effect of substitution on the strength of the interaction between the catalyst and adsorbed species is considered. According to the Sabatier principle, the metal - heteroatom bond energy for an ideal catalyst should not be too strong nor too weak [81]. As seen in carbon monoxide (CO) adsorption on Pt, the bond energy decreases with increasing temperature, eventually leading to more facile oxidation and de-adsorption [82]. It is entirely possible that the addition of substituents has altered the stability of any one or all of the ORR intermediates at higher temperatures to such an extent that as soon as it is formed, it decomposes before it has any chance to react further. It follows that the change in n could simply indicate any one of the adsorbed intermediates decomposes and/or de-adsorbs without any change in the ORR mechanism. Another possibility is the change to n = 1 could indicate a one electron reduction from Fe^{III+} to Fe^{II+} followed by the binding of O_2 to Fe^{II+} and a subsequent heterogeneous catalysis, otherwise known as redox mediation. Again, further experiments, such as using an RRDE, are required.

3.3.6 Mechanism discussion

As shown in Table 3.3, the average $n_\alpha \alpha_c$ value for the five FePc species studied is around 0.6. If the electron transfer coefficient is assumed to be 0.6, the value of n_α, the electron transfer number in the rate determining step for the ORR, would be 1. This is well-cited for the ORR in the literature [23]. Based on this information, and the current literature, the following FePc species catalyzed ORR mechanism in acidic media can be suggested [3,7,33,37,40,51,67,72,75,80,83]:

$Fe^{III}Pc + e^- \leftrightarrow Fe^{II}Pc$ (I)

$Fe^{II}Pc + O_2 \leftrightarrow O_2\text{-}Fe^{II}Pc$ (II)

$O_2\text{-}Fe^{II}Pc + e^- + H^+ \leftrightarrow [HO_2\text{-}Fe^{III}Pc]$ (Rate determining step) (III)

$[HO_2\text{-}Fe^{III}Pc] \rightarrow HO_2^{\cdot} + Fe^{III}Pc$ (Hydroperoxyl radical formation) (IV)

$[HO_2\text{-}Fe^{III}Pc] + e^- + 1H^+ \rightarrow H_2O_2 + Fe^{III}Pc$ (Hydrogen peroxide formation) (V)

$[HO_2\text{-}Fe^{III}Pc] + 3e^- + 3H^+ \rightarrow 2H_2O + Fe^{III}Pc$ (Water formation) (VI)

In this mechanism, the $Fe^{III}Pc$ surface species produced in reaction (VI) will be reduced back to the $Fe^{II}Pc$ surface species according to reaction (I) at the potential range where the ORR occurs, forming a catalytic reaction cycle. Reaction (II) is a chemical reaction between O_2 and the surface FePc species catalyst to form an adduct. Reaction (III) is believed to be the rate-determining step with one electron transfer from the catalyst center (Fe^{II}) to O_2. After reaction (III), three reactions are possible. Reaction (IV) is a chemical reaction forming

the free hydroperoxyl radical, reaction (V) is an additional one-electron transfer process to form hydrogen peroxide, and reaction (VI) is an additional three-electron process to form water. Reaction (VI) may not necessarily be an elementary reaction as it is quite challenging for three electrons and three protons to meet together for this reaction to occur. Reaction (VI) could include several fast elementary reactions. Depending on the FePc ring's substituents and the temperature, the reaction could end either at reaction (IV), reaction (V) or reaction (VI). The chemical decomposition of H_2O_2 is also possible, which could remove any H_2O_2 formed from reaction (V). Decomposition could also stop reaction (VI) after the adsorbed peroxide intermediate is formed as it has been stated in the literature that a TM macrocycle catalyzed four electron ORR could proceed via an adsorbed peroxide species [30]. It is also possible for the reaction to stop after the first proton transfer in reaction (V) without any further electron or proton transfers, forming the hydroperoxyl radical.

3.4 Summary

Five different phthalocyanine macrocycle-based iron complexes, which all irreversibly adsorb on a pyrolytic graphite electrode, were studied using surface electrochemical techniques (surface voltammetry). These FePc species showed strong catalytic activity towards the O_2 reduction reaction when they were adsorbed on the electrode surface. The kinetics and corresponding parameters such as overall ORR electron transfer numbers, reaction rate constants, Tafel slopes, electron transfer number in the rate-determining step, and electron transfer coefficients were all obtained through RDE measurements in the

temperature range of 20°C to 80°C. These parameters were calculated using the Koutecky-Levich theory and the cathodic Tafel Equation, respectively.

The surface electrochemical responses of the FePc species were characterized with respect to their surface concentrations and adsorbed surface orientations. Depending on the type of substituent, the adsorption mode could be flat, edge-on, as a dimer, or as an agglomerate, suggesting that the substituent has a strong effect on the FePc species' adsorption mode. Substitution also has a significant effect on stability. Of the four FePc species tested, $FePcCl_{16}$ was the most stable in an acidic ORR environment. With respect to their electrocatalytic activity, both temperature, substitution and possibly mode of adsorption can significantly affect the ORR mechanism. For example, the overall electron transfer number observed can change from 1 to 3 depending on the type of substituent and the reaction temperature. Further research is required to determine if this change in *n* reflects a change in the ORR pathway, and/or a decrease in the stability of the adsorbed ORR intermediates. The possibility of redox mediation at 80°C should also be examined. Based on our experimental results, the various approaches found in the literature, and our current understanding, a mechanism for the FePc species catalyzed ORR was suggested.

Chapter 4

Comparison of Different O_2 Reduction Mechanisms for Iron Phthalocyanines as a Function of Substitution Using Rotating Disk, and Rotating Ring Disk Electrode, Voltammetries

4.0 Objective

In this Chapter, the electrocatalytic activities of all five FePc species towards the ORR, were evaluated using a Pt ring and pyrolytic graphite disk RRDE and then compared to the RDE results presented in Chapter 3. Three sets of RRDE scans were run for each FePc species. From the RRDE results, the fraction of H_2O_2 produced (X_{H2O2}) at the disk was calculated. Except for FePc, the X_{H2O2} values presented confirmed the results for *n* shown in Chapter 3.

4.1 Description

It is desirable for ORR electrocatalysts to proceed via the 4 e^- mechanism directly to H_2O with as little production of H_2O_2 via the 2 e^- mechanism as possible. RRDE allows the determination and quantification of any H_2O_2 produced by the electrocatalyst at the disk surface and hence the FePc species ability to reduce O_2 via the 4 e^- mechanism.

4.2 Experimental

The chemicals, synthesis, spectroscopy, method of surface attachment, and electrochemical measurements have been previously described in Chapters 2 and 3, unless noted differently below.

4.2.1 Chemicals

Sodium hydroxide (NaOH reagent grade 97%, cat. no. 367176, batch no. 65123ED) was purchased from Sigma Aldrich and used as received.

4.2.2 Working electrode preparation

The in-house pyrolytic graphite electrodes were mounted such that the basal planes were exposed on the face of the disk. The active electrode area of 0.15 cm^2 was electrochemically determined with a 1.00×10^{-3} M $K_3[Fe(CN)_6]$ solution. A full description of WE preparation is described in Chapter 2 [1,3,67].

4.2.3 Surface attachment

Irreversible adsorption of the TM macrocycle onto the WE disk surface was achieved by immersion in an approximately 1.0×10^{-4} M solution of the FePc species for no longer than 30 seconds. Full details of this technique are described in Chapter 2 [1,3,67].

4.2.4 Rotating ring disk electrode

Two Pine model number AFE6R1PT RRDE's, with changeable disk inserts were used. These RRDE's (Pine electrode serial numbers 12323 and 12324) contained a basal plane pyrolytic graphite disk and Pt ring. The changeable disk inserts were custom made in house out of the same basal plane pyrolytic graphite material used in Chapter 3. Pine's AFE6M shaft was used to connect

the change disk RRDE to the Pine MSR rotator. The pyrolytic graphite disk had a geometric area of 0.19 cm^2. The Pt ring's collection efficiency (*N*) was found experimentally to be 0.21 +/- 0.01, according to the method reported by Paulus et al. [84]. The experimental determination of collection efficiency (*N*) is further described in section 4.3.2.1.

4.2.5 Electrochemical measurements

Unless described otherwise in this section, the half cell, as well as all electrochemical measurements, equipment and materials, are the same as found in the corresponding sections of Chapters 2 and 3, respectively. RRDE voltammetry was performed using a Pine MSR rotator (model AFMSRX) run using a Pine MSRX speed controller, connected to a Pine bipotentiostat (model AFCBP1) that was operated using *PineChem 2.8* bipotentiostat software.

4.3 Results and discussion

4.3.1 O_2 reduction evaluated by rotating disk electrode voltammetry

RDE ORR scans as well as Koutecky Levich analysis of the five substituted FePc species are described in Chapter 3. At a pH of 1, the Koutecky Levich analysis results seen in Table 3.4 of Chapter 3 indicated the observed number of electrons transferred (*n*) was 3.3, 1.7, 2.1, 2.5 and 2.9, for FePc, $FePc(SO_3H)_4$, $FePcCl_{16}$, $FeNpPc(tBu)_4$ and $FePc(tBu)_4$, respectively [1]. Taking into account the possible effect of catalyst loading, or surface concentration (Γ) [85] on *n*, and hence the observed ORR mechanism it is reasonable that $FePc(SO_3H)_4$ and $FePcCl_{16}$ both showed 2 electron reduction mechanisms considering both adsorbed in sightly less than one monolayer. This observed decrease in *n* for

$FeNpPc(tBu)_4$, however, was unusual considering it along with FePc and $FePc(tBu)_4$ all had Γ's which yielded monolayer equivalents of 2.7, 2.1, and 4.5, respectively.

4.3.2 O_2 reduction evaluated by rotating ring disk electrode voltammetry

To confirm the *n*'s reported here, RRDE voltammetry was performed at room temperature (20 +/- 1 °C).

4.3.2.1. Collection efficiency of the change disk RRDE

For the experimental determination of the collection efficiency (*N*) [84], a solution of 0.1 M NaOH with 10 mmol $K_3Fe(CN)_6$ in DI H_2O was made and deaerated with N_2. The disk potential was swept between 0.81 and -0.01 V vs RHE at a scan rate of 20 mV s^{-1}. The ring was held at a constant potential of 0.81 V vs RHE. At these potentials, the redox cycle for $K_3Fe(CN)_6$ occurs under purely diffusion control, and the oxygen evolution reaction (OER) currents are negligible at the ring [84]. *N* is obtained from the ratio of ring to disk currents according to Equation (4.1) [84]:

$$N = -\frac{I_R}{I_D} \tag{4.1}$$

where I_R is the ring current, *N* is the collection efficiency, and I_D is the disk current, respectively.

It should be noted that due to the design of the change disk RRDE's, both the in house built PTFE cup and pyrolytic graphite disk were not exactly co-planar with the rest of the RRDE assembly, including the Pt ring. Their height relative to

the Pt ring also changed slightly for each assemblage, and for each different PTFE cup. As a result, the RRDE was removed, disassembled, the disk was polished and then cleaned (both according to the experimental section of Chapter 2) followed by re-insertion and re-assembly. This process was repeated three separate times for each measurement to obtain an average value of *N*. The reductive scans shown in Figure 4.1 were used to calculate the value of 0.26 +/- 0.01 for *N*.

Fig. 4.1. Current potential curves for a rotating ring and disk electrode at rotation rates as marked on each trace for determining the collection efficiency of a pyrolytic graphite disk and Pt ring change disk RRDE in 0.1 M H_2SO_4 as the electrolyte with 10 mM $K_3Fe(CN)_6$. Experimental conditions were 20°C +/- 1°C and 1 atm. Scan rate of 20 mV s^{-1}. Ring potential of 0.81 V vs RHE.

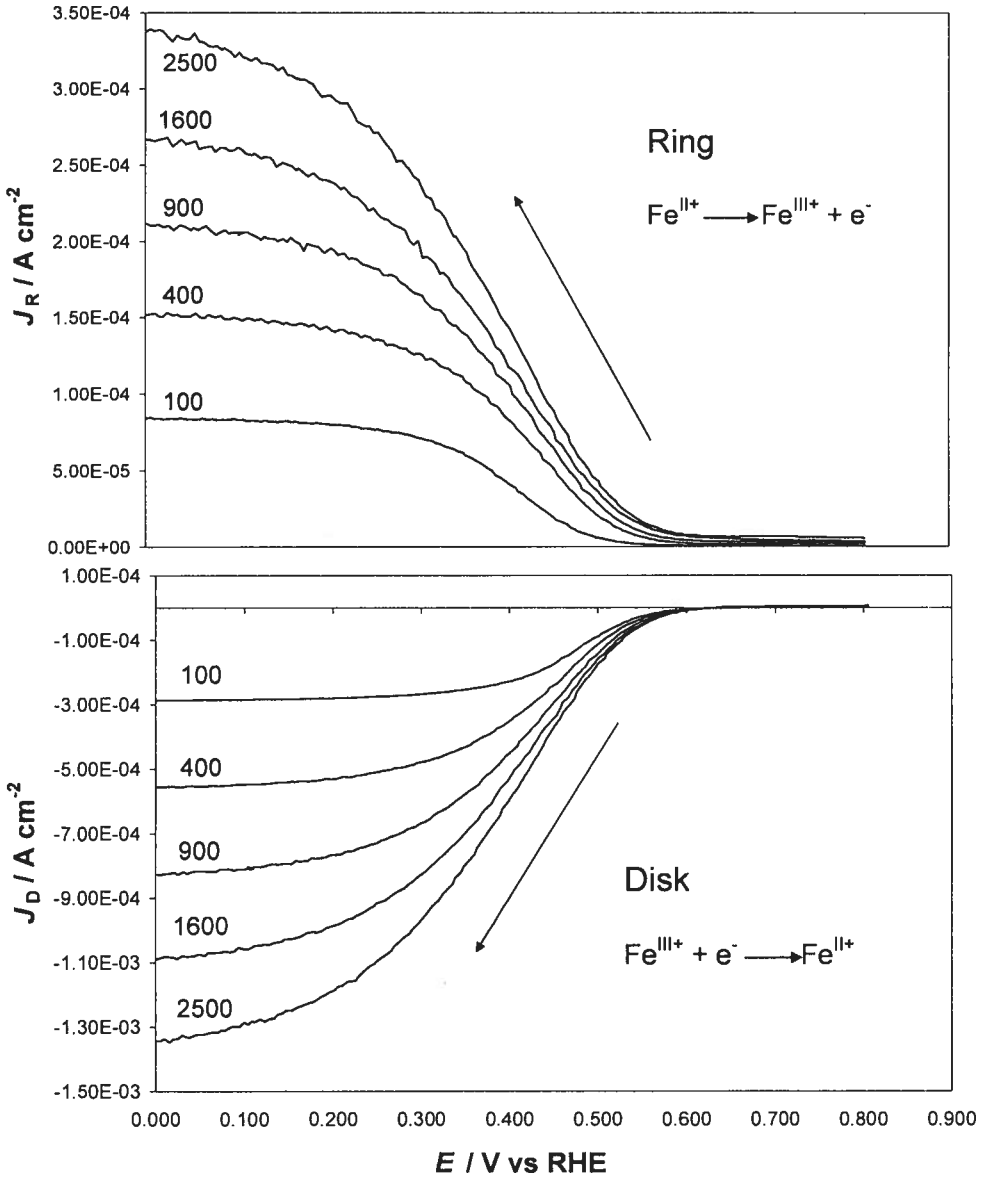

4.3.2.2. Fraction of H_2O_2 produced by the FePc species catalyzed O_2 reduction

For each RRDE experiment, scans were run of the bare WE in the N_2 purged electrolyte to confirm the disk surface was clean and that the ring / cup / disk assembly formed a water tight seal. The same RRDE WE was then scanned in the air saturated electrolyte again to ensure the disk surface was clean. The FePc species was subsequently adsorbed onto the disk surface, and scans in the N_2 purged electrolyte were run once more to obtain surface waves. Finally the FePc adsorbed WE was scanned in the air saturated electrolyte to obtain the FePc catalyzed ORR RRDE traces. A minimum of three sets of RRDE scans were performed, each using a freshly adsorbed FePc species surface. All RRDE scans shown were at 400 rpm. The reductive portions of the three scans for each of the five FePc species are shown in Figure 4.2. The RRDE scans shown in Figure 4.2(a) were obtained using a change disk RRDE with a *N* of 0.26 +/- 0.01, while those for Figures 4.2(b-e) were obtained using a change disk RRDE with a *N* of 0.21 +/- 0.01.

Fig. 4.2. Current potential curves for a Pt ring and (a) FePc; (b) $FePc(SO_3H)_4$; (c) $FePcCl_{16}$; (d) $FeNpPc(tBu_4)$; and (e) $FePc(tBu_4)$ adsorbed pyrolitic graphite disk electrodes at 400 rpm and a scan rate of 10 mV s^{-1} recorded in a 0.1 M H_2SO_4 air saturated electrolyte at 20°C and 1 atm.

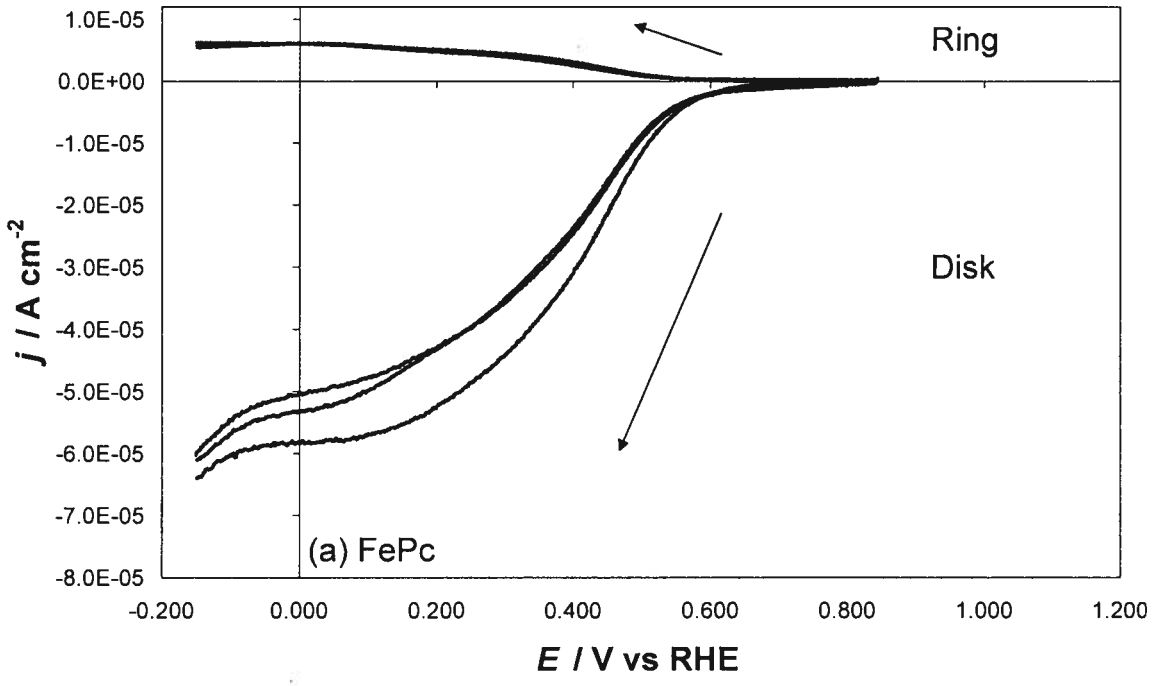

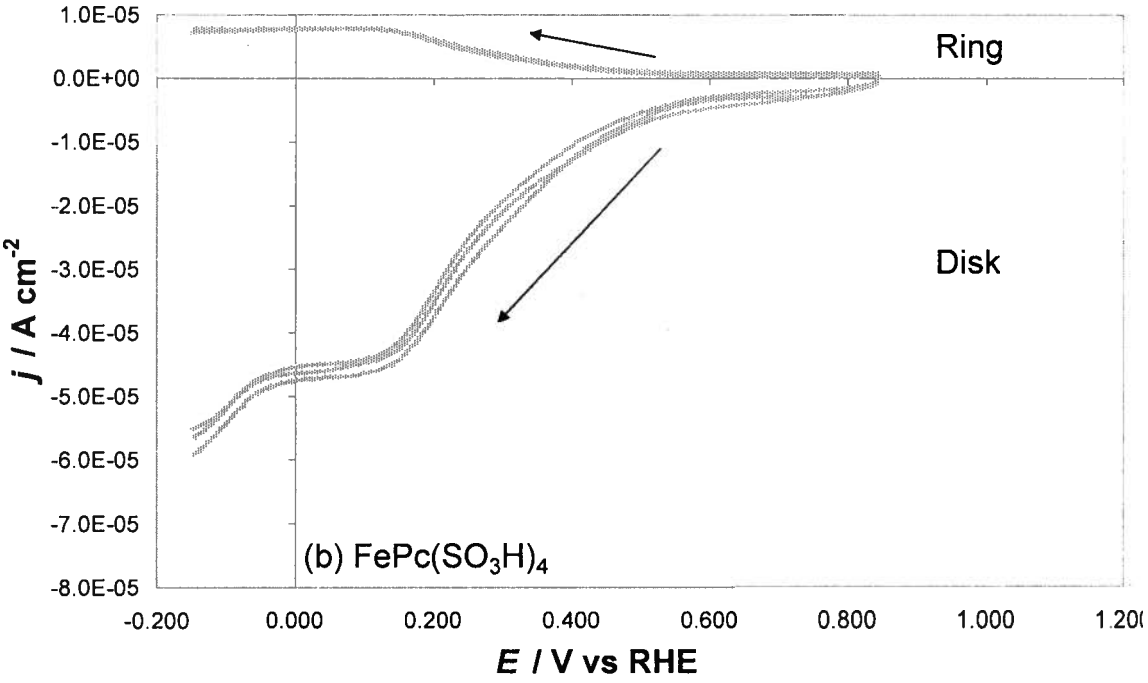
1.0E-05
0.0E+00
-1.0E-05
-2.0E-05
-3.0E-05
-4.0E-05
-5.0E-05
-6.0E-05
-7.0E-05
-8.0E-05
j / A cm-2
Ring
Disk
(b) FePc(SO3H)4
-0.200
0.000
0.200
0.400
0.600
0.800
1.000
1.20(
E / V vs RHE

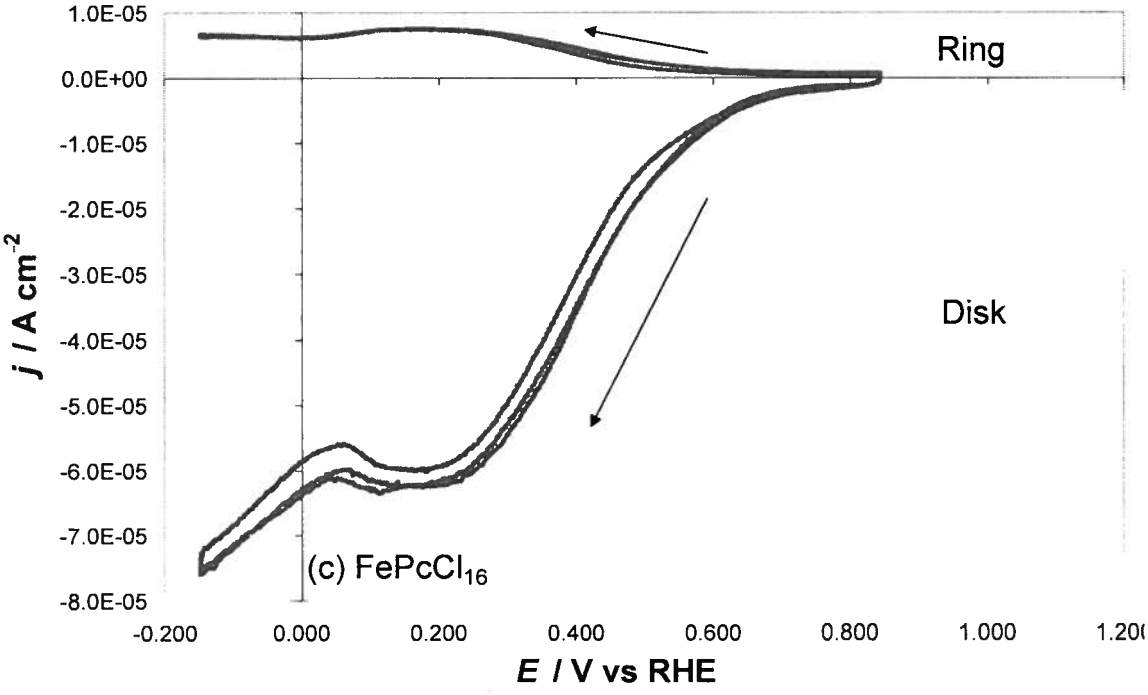
1.0E-05
0.0E+00
-1.0E-05
-2.0E-05
-3.0E-05
-4.0E-05
-5.0E-05
-6.0E-05
-7.0E-05
-8.0E-05
j / A cm-2
Ring
Disk
(c) FePcCl16
-0.200
0.000
0.200
0.400
0.600
0.800
1.000
1.20(
E / V vs RHE

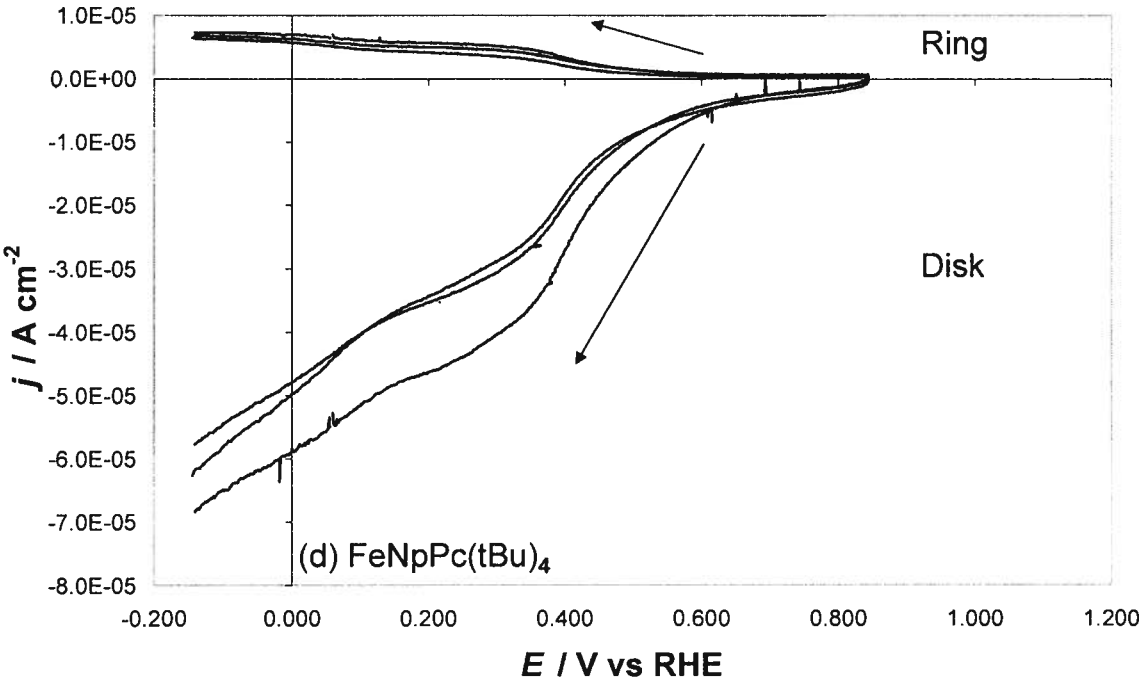
1.0E-05
0.0E+00
-1.0E-05
-2.0E-05
-3.0E-05
-4.0E-05
-5.0E-05
-6.0E-05
-7.0E-05
-8.0E-05
j / A cm-2
Ring
Disk
(d) FeNpPc(tBu)4
-0.200
0.000
0.200
0.400
0.600
0.800
1.000
1.200
E / V vs RHE

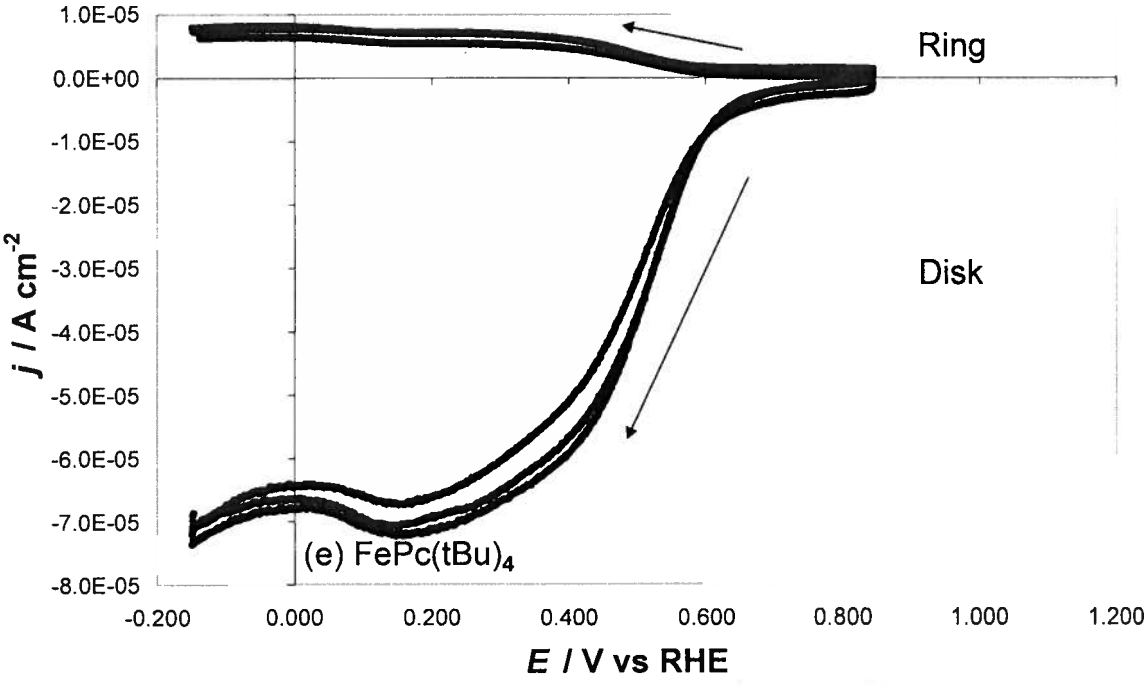
1.0E-05
0.0E+00
-1.0E-05
-2.0E-05
-3.0E-05
-4.0E-05
-5.0E-05
-6.0E-05
-7.0E-05
-8.0E-05
j / A cm-2
Ring
Disk
(e) FePc(tBu)4
-0.200
0.000
0.200
0.400
0.600
0.800
1.000
1.200
E / V vs RHE

Using the collection efficiency, the ring and disk currents can be compared for each FePc species to quantify relative amounts of H_2O and H_2O_2 produced via the 4 and / or 2 electron ORR mechanisms, respectively. The fraction of H_2O_2 (X_{H2O2}) produced at the FePc species adsorbed disk can be determined according to Equation 4.2 [84]:

$$X_{H_2O_2} = \frac{2I_R / N}{|I_D| + I_R / N} \tag{4.2}$$

where I_R, N, and I_D are as described in Equation (4.1). Values calculated for X_{H2O2} from the experimental data shown in Figure 4.2 are summarized in Table 4.1.

Table 4.1. Number of electrons observed for the ORR, average fraction of H_2O_2 produced (X_{H2O2}) and number of scans, including standard deviation for different FePc species adsorbed on a rotating pyrolytic graphite disk, with Pt ring, electrodes. Data from Figure 4.2 and Chapter 3.

Species	*n*	X_{H2O2}	No. scans	Std Dev	*N*
FePc	3.3	59%	3	3%	0.26
$FePc(SO_3H)_4$	1.7	88%	3	1%	0.21
$FePcCl_{16}$	2.1	74%	3	1%	0.21
$FeNpPc(tBu)_4$	2.5	77%	3	3%	0.21
$FePc(tBu)_4$	2.9	60%	3	7%	0.21

All five FePc species' X_{H2O2} values agree approximately with the *n*'s reported in Chapter 3. RRDE and RDE scans were run on different electrodes, but both used the same pyrolytic graphite material. Except for $FeNpPc(tBu)_4$, all of the other FePc species yielded X_{H2O2} and *n* values that could be a reflection of their respective Γ's [85]. It is unusual that $FeNpPc(tBu)_4$ exhibited X_{H2O2} and *n* values similar to those for $FePc(SO_3H)_4$ and $FePcCl_{16}$, which adsorbed as monolayers, when it adsorbed in a much larger monolayer equivalent of 2.7, similar to FePc's 2.1 and $FePc(tBu)_4$'s 4.5. In comparing FePc, $FePc(tBu)_4$, and $FeNpPc(tBu)_4$, tetra *tert* butyl substitution appears to have little effect on the ORR RDE trace and hence *n* of $FePc(tBu)_4$, but the same substituents on $FeNpPc(tBu)_4$ significantly reduce the ORR activity and change *n* to the point that the main product is essentially H_2O_2. As mentioned in Chapter 3, this reduction in ORR activity is more likely due to the additional fused benzene ring.

Other workers have reported on the ORR activity of FePc, FeNpPc, as well as CoPc and CoNpPc, where 4 and 2 electron reduction mechanisms for these Fe and Co phthalocyanines were shown, respectively [11-15]. The ORR activities for FeNpPc and CoNpPc were lower than those for both FePc and CoPc, regardless of the type of WE or carbon support used. This agrees with the results presented here in so much as a decrease in activity relative to the unsubstituted species. It is the decrease in *n* from 4.0 to 2.5 for FeNpPc and $FeNpPc(tBu)_4$, which is unusual.

Examining the effect of substitutents on the FePc's electronic orbitals can help explain these changes. Chapters 1 and 2 discussed UV-Vis spectroscopy

as a good method to determine the energy levels of the highest molecular orbital (HOMO), referred to as the Q band (600-700 nm) and of the lowest unoccupied molecular orbital (LUMO) referred to as the Soret band (300-450 nm) [5,8]. UV-Vis spectra for CoNpPc, and CoPc analogues in the literature show a similar shift in the Q-band, or decrease in the TM naphtlalocyanine's HOMO energy level [8,10,11,13]. In Chapter 2 the UV-Vis spectra for the two tetra-*tert*-butylated FePc's were compared. The comparison revealed, in agreement with the literature, that the four additional fused aromatic substituents in $FeNpPc(tBu)_4$ increased the energy of the HOMO while that of the LUMO remained essentially unchanged [10-13]. This meant the HOMO-LUMO gap for $FeNpPc(tBu)_4$ is smaller than that for $FePc(tBu)_4$, and relative to $FePc(tBu)_4$ as well as FePc, a decrease in stability as well as ORR activity.

This does not fully explain both the poor activity and decrease in *n* for $FeNpPc(tBu)_4$. A secondary effect may be influencing this change in *n*. Biloul and co-workers examined the difference between the 1,2 and 2,3 isomers of pyrolized and unpyrolized FeNpPc supported on different carbons, as ORR electrocatalysts [11,12]. Recall the 2,3 isomer of $FeNpPc(tBu)_4$ is studied in this thesis. In comparing the different stabilities and activities of the two FeNpPc as well as CoNpPc isomers, Biloul et. al. found the 2,3 isomer to have both lower activity towards the ORR as well as a lower stability [11,12]. This was ascribed to the steric hindrance and inflexibility of the 2,3 isomer in adsorbing onto the respective carbon supports. This can be explained by the interaction between the basal planes of the pyrolytic carbon support and the physisorbed

$FeNpPc(tBu)_4$ catalyst. The graphene sheets of the pyrolytic graphite and the conjugated hetero aromatic rings of $FeNpPc(tBu)_4$ have similar structures. Weak van der Waals interactions exist between the sp^2 orbitals of the graphene sheet and those of the macrocyclic rings. As the support can also act as an axial ligand to the TM centre [5], the overlap between the p orbitals of the pyrolytic, and the d orbitals of Fe can also affect the catalytic activity. It follows that if these overlaps are poor, then the activity and stability of the adsorbed 2,3 TM NpPc isomer could be diminished. The addition of four bulky tetra *tert* butyl groups on the ends of the 2,3 FeNpPc's "naphthalene arms" could very well increase the steric hindrance between the pyrolytic graphite support and the adsorbed $FeNpPc(tBu)_4$ electrocatalyst, even more so than for the 2,3 FeNpPc analogue.

It follows that if the M.O. considerations for $FeNpPc(tBu)_4$ and FeNpPc are similar, then the key difference in substitutent effects as a result of the four tetra *tert* butyl moeties, could be more steric than electronic in this case. If the FePc species catalysed ORR involves more than one FePc species molecule, it follows that the tetra *tert* butyl's additional steric hindrance would increase the distance between reactive sites on adjacent FeNpPc molecules and / or hinder the formation of μ-oxo dimers and hence affecting the ORR mechanism.

4.4 Summary

The RRDE results and calculated X_{H2O2} values for all the FePc species tested, with the exception of FePc, agreed with the RDE results presented in Chapter 3. The same trend in disk current traces at 20 °C for all five FePc species was observed for the RRDE scans, when compared to the corresponding RDE scans in Chapter 3. Both $FeNpPc(tBu)_4$ and $FePc(tBu)_4$ showed a reduction in ORR activity as well as an increase X_{H2O2} relative to FePc, confirming the de-activating effect of electron donating substitutents. However, $FePc(SO_3H)_4$ and $FePcCl_{16}$ also showed these trends, likely due to their low Γ's. Given the large increase in X_{H2O2} for $FeNpPc(tBu)_4$ and a Γ similar to those of FePc and $FePc(tBu)_4$, this change in $FeNpPc(tBu)_4$'s ORR mechanism was unusual. Although electronic effects were shown in Chapter 2 to decrease stability and ORR activity, they do not fully explain the change. Rather, the substituent effect on $FeNpPc(tBu)_4$'s ORR mechanism could be more steric than electronic in this case, affecting adsorption and activation on the pyrolytic graphite surface as well as hindering inter molecular ORR mechanisms and μ-oxo dimer formation.

Chapter 5

Evaluation and Comparison of a Substituted and an Unsubstituted Iron Phthalocyanine as Supported Fuel Cell Cathode Catalysts

5.0 Objective

$FePcCl_{16}$ was down selected as the most stable and ORR active substituted FePc. Together with the unsubstituted or baseline FePc, both were evaluated and compared as carbon supported ORR catalyst inks first coated on a CFP WE, followed by incorporation of the same catalyst ink as the cathode of an MEA in an operating PEM fuel cell.

5.1 Description

$FePcCl_{16}$ and FePc were supported on a pyrolytic graphite carbon and then made into an ink. The in-situ FePc species catalyst inks on CFP WE's were tested in the novel half cell using CV as an ex-situ technique. The same FePc species inks were then used to make the cathodes of a PEM MEA and subsequently tested in an in-situ, in house designed and built PEM fuel cell using a FC test station.

5.2 Experimental

5.2.1 FePc and $FePcCl_{16}$ catalyst ink calculations

Using weight percent compositions to prepare non noble metal catalyst inks was not desirable. This was because of the vast differences in molecular weights as well as active site densities between noble metal (such as Pt and Ru) and non-noble metal (such as FePc species) electrocatalysts [86]. Even among similar non noble metal catalysts, including different FePc species, these differences rendered weight percentage composition calculations meaningless, making it difficult to quantify and compare not only the number of active sites but also the amount of Nafion and carbon support in the catalyst ink and catalyst layers.

To take these differences into account the FePc species catalyst ink calculations were made based on the following considerations:

1. Monolayer coverage of the FePc species on the carbon was assumed, and thus a pyrolytic graphitic carbon powder support was used with the largest BET active surface area.
2. Monolayer coverage of the FePc species with the largest molecular plane area on the chosen carbon support was calculated to set a baseline for the active site density.
3. The active site density was set for the largest FePc species molecular plane area such that the Fe:Fe mol ratio stays at 1:1 per gram of carbon support for both FePc species catalyst inks.

4. The Nafion loading was based on the mass of carbon and Nafion only as the relative difference in radii between the bare carbon support and carbon supported FePc species is negligible. Thus the amount of Nafion added served only to adequately coat the FePc species and carbon support. The same mass of Nafion was used per gram of carbon support for all catalysts.

It follows that Black Pearls 2000 (BET active surface area: 1500 $m^2 g^{-1}$) was chosen as the carbon support, the largest FePc species molecular plane area was for $FePcCl_{16}$, and the Nafion loading was chosen to be 25 wt% (based on a total dry mass of carbon and Nafion only).

The literature shows that catalyst inks made based on monolayer coverage of TM macrocycles (1.56 g of $FePcCl_{16}$ per 1.00 g^{-1} BP 2000) tends to yield catalyst layers that are quite thick and hence show poor performance [22,57,58,87,88]. After consulting the literature, it was decided to base the initial $FePcCl_{16}$ loading on a value of 10.0 mg cm^{-2}, which was based on an optimum active TM site loading of 3 % w/w [22,57,58]. This value of 3 % w/w was calculated by dividing the mass of the TM centre alone by the sum of the masses of the TM macrocycle, the carbon support, and the Nafion. For example, a value of approximately 3 % w/w corresponded to FePc and carbon loadings of approximately 4 mg cm^{-2} each, and a Nafion loading of 2 mg cm^{-2}, for a total dry mass of 10 mg cm^{-2} in the catalyst layer [58]. This approach reduced the thickness of the catalyst layer. This value of 10.0 mg cm^{-2} was adjusted by compensating for the difference in molecular weights between CoTMPP and

$FePcCl_{16}$. Thus the literature value was multiplied by the calculated composition value of 52% w/w for monolayer coverage of $FePcCl_{16}$ in the catalyst layer ($FePcCl_{16}$, Carbon and Nafion), yielding the value of 5.2 mg cm^{-2} which the $FePcCl_{16}$ and in turn FePc catalyst inks were based on.

5.2.2 Chemicals

Perfluorosulfonic Acid-PTFE copolymer 5% w/w solution (Stock no. 42118, lot no. K16Q056) and Cabot Black Pearls 2000 (GP 3848, 08/04/2005) were purchased from Alfa Aesar and The Cabot Corporation, respectively, and used as received. 20% w/w Pt on Vulcan XC-72R (E-Tek C1-20, P.O. 566212, W.O. 0008572, lot no. C0040211) was purchased from E-Tek / De Nora and used as received. The SGL GDL 25BC CFP with micro porous layer (MPL) containing 5% w/w PTFE in the MPL, was purchased from SGL and then used as received. All other chemicals and materials were as described in Chapters 3 and 4.

5.2.3 Preparation of FePc catalyst ink

All glassware, including the ceramic Buchner funnel was thoroughly cleaned and dried before each use. The masses weighed for FePc, carbon and Nafion were calculated by multiplying the target loading (2.8 mg cm^{-2} for FePc), of each of the catalyst ink components by a factor of three (to compensate for overspray), and again by the total area to be sprayed (25 cm^2) then if applicable, dividing by the component's purity (0.95 for FePc) to give a calculated mass of 0.222 g for FePc. Experimentally, 0.2220 g of FePc was weighed into a pyrex flask containing 50 ml of N,N-DMF and sonicated (Branson 1510) at room temperature for 75 minutes to dissolve the catalyst. The FePc and N,N-DMF mixture was

then filtered through a Whatman 542 55 mm diameter filter paper in a Buchner funnel on top of a vacuum flask to remove any insoluble matter. An insignificant amount of insolubles (ca. 2% w/w) were retained on the filter paper. 0.2518 g of BP 2000 was weighed into a second pyrex flask and mixed with 50 ml of IPA. The FePc and N,N-DMF filtrate was combined with the BP 2000 / IPA mixture and then sonicated for over 30 minutes. The BP 2000 supported FePc slurry was left overnight in a vacuum oven (Isotemp Fisher Vacuum Oven, model 280A) at –30 in. Hg and 80°C.

0.5244 g of the dried FePc/C catalyst was combined with 2.105 g of the 5% w/w Nafion solution in 10 ml of DI H_2O and 10 ml of IPA followed by sonication for 30 minutes. Table 5.3 summarizes these values for the FePc catalyst ink component loadings.

5.2.3.1 FePc catalyst ink solubility test

To ensure the adsorption of FePc onto BP 2000 was irreversible, simple solubility tests were performed by taking four 5 mg FePc/C samples and placing each one of them in a conical filter paper (Whatman, as described in this section) placed inside a glass funnel draining into a pyrex flask. Four different solvents were then separately poured into each filter paper containing the FePc samples. They were: methanol, ethanol, 1-propanol, and 2-propanol (IPA). The solvents sat in the funnels, in contact with the FePc/C samples for a few hours before draining by gravity into the flask. No colour changes were observed for any of the four solvent filtrates. As $FePcCl_{16}$ is known to be insoluble in these four solvents, this qualitatively indicated FePc and $FePcCl_{16}$ would not de-adsorb off

the BP2000 and into solution during the catalyst ink fabrication and spraying process.

5.2.4 Preparation of $FePcCl_{16}$ catalyst ink

The glassware and Buchner funnel were cleaned as described in section 5.2.3. Similar to section 5.2.3, the masses weighed for $FePcCl_{16}$, carbon and Nafion were calculated by multiplying the target loading (5.2 mg cm^{-2} for $FePcCl_{16}$), of each of the catalyst ink components by a factor of three (to compensate for overspray), and again by the total area to be sprayed (25 cm^2) then if applicable, dividing by the component's purity (0.80 for $FePcCl_{16}$) to give a calculated mass of 0.490 g for $FePcCl_{16}$. Experimentally, 0.4918 g of $FePcCl_{16}$ was weighed into a pyrex flask containing 50 ml of N,N-DMF and sonicated at room temperature for 75 minutes to dissolve the catalyst. The $FePcCl_{16}$ and N,N-DMF mixture was then filtered through a Whatman 542, 55 mm diameter filter paper in a Buchner funnel on top of a vacuum flask to remove any insoluble matter. An insignificant amount of insolubles (ca. 2% w/w) were retained on the filter paper. 0.2553 g of BP 2000 was weighed into a pyrex flask and mixed with 50 ml of IPA. The $FePcCl_{16}$ and N,N-DMF filtrate was combined with the BP 2000 / IPA mixture and then sonicated for over 30 minutes. The BP 2000 supported $FePcCl_{16}$ slurry was left overnight in a vacuum oven at –30 in. Hg and 80°C.

0.7336 g of the dried $FePcCl_{16}$/C was combined with 2.111 g of the 5% w/w Nafion solution in 10 ml of DI H_2O and 10 ml of IPA and then sonicated for 30

minutes. Table 5.3 summarizes these values for the $FePcCl_{16}$ catalyst ink component loadings.

5.2.5 FePc and $FePcCl_{16}$ cathode GDL fabrication

Prior to any spraying, the cathode catalyst ink was sonicated for 30 minutes. A plastic syringe was used to draw the ink up via a flexible perfluoroalkoxy (PFA) cannula and then secured in a Harvard Apparatus PhD 2000 Programmable syringe pump. The PFA cannula was connected to a custom fabricated spray nozzle. The outlet of the spray nozzle consisted of a concentric set of 316SS tubes, 0.34 mm for the ink and 1.07 mm for the carrier gas. The carrier gas was air, controlled via a Cole Parmer manually adjustable flow meter. The nozzle motion was controlled by a modified XY table (Vexta, stepper motor, 1.8° $step^{-1}$, model no. PK266-03A-P1) coupled to a Velmex VXM stepping motor controller. The carbon paper used was SGL's GDL 25BC with micro porous layer (MPL) and 5% w/w PTFE in the MPL. The carbon paper was placed under the spray nozzle, MPL side up, and on top of a temperature controlled aluminum heating plate.

The syringe pump flow rate was 0.5 ml min^{-1}, the air flow rate was 6 L min^{-1}, the nozzle tip to sample distance was 70 mm, the heating plate temperature was 80°C and the XY table was set to a 48 mm by 48 mm spray area with 2 mm $step^{-1}$ and at 3 mm sec^{-1}. During spraying, the GDL was periodically removed to be weighed. After the target loading was reached, the catalyst coated carbon paper was placed in a Barnstead Thermolyne 62700 furnace for 35 minutes at 80°C to remove any residual IPA or water. After cooling to room temperature, the

catalyst coated carbon paper was re-weighed. It was noted that the catalyst ink was quite thick, and tended to lose small amounts of dry catalyst ink.

Using the same spray system and settings, approximately 0.2 mg cm^{-2} of Nafion was deposited on top of the FePc and $FePcCl_{16}$ catalyst ink coated GDL's. Both GDL's were then dried in the same oven at the same temperature, air cooled to room temperature and re-weighed.

5.2.6 FePc and $FePcCl_{16}$ cathode GDL custom electrodes

A similar experimental method is described elsewhere [2]. An modified version was described here to better test the activity of the two FePc and $FePcCl_{16}$ catalyst coated carbon papers. Briefly, these modifications were: (1) change the WE's dimensions to accommodate the smaller dimensions and save material of both FePc species catalyst ink coated CFP GDL's, (2) use stainless steel (SS) shims as the current collectors, not the CFP, above the level of the electrolyte, (3) eliminate hot pressing of the CFP electrodes due to their fragility and (4) use PFA and PTFE instead of graphite to make the WE holders. Using PFA and PTFE minimized double layer currents and excluded possible contamination from the graphite. Thus before making MEA's, 0.5 cm by 7.0 cm strips were cut from the FePc species catalyst coated carbon paper and covered such that the tip exposed a 0.5 cm by 1.0 cm geometric area of catalyst for the WE. A total of five such electrodes for each of the FePc and $FePcCl_{16}$ catalysts were made. To run voltammetry experiments, each strip was secured in a custom electrode holder. This custom electrode holder is a modified version of one used previously [2], and is shown in Figure 5.1.

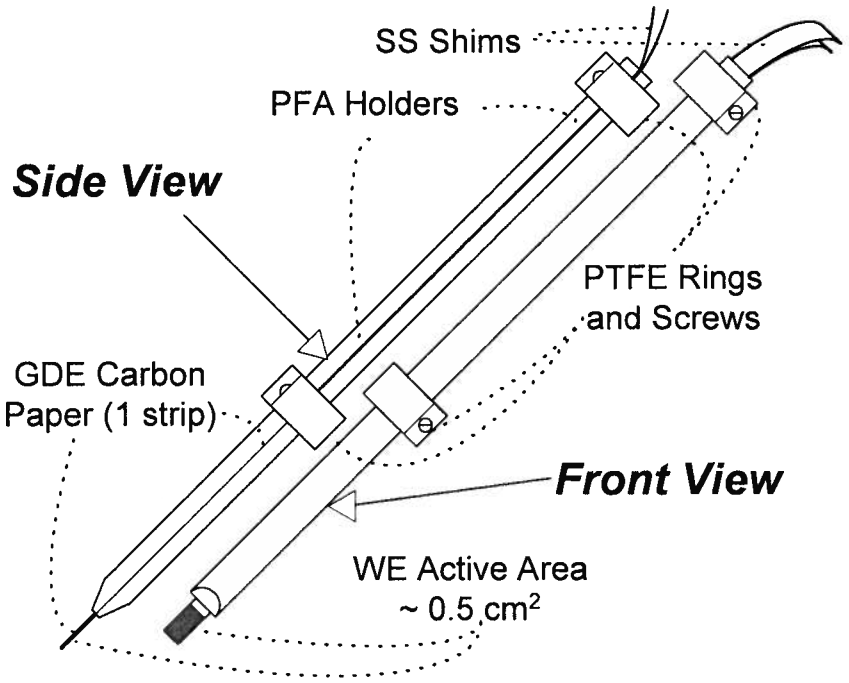

Fig. 5.1. Side and front views of modified working electrode assembly with 0.5 cm^2 geometric area. Based on a similar design [2].

The electrode holder consisted of a PFA rod, cut in half axially, with one end having a bevelled tip. The catalyst coated carbon paper was sandwiched between two 316SS shims and then held to one of the PFA halves with wound Teflon tape, before the other PFA half was placed on top of it. The assembly was made so that the 0.5 cm by 1.0 cm catalyst coated tip was exposed at the bevelled end of the PFA, and the two SS shims contacted the carbon paper inside the PFA rod, covering the last two centimetres of the carbon paper. Two PTFE rings with adjustable threaded screws were used. One ring was used to hold the electrode holder assembly together where the SS contacted the carbon paper, and the second ring was placed at the other end of the PFA rod. An o-ring was also used between the two PTFE rings to help position the electrode

holder. The electrode assembly was placed in the custom three electrode half cell described in Chapter 2. Care was taken to make sure the electrolyte level was below the carbon paper and SS interface, as well as ensure the o-ring described previously fixed the electrode assembly repeatedly in the same position. The SS shims protruding from the top of the electrode assembly were used as a current collector and as an attachment point for the WE leads.

The same equipment as outlined in Chapters 3 and 4 was used to test the carbon paper test electrodes. Before running any cyclic voltammograms in either N_2 or air saturated electrolyte, open circuit potentials (OCP's) were run for ten minutes to verify the stability of the catalyst ink.

5.2.7 Pt anode GDL fabrication

All glassware was thoroughly cleaned and dried before each use. The same CFP and Nafion solution used in section 5.2.5, respectively, was also used for the anodes. 0.605 g of 20% w/w Pt/C was weighed out, placed in a pyrex flask, and made into a paste with DI H_2O. 50 ml each of DI H_2O and IPA were combined and then added to the Pt/C slurry. 4.040 g of 5% w/w Nafion solution was then weighed out and placed in the flask. The Pt/C and Nafion in IPA / H_2O catalyst ink was sonicated for 60 minutes. A summary of calculated and actual experimental anode catalyst layer loadings is found in Table 5.6.

A magnetic stir bar was added to the flask, which was then placed in an air pressurized reservoir operating at 3 to 4 psig. The reservoir was placed on top of a Corning Stirrer Hot Plate with only the stirrer on. The ink was drawn up a ¼" PFA tube into a Nordson EFD Ultra TT Series automated spray machine. The

automated sprayer bed was heated to 80°C, using a J-KEM Scientific Model 1210 heater controller. The carbon paper was placed on the automated spraying bed and covered by a custom aluminum template with four 25 cm^2 cut outs. The automated spray machine's nozzle was cleaned before each use and set to dial position of approximately 3.5 (no units) during spraying. Automated spray program # 69 (a modification of program # 36) was used to coat the Pt/C ink onto the CFP. Some parameters for program # 69 are described in Table 5.1. In general, the spray nozzle swept the CFP in a serpentine pattern from the left side to the right side (1^{st} scan, +X axis), paused, then the heated bed moved backwards one increment (-Y direction), before the spray nozzle swept the CFP in the opposite direction (2^{nd} scan, -X direction), and paused again. The process was repeated until the nozzle reached the back of the CFP where, after a pause to let the catalyst ink solvent evaporate, the pattern reversed and the nozzle moved forward (+Y direction). When the nozzle returned to its' original start position, this was termed one pass or run. After ten passes, the CFP was removed for weighing and a calculation of the average catalyst ink deposition rate to estimate the number of passes required to reach the target weight. Once the target weight was reached, it was dried at 80°C (in a different oven than was used for drying the $FePcCl_{16}$ ink coated CFP) before being re-weighed a final time.

Table 5.1. Program details of automated spray program # 69 for Pt anodes.

Parameter	Value	Units
Nozzle height	54	/ mm
Scan: X axis, one direction	side to side	
Scan speed	25	/ mm s^{-1}
Pass: Y axis, return	front to back	

* The CFP was covered with an aluminum template that contained four 50 mm by 50 mm cut outs, arranged in a square, approximately 20 mm a part.

Again, using the same set up and procedure described immediately above, a layer of approximately 0.4 mg cm^{-2} of Nafion was added on top of the Pt/C catalyst coated carbon paper.

5.2.8 MEA fabrication

Eight pieces of Nafion 112, roughly 4 cm by 4cm, were cut and placed in a 3% v/v solution of H_2O_2 at 80°C and left to stir for two hours. The Nafion pieces were rinsed in DI H_2O and then placed in a 15% v/v solution of H_2SO_4 also at 80°C and left to stir for an additional two hours. The cleaned Nafion pieces were given a final rinse with DI H_2O and stored in a clean, sealed pyrex flask in DI H_2O.

A clean, custom made 2.2 cm by 2.2 cm die was used to separately cut out the cathode and anode GDL's. A small piece was cut off all the corners of all the anodes so that the anode and cathode could be easily identified.

A Carver hot press (Auto Series, model no. 3893.4DIOAOO) with a pair of Niobium plates as well as PTFE sheets was used to bond the MEA's. The pump

speed was 25%, the press or dwell time was 1.5 minutes, the temperature of both press plates was 135°C, and the pressure was 3114 Kpa, or 452 psi.

The Niobium plates and PTFE sheets were thoroughly cleaned with IPA and then DI H_2O. The cathode side PTFE was exclusively used for non noble metal catalysts to avoid contamination. One PTFE sheet was placed on top of the Niobium plate. Onto the PTFE sheet, four MEA's were aligned and assembled, anode side down. The designated non noble metal PTFE sheet was placed on top of the four MEA's, followed by the second Niobium plate. These components were carefully placed inside the Carver press and then immediately hot pressed. After pressing, the Niobium / PTFE / MEA / PTFE / Niobium sandwich was quickly removed and left to air cool before gently removing the MEA's. Away from the active area each MEA was labelled with an indelible marker outside the active area, designated by the cathode catalyst abbreviation (FePc or $FePcCl_{16}$) and the MEA number (1 to 3).

5.2.9 Fuel cell testing

An in house custom designed and built fuel cell (FC) hardware was used to test the MEA's described in section 5.2.8. An exploded view of the original FC design with modifications as marked is shown in Figure 5.2.

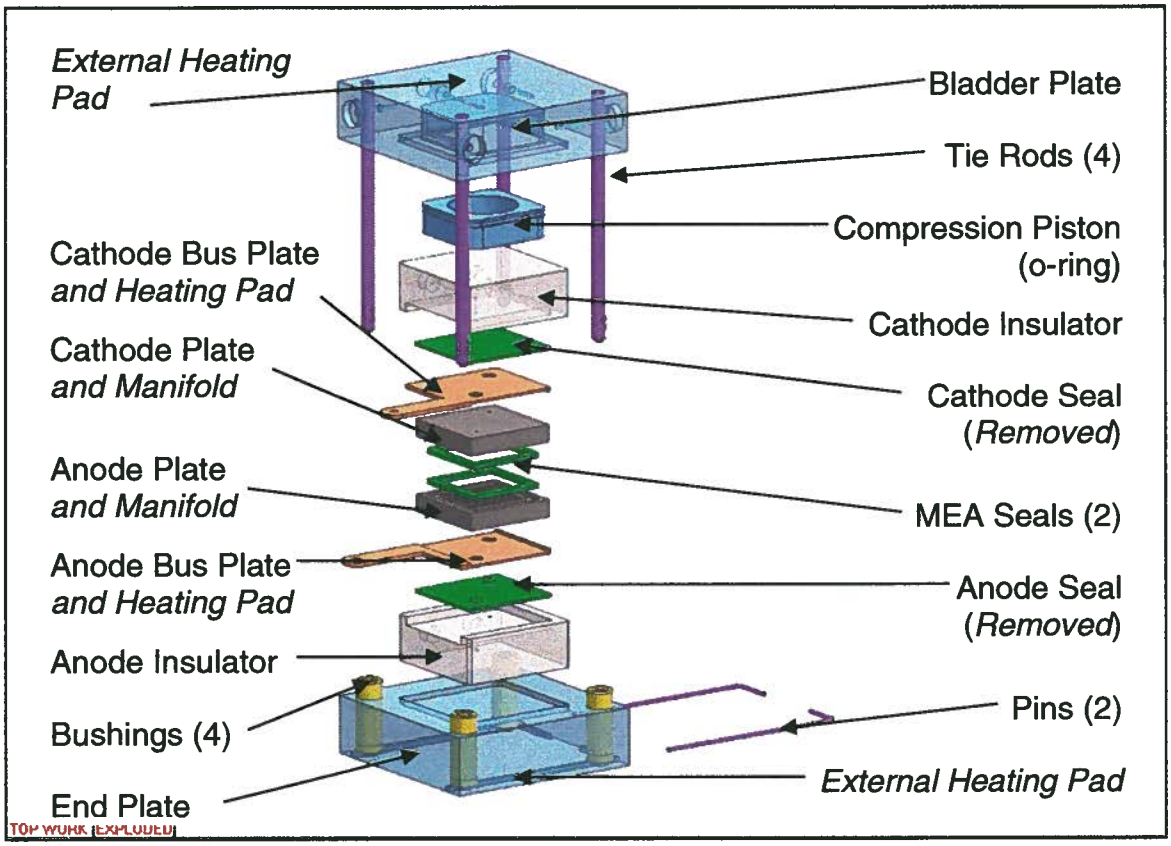

Fig. 5.2. Exploded view of in house designed and built fuel cell with modifications as marked in italics, and 4.4 cm^2 active area with serpentine flow fields.

The fuel cell used in this work was a modification of the design shown in Figure 5.2, with the same active area of 4.4 cm^2. A labelled photo of the assembled FC can be seen in Appendix V. The modifications were to connect the fuel and oxidant lines directly to a thicker graphite plate with the same serpentine flow field patterns. The Au plated current collectors had a cut out facing the ultem anode and cathode electrical plate insulators. The cut out was for a heating pad (Watlow K005011500 / 0506C-04, 12 VDC, 10 W). The ultem insulators sat inside a recess cut into the end plate. A set of external heating pads (Watlow 020020135 / 0226C-00, 120 VAC, 60 W) was placed on the

outside of both aluminum end plates. An air bladder in one end plate was used to compress the FC. The bladder pressure was set to 50 psig for all FC tests. The fuel cell testing system (vide infra) is also represented in Figure 5.3.

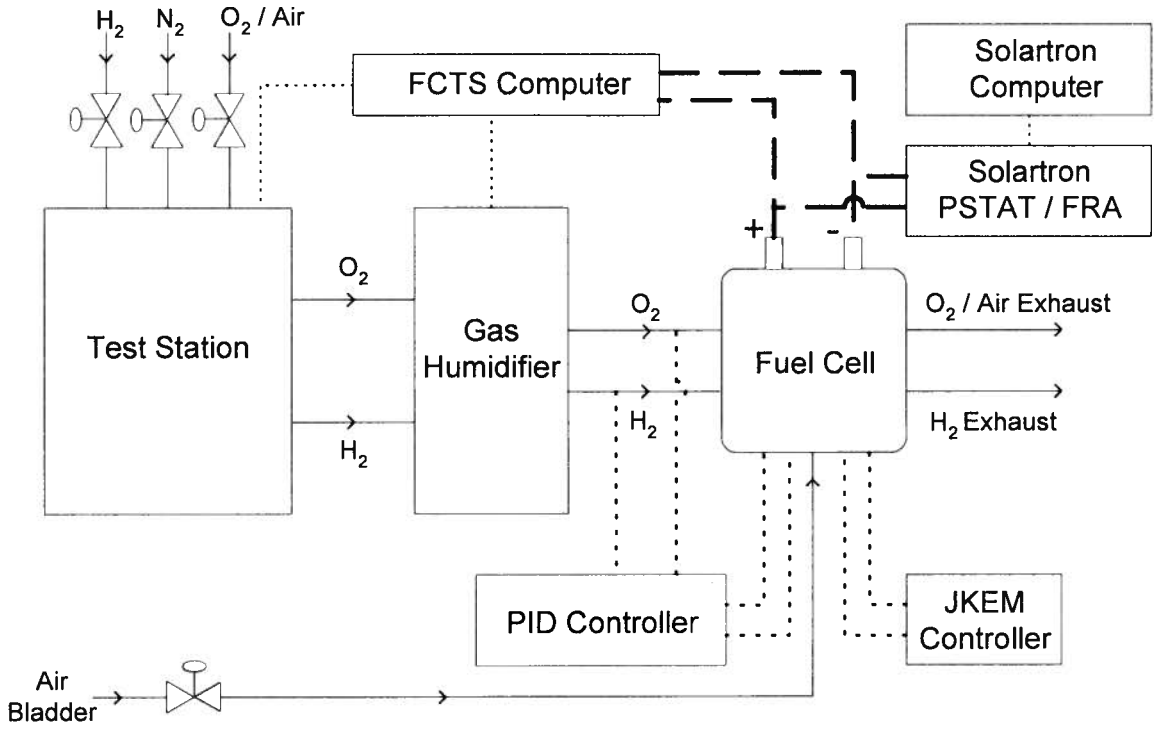

Fig. 5.3. Schematic of fuel cell test system, with gas lines as marked (solid lines), anode and electrode leads (thick dashed lines), computer interface cables (thin dotted lines), as well as heater wires with K-type thermocouples (thick dotted lines). Schematic shown is for the second MEA testing method.

A J-KEM Scientific four channel heater controller set to a 300 mL - 2 L heating rate at 81°C on channels 1 and 4 was used to power the Watlow 12 VDC heating pads through two 120 VAC to 12 VDC / 1000 mA adaptors. Two Omega K-type thermocouples placed inside each graphite plate were used to monitor the anode and cathode temperatures for the J-KEM heater controller.

Fuel and oxidant lines to and from the FC were all ¼" tubes. The lines to the FC were all insulated and heated, controlled by a custom, in house PID controller rack monitored with Omega K-type thermocouples. The same PID controller rack was used to control the 120 VAC Watlow heating pads on the FC's end plates, also fitted with Omega K-type thermocouples. All transfer lines were kept at 85°C and the end plates were kept at 130°C. These temperature settings allowed the anode and cathode plate temperatures, and hence MEA temperature, to be 80°C.

Nitrogen (N_2) (99.9999%, BOC), hydrogen (H_2) (5.0 UHP, Praxair), air (filtered, oil-free, -40°C dew point), domestic water (for cooling), DI H_2O (see section 2.1), and oxygen (O_2) (Praxair, UHP 4.3) were fed into a Fideris FCTS GMET / FCTS GH test station and then through a Fideris FCTS BH humidifier, both controlled by Fideris FC Power software, before being fed into the FC by the heated, insulated transfer lines described previously. N_2 was used as the purge gas for both the fuel (H_2) and oxidant (O_2) lines. The FC Power software was used to control the H_2 and O_2 flow at 0.03 and 0.09 L m^{-1}, respectively, as well as the gas humidifier at 80°C for the anode and cathode feed streams. This software also recorded voltage versus time plots for all MEA's. The anode and cathode backpressures were both 30 psig, or 3 atm absolute. Some of the fuel cell operating conditions are summarized in Table 5.2.

Table 5.2. Summary of final operating conditions for MEA evaluation using the fuel cell shown in Figure 5.2 and the second MEA testing method.

Fuel / Oxidant	Back pressure	30 / psig
	Temperature	80 / C
	RH	100 / %
Fuel cell	Bladder press.	50 / psig
	External heaters	130 / C
	Internal heaters	81 / C
	MEA temperature	80 / C

For galvanostatic testing, a Solartron SI-1260A frequency response analyser (FRA) was connected to a TDI load bank (model no. RBL488 100-60-400) via a custom manual interface and then controlled using Scribner's ZPLOT software with the appropriate settings. The TDI loadbank was connected to the FC current collectors using a Flexapreen H.D. welding cable, 600V. The FRA was used to control the loadbank both to gain better control at lower current settings (than could be provided by the manual controls) as well as perform EIS experiments simultaneously. For linear scan voltammetry, the FRA was coupled to a Solartron SI-1287A PSTAT / GSTAT which was directly connected to the FC. Scribner's CorrWare software was used to control the FRA and PSTAT / GSTAT as well as to record experimental data.

5.3 Results and discussion

Prior to MEA hot pressing, the cathode catalyst (FePc or $FePcCl_{16}$), as well as associated materials and equipment, were kept out of contact with the respective Pt anode catalyst, as well as its' associated materials and equipment. This was to avoid any contamination of either FePc species with Pt, which even at the ppb level would significantly alter the MEA's performance. Calculated values for FePc and $FePcCl_{16}$ cathode catalyst inks are shown in Table 5.3.

Table 5.3. Calculated loading values for catalyst, Nafion and carbon components of $FePcCl_{16}$ and FePc ink coated cathode GDL's.

	Catalyst Mol wt / mg mol^{-1}	Catalyst Loading / mg cm^{-2}	Fe catalyst moles / mol cm^{-2}	Nafion Loading / mg cm^{-2}	Carbon Loading / mg cm^{-2}	Total Loading / mg cm^{-2}	Nafion Top coat / mg cm^{-2}	Target mass 25 cm^2 GDL / mg
$FePcCl_{16}$	1119490	5.2	4.66E-06	1.4	3.3	10.0	0.20	250.0
FePc	603820	2.8	4.66E-06	1.4	3.3	7.6	0.20	189.9

As can be seen in Table 5.3, both catalyst target mass loadings were in equimolar amounts. The Nafion and carbon mass loadings were also equivalent for the two FePc catalyst inks. In this manner, both inks theoretically had the same active site density, the same amount of Nafion and the same amount of carbon per unit area of GDL. Both of these inks were thus more easily compared. These mass loadings have been converted to weight composition in Table 5.4.

Table 5.4. Calculated weight percent values for $FePcCl_{16}$ and FePc catalyst inks based on values presented in Table 5.3. Values are only or components in the catalyst layer.

	Catalyst / wt %	Nafion / wt %	Carbon / wt %
$FePcCl_{16}$	52.2	14.3	33.4
FePc	37.1	18.9	44.0

In contrast to the values shown in Table 5.3 it is apparent that percent weight compositions for supported TM macrocycle based catalyst inks did not give a clear indication of the actual amount of each component in the catalyst layer.

The calculated target loadings are compared to the experimental target loadings in Table 5.5 for FePc and $FePcCl_{16}$ cathode catalyst ink coated GDL's. For these cathode GDL's, the experimental loadings were quite close to the target loadings, except for the lower Nafion top coat loading for $FePcCl_{16}$. This lower Nafion top coat loading could have had an effect on the MEA's performance. Possible effects are further discussed in section 5.3.3.

Table 5.5. Calculated and experimental (actual) values for total catalyst dry mass loading and Nafion top coat loading on cathode GDL's.

	Calculated	Actual	Units
FePc+C+Nafion	7.6	8.0	mg cm^{-2}
Nafion top layer	0.20	0.19	mg cm^{-2}
$FePcCl_{16}$+C+Nafion	10.0	10.9	mg cm^{-2}
Nafion top layer	0.20	0.12	mg cm^{-2}

Both the Pt anode catalyst ink and ink coated GDL as well as target and experimental loadings are shown in Table 5.6. The target and experimental values were very close to each other. The Nafion top coat was almost double the target loading due to an experimental error. As H_2 / O_2 FC performance is overwhelmingly dictated by the ORR, even more so by the FePc cathode catalyst, overshooting the Nafion top coat loading on the anode should not have had a significant effect on the overall MEA performance.

Table 5.6. Calculated and experimental (actual) values anode catalyst layer components including Nafion coating on top of the catalyst layer. SGL GDL 25BC carbon fibre paper was used as the substrate with 5 % w/w PTFE in the micro porous layer.

Anode composition	Target	Actual	/ Units
20% w/w Pt/C loading	0.40	0.41	/ mg cm^{-2}
% Nafion in cat. Layer*	25	25	/ % w/w
Nafion loading in cat. layer	0.68	0.68	/ mg cm^{-2}
Nafion top coat on cat. layer	0.20	0.39	/ mg cm^{-2}

*based on mass of Nafion divided by the sum of the masses of the Pt, carbon and Nafion in the catalyst layer.

5.3.1 FePc and $FePcCl_{16}$ catalyst layer GDL electrode testing

The activity of both FePc species was evaluated separately as the catalyst alone, and then in a catalyst ink coated GDL, as described in Chapters 3 and in another work [2]. The MPL on the CFP GDL served two purposes. The first was to prevent catalyst from being lost into the GDL's macro pores, which increased catalyst utilization. The second was to improve water management in the

cathode whereby the MPL with PTFE acted as a wicking layer. The Nafion top coat served to create better adhesion of the catalyst coated GDL to the Nafion membrane.

Four electrodes were cut from each FePc species GDL as described in section 5.2.6. This was to test for significant variability in the catalyst layer. Then CV's of each electrode were run three times in order to ensure repeatability as well as stability. As the geometric area was not exactly 0.5 cm^2, the real geometric area was measured for each electrode and the current densities were then corrected.

5.3.1.1 Surface electrochemical response of FePc species catalyst ink on CFP GDL electrodes

CV's for each of the FePc as well as $FePcCl_{16}$ catalyst coated electrodes were run in a N_2 purged 0.1 M H_2SO_4 electrolyte and are shown in Figures 5.4 and 5.5, respectively. Several scans were necessary to bring the catalyst ink surface to steady state. After 25 scans, the catalyst surface was essentially stable. There was more hysteresis for the first 25 scans of the FePc WE which could be due to either penetration of the pores by water, or could be polymerization of the FePc catalyst ink, including some other ring to ring electron transfer. This hysteresis was not as pronounced for the $FePcCl_{16}$ catalyst ink, whose CV's showed a smaller double layer. The chlorine substituents do make $FePcCl_{16}$ more hydrophobic and could make pore penetration by water more difficult. In addition, the chlorine substituents could hamper any ring to ring

electron transfer. Finally, $FePcCl_{16}$'s lower Nafion top coat loading could have also caused this difference in hysteresis.

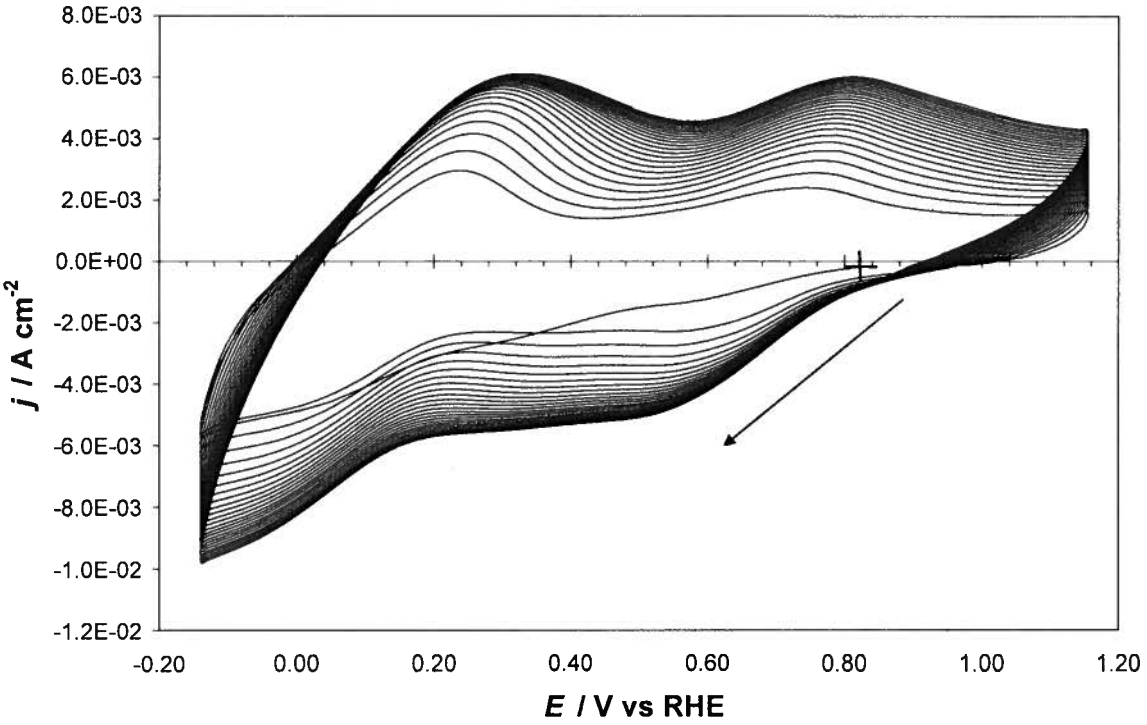

Fig. 5.4. Cyclic voltammograms at a scan rate of 100 mV s^{-1} for the supported 2.8 mg cm^{-2} FePc catalyst ink coated carbon fibre paper working electrode assembly. Scans performed at 20°C, and 1 atm, in a N_2 purged 0.1M H_2SO_4 electrolyte.

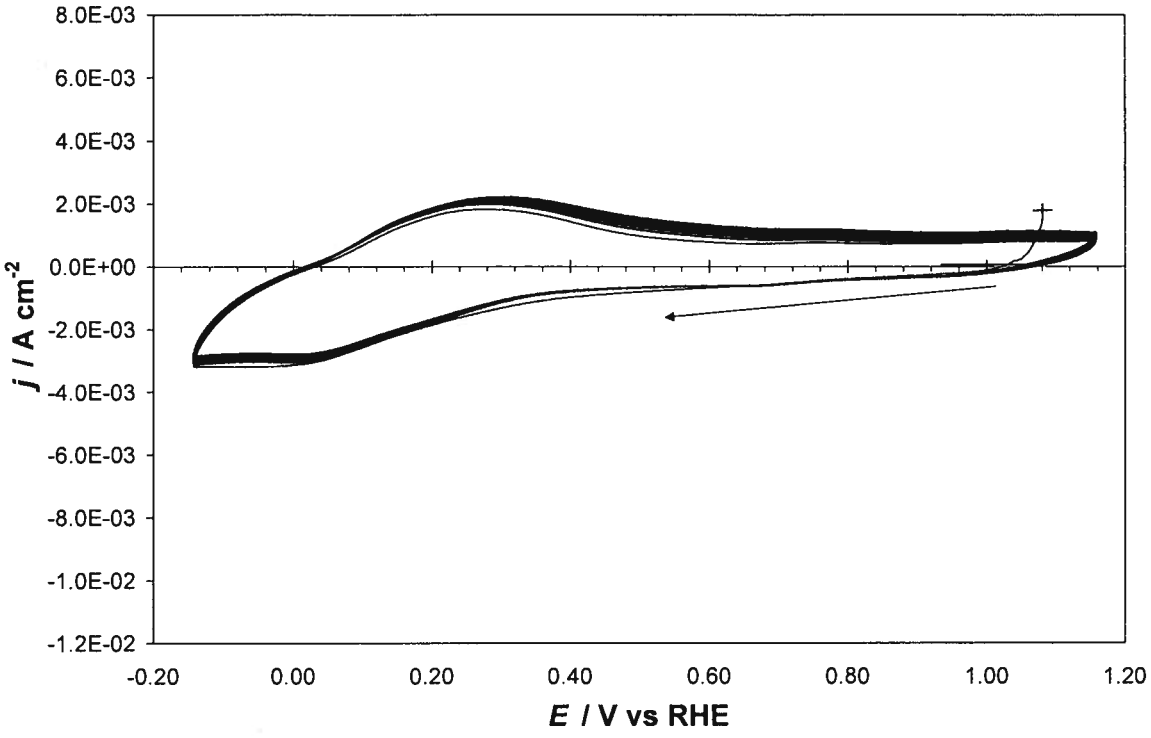

Fig. 5.5. Cyclic voltammograms at a scan rate of 100 mV s^{-1} for the supported 5.2 mg cm^{-2} $FePcCl_{16}$ catalyst ink coated carbon fibre paper working electrode assembly. Scans performed at 20°C, and 1 atm, in a N_2 purged 0.1M H_2SO_4 electrolyte.

All four electrodes for each FePc species gave very similar performances, indicating good repeatability and uniformity of the catalyst layer. It was interesting to note the difference between redox peaks of both FePc species catalyst inks when compared to those for the same FePc species adsorbed on a pyrolytic graphite electrode, as were shown in Chapter 3. The CV's in Figure 3.3 show less hysteresis, smaller double layers, and well defined, reversible redox peaks (0.11, 0.65 V vs RHE, and 0.10, 0.22, 0.60, 0.95 V vs RHE, for FePc and $FePcCl_{16}$, respectively). These differences demonstrated an effect of the FePc species being in a catalyst ink and on a different WE.

5.3.1.2 Electrocatalytic activity of FePc species catalyst inks towards O_2 reduction

Cyclic voltammograms of each FePc species were run in an air saturated 0.1 M H_2SO_4 electrolyte. For each CV, five scans were run, and again each of the four electrodes for both FePc species were tested three times. For comparison, Figures 5.6 and 5.7 show all five scans of the ORR CV is shown along with the final surface wave for the same electrode in N_2 saturated electrolyte.

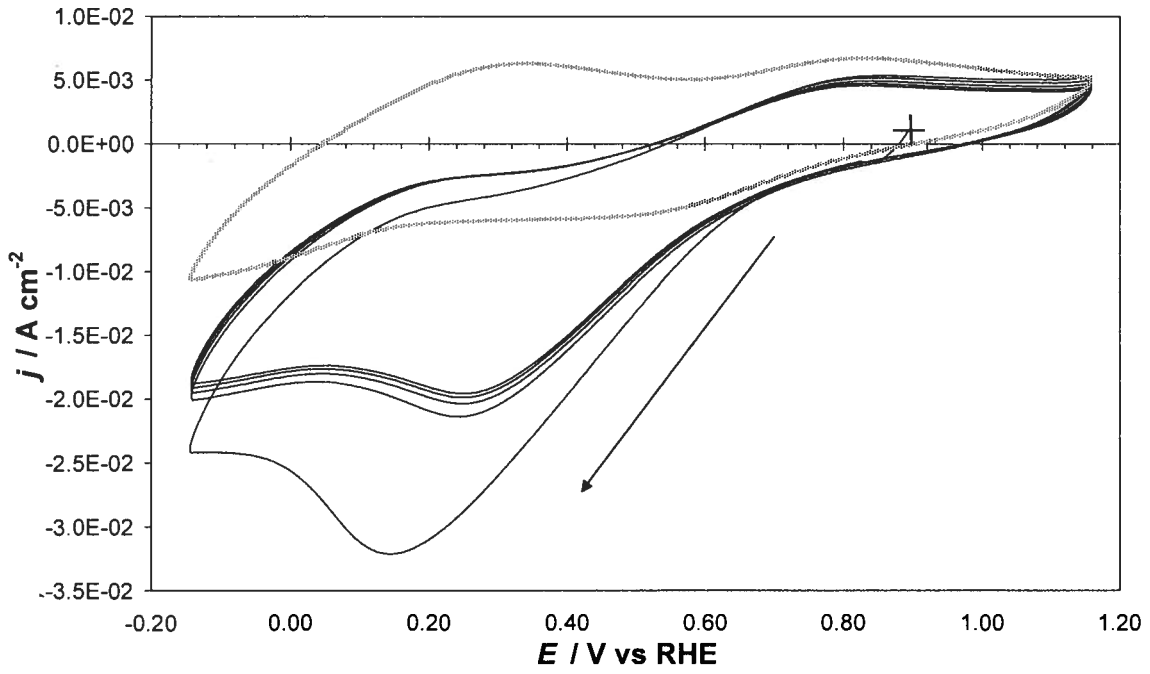

Fig. 5.6. Cyclic voltammograms at a scan rate of 100 mV s^{-1} for the same supported 2.8 mg cm^{-2} FePc catalyst ink carbon fibre paper working electrode assemblies in both the N_2 purged (grey trace) and air-saturated (black traces) 0.1 M H_2SO_4 electrolyte at 1 atm and 20°C. Scans for the N_2 purged electrolyte are taken from Fig. 5.4 at steady state.

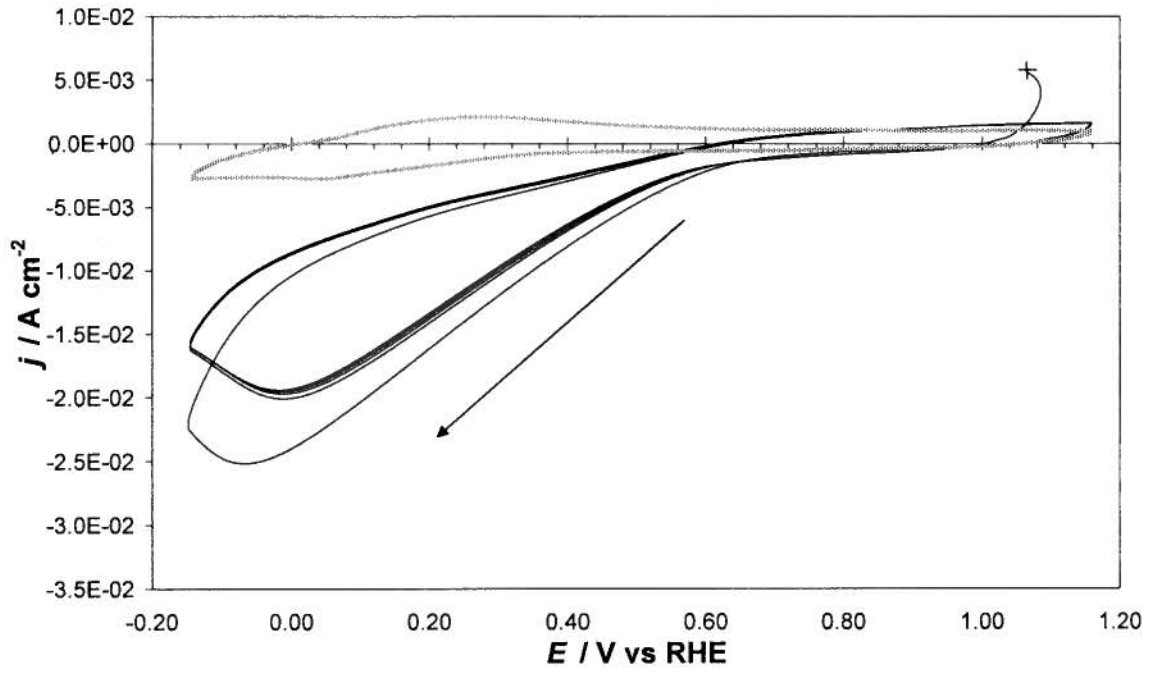

Fig. 5.7. Cyclic voltammograms at a scan rate of 100 mV s^{-1} for the same supported 5.2 mg cm^{-2} $FePcCl_{16}$ catalyst ink carbon fibre paper working electrode assemblies in both the N_2 purged (grey trace) and air-saturated (black traces) 0.1 M H_2SO_4 electrolyte at 1 atm and 20°C. Scans for the N_2 purged electrolyte are taken from Fig. 5.5 at steady state.

Both the FePc as well as $FePcCl_{16}$ catalyst inks showed definite ORR activity. Large double layer currents were again also seen. All three CV's for each electrode showed excellent reproducibility. After correcting for the individual geometric areas for each electrode, the difference in peak currents between each set of four electrodes was small. Of the two sets of four electrodes, only #1 for FePc and #3 for $FePcCl_{16}$, showed different performances relative to the remaining three of each FePc species even after correcting for the geometric

area. This was likely a result of visible damage to the WE tip before or during the experiment. The results for these two electrodes were thus discarded.

For both FePc species, the largest reduction current was obviously seen for the first scan. However, the second scan did not change appreciably from the fifth. This supported the possibility that the Nafion top coat limits mass transport to the catalyst active sites, before the dissolved O_2 is significantly depleted from the diffusion layer.

The difference in shape of the ORR CV's between the two FePc species was influenced by their respective surface waves in the N_2 purged electrolyte. In the next section, these surface waves in N_2 were subtracted from the respective ORR CV's to better compare the two FePc species catalyst ink ORR activity.

5.3.1.3. Comparison of FePc species ORR activities, both alone and in a catalyst ink

Figures 5.8 and 5.9 compare the ORR activity of the two FePc species, as well as between the catalyst alone and catalyst ink environments. In both figures, it is important to note that the geometric area for each electrode has been compensated for, and the FePc species' surface waves in N_2 saturated electrolyte have been subtracted. This allows more accurate activity comparisons to be made.

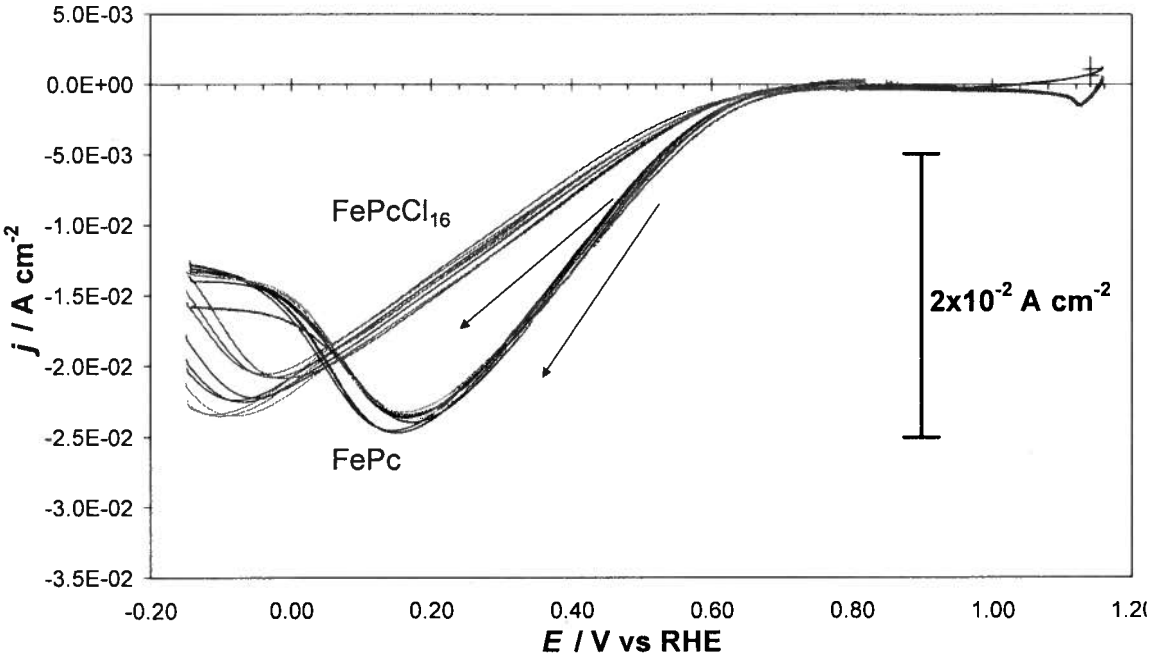

Fig. 5.8. Cyclic voltammograms at a scan rate of 100 mV s^{-1} for supported 2.8 mg cm^{-2} FePc and 5.2 mg cm^{-2} $FePcCl_{16}$ catalyst ink carbon fibre paper working electrode assemblies in an air-saturated 0.1 M H_2SO_4 electrolyte at 1 atm and 20°C. Current densities were normalized per cm^2 of geometric area and then corrected for surface waves at steady state for the same FePc catalyst ink CFP electrode in the N_2 saturated electrolyte. For both FePc and $FePcCl_{16}$ the first scan of each of three CV's for each of the three working electrode assemblies are shown.

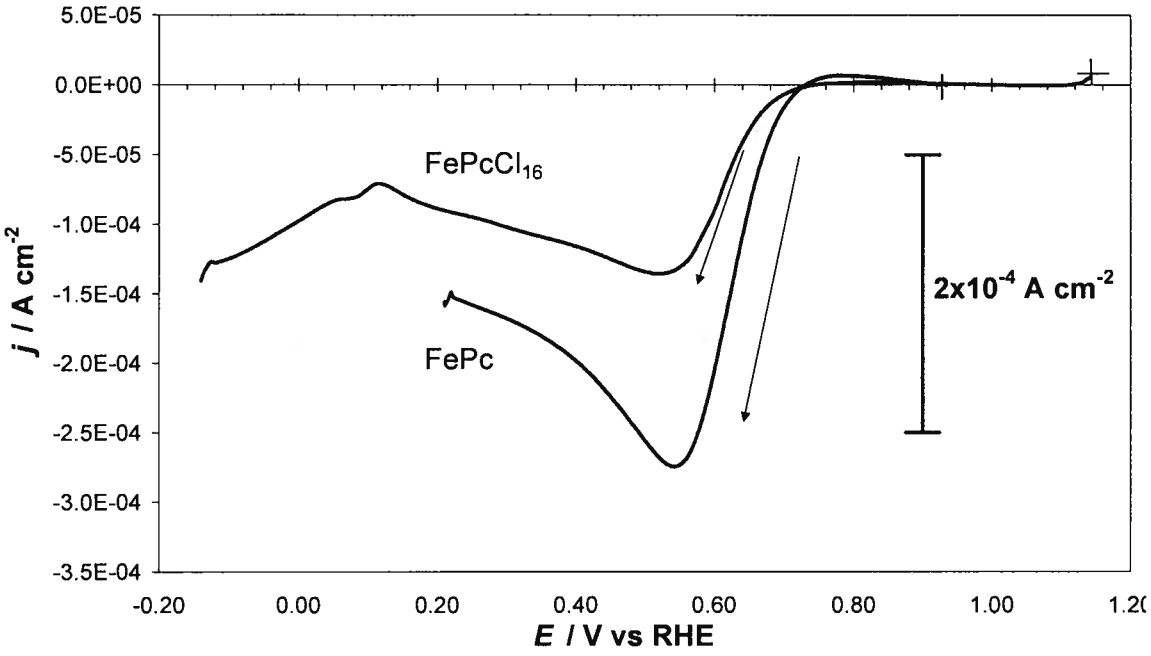

Fig. 5.9. Cyclic voltammograms at a scan rate of 100 mV s^{-1} for the unsupported 2.4 x 10^{-10} mol cm^{-2} FePc and 8.0 x 10^{-11} mol cm^{-2} $FePcCl_{16}$ adsorbed pyrolytic graphite working electrodes, as marked on each trace, in an air-saturated 0.1 M H_2SO_4 electrolyte at 1 atm and 20°C. Curent densities taken from Chapter 3 were normalized per cm^2 of geometric area and then corrected for the adsorbed FePc species surface waves in the N_2 purged electrolyte.

The first scan for all three CV's for each of the three good electrodes of both FePc species are shown in Figure 5.8. In viewing all these scans, the repeatability of each electrode as well as the reproducibility between the three electrodes for each FePc species were quite good. The ORR CV's from Chapter 3 for the FePc species adsorbed on a pyrolytic graphite electrode, shown in Figure 5.9, only showed one scan each but demonstrated an approximate factor of two difference between the peak currents. Koutecky-Levich analysis from

Chapter 3 gave n = 2.1 and n = 3.3 for the observed number of electrons transferred for the $FePcCl_{16}$ and FePc catalyzed ORR's, respectively. It follows that the peak reduction current for FePc was nearly double that for $FePcCl_{16}$.

This was in contrast to Figure 5.8, where both FePc species peak reduction currents are similar. Much effort was made to ensure that the calculations for, and preparation of, both FePc species catalyst inks were the same. It follows that in a catalyst ink environment, both FePc species gave similar ORR peak currents. Considering the geometric areas had been corrected for, it is interesting to note the difference in Γ and in peak currents between FePc and $FePcCl_{16}$ when they were absorbed alone on the pyrolytic graphite WE, but no such difference was seen for the catalyst ink coated CFP WE where per cm^{-2} they had the same number of active sites. The literature has recently noted the effect of TM macrocyclic catalyst ink loading on the ORR [85] and concluded an optimum is required to accurately test its' activity. Furthermore, Bonakdarpour and co workers found that too low of a loading for pyrolized TM macrocycles increased the amount of H_2O_2 detected at the Pt ring, indicating that not enough catalyst was present to fully reduce O_2 to H_2O. The contrast in peak currents between the two catalyst testing environments would have to be repeated with RRDE analysis to confirm if the difference was due to catalyst loading for the work presented in Figures 5.8 and 5.9.

The difference in onset potentials, and the different potentials at which the reduction current peaks were reached for the FePc species in Figure 5.8, could be due to any number of factors resulting from the different WE as well as

catalyst ink components. Further experimentation would be required to elucidate these effects and is beyond the scope of this thesis.

The absolute difference in peak currents between Figure 5.8 and 5.9 was approximately two orders of magnitude. In comparing the relative change in available surface areas between the polished pyrolytic graphite surface, and that of the BP 2000 carbon support (1500 $m^2\ g^{-1}$), an increase by a factor of $5x10^4$ is possible, and of at least three orders of magnitude is expected (in practice less surface area is active), when the unsupported catalyst is made into an ink. Clearly, the initial FePc species catalyst ink tests showed that either further optimization of the cathode catalyst layer is required, or a better carbon support should be used. However, choosing the best support and the following optimization of non noble metal cathode catalyst layers is a separate research topic in of itself, and beyond the scope of this thesis.

5.3.2. Fuel cell testing of FePc and $FePcCl_{16}$ MEA's

Great care was taken to ensure as little catalyst ink as possible fell off the FePc species cathode GDL's before hot pressing. After hot pressing, the FePc species cathode MEA's were tested in the custom fuel cell shown previously in Figure 5.5. Initial tests were performed using a Pt/Pt MEA made with the same Pt coated GDL's, and according to the same procedures described in sections 5.2.7 and 5.2.8, respectively. This was to validate the fuel cell testing hardware before evaluating the FePc species MEA's. Initially the fuel cell did not achieve an operating temperature of 80°C. This was resolved by using a pair of external heating pads as described in Table 5.11.

The initial Pt MEA tests were successful, and thus the FePc species cathode catalyst MEA's were then evaluated. MEA performances for Pt and FePc species cathode catalysts are discussed in section 5.3.2.4. A second hardware challenge was encountered where the FePc species MEA's would not form an airtight seal. A combination of a thicker cathode catalyst layer and the unavoidable wrinkling of the Nafion around the GDL caused this. Leaking was resolved by adding a soft, thin white silicon gasket to both the anode and cathode seals. With the FC hardware operating properly, two main methods were then used to test the MEA's.

5.3.2.1. First MEA testing method

Initial tests were based upon galvanostatic control of the fuel cell using the Solartron FRA to control the TDI load bank. Only voltage versus time plots were recorded by the Fideris FCTS software, and the corresponding currents were thus written into the experimental log book. The general procedure was to record the OCV for 30 minutes, followed by conditioning the MEA under galvanostatic control for 10 minutes at small, but monotonically increasing, currents. Once the cell voltage was stable, and no longer increasing, the MEA was considered conditioned and the current was decreased in the same order at 5 minute intervals. At each interval of the decreasing current, an EIS spectra was recorded under load. Recording voltage as a function of current while simultaneously performing EIS allowed essentially two experiments to be run at the same time. EIS spectra was desired to separate the many simultaneous processes, occurring within the FePc species catalyst layer.

However, due to unstable performance repeated attempts failed to give both enough current and voltage data points as well as EIS spectra to generate a reasonable polarization curve and obtain repeatable impedance spectra, respectively. The flow rates, followed by the cathode relative humidity (RH) were optimized. The initial flow rates attempted were 200 mL min^{-1} H_2 and 500 mL min^{-1} air [22]. The flow rates were then changed to 20 mL min^{-1} H_2 and 300 mL min^{-1} air. The best performance was with flow rates of 30 mL min^{-1} H_2 and 90 mL min^{-1} O_2. Reducing the relative humidity (RH) of the cathode to 55% initially gave a more stable MEA performance.

In summary, only one complete set of voltage versus current data, without EIS, was obtained. This data is discussed further in Section 5.3.2.4. It became evident that the test conditions and procedures would have to be improved in order to overcome challenges with voltage stability under galvanostatic control.

5.3.2.2. Second MEA testing method

As the cathode catalyst layer was not yet optimized, it became very challenging to obtain stable individual voltage readings over 5 to 10 minute time scales while at the same time minimizing the overall length of the experiment to avoid significant catalyst decomposition. As a result a more rapid technique was employed. Using a Solartron potentiostat to control the fuel cell tests solved this. The potentiostat was used to record OCV followed by CV experiments. The scan rate was chosen such that the MEA's electrochemical processes were approximately steady state and could thus be compared with the galvanostatic control results.

Similar to the first MEA testing method, an OCV was recorded for 30 minutes, followed by a CV. A number of parameters were varied in order to find the optimal MEA testing conditions:

1. Cathode RH was varied between 55% and 100%
2. Two cell operating temperatures of 21°C and 81°C (including anode and cathode streams) were used
3. Scan rates of 5 mV s^{-1} and 1 mV s^{-1} were used
4. Different potential windows were also used

Of the four parameters varied above, the best operating conditions were found to be 100% RH on the cathode and anode, an initial OCV experiment for 30 minutes, a scan rate of 5 mV s^{-1}, a potential window from OCV to 0 V and back to OCV, followed by another 10 to 20 minutes at OCV before running any additional CV's.

5.3.2.3. Comparison of both FePc species MEA voltages with time

To view any possible trends, as far as a change in current with respect to total MEA testing time at a constant potential, this data was graphed for all MEA's (not shown). As the data was a mix of galvanostatic and cyclic voltammogram experiments, it was difficult to show any quantitative trends. However, a general behaviour was observed for both FePc species, summarized in point form below:

1. The FePc MEA's showed a decay curve, suggesting monotonic loss in performance with both increasing time and current
2. The $FePcCl_{16}$ MEA's showed more of an activation, or conditioning effect, up to a maximum voltage at each current near t = 40000 sec (11 hrs) for the March 25 experiment
3. $FePcCl_{16}$ also showed little sign of either conditioning or deactivation at low currents, significant conditioning at moderate currents and greater deactivation at higher currents

5.3.2.4. FePc species MEA testing results

A summary of fuel cell tests at room temperature, fuel cell test challenges and solutions, as well as tabulated FePc species MEA test conditions can be found in Appendix XV. EIS experiments were attempted, but as the cathode catalyst layer was not yet optimized, it was difficult to achieve steady state in turn making it impossible to obtain repeatable EIS spectra. While the MEA testing methods were being improved, only one MEA for each FePc species (MEA # 1 for FePc and MEA # 3 for $FePcCl_{16}$) was used so as not to waste the other two. The first MEA testing method only gave one usable polarization curve just for $FePcCl_{16}$

MEA # 3 near 15 hours of use, after it was subjected to 0.27 A cm^{-2} and 0.36 A cm^{-2} for approximately half an hour on March 25, which likely reduced the activity of the MEA. After March 25 (see Table 5.8), the MEA's performance was diminished.

Both FePc MEA # 1 and $FePcCl_{16}$ MEA # 3 had thus been in use for several hours and were likely somewhat deactivated by the time the second testing method was developed. Fresh MEA's were thus used for the second MEA testing method. The CV's generated yielded polarization curves that showed good performance for the first forward scan of FePc MEA # 3. The return scan, however, showed a significant loss in performance. This hysteresis was seen for FePc MEA #2 as well. After the first test of FePc MEA # 3, a reddish black condensate was also observed in the cathode outlet.

The first such polarization curves for $FePcCl_{16}$ MEA's 1 and 2 also showed hysteresis and increasingly unstable performances. For $FePcCl_{16}$ MEA # 1 this was because the cathode GDL delaminated before testing and thus no usable polarization data could be attained, other than OCV data. Subsequent examination of $FePcCl_{16}$ MEA # 2 also revealed the cathode had delaminated during testing. Polarization curves for these new FePc species MEA's are shown in Figure 5.10.

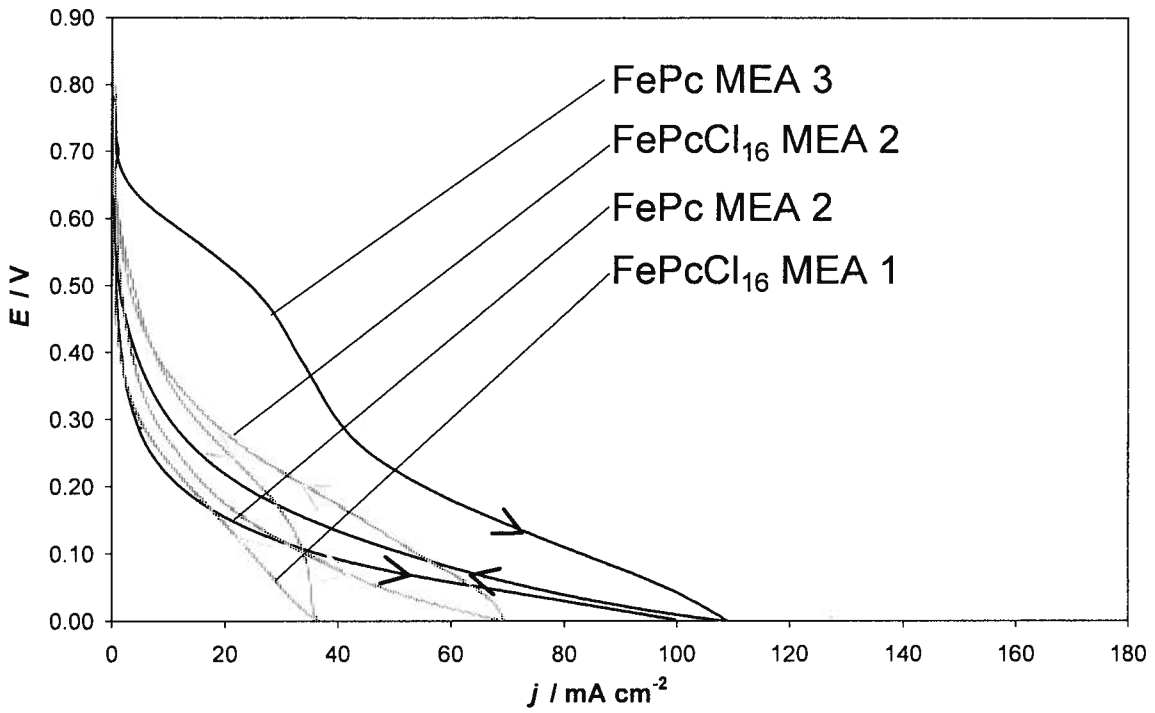

Fig. 5.10. Polarization curves using cyclic voltammetry (second MEA testing method) at a scan rate of 5 mV s^{-1} for 2.8 mg cm^{-2} FePc (black trace) and 5.2 mg cm^{-2} $FePcCl_{16}$ (grey trace) MEA's as marked. Operating times for each MEA were: 0 hrs for FePc MEA 3 (April 06 2008), 2 hrs for $FePcCl_{16}$ MEA 2 (April 03 2008), 9 hrs for FePc MEA 2 (April 02 2008), and 1 hr for $FePcCL_{16}$ MEA 1 (April 05 2008). Geometric area for all MEA's was 4.4 cm^{-2}. Operating conditions as described in Tables 5.7 and 5.8.

As $FePcCl_{16}$ MEA's 1 and 2 delaminated before testing, and during testing, respectively, it follows that any reasonable polarization data using the second MEA testing method was only possible for $FePcCl_{16}$ MEA # 3. As $FePcCl_{16}$ MEA # 3 had been used for several hours (Table 5.8) prior to using the second MEA testing method, new, or fresh MEA performance data for $FePcCl_{16}$ MEA # 3 was only available from earlier experiments that used the first MEA testing method.

Used MEA numbers 1 and 3 for FePc and $FePcCl_{16}$, respectively, showed minimal hysteresis and gave very repeatable polarization curves using the second MEA testing method as seen in Figure 5.11. However, their performance was noticeably diminished compared to the corresponding fresh MEA's shown in Figure 5.10.

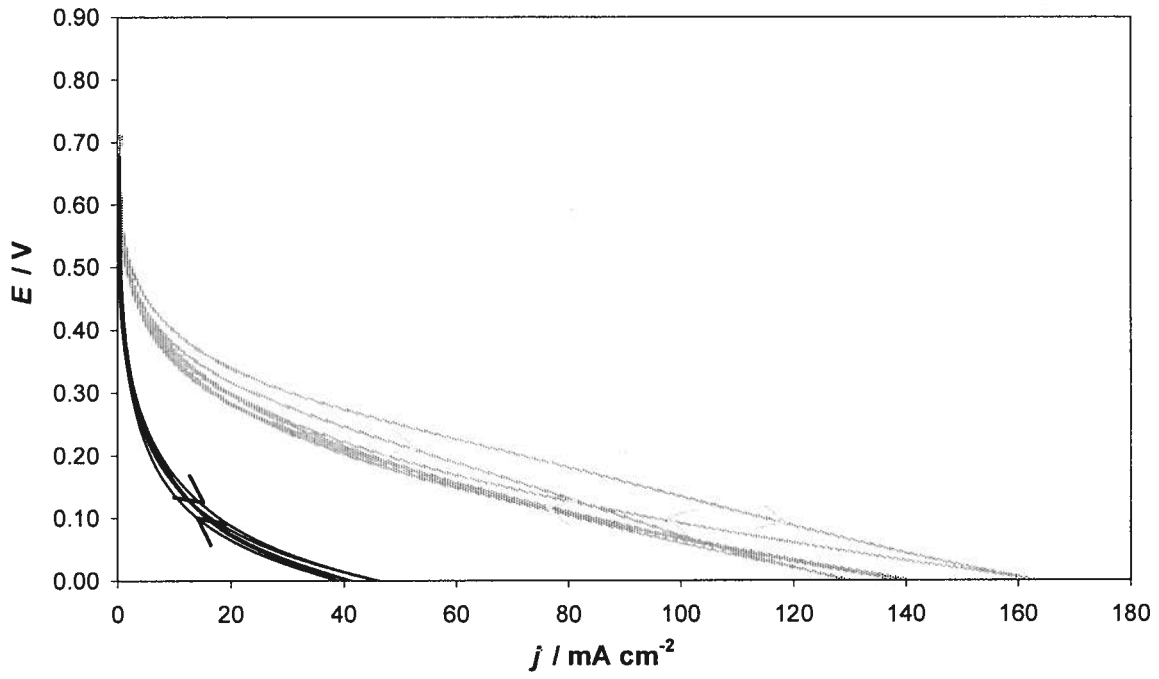

Fig. 5.11. Polarization curves using cyclic voltammetry (second MEA testing method) at a scan rate of 5 mV s^{-1} for 2.8 mg cm^{-2} FePc (black trace) and 5.2 mg cm^{-2} $FePcCl_{16}$ (grey trace) MEA's. Polarization curves shown for FePc MEA 1 and $FePcCl_{16}$ MEA 3 at 32 hours and 24 hours of use, respectively, both on April 6 2008. Geometric area for all MEA's was 4.4 cm^{-2}. Operating conditions as described in Tables 5.7 and 5.8.

Some of the first MEA test method data recorded in the experimental log book did yield polarization curves, for the fresh, or new, $FePcCl_{16}$ MEA # 3. These polarization curves are shown in Figure 5.12.

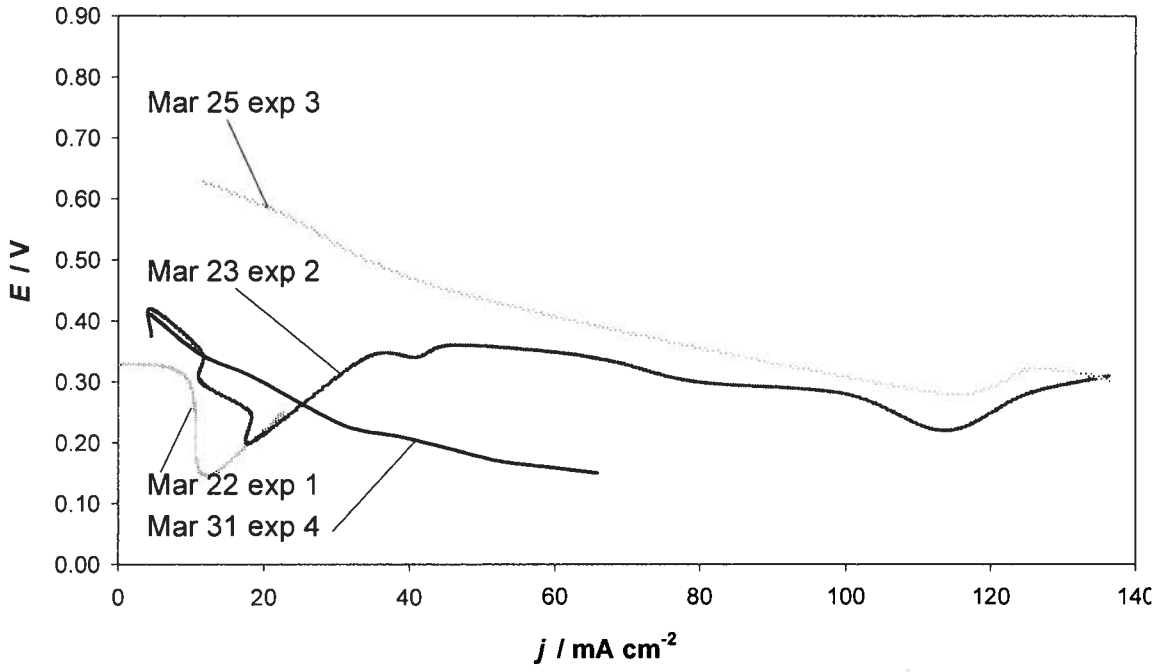

Fig. 5.12. Polarization curves under galvanostatic control (first MEA testing method) showing conditioning and deactivation of 5.2 mg cm^{-2} $FePcCl_{16}$ MEA 3. Experiment date and number as marked on each trace. Geometric area for all MEA's was 4.4 cm^{-2}. Operating conditions as described in Tables 5.7 and 5.8.

These polarization curves showed an activation with an increase in time and current, followed by a decrease in performance after the March 25 experiment. Recall the March 25 experiment gave the best performance, but as a final test, the current was increased to the point that it reduced the activity of the MEA. Data taken using the first MEA testing method is compared to the data taken using the second MEA testing method for $FePcCl_{16}$ MEA # 3 in Figure 5.13.

Chronologically, these two experiments were performed right after each other, so the MEA was in the same condition at the end of the March 31st experiment as it was at the beginning of the April 6th experiment.

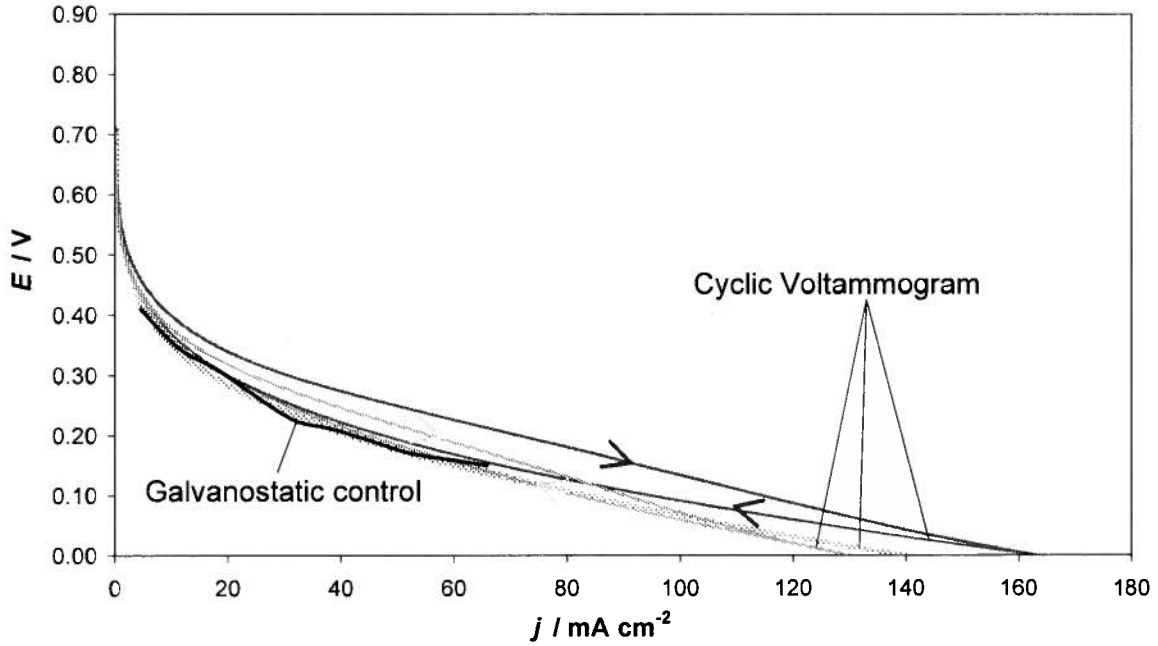

Fig. 5.13. Comparison of polarization curves obtained using first (Galvanostatic control, March 31 2008) and second (Cyclic Voltammogram, April 6 2008) MEA testing methods as marked on each trace for 5.2 mg cm^{-2} $FePcCl_{16}$ MEA # 3. Geometric area for all MEA's was 4.4 cm^{-2}. Operating conditions as described in Tables 5.7 and 5.8.

The overlap of the polarization curves generated using both the second and first methods indicates that the cyclic voltammograms at a scan rate of 5 mV s^{-1} yielded similar polarization curves to those recorded using steady state galvanostatic methods, respectively. More data would be necessary to make a thorough comparison, but for the purposes of this work, the results shown in Figure 5.13 indicate that polarization curves recorded using both the first and

second MEA testing methods can be shown on, and compared in, the same graph. The best MEA test data, polarization as well as power curves for the "new" and "used" FePc and $FePcCl_{16}$ MEA's, respectively, are summarized in Figure 5.14.

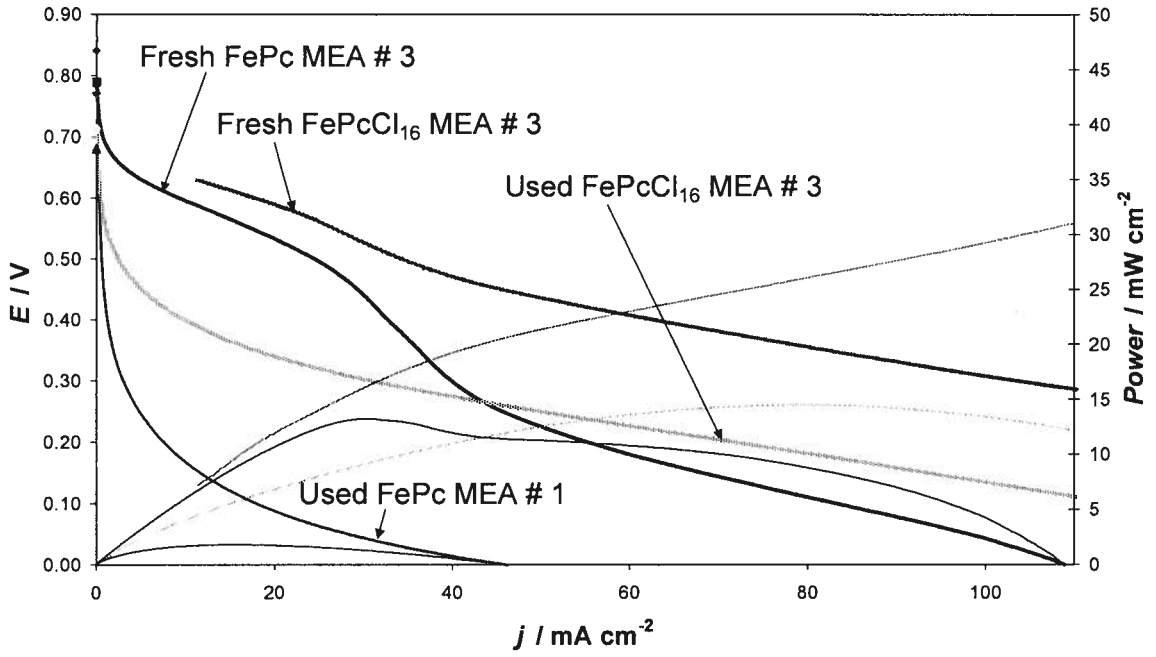

Fig. 5.14. Best polarization (monotonically decreasing with increasing current) and power (thin trace) curves for new and used 2.8 mg cm^{-2} FePc and 5.2 mg cm^{-2} $FePcCl_{16}$ MEA's as marked. OCV's for each trace are marked with symbols. Power curves are calculated from the polarization curves. The scan rate for the cyclic voltammograms was 5 mV s^{-1}. FePc, MEA 3 (April 6, 2008) and MEA 1 (April 6, 2008) were used for the new and used cyclic voltammogram polarization curves, respectively. For $FePcCl_{16}$, MEA 3 was used for the new (April 6 2008, cyclic voltammogram) and used (March 31 2008, galvanostatic) polarization curves. Geometric area for all MEA's was 4.4 cm^{-2}. Operating conditions as described in Tables 5.7 and 5.8.

The $FePcCl_{16}$ MEA clearly had the lowest overpotential (η) and highest OCV, as well as the largest currents and power production at all voltages for both the new and used MEA's of either FePc species. When comparing the losses in performance between new and used MEA's, $FePcCl_{16}$ appeared to show the greatest decrease, possibly due to the deactivating experimental conditions stated earlier. The FePc MEA was never subjected to the same deactivating experimental conditions as was the $FePcCl_{16}$ MEA. To show the differences in performance between the FePc and $FePcCl_{16}$ MEA's both new and used, OCV as well as current and current density values are displayed in Tables 5.7, 5.8 and 5.9.

Table 5.7. Comparison of new and used FePc and $FePcCl_{16}$ MEA open circuit voltages (OCV's). Data from Figure 5.14.

	New	Used	Degradation
	E	***E***	***E***
	/ V vs RHE	/ V vs RHE	/ V
FePc	0.793	0.700	0.093
$FePcCl_{16}$	0.860	0.730	0.130
Difference	0.067	0.030	0.037

Table 5.8. Comparison of new and used FePc and $FePcCl_{16}$ MEA currents as well as current densities at 0.45 V. Data from Figure 5.14.

	New		Used		Degradation	
	i	***j***	***i***	***j***	***i***	***j***
	/ mA	/ mA cm^{-2}	/ mA	/ mA cm^{-2}	/ mA	/ mA cm^{-2}
FePc	129	29	4.0	0.9	125	28
$FePcCl_{16}$	200	45	22	5.0	178	40
Difference	71	16	18	4.1	53	12

Table 5.9. Comparison of new and used FePc and $FePcCl_{16}$ MEA currents as well as current densities at 0.28 V. Data from Figure 5.14.

	New		Used		Degradation	
	i / mA	*j* / mA cm^{-2}	*i* / mA	*j* / mA cm^{-2}	*i* / mA	*j* / mA cm^{-2}
FePc	184	42	16	3.6	168	38
$FePcCl_{16}$	500	114	167	38	333	76
Difference	316	72	151	34	165	38

It can be seen that the substituted $FePcCl_{16}$ cathode catalyst MEA showed the lowest η, the largest currents at all potentials, and the best stability when compared to the baseline, or unsubstituted FePc cathode catalyst MEA. This is shown in the difference row of the three Tables above. When comparing the decrease in current from new to used MEA's at a given potential in the degradation column, $FePcCl_{16}$ deactivated more than FePc. Again, during the March 25th experiment, $FePcCl_{16}$ MEA # 3 sustained the highest currents for the longest period of time of any of the FePc cathode MEA's tested in this thesis. These conditions could have accelerated cathode decomposition and thus been the cause for the larger decrease in activity relative, to FePc. New and used currents as well as current densities at a given potential are summarized in Table 5.10.

Table 5.10. Comparison of new and used FePc and $FePcCl_{16}$ MEA currents as well as current densities in the potential range from 0.63 to 0.30 V. Data from Figure 5.14.

	New		Used		New		Used	
	$FePcCl_{16}$	$FePcCl_{16}$	$FePcCl_{16}$	$FePcCl_{16}$	FePc	FePc	FePc	FePc
E	*i*	*j*	*i*	*j*	*i*	*j*	*i*	*j*
/ V vs RHE	/ mA	/ mA cm^{-2}	/ mA	/ mA cm^{-2}	/ mA	/ mA cm^{-2}	/ mA	/ mA cm^{-2}
0.63	50	11	1.5	0.3	22	5.0	1.0	0.2
0.60	80	18	2.1	0.5	40	9.1	1.5	0.3
0.55	115	26	5.0	1.1	76	17	2.0	0.5
0.50	150	34	11	2.5	107	24	2.6	0.6
0.45	200	45	22	5.0	128	29	3.7	0.8
0.40	280	64	44	10	143	33	5.5	1.3
0.35	360	82	78	18	160	36	8.5	1.9
0.30	460	105	133	30	175	40	14	3.2

Although far from being optimized, the new $FePcCl_{16}$ species MEA did show voltages of 0.45 V and 0.30 V, at current densities of 50 mA cm^{-2} and 100 mA cm^{-2}, respectively, which compared well to Liu et. al.'s voltages of 0.35 V and 0.25 V for their conventional pyrolized CoTMPP/C catalyst at the same current densities [22]. Liu and co-workers used a similar active area, and similar MEA fabrication procedure as well as similar testing hardware, although at different flow rates. The results for $FePcCl_{16}$ also compare well to those reported by Faubert and co-workers [20]. However, these performance results were below those reported by Jaouen et. al. where at a current density of 100 mA cm^{-2} their best pyrolyzed FeN_x/C catalyst gave 0.65 V, and the standard 0.30 mg Pt cm^{-2} Gore MEA they used for comparison gave 0.85 V [19]. Other MEA polarization curves for pyrolyzed FeN_x/C catalysts reported in the literature also showed superior performance to those shown here for the unpyrolyzed $FePcCl_{16}$ [18,21], but again all lower than the commercially available 0.35 mg Pt cm^{-2} MEA from E-Tek [18]. For the used $FePcCl_{16}$ species MEA the decrease in performance after 25 hours of operation (including the deactivating experiment) was noticeable. At

the same current densities described above, the voltages now decreased to 0.25 V and 0.10 V, respectively.

5.3.3. FePc cathode catalyst MEA challenges and future work

A table summarizing these challenges along with the corresponding solutions is shown in Table 5.11. Some of these challenges and solutions have already been described (vide supra).

Table 5.11. Summary of FePc and $FePcCl_{16}$ MEA fuel cell testing challenges and successes.

Challenges	Successes
Cell won't achieve 80°C	Use additional heaters on end plates
MEA's won't seal	Use Kapton tape: 1/6 now seal
Some MEA's won't seal	Add thin Si gasket to the cathode: 2/6 now seal
Some MEA's won't seal	Laminate MEA's: 3/6 now seal
Some MEA's won't seal	Additional thin Si gasket on Anode: all 6 seal
Unstable voltages	Improve fuel and oxidant flow rates
Unstable voltages	Improve conditioning procedure
Unstable voltages	Increase stability and activity by using O_2
Unstable voltages	Increase stability by decreasing RH
Unstable voltages	Vary cell operating temperature
Unstable voltages	Vary bladder pressure and run EIS
Unstable voltages	Change testing method and equipment
Unstable voltages	*Modify cat ink, improve cathode cat structure*
Delamination	*Modify cat ink, improve cathode cat structure*

In summary, the testing procedures and equipment could only be optimized to a certain point before either the cathode catalyst significantly deactivated, or in the case of the two $FePcCl_{16}$ MEA's, the cathode GDL's delaminated completely. This necessitateds the fabrication of new MEA's and moreover, more detailed cathode catalyst layer optimization. Catalyst layer optimization is the subject of an entire project in of itself and unfortunately well outside the scope of this thesis.

It follows that unstable voltages due to water management problems and or cathode delamination were the biggest detriment to performance, more so than catalyst decomposition, for the FePc species cathode catalyst MEA's tested here. On several occasions, MEA voltages were the most stable shortly after start up, before becoming unstable, rising, bumping, and eventually falling to zero. This behaviour repeated itself several times. Water management may have been difficult due to the large thickness of the cathode catalyst layer, and / or variability of the in plane catalyst layer thickness along the MEA. Delamination could have been a result of the lower Nafion top coat loading for $FePcCl_{16}$. Delamination could also have been from agglomeration of the catalyst seen after spraying, due to a low Nafion loading in the ink and / or an ink solvent that was too hydrophilic. It is also possible that these FePc species MEA's performed best at room temperature, possibly due to a high RH of 140%. These topics could again be the subject of future work.

To improve MEA performance, increasing the amount of IPA in the catalyst ink would address the hyrdophobicity of both the GDL and supported FePc catalysts, especially $FePcCl_{16}$. This could help make the cathode catalyst

deposition more uniform by decreasing the hydrophobicity / hydrophilicity between the catalyst, its' solvent, and the MPL on the CFP GDL. Increasing the loading of Nafion in the catalyst layer as well as ensuring that subsequent Nafion top coat loadings for the $FePcCl_{16}$ MEA are on target could also decrease delamination. Using a different carbon support, such as pyrolytic graphite with a higher BET surface area could reduce the catalyst layer thickness. Pyrolyzing the FePc species alone and then making a catalyst ink would be another possible approach. If the adhesion of catalyst to the membrane was suitable, a catalyst coated membrane (CCM) could be an additional approach.

5.4 Summary

The substituted, down-selected $FePcCl_{16}$ and unsubstituted, or baseline FePc were evaluated and compared as supported catalyst inks on a CFP WE and as the cathode of an MEA in an operating PEM fuel cell. In comparing the ORR CV's of the two supported FePc catalyst ink CFP WE's, results showed both $FePcCl_{16}$ and FePc had similar performances whereas the peak current for the corresponding ORR CV's in Chapter 3 showed very different peak currents. This supported the possibility that surface orientation and Γ can affect the ORR mechanism. The increase in peak current when both FePc species were supported on carbon and made into catalyst inks was less than what was expected from theory. MEA's were made using the supported FePc species as cathode catalysts and FC tests were run using a custom, in house designed and built PEM fuel cell. The tests revealed the cathode catalyst layer required optimization, which includes testing different carbon supports.

Although preliminary, the results presented indicated the down selected, substituted $FePcCl_{16}$ showed better stability and activity towards the ORR than the unsubstituted, or baseline FePc. Cathode layer optimization could be the subject of future work. As expected, both FePc species showed reduced stability and performance when compared to the pyrolyzed FeN_x/C analogues and current state of the art Pt/Pt MEA's.

Chapter 6

Conclusions

Five FePc TM macrocycles were examined as possible PEM fuel cell electrocatalysts for the O_2 reduction reaction (ORR) as a function of both temperature as well as different substituents on the phthalocyanine (Pc) ring. Two of the FePc species had electron withdrawing substituents, which increase stability as well as ORR activity, while another two had electron donating substituents, which decrease stability as well as ORR activity. The last FePc was unsubstituted, and served as the baseline to which the other four could be compared to. The objective was to experimentally determine these temperature and substituent effects to obtain the associated kinetic parameters for the ORR and possibly gain insight into the mechanisms and active site(s) of pyrolized FeN_x/C analogues. The knowledge gained can be used to better understand the fundamental behavior of TM macrocycles and then applied to the design of new electrocatalysts.

The five FePc species were evaluated using three successive approaches. The first approach was ex-situ, in a 3 electrode cell arrangement using classical electrochemical techniques, which included CV, RDE, as well as RRDE voltammetries, to test the unsupported FePc electrocatalyst(s) alone. The second approach combined the ex-situ technique of CV in a novel half cell arrangement with an in-situ catalyst ink coated CFP WE made with the supported FePc species. The third approach was in situ, where larger portions of the same

FePc species catalyst ink coated CFP were used as the cathodes, to make a PEM MEA and subsequently test it using CV and EIS in a custom designed and built fuel cell.

6.0 Ex-situ testing

The purely ex-situ tests were used to down select the best substituted FePc in terms of stability and ORR activity. First the novel half cell was validated using CV and EIS, to obtain kinetic data for a model fuel cell reaction. The successful validation of both the half cell design and the catalyst ink CFP WE demonstrated that this approach can be used to study PEM fuel cell electrocatalysts in a simulated PEM fuel cell environment. This approach can accelerate lab scale catalyst down selection as well as catalyst ink evaluation.

As two of the five FePc species were not commercially available, two new FePc's with de-activating substituents were successfully synthesized in house using a simplified method from the literature. Successful synthesis was confirmed using UV-Vis spectroscopy and MALDI-TOF mass spectrometry. UV-Vis spectroscopy showed a decrease in stability and ORR activity for $FeNpPc(tBu)_4$ compared to $FePc(tBu)_4$. The associated shift in the Q-band agreed with the literature results for similar TM Pc species. This synthesis method can be used to rapidly make a number of substituted FePc species in a cost effective manner. The synthesis technique can be useful for lab scale research. For the first time, these two new substituted FePc's were synthesized and their stabilities as well as ORR activities compared. Preliminary ORR data

indicated $FeNpPc(tBu)_4$ shows a marked decrease in activity, to the point that the mechanism possibly changed.

All five FePc species were then adsorbed onto the surface of a pyrolytic graphite electrode and evaluated using CV, and RDE techniques. It was shown using CV that the adsorption was irreversible, the Fe centre displayed a reversible one electron (+III/+II) redox cycle that was surface and not diffusion controlled, and that the $Fe^{III/II}$ redox couple of the FePc species was stable at steady state. FePc, $FePc(SO_3H)_4$, and $FePc(tBu)_4$ showed two reversible redox couples, $FeNpPc(tBu)_4$ showed only one, while $FePcCl_{16}$ showed four. ORR and H_2O_2 oxidation reaction CV's as a function of temperature were also recorded. All FePc species showed ORR activity, but in terms of H_2O_2 reduction activity, $FePc(SO_3H)_4$ showed none. Kinetic parameters such as the overall ORR electron transfer number, reaction rate constants, Tafel slopes, electron number in the rate determining step, and the electron transfer co-efficient for all five FePc species were determined with RDE in the temperature range of 20 to 80°C using Koutecky-Levich theory and the cathodic Tafel equation. Increasing temperature improves ORR activity, but the kinetic effects only dominate up to 60°C, while at 80°C it decreases likely due to the greater decrease in O_2 concentration. These kinetic parameters compared well to the literature values, but the overall ORR electron transfer number (*n*) values for the substituted FePc species were unusual. Their *n*'s decreased with increasing temperature to the point where at 80°C, *n* observed became 1, except for $FePc(tBu)_4$, whose *n* decreased to 2. No significant temperature effect was observed for the baseline FePc. The *n*'s for

$FePcCl_{16}$, $FePc(SO_3H)_4$ and $FeNpPc(tBu)_4$ at 20°C were lower than expected. Recent work has shown that surface concentration, Γ, could affect the ORR mechanism, and hence *n*. This can possibly explain the results for $FePcCl_{16}$ and $FePc(SO_3H)_4$, whose Γ's were slightly less than one monolayer, but not for $FeNpPc(tBu)_4$ whose Γ was larger in comparison, and similar to those for the remaining two FePc species who both showed *n*'s of approximately 3. It follows that temperature, substitution and possibly mode of adsorption can all affect the ORR mechanism. Further experimentation is required to examine the cause of this observed decrease in *n*.

Substitution had a significant effect on FePc stability, where $FePcCl_{16}$ showed the greatest stability while $FeNpPc(tBu)_4$ showed the least. $FeNpPc(tBu)_4$ also showed the lowest ORR activity. Of the substituted FePc species, $FePcCl_{16}$ was down selected as having both the greatest stability and highest ORR activity.

The RDE results for *n* observed were confirmed using RRDE on all five FePc species at room temperature. Using a Pt ring and pyolytic graphite disk (made in house from the same material as was used for the RDE disk), X_{H2O2} values were calculated from three experimental runs for each FePc species. With the exception of FePc (which will be repeated), the experimental X_{H2O2} values agreed with the previous RDE results. The results for $FeNpPc(tBu)_4$ are unusual given its' large surface concentration, similar to those of FePc and $FePc(tBu)_4$, but its' comparatively lower *n*. UV-Vis spectra can show the decrease in stability and ORR activity, but don't explain the change in mechanism. MALDI-TOF mass spectra showed the possibility of μ-oxo dimers being formed, perhaps more so

for $FePc(tBu)_4$ than for $FeNpPc(tBu)_4$ possibly due to its' steric hindrance. The known steric hindrance preventing adsorption of the (2,3) FeNpPc isomer onto the pyrolytic graphite surface could be exacerbated by the additional bulky tetra *tert* butyl groups. It follows that in the case of $FeNpPc(tBu)_4$ steric effects could be the main cause for this change in ORR mechanism either via a weaker interaction with the pyrolytic graphite WE surface, preventing the formation of μ-oxo dimers, or making the distance between adjacent reactive sites too great.

6.1 Combined ex-situ and in-situ testing

A calculation method and experimental procedure was developed to better compare the ORR activities of different TM macrocyclic catalysts. This was accomplished by standardizing the number of active sites per unit geometric area of the supported FePc catalyst in the catalyst ink. Both the baseline FePc and down selected $FePcCl_{16}$ were supported on BP 2000 a powdered graphitic carbon. Once bound to the carbon support, the unsubstituted FePc did not de-adsorb in any of the catalyst ink solvents, most notably isopropanol. These supported FePc's were in turn made into catalyst inks. The inks were spray coated onto GDL CFP with MPL. The FePc catalyst ink spraying method was a great improvement over brushing and hand spraying methods. The FePc catalyst ink coated CFP WE and WE holder were improved, making them easier to handle, easier to clean, less likely to get contaminated, and decreased the double layer capacitance due to excess carbon contacting the electrolyte. The combination ex and in situ experiments compared the activities of the supported baseline FePc and down selected $FePcCl_{16}$ catalyst inks. The corrected ORR

CV's for the supported FePc and $FePcCl_{16}$ catalyst inks both show essentially the same peak current densities. This supports the idea that Γ and orientation for the unsupported FePc species alone could play a role in the ORR mechanism as once both FePc's were in similar catalyst ink environments and with similar active site densities, they showed almost the same activity. Comparing the corrected ORR CV's for the adsorbed unsupported FePc species alone to the supported FePc species catalyst ink CFP WE, showed an increase in j for the catalyst ink of approximately two orders of magnitude. A larger increase in the range of 3 to 4 was expected but was not found likely because the catalyst ink was not optimized and on average, not all the BET surface area is active.

6.3 In-situ testing

With the best substituted FePc species down selected and the performance of the supported FePc catalyst ink established, the two FePc species cathode GDL's were made into MEA's and compared in-situ in a PEM fuel cell to evaluate OCV's, polarization curves, and stability. More testing would be required at this stage, but preliminary results showed $FePcCl_{16}$ had the highest OCV, and lowest η, greatest j at all voltages and the greatest stability. The best results for the new, conditioned, $FePcCl_{16}$ MEA compared well to those reported in the literature for unpyrolized TM macrocyclics, but below those reported for pyrolyzed TM macrocyclics and well below the current stat of the art, commercially available Pt/Pt MEA's. Future carbon support and catalyst ink optimization is required.

When supported on carbon and made into a catalyst ink, FePc's with symmetrically substituted electron withdrawing substituents with inductive effects,

such as $FePcCl_{16}$ appear to exhibit greater stability, higher ORR activities and lower overpotentials than the unsubstituted FePc when incorporated as a catalyst ink in an operating PEM fuel cell.

The experimental results demonstrated how in three different and successive approaches using a PEM fuel cell-like testing environment how the best FePc species can be down selected as a function of substitution and temperature and then evaluated as a cathode catalyst in a real PEM fuel cell. Results also indicate that substituent effects according to molecular orbital theory reported in the literature agree with real life catalyst stability and ORR activity.

6.4 Future work

Some of the results presented here deserve further exploration to make them more conclusive. The scope of work was broad, and gave an excellent introduction to the field of non noble metal cataysts. Many additional experiments are possible, and would lend much value to the work already begun. Possible future work and approaches are listed in point form below.

1. Use at least one other technique to calculate the adsorbed surface concentration of the FePc species. For example, use integration to obtain the area under the $Fe^{III/II}$ redox couple curve and average it for the anodic and cathodic peaks.
2. Properly assign all of the FePc species' surface waves to appropriate redox processes.
3. Determine the number of electrons, the pH dependence and the number of protons involved in each redox step described in 2 above.
4. Improve the half cell design such that the entire apparatus can be kept at the desired temperature, including the purge gas. This is to minimize or eliminate any thermal gradients in the electrolyte when operating at or near 80°C. Thermal gradients give rise to small changes in density and hence the electrolyte and diffusion layer can never be totally quiescent. This became an issue only when working with Pt micro electrodes.
5. With item 3 complete, repeat the dissolved O_2 concentration experiments described in Chapter 3 to verify that the experimental and theoretical

diffusion co-efficient values agree. This is to confirm the change in *n* observed at 80°C is not an experimental artifact.

6. Determine if the decrease in *n* to 1 at 80°C for the substituted FePc species indicates a change in the ORR mechanism from an inner sphere to an outer sphere process. This would be an important experiment, once all other experimental artifacts are ruled out.
7. Further to number 6, this change could also be the result of a change in mechanism to redox mediation. Such a change in mechanism would also have to be researched and tested experimentally.
8. Make a plot of log *k* (at constant potential) vs the M(III)/(II) formal potential of the FePc species.
9. Perform RDE and RRDE experiments on FeNpPc and compare the results to those for $FeNpPc(tBu)_4$.
10. Perform RRDE experiments for all five FePc species at 20, 40, 60 and 80°C to calculate X_{H2O2} as a function of temperature and compare to the RDE results at the same temperatures.
11. Perform RRDE analysis to quantify the catalase activity of these FePc species towards H_2O_2 decomposition in O_2 free electrolyte, with 28 mM H_2O_2 and at room temperature.
12. Quantify the actual active surface area available for FePc species to adsorb on different pyrolytic graphite carbon supports using anthroquinone adsorption / de-adsorption CV's on Vulcan XC-72R, BP 2000 and

Spectracarb 2225. Use the pyrolytic graphite support with the highest active SA to support each of the five FePc species.

13. Use the supported FePc species to make catalyst inks and then deposit them onto a glass carbon (GC) RDE or RRDE disk according to the method reported by Bonakdarpour and co workers. Then repeat RDE and RRDE experiments using these five FePc species inks. The electrolyte could be buffered to a pH of 4.5, where the decomposition of FePc species is reduced.
14. DFT analysis of $FePc(tBu)_4$, $FeNpPc(tBu)_4$'s ability to form μ-oxo dimers.
15. DFT analysis of all five FePc species ability to bind O_2.
16. Optimize the FePc catalyst ink for MEA spraying. The main goals are to minimize cathode delamination, decrease the cathode catalyst layer thickness, as well as make the cathode catalyst layer thickness uniform.
    a. Either obtain CFP with a MPL that does not have any PTFE, or increase the amount of IPA in the ink solvent to make the ink more hydrophobic. This could reduce the beading seen on the MPL surface after spraying and in turn make the cathode layer thickness more homogeneous.
    b. Then make sure the target loading for the Nafion top coat is reached, and the same for all FePc catalyst ink coated GDL's. This could decrease delamination.
    c. The wt% Nafion in the catalyst layer could be increased to reduce delamination.

17. Try hot pressing the current FePc catalyst ink coated CFP WE's to see if the predicted increase in *j* can be achieved. Also the FePc species catalyst ink coated CFP electrodes can be made and then tested using different carbon supports to see if an increase in *j* of three to four orders of magnitude is possible.
18. Compare the FePc species catalyst coated CFP WE ORR CV's at 80°C to the FePc species MEA PEM fuel cell performances at 20°C to see if a similar effect is seen to that of the observed decrease in *n* at 80°C for the unsupported FePc species alone.
19. With an optimized FePc catalyst layer, and stable MEA performance, obtain EIS spectra.
20. RDE, as well as RRDE analysis, and MEA PEM fuel cell performance of all five FePc species, both pyrolyzed and unpyrolyzed, could be compared. FePc species loading could be optimized for the unsupported FePc species alone, followed by making the active site concentration the same for all pyrolyzed and unpyrolyzed FePc species.

References

[1] R. Baker, D.P. Wilkinson, J.J. Zhang, Electrochim. Acta 53 (2008) 6906.

[2] R. Baker, Z. Xie, J.J. Zhang, D.P. Wilkinson, Fuel Cell and Hydrogen Technologies, 44th Annual Conference of Metallurgists, Calgary, Alberta, 21 Aug., 2005; Canadian Institute of Mining, Metallurgy and Petroleum, (2005) 3.

[3] C. Song, L. Zhang, J.J. Zhang, D. Wilkinson, R. Baker, Fuel Cells 7 (2007) 9.

[4] J. Larminie, A. Dicks, Fuel Cell Systems Explained, 1st ed., John Wiley and Sons, New York, NY, USA, 2000.

[5] J.H. Zagal, F. Silva, M. Paez, in: J.H. Zagal, F. Bedioui, J.P. Dodelet (Eds.), N4 Macrocyclic Metal Complexes, Springer, New York, 2006, (Chapter 2).

[6] J.P. Dodelet, in: J.H. Zagal, F. Bedioui, J.P. Dodelet (Eds.), N4 Macrocyclic Metal Complexes, Springer, New York, 2006, (Chapter 3).

[7] A.B.P. Lever, Y. Ma, in: A.J.L. Pomeiro, C. Amatore (Eds.), Trends in Molecular Electrochemistry, FontisMedia S.A., Lausanne, Switzerland, 2004, (Chapter 3).

[8] A.B.P. Lever, E.R. Milaeva, G. Speier, Phthalocyanines, vol. 3, 1993.

[9] V.N. Nemykin, N.A. Kostromina, N.B. Subbotin, S.V. Volkov, Russ. Chem. Bull. 45 (1996) 89.

[10] N. Kobayashi, S.I. Nakajima, H. Ogata, T. Fukuda, Chem. Eur. J. 10 (2004) 6294.

[11] A. Biloul, O. Contamin, G. Scarbeck, M. Savy, D. van den Ham, J. Riga, J.J. Verbist, J. Electroanal. Chem. 335 (1992) 163.

[12] A. Biloul, F. Coowar, O. Contamin, G. Scarbeck, M. Savy, D. van den Ham, J. Riga, J.J. Verbist, J. Electroanal. Chem. 289 (1990) 189.

[13] M. Isaacs, M.J. Aguirre, A. Toro-Labbe, J. Costamagna, M. Paez, J.H. Zagal, Electrochim. Acta 43 (1998) 1821.

[14] C. Hinnen, F. Coowar, M. Savy, J. Electroanal. Chem. 264 (1989) 167.

[15] F. Coowar, O. Contamin, M. Savy, G. Scarbeck, J. Electroanal. Chem. 246 (1988) 119.

[16] M.N. Golovin, P. Seymour, K. Jayaraj, Y.S. Fu, A.B.P. Lever, Inorg. Chem. 29 (1990) 1719.

[17] D. Chu, R. Jiang. Methanol tolerant catalyst material. The United States of America as represented by the Secretary of the Army. US19990429702 19991028[US6245707]. 2001. Washington, DC/US. 28-10-1999.

[18] D. Villers, X. Jacques-Bédard, J.P. Dodelet, J. Electrochem. Soc. 151 (2004) A1507.

[19] F. Jaouen, F. Charreteur, J.P. Dodelet, J. Electrochem. Soc. 153 (2006) A689.

[20] G. Faubert, R. Cote, J.P. Dodelet, M. Lefevre, P. Bertrand, Electrochim. Acta 44 (1999) 2589.

[21] H. Wang, R. Côté, G. Faubert, D. Guay, J.P. Dodelet, J. Phys. Chem. B 103 (1999) 2042.

[22] H. Liu, C. Song, Y. Tang, J. Zhang, J.J. Zhang, Electrochim. Acta 52 (2007) 4532.

[23] A.J. Appleby, J. Electroanal. Chem. 357 (1993) 117.

[24] G.J.K. Acres, J.C. Frost, G.A. Hards, R.J. Potter, T.R. Ralph, D. Thompsett, G.T. Burstein, G.J. Hutchings, Catal. Today 38 (1997) 393.

[25] R. Adzic, in: J. Lipkowski, P.N. Ross (Eds.), Electrocatalysis, Wiley-VCH, 1998, (Chapter 5).

[26] J. Zagal, M. Paez, A.A. Tanaka, J.R. dos Santos, C.A. Linkous, J. Electroanal. Chem. 339 (1992) 13.

[27] J.H. Zagal, Coord. Chem. Rev. 119 (1992) 89.

[28] D. Thompsett, in: G. Hoogers (Ed.), Fuel Cell Technology Handbook, CRC Press, Boca Raton, Fla, 2003, (Chapter 6).

[29] J. Manassen, J. Catal. 33 (1974) 133.

[30] J. Collman, P.S. Wagenknecht, J. Hutchison, Angew. Chem. 33 (1994) 1537.

[31] H.H. Yang, R.L. McCreery, J. Electrochem. Soc. 147 (2000) 3420.

[32] C. Song, L. Zhang, J. Zhang, J. Electroanal. Chem. 587 (2006) 293.

[33] F. Beck, J. Appl. Electrochem. 7 (1977) 239.

[34] M. Bron, J. Radnik, M. Fieber-Erdmann, P. Bogdanoff, S. Fiechter, J. Electroanal. Chem. 535 (2002) 113.

[35] T. Okada, K. Katou, T. Hirose, M. Yuasa, I. Sekine, J. Electrochem. Soc. 146 (2005) 2562.

[36] R. Jasinski, Nature 201 (1964) 1212.

[37] H.G. Jahnke, M.F. Schonborn, G. Zimmerman, Top. Curr. Chem. 61 (1975) 133.

[38] N. Phougat, P. Vasudevan, N.K. Jha, D.K. Bandhopadhyay, Transition Met. Chem. 28 (2003) 838.

[39] A.B.P. Lever, C. Leznoff. Phthalocyanine compounds. WO2004CA00808 20040531[WO2004106436], (2004) 1-29. Canada. May 31 2004.

[40] A.J. Appleby, M. Savy, Proc. Symp. Electrode Mat. Process. Energ. Convers. Stor. 77 (1977) 321.

[41] C. Alexiou, A.B.P. Lever, Coord. Chem. Rev. 216-217 (2001) 45.

[42] J.P. Randin, Electrochim. Acta 19 (1974) 83.

[43] J. Ouyang, K. Shigehara, A. Yamada, F.C. Anson, J. Electroanal. Chem. 297 (1991) 489.

[44] C. Alexiou, A.B.P. Lever, Coord. Chem. Rev. 222 (2001) 273.

[45] G.I. Cárdenas-Jirón, J. Phys. Chem. A 106 (2002) 3202.

[46] M.S. Liao, T. Kar, S.M. Gorun, S. Scheiner, Inorg. Chem. 43 (2004) 7151.

[47] H.L. Chen, P.E. Ellis, T. Wijesekera, T.E. Hagan, S.E. Groh, J.E. Lyons, D.P. Ridge, J. Electrochem. Soc. 116 (1994) 1086.

[48] A.B.P. Lever, J. Porphyrins Phthalocyanines 3 (1999) 488.

[49] F.C. Anson, C. Shi, B. Steiger, Acc. Chem. Res. 30 (1997) 437.

[50] M.P. Somashekarappa, J. Keshavayya, B.S. Sherigara, Spectrochim. Acta Part A: Mol. Biomol. Spectrosc. 59 (2003) 883.

[51] C. Shi, F.C. Anson, Inorg. Chem. 29 (1990) 4298.

[52] V.S. Bagotzky, M.R. Tarasevich, K.A. Radyushkina, O.A. Levina, S.I. Andrusyova, J. Power Sources 2 (1978) 233.

[53] G. Lalande, G. Tamizhmani, R. Cote, L. Dignard-Bailey, M.L. Trudeau, R. Schulz, D. Guay, J.P. Dodelet, J. Electrochem. Soc. 142 (1995) 1162.

[54] P. Bogdanoff, I. Herrmann, M. Hilgendorff, I. Dorbandt, S. Fiechter, H. Tributsch, J. New Mater. Electrochem. Syst. 7 (2007) 85.

[55] S. Marcotte, D. Villers, N. Guillet, L. Roue, J.P. Dodelet, Electrochim. Acta 50 (2004) 179.

[56] A.L. Bouwkamp-Wijnoltz, W. Visscher, J.A.R. van Veen, Electrochim. Acta 43 (1998) 3141.

[57] S. Baranton, C. Coutanceau, E. Garnier, J.M. Leger, J. Electroanal. Chem. 590 (2006) 100.

[58] S. Baranton, C. Coutanceau, C. Roux, F. Hahn, J.M. Leger, J. Electroanal. Chem. 577 (2005) 223.

[59] G.I. Cardenas-Jiron, J.H. Zagal, J. Electroanal. Chem. 497 (2001) 55.

[60] G.I. Cardenas-Jiron, M.A. Gulppi, C.A. Caro, R. del Rio, M. Paez, J.H. Zagal, Electrochim. Acta 46 (2001) 3227.

[61] X. Ji, C.E. Banks, A. Crossley, R.G. Compton, ChemPhysChem 7 (2006) 1337.

[62] K. Oyaizu, A. Haryono, J. Natori, E. Tsuchida, J. Chem. Soc., Faraday Trans. 94 (1998) 3737.

[63] V.N. Nemykin, V.YA. Chernii, S.V. Volkov, N.I. Bundina, O.L. Kaliya, V.D. Li, E.A. Lukyanets, J. Porphyrins Phthalocyanines 3 (1999) 87.

[64] R. Battino, T.R. Rettich, T. Tominaga, J. Phys. Chem. Ref. Data 12 (1983) 163.

[65] C.R. Wilke, P. Chang, AIChE J. 1 (1955) 264.

[66] R.C. Weast (Ed.), CRC Handbook of Chemistry and Physics, 50th ed., 1969.

[67] L. Zhang, C. Song, JJ. Zhang, H. Wang, D.P. Wilkinson, J. Electrochem. Soc. 152 (2005) A2421.

[68] A.J. Bard, L. Faulkner, Electrochemical Methods: Fundamentals and Applications, John Wiley & Sons, New York, NY, 1980.

[69] J. Zhang, Y.H. Tse, W.J. Pietro, A.B.P. Lever, J. Electroanal. Chem. 406 (1996) 203.

[70] N. Kobayashi, P. Janda, A.B.P. Lever, Inorg. Chem. 31 (1992) 5172.

[71] S. Zecevic, B. Simic-Glavaski, E. Yeager, A.B.P. Lever, P.C. Minor, J. Electroanal. Chem. 196 (1985) 339.

[72] J. Zagal, P. Bindra, E. Yeager, J. Electrochem. Soc. 127 (1980) 1506.

[73] M.A. Enayetullah, T.D. DeVilbiss, J.O'M. Bockris, J. Electrochem. Soc. 136 (1989) 3369.

[74] J. Koutecky, V.G.Levich, Zh. Fiz. Khim. 32 (1958) 1565.

[75] K. Shigehara, F.C. Anson, J. Phys. Chem. 86 (1982) 2776.

[76] Z. Shi, J.J. Zhang, J. Phys. Chem. C 111 (2007) 7084.

[77] J.H. Zagal, M. Gulppi, M. Isaacs, G. Cardenas-Jiron, M.J. Aguirre, Electrochim. Acta 44 (1998) 1349.

[78] A.L. Ocampo, R.H. Castellanos, P.J. Sebastian, J. New Mat. Electrochem. Syst. 5 (2002) 163.

[79] R.N. Itoe, G.D. Wesson, E.E. Kalu, J. Electrochem. Soc. 147 (2000) 2445.

[80] A. Bettelheim, T. Kuwana, Anal. Chem. 51 (1979) 2257.

[81] P. Sabatier, Ber. Deutsch. Chem. Ges. 44 (1911) 2001.

[82] T. Kawaguchi, W. Sugimoto, Y. Murakami, Y. Takasu, Electrochem. Comm. 6 (2004) 480.

[83] C. Coutanceau, A. El Hourch, P. Crouigneau, J.M. Leger, C. Lamy, Electrochim. Acta 40 (1995) 2739.

[84] U.A. Paulus, T.J. Schmidt, H.A. Gasteiger, R.J. Behm, J. Electroanal. Chem. 495 (2001) 134.

[85] A. Bonakdarpour, M. Lefevre, R. Yang, F. Jaouen, T. Dahn, J.P. Dodelet, J.R. Dahn, Electrochem. Solid-State Lett. 11 (2008) B105.

[86] A. Elzing, A. Van Der Putten, W. Visscher, E. Barendrecht, J. Electroanal. Chem. 200 (1986) 313.

[87] C.W.B. Bezerra, L. Zhang, K. Lee, H. Liu, A.L.B. Marques, E.P. Marques, H. Wang, J.J. Zhang, Electrochim. Acta 53 (2008) 4937.

[88] A. Biloul, O. Contamin, G. Scarbeck, M. Savy, B. Palys, J. Riga, J. Verbist, J. Electroanal. Chem. 365 (1994) 239.

[89] N. Kobosev, W. Monblanova, Zh. Fiz. Khim. 7 (1936) 645.

[90] Wikipedia on-line. Activation energy. http://en.wikipedia.org . 2006.

[91] P. Sivakumar, V. Tricoli, Electrochim. Acta 51 (2006) 1235.

[92] M.H. Atwan, D.O. Northwood, E.L. Gyenge, Int. J. Hydrogen Energy 30 (2005) 1323.

[93] D. Chu, R. Jiang. Methanol tolerant catalyst material. The United States of America as represented by the Secretary of the Army. US19990429702 19991028[US6245707]. 2001. Washington, DC/US. 28-10-1999.

[94] T.R. Ralph, G.A. Hards, J.E. Keating, S.A. Campbell, D.P. Wilkinson, M. Davis, J. St-Pierre, M.C. Johnson, J. Electrochem. Soc. 144 (1997) 3845.

[95] K.R. Cooper, V. Ramani, J.M. Fenton, H. Russell Kunz, Experimental Methods and Data Analyses for Polymer Electrolyte Fuel Cells, edition 1.2, Scribner Associates, Inc., Southern Pines USA, 2005.

Appendix I

Background electrochemistry theory

Introduction

For a particular reaction, such as an electrochemical or redox reaction, an oxidized species is transformed to a reduced species via the consumption of electrons.

$$Ox^{(Z)} + ne^- \leftrightarrow Red^{(Z-n)} \quad (1)$$

Using the standard convention, the reactant is the oxidant and the product is the reductant. The Nernst equation (Eq. 2) is a relation that calculates the potential of the redox electrode as a function of the reductant and oxidant activities with the normal hydrogen electrode (NHE) as the RE

$$E_e = E^o - \frac{RT}{nF}\ln\left[\frac{\alpha_{red}}{\alpha_{ox}}\right] \quad (2)$$

where E_e is the equilibrium potential, E^o is the standard potential for the redox couple at 298°K and 1atm, R is the universal gas constant, T is the temperature, n is the number of electrons, α_{red} and α_{ox} are the activities of the reductant and oxidant, respectively. The overpotential is defined as the difference in applied and equilibrium potentials necessary to enact reactant transformation

$$\eta = E - E_e \quad (3)$$

where η is the overpotential, E is the applied potential, E_e is the equilibrium potential found from the Nernst equation. The overpotential can be positive, negative, or zero.

The observed current density is the sum of the partial cathodic and partial anodic current densities.

$$j = \vec{j}_c + \overleftarrow{j}_a \qquad (4)$$

Where j_c is the partial cathodic current density, or negative reduction current, and j_a is the partial anodic current density, or positive oxidation current. By definition, when E applied is equal to E_e, both η and j are zero. Current densities can either be expressed as current: per unit geometric area, per unit area of electroactive catalyst, per unit mass of electroactive catalyst (mass specific current density), depending on the electro-catalysts to be studied.

For many reactions, the energy of activation is substantial due to the difficulty in breaking stable, strong intramolecular bonds. For example, multi electron redox reactions are quite complex and require a significant energy input [23,30]. Multi electron redox reactions are among the most challenging of chemical transitions mediated by catalysts [23,30]. This is because even though the thermodynamic potentials for the overall multi electron process maybe favourable, the catalysis of such redox processes can still be very challenging from a kinetic point of view [30].

Multi electron redox reactions can be considered as series of single electron transfer steps. Within the overall thermodynamically favourable multi electron redox process, one or more of these individual redox potentials can be highly unfavourable. Thus, at an otherwise inert electrode, carrying out these reactions via outer sphere electron transfer processes is not feasible. This necessitates the use of catalysts [30].

"Electrocatalytic reactions may be defined as an electrochemical or kinetic or electrodic process in which the material of the electrode intervenes in determining the reaction rates" [89]. Catalysts enable processes that would be otherwise unfeasible or inefficient.

The electrode or the electrolyte can intervene catalytically. The first case is more important [23]. The overall electrocatalytic reaction comprises of one or more individual steps or mechanisms. The reaction mechanisms can be purely chemical or electrochemical. Within each reaction mechanism studied, it is the chemical properties of the combined catalyst substrate complex that is more important than each one separately [30].

Key to a catalyst's function is its' ability to either raise the energy of the substrate or lower the energy of the transition state or intermediates [30].

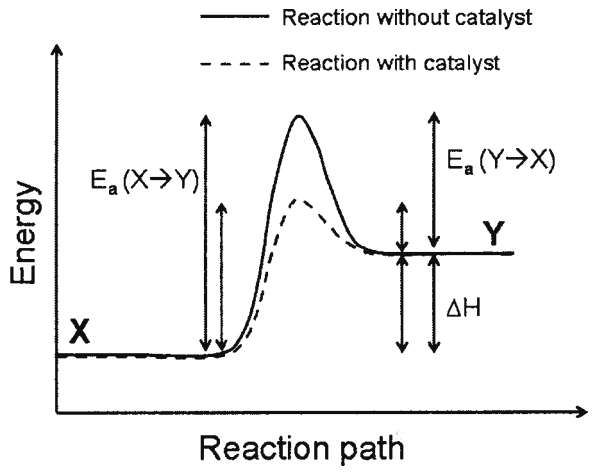

Fig. I.A. Energy of species involved in a reaction as a function of the reaction path for the catalysed and uncatalysed reaction [90].

Figure I.A shows the case for decreasing E_a by lowering the energy of the transition state. Of the many possible reaction steps or mechanisms only single electron transfer reactions are permitted, since simultaneous two electron transfers will involve a re-arrangement energy and hence an activation energy which is four times greater [23].

According to Arrhenius theory, each step will have a different rate constant and thus different reaction rates. The slowest, or rate limiting, step dictates the overall rate of the process. The rate-determining step can be either chemical (non electron transfer) or electrochemical (electron transfer) [23].

$$K_s = k_s^o \exp^{-Ea/RT} \qquad (5)$$

where k_s is the rate constant, k_s^o is the pre-exponential factor, both for the reactant species, and E_a is the reaction activation energy.

The rate determining step can involve purely chemical reactions if the electrochemical process can not adjust to alternating electrochemical steps which are more rapid in that overpotential range [23]. Rate limiting steps in the catalytic cycle include: substrate binding, proton transfer, electron transfer and product release [30].

The catalyst should also bind the reactant, but exclude inhibiting ligands. It is of key importance in choosing and characterizing a suitable electrocatalyst and electrode to avoid undesired reaction pathways or mechanisms. It is desired to have a catalyst that transforms the reactant at or near the thermodynamic potential with little or no η. Efficient reactant transformation by the catalyst in turn means electrons can be transferred at a high rate that translates to large j [30].

For an electrochemical process, an immobilized catalyst on the surface of an electrode will be referred to in this paper as the electrocatalyst. The electrocatalyst, oxidant and reductant can each be separately mobile in the gas and/or liquid electrolyte, or fixed either on, or part of, the electrode. The examples given in this paper will show fixed electrocatalysts, bound to the electrodes with the oxidant(s) and reductant(s) mobile in an aqueous electrolyte.

In summary, there are essentially two main criteria to define electrocatalyst efficiency [30]:

1. Overpotential, η. It is desirable to minimize η required to *transform the reactant*.
2. Catalyst turnover rate. It is desirable to increase/maximize the current density, *j*.

In commercial and industrial processes it is essential to minimize losses (increase efficiency) as well as increase the output per unit material and energy input. Electro-chemical industrial processes consume significant amounts of power. Thus electro-catalysts that can minimize η and/or maximize *j* reduce both the cost and the environmental impact.

For example, the ORR has a thermodynamic reduction potential of +1.229 V vs. NHE, but all known electrocatalysts reduce O_2 at more negative potentials, that is larger η. The electrocatalyst of choice for the cathodic ORR in PEM fuel cells is Pt which has an η of 600 mV for the reaction [30]. The use of prohibitively expensive Pt catalysts in PEM fuel cells is a significant factor hindering their commercialization. It follows there is a significant amount of

research for a low cost electrocatalysts that promote the ORR at the same or lower η and the same or greater j than Pt.

In order to evaluate possible electrocatalysts, η and j must be quantified in an accurate, repeatable manner that allows comparison. Given the complex, multi-step, multi-electron mechanisms that exist, more detailed parameters of the reaction kinetics are needed in addition to η and j. For these two reasons, electrochemical evaluation techniques such as Chronoamperometry, Chronopotentiometry, Voltammetry, RDE and RRDE, EIS and ECM are essential tools in electrode catalyst characterization.

A thorough summary of all electrochemical techniques and methods is beyond the scope of this paper. Those mentioned previously as they apply to the author's thesis will be considered.

Experimental

Half Cell

Measuring electrocatalytic activity is most commonly performed using a three electrode half cell. In the standard three electrode half cell, the CE, WE and RE must be separated by ion permeable materials. This is so the reaction at each respective electrode does not affect any of the others. Porous glass frits as well as Luggin capillaries are the most common ion separator in half cells.

It is also imperative that the measured current through the cell is determined solely by the behaviour at the WE. Most state of the art voltammetric equipment controls this automatically. Otherwise the CE must have a considerably larger active surface area that the WE.

Impurities

Purity is crucial in electrochemistry. Impurities have a significant effect on activity. To avoid interfering reactions from unwanted reactants, such as dissolved gasses, the electrolyte solution should be bubbled with either the desired reactant (if the reactant is a gas) or an inert gas such as Nitrogen (N_2) or Argon (Ar) for at least twenty minutes. The electrolyte must then be immediately blanketed with the same gas for the duration of the experiment(s) [91].

Energy dispersive spectroscopy (EDX or EDS) and X-ray photoelectron spectroscopy (XPS) can be used to detect and quantify impurities [91].

Electrodes

A number of different electrode materials can be used for the WE. WE's can be separated into 2 types: either unmodified (electrode material and catalyst are one in the same) or chemically modified (electrode material and catalyst are different materials). In this thesis, CMEs are used.

Normally non graphitic surfaces, such as glassy carbon, are used as electrode materials. For certain catalysts, however, non graphitic surfaces yield poor results [30]. For example, TM macrocyclic electrocatalysts supported with EPPG and BPPG electrodes give the best electrocatalytic activity, whereas those supported with glassy carbon electrodes show little activity [51]. This might be because of the interaction between the graphene sheets of the pyrolytic graphite and both the TM centre as well as similar structures of the macrocyclic ring[51]. The polishing of the pyrolytic graphite electrodes also introduces functional groups on the exposed graphite planes that could also act as anchors for the

adsorbed complexes [51]. Some of the benefits of using EPPG and/or BPPG electrodes for TM Macrocyclic catalysts include [30]:

1. Less catalyst needed
2. Electron transfer to electrode confined species is very fast
3. Inexpensive, high S.A. and strong, irreversible adsorption of macrocyle to electrode surface

Other types of CME's include CFP WE, where the electrocatalyst has been supported, spray coated as an ink onto the electrode and then heat pressed [2]. The WE must be cycled in the intended potential window thirty times in the absence of the reactant, or substrate, to be examined. This simultaneously removes or "burns off" any remaining impurities and conditions the electrode for a reproducible response. Potentials that de-activate, decompose or dissolve the electrocatalyst must be avoided [91].

Techniques

Faradaic processes are those occurring at an electrode that are governed by Faraday's law, such as charge transfer across the metal-solution interface.

Non-faradaic processes, are those for which a range of potentials is shown where no charge transfer reactions occur. These include adsorption and desorption, for example. In this case, the charge transfer reactions may be thermodynamically or kinetically unfavourable.

Of the different electrochemical techniques to be discussed in this summary, all stem from two basic methods. As electrochemical reactions are measured via their voltage and Faradaic current, one can either vary the potential as a function of time and measure the current response or vary the current as a function of time and measure the potential response. When either the voltage or the current is not varied with time, or only varied as a step function, then this is referred to as chronoamperometry (potentiostatic) and chronopotentiometry (galvanostatic), respectively.

For both chronoamperometry and chronopotentiometry experiments, the underlying assumption is the ratio of electrode area to solution volume is at a minimum. It must also be assumed that the mass transport of the electroactive species or reactant occurs only by diffusion.

Chronopotentiometry

Chronopotentiometry is a galvanostatic technique whereby a constant current is applied between the working and auxiliary electrodes using a current source. Starting at the open circuit potential (E_{oc} or OCP), the potential increases with

time until the overpotential is reached. The potential (as a function of time) between the WE and RE is measured. In this way the anodic (η_a) and cathodic (η_c) overpotentials can be determined [68,92].

In comparison with chronoamperometric techniques, a major drawback of chronopotentiometry is the double layer charging effect. They are more often larger and more prevalent throughout the experiment in such a manner that correcting for them can be difficult. Despite this, chronopotentiometry is still one of the most popular screening methods to evaluate catalyst activity [68]. The lower the operating potential, the more negative relative to other catalysts, the more desirable [92]. The most common experiment is constant current chronopotentiometry.

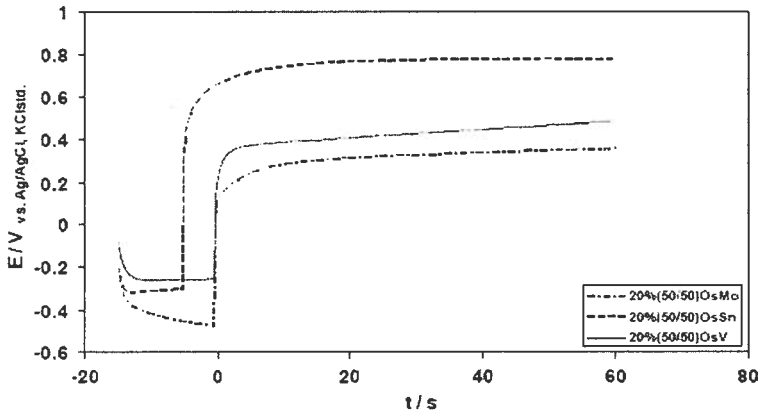

Fig. I.B. Chronopotentiometry of 0.03M BH_4^- in 2M NaOH with 1.5 × 10^{-3} M TU on colloidal 20 wt% (50/50 atomic) OsMo, OsSn and OsV, current step of 25 mA cm^{-2} at 298°K [92].

From Figure I.B it can be seen the OsMo colloidal catalyst has the lowest operating overpotential of the three for the given reaction and conditions.

Voltammetry

There are two types of voltammetry: linear sweep and cyclic. In both cases, voltammetry examines the Faradaic response to a linear change in applied potential. This is accomplished by starting from an initial potential, E_i, and linearly sweeping it at a constant rate, ν (/ V sec^{-1}), to a final target potential [68].

$$E(t) = E_i - \nu * t \qquad (6)$$

The starting potential is ideally one that the electrode catalyst and substrate are un-reactive, and the final potential is as well one which the desired reactant transformation is complete. This allows either the oxidation or reduction reaction to be examined.

In CV, after a certain time, *t*, the potential sweep reverses such that the final potential is the same or near E_i, resulting in a voltammogram that shows both oxidation and reduction reactions. The oxidation and reduction scans can be sequentially repeated as many times as desired.

The respective Faradaic maxima and minima (peak currents) on the voltammogram will occur at specific potentials called peak potentials (E_P). As well, the potential at which the Faradaic response is no longer constant and begins to monotonically increase or decrease to the respective peak potential is called the onset potential. It is the potential at which the catalyst promotes the reactant transformation. A good electrocatalyst will shift this onset potential closer to the thermodynamic equilibrium potential.

It follows that a good catalyst will show a decrease in reactant transformation overpotential η (difference between the onset potential and E_e), or an increase in current j density shown by the peak currents (at the respective peak potential), or both [30,91].

Electrode catalysts must be able to cycle between their oxidized and reduced states in a reversible manner [68]. CV's are used to test the reversibility of the electrocatalytic reaction by repeating the CV under the same conditions, varying only the scan rate, ν. Each successive scan can then be overlaid for comparison.

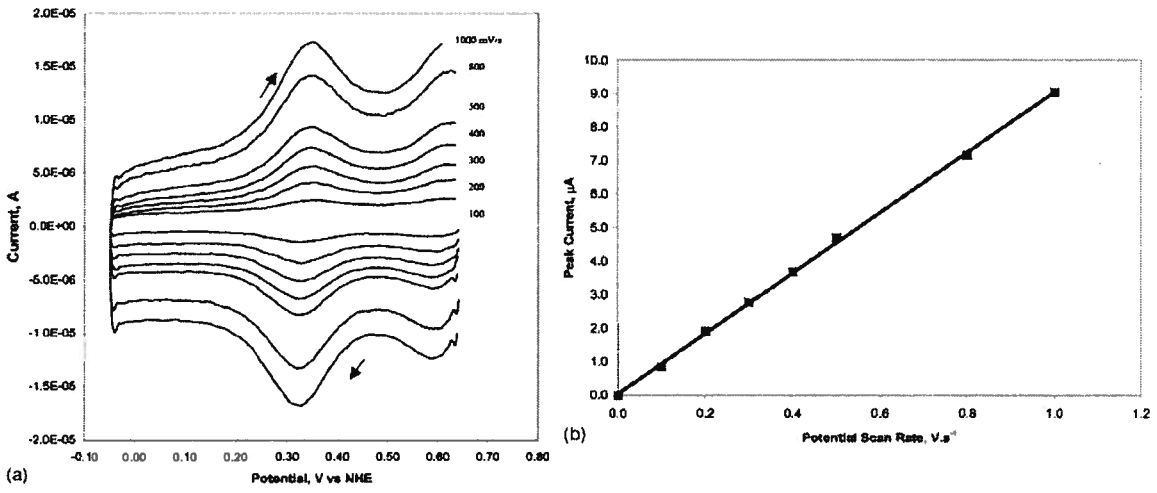

Fig. I.C. a) CV's of 5,10,15,20-tetrakis(pentafluorophenyl)-21H, 23H-porphine iron (III) or Fe^{III}TPFPP adsorbed on a graphite electrode at room temperature. Argon-purged solution containing 0.5 M H_2SO_4 as supporting electrolyte. Potential scan rates as marked beside each trace. b) Peak current as a function of the potential scan rate. Data from a) [67].

A completely reversible process will show an E_P which is independent of ν. The above two figures, similar to the work in this thesis, are for a fully reversible

surface process whereby the electrocatalyst is immobilized on the WE surface, and the reactant is dissolved in the aqueous electrolyte

If all surface waves show the current is linearly dependant on scan rate, this indicates a surface rather than diffusion controlled process [75]. This is the case for the work shown in Figure I.C. and presented in this thesis. Alternately, if the surface waves show the current is linearly dependant on the square root of the scan rate, this indicates a diffusion process.

The reversible redox peak current for a surface adsorbed species is given by [67]:

$$I_p = (n_{cat}^2 F^2 / 4RT) A v \Gamma_{cat} \qquad (7)$$

where n_{cat} represents the electron transfer number involved in the electrochemical reaction of the electrode catalyst, F is Faraday's constant, R is the universal gas constant, T is the temperature in degrees Kelvin, A is the geometric electrode area, v is the potential scan rate, and Γ_{cat} is the surface concentration of the adsorbed catalyst. The electron transfer number or the surface concentration of adsorbed catalyst can be calculated from the slope.

From the surface waves the average peak potential, E_f, can be calculated and then plotted as a function of pH. This determines the number of protons involved in the surface redox process. If the slope is zero, then the process is independent of pH. When the slope isn't zero, the surface redox process is dependant on pH and the value of the slope can be compared with the literature to obtain the number of protons and electrons involved. From this data, reaction mechanisms can be proposed [67]. Voltammograms are also used to compare

the relative activities of TM macrocyclic PEM fuel cell electrocatalysts in the patent literature [93].

Electrochemically active surface area and catalyst utilization

Cyclic voltammetry is also used to quantify the number of active sites for an electrocatalyst. The geometric area and the true surface area of an electrode can be two very different quantities. This is because the surface morphology, or three dimensional structures makes the actual surface area considerably larger than the geometric area. Similarly, the portion of an electrode catalyst's surface that actively participates in the reactant transformation must also be accurately calculated. The catalyst electrochemical active surface area (ECA, in units of cm^2 Pt g^{-1} Pt) is a well established method [94] that expresses the ECA as the ratio of the experimentally determined atomic hydrogen adsorption charge density (q in C cm^{-2}) to both the quantity for the charge to reduce a monolayer of protons on Pt (Γ = 210 μC cm^{-2}) and the Pt content or loading in the electrode (L in g Pt c^{-1} m^{-2} electrode) [94,95]:

$$ECA = q/(\Gamma L) \qquad (8)$$

For non-Pt electrode catalysts, such as TM macrocycles, calculating the equivalent ECA has been successfully performed by Anson and co-workers [51,75]. The active area of the bare electrode is obtained by electrochemical calibration with a known concentration of $K_3[Fe(CN)_6]$. The surface concentration, Γ_{cal}, of the CME in the absence of any reactants is then calculated from a plot of I_P against ν, using Eq. 7. The surface, or molecular plane, area of an individual electrocatalyst molecule is estimated from the bond lengths and

bond angles. By dividing the molecular plane area by the active surface area, a theoretical or calculated surface concentration (Γ_{cal}) is obtained. By comparing the calculated and experimental surface concentrations, the existence of a flat, monolayer adsorption can be verified. In this way, the effective surface concentration of the TM macrocycles can be obtained [67]. Not all TM Macro's adsorb as monolayers on pyrolytic graphite, so for surface concentrations greater than one monolayer, their orientation is more challenging to deduce. If the TM macrocycle electrocatalyst is supported on carbon, dispersed in a catalyst ink, a new method must be devised to obtain the ECA equivalent.

Temperature effect

The effect of temperature on the surface wave peak potential can also be examined. For example, it can be determined if the effect of temperature on formal potential of the redox couple can be described by a thermodynamic Nernst equation [67]:

$$E^f_{II} = E^\circ - (2.303RT/F)\text{pH} \qquad (9)$$

Multiple reactions

To separate the different redox process effects of the catalyst, supporting electrode and possible electroactive intermediate(s), identical CV scans are run changing only one parameter at a time. Contributions of the bare electrode in the presence of and absence of the reactant as well as any reactive intermediates are measured. This also detects for any residual impurities. The electrocatalyst is then immobilized, or adsorbed, on the electrode surface and the

aforementioned scans are repeated. The scans of the bare and adsorbed catalyst WE's are then compared.

From these CV's if the electrochemical onset potential for the adsorbed electrocatalyst in the presence of the reactant is the same as the onset potential for the same electrocatalyst's redox couple in the absence of any reactants, it suggests that the electrocatalyst catalyses the reactant transformation. If the same is true for the onset potential of the electroactive intermediate(s), it can be inferred the electrode catalyst catalyses that transformation as well [67]. The reactant and reactive intermediate concentrations must be the same for the results to be comparable.

Rotating disk electrode

Many important kinetic parameters can't be obtained using CV's. In order to accurately calculate the number of electrons involved in the overall process, as well as the substrate rate constant, another technique must be used [67].

RDE voltammetry examines the Faradaic response to a linear voltage sweep for a WE rotating at a particular rate of rotation (ω). The WE is a disk concentrically held in a chemically inert electrical insulator, such as PTFE, whereby the entire assembly functions as a rotating shaft. By rotating the WE, electrolyte at the electrode surface is being continuously replenished by convection at a constant, and measurable rate.

At the start of the potential sweep, the current response is primarily under kinetic control. The current then follows a sigmoidal shape, under mixed kinetic and mass transfer control. Eventually, the mass transfer limiting current density

is reached which appears as a plateau. This is called the peak or limiting current. The current recorded at the rotating disk (i_{disk} or i_{Tot}) thus is a function of the mass transfer or diffusion limited (i_{diff}) and kinetic (i_{kin}) currents [74]:

$$1/i_{Tot} = 1/i_{diff} + 1/i_{kin} \quad (10)$$

The procedure is then repeated, at increasing ω. As the rotation rate increases, the convection replenishes the electrode surface with fresh electrolyte and reactant(s), effectively increasing the transport of reactant to the WE or disk surface and thus increasing i_{Tot}. In each case, a new plateau at a greater limiting current density is observed. The key advantage of RDE is it separates the effects of the kinetic (i_{kin}) and mass transfer limited (i_{diff}) currents [68].

By plotting the inverse of each limiting current as a function of the inverse of the square root of the rotation rate, a straight line is obtained. This plot is compared to one generated from Koutecky Levich theory for a redox process of n electrons. If the Levich slope and experimental slope are the same, the total number of electrons for the process is known. The Koutecky Levich plot and slope can then be used to obtain a more quantitative determination of n where i_{diff} is known as the Levich diffusion current (i_{Lev}) [67]:

$$i_{Lev} = 0.201nFAC_S D_S^{2/3} \gamma^{-1/6} \omega^{1/2} \quad (11)$$

where n is the overall electron transfer co-efficient number calculated from the Levich slope, D_S is the reactant species diffusion coefficient, C_S is the reactant species concentration, γ is the kinetic viscosity of the electrolyte solution and ω is the rotation rate. From the y-intercept, i_{kin} is the kinetically limited current:

$$i_{kin} = nFAK_S C_S \Gamma_{exp} \quad (12)$$

where K_S is the rate constant of the chemical reaction which limits the plateau current and Γ_{exp} is the surface concentration of the electrode catalyst (determined experimentally). If all other parameters are known, K_S can be calculated.

E_a and K_S^o

RDE experiments can also be conducted at different temperatures to examine the effect of temperature on reactant transformation. Re-arranging equation 5 allows the expression of reaction rate as a function of temperature:

$$\ln(k_S) = \ln(k_S^o) - E_a/RT \qquad (13)$$

where k_S, A, Ea, R, T are as previously described, and k_S^o is the absolute reaction rate constant at T = ∞. A plot of $\ln(k_S)$ against $1/T$ for different temperatures (in K) yields a straight line. E_a and k_S^o are then obtained from the slope and y-intercept, respectively [67].

Rotating ring disk electrode

RRDE voltammetry has an additional electroactive ring concentric to the disk, separated by an additional chemically inert and electrically insulating material, usually PTFE. The key difference between a RDE and a RRDE lies in the ability to control the ring's potential in a manner specific for detecting electroactive reaction products from the disk as the disk potential changes [30]. The detection of electroactive intermediates using the ring is a major advantage. RRDE determines if the catalyst does or does not promote a specific electrochemical reaction, and if so, in what potential window. In this way, reaction mechanisms occuring on the disk surface can be verified.

A key distinction must be made between the electrocatalytic, and purely chemical catalytic activities [30]. If the electrocatalyst promotes the reactant transformation without the consumption of any electrons, clearly this chemical catalysis must be quantified and separated from the electrocatalytic properties being studied. For example, some TM macrocycles such as FePor and FePc can directly catalyse the disproportionation of H_2O_2 to O_3 and H_2O in addition to their ability to reduce H_2O_2 electrochemically [29,75].

By separately measuring the reaction rates of the purely chemical and electrochemical processes under the same conditions, one can determine if the chemical reaction will interfere significantly with the electrochemical process measurements. In the case of some Fe Macro species [30], the relative rates are such that the effect of the purely chemical path can be ignored.

If the purely chemical path can't be ignored, one way in which it can be quantified is has been described in the literature [75]. After performing the desired ORR RRDE experiment, the same experiment is repeated, but in the absence of O_2 with H_2O_2 as the only reactant and at the same concentration. The disk is held at a constant potential, away from the potential window for the reduction of H_2O_2, so that the only reaction is the purely chemical one. Simultaneously, the ring potential is swept in the potential window for the ORR. The ring must not be active for any chemical or electrochemical reactions with H_2O_2 for the given experimental conditions. In this way, any O_2 produced from the chemical catalysis of H_2O_2 will be detected [75,80].

Electrochemical impedance spectroscopy

In order to make effective use of the electrocatalyst and incorporate it into an operating fuel cell, it is necessary to disperse the electrocatalyst onto a support, such as carbon, mix the supported electrocatalyst with a binder and proton conductor, such as Nafion®, and on occasion a binder with hydrophobic properties, such as PTFE. The carbon support, the binders, the interfaces with the membrane electrolyte and GDL all add different electrochemical processes to the overall FC reaction. These multiple and simultaneous processes make it difficult to separate out the effect of the electrocatalyst alone. Because many of the processes of interest in a fuel cell take place over a large spectrum of time scales, the aforementioned techniques may not be the best methods to obtain reaction mechanism parameters such as mass transfer resistance, ionic conductivity, etc. EIS has been recognized as a powerful tool to investigate and diagnose these electrochemical reaction mechanisms.

There is a class of voltammetry experiments and techniques that yield the same results as EIS. A constant potential step is imposed for a finite time on top of a steady state potential. The relaxation response is then observed. During the relaxation, the different reaction mechanism parameters can be separated as a function of time.

For the work described in this thesis, EIS was chosen to diagnose the different processes occurring in the MEA. Perturbing the cell over a large, continuous range of frequencies (that covers the time scales necessary for the many different processes occurring at the WE), allows for the separation of these

processes [95]. Revealing their effect at different frequencies is the basis for electrical impedance spectroscopy (EIS).

The technique operates by imposing a small sinusoidal (AC) voltage or current signal of known amplitude and frequency, referred to as the perturbation, to the electrochemical cell. The AC amplitude and phase response of the cell is then monitored. The Ohm's law ratio of the voltage perturbation to the AC response yields the complex impedance which contains both real and imaginary parts [95].

$$Z(j\omega) = V(j\omega)/I(j\omega) \quad (14)$$

$$Z = Z' + Z'' \quad (15)$$

$$Z' = Re(Z) = |Z| \cos\theta \quad (16)$$

$$Z'' = Im(Z) = |Z| \sin\theta \quad (17)$$

Z" is plotted against Z' as the frequency is swept from approximately 20 kHz to 2 Hz. These diagrams are referred to as Nyquist plots. Typical Nyquist plots, show a Z' intercept, a discernable small arc in the high-frequency (HF) region and a well-developed semicircle in the mid-frequency (MF) region, followed sometimes by an inductive arc in the low-frequency (LF) region. The curve intercept at the HF end normally represents the solution electrolyte resistance, the HF arc could be ionic resistance within catatyst layer, the MF arc is usually associated with charge transfer process, and the LF inductive loop, if present, can be caused by oxidative removal of adsorbed intermediates. To derive useful information about the various electrochemical processes observed, it is desirable to fit a curve to the experimental data points whereby the mathematical equation

used to describe the fitted curve can yield data describing each of these different electrochemical processes[2]. Great care must be taken to ensure the theoretical fitting equation accurately represents the real electrochemical processes occuring inside the MEA.

Equivalent Circuit Model

In order to interpret and extract the properties from EIS data, the experimental impedance data can be modeled using an ECM comprised of ideal resistors, capacitors, constant phase elements and inductors in series and parallel configurations. The ECM represents conductive pathways for ion and electron transfer [95].

In the ECM, the ohmic resistance of the solution electrolyte (R_s), both the ionic ohmic resistance (R_i) and ionic capacitance (C_i) in the catalyst layer, as well as the charge transfer resistance (R_{CT}) and interfacial double layer capacitance (C_{DL}), can be represented. Intermediate adsorbate resistance (R_{ads}) due to the increase in intermediate adsorbate coverage on the reaction sites of the catalyst surface, along with inductance (L_{ads}) due to the oxidation or reduction of an adsorbed intermediate can also be represented.

The fitting of the ECM curve data to experimental data can be performed using software, such as Scribner's Z-Plot complex non-linear least squares-fitting program. The mathematical terms generated from the fitted curve can then be used to quantify the various reaction parameters previously mentioned.

ECM's should be treated with caution. As with any data fitting model, they infer the electrochemical processes and can't be taken as fact, just because the

model fits the experimental data. By definition, it can only be corroborated experimentally and via the literature as an "equivalent model". This is not unusual for any computer based semi-empirical model that correlates experimental data.

Summary

Complex, multi electron catalytic pathways can be broken down into individual steps which can be studied independently and quantified through the use of chronopotentiometry, voltammetry, RDE, RRDE and EIS with ECM to mention a few. In addition to key parameters such as η_a, η_c and j, more insightful details are obtained on the *ECA* (or equivalent), E_f, b, i_0, j_0^0, n, I_k, k_S, k^o_S, Ea, R_s, R_i, C_i, R_{CT}, C_{DL}, R_{ads}, and L_{ads}, among others.

Appendix II

Image of $FeNpPc(tBu)_4$ and $FePc(tBu)_4$ synthesis set up

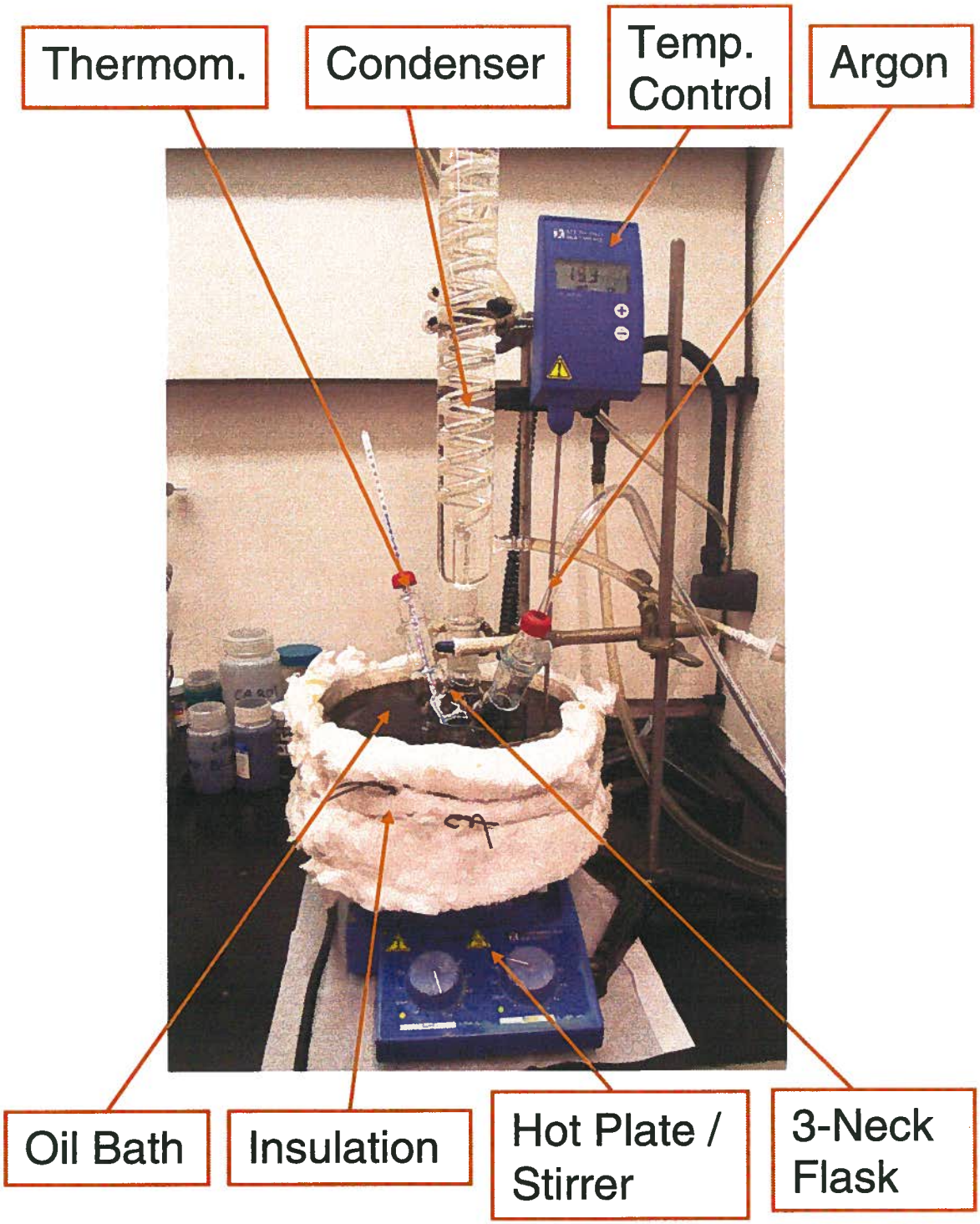

Appendix III

Image of RDE experimental set up

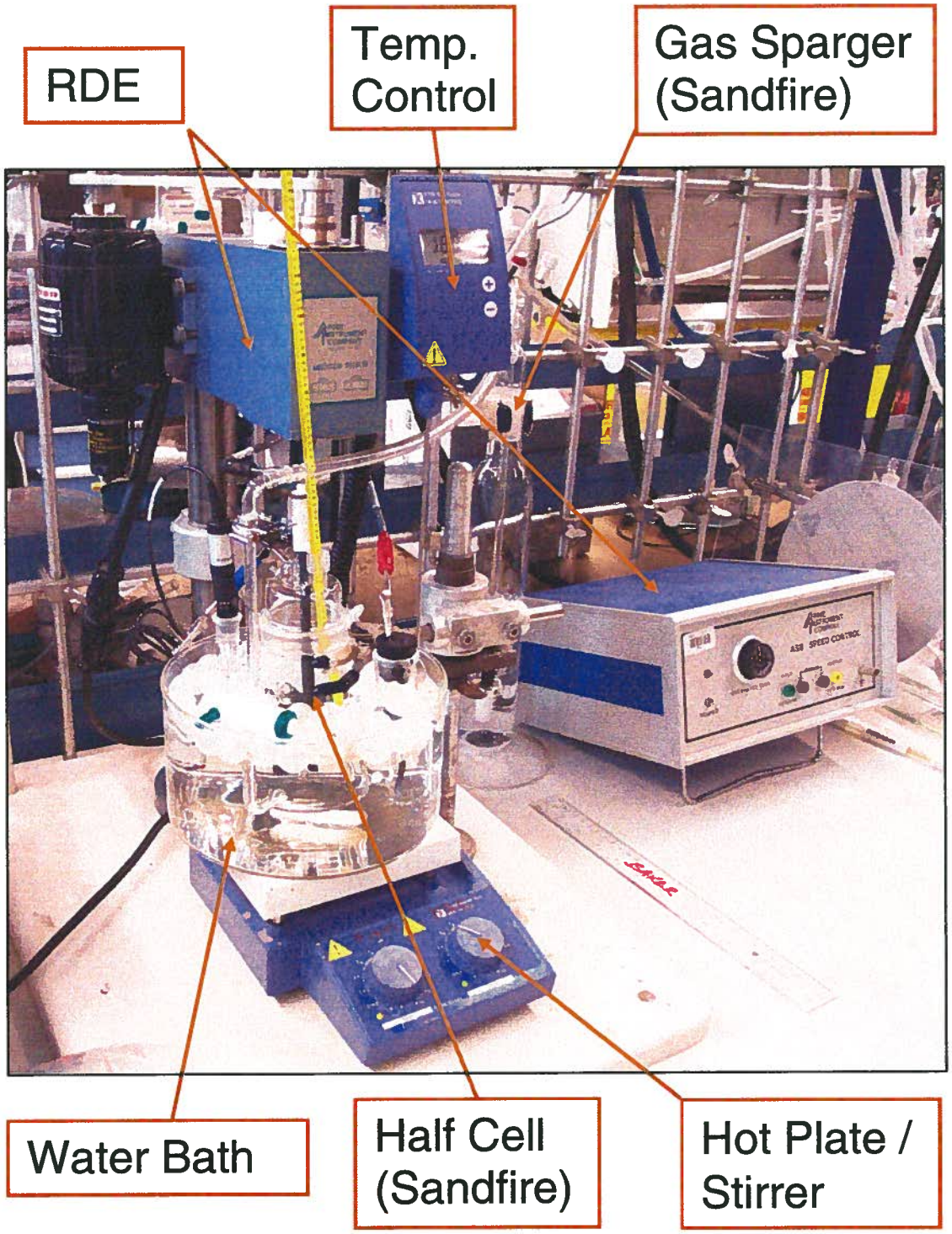

Appendix IV

Image of in house designed and built fuel cell

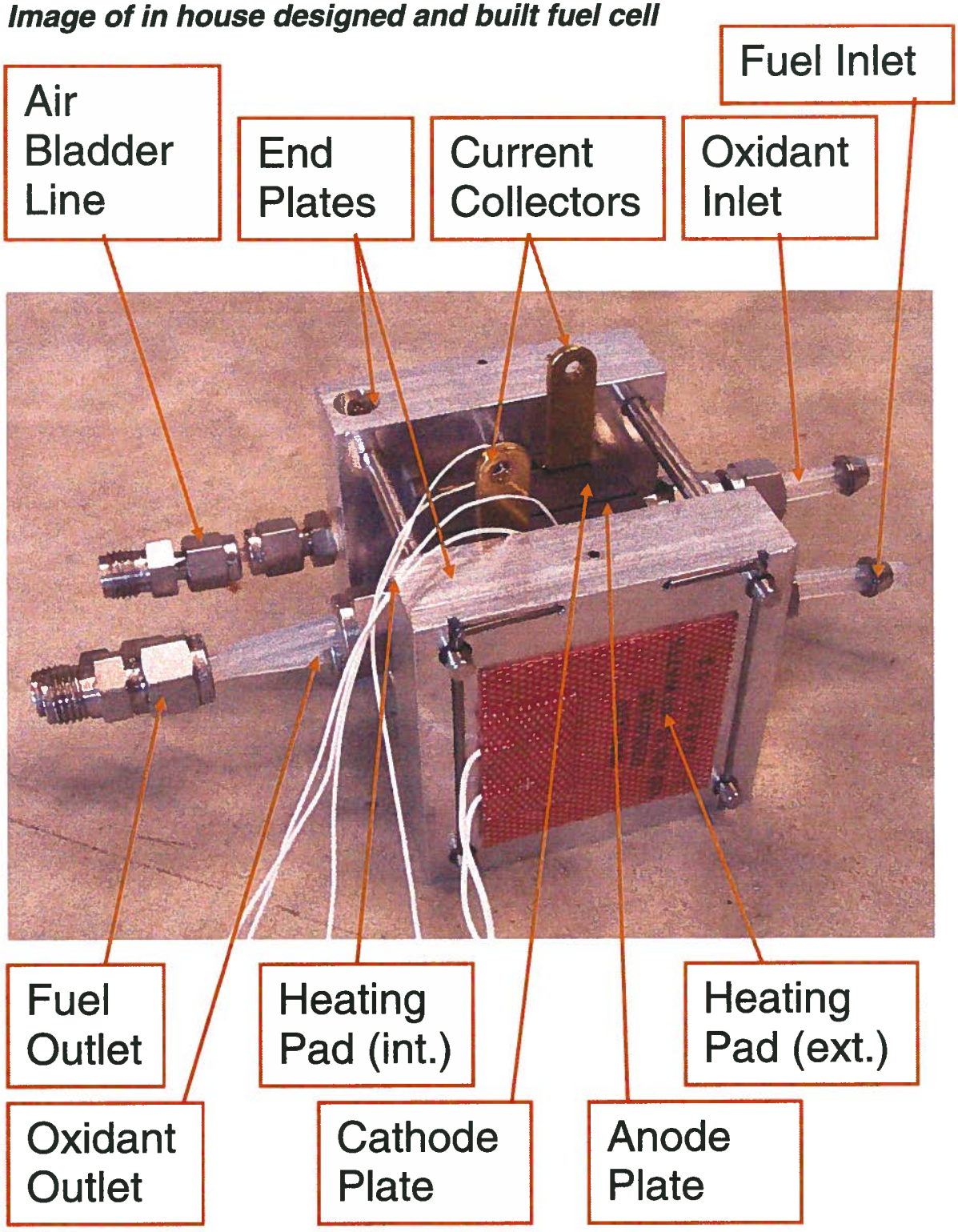

Appendix V

SCE care and checking calibration

Due to the differences between the SCE's internal electrolyte and that of the half cell, as well as due to the high temperatures and sometimes long immersion times associated with the experiments, care of, and checking the calibration of, the SCE RE was a priority.

SCE care

Before and after use, the SCE was rinsed thoroughly with DI H_2O. When not in use, the SCE was stored in a sealed Erlenmeyer flask containing only a pure solution of saturated KCl in DI H_2O.

SCE calibration check

At least three times a year, the SCE was checked against an identical SCE. This identical or "standard" SCE was purchased at the same time, never used other than for calibration checks, and was stored in a sealed pure solution of saturated KCl. Using a digital multimeter (either a Keithley 2000 multimeter, s/n: 0760583, or a Fluke 79III True RMS multimeter, s/n: 74520082) the OCV between the experimental and "standard" SCE was measured in a pure solution of saturated KCl in DI H_2O. The difference from the "standard" SCE was never more than +/- 2.5 mV over the entire period of the thesis.

Appendix VI

Converting SCE to RHE in the temperature range 20 – 80°C

As the SCE's potential is temperature dependant, all potentials were converted to the RHE scale. The conversions used in this thesis were measured experimentally and then compared to calculated values.

Experimental

Using the same set up as for CV, RDE and RRDE work (see Chapter 2), the SCE and RHE were both placed in the WE compartment of the novel half cell. The electrolyte used was 0.1 M H_2SO_4 at 1 atm. The RHE was made in-house, with a platinized Pt wire coil, and 0.1 M H_2SO_4 as the internal electrolyte (covering the Pt wire). Pure H_2 was bubbled through the RHE. At least 30 minutes of equilibration time at the desired temperature (20, 40, 60, 80°C) passed before recording data. OCV's as a function of time were then recorded at each of the four temperatures and on two separate occasions, using two different, calibrated, temperature compensated pH meters (first with a Fisher Science Accumet Basic AB15 Plus s/n: AB92323473 and second with a Denver Instruments Ultra Basic UB-10 pH mV meter, s/n: UB10015112). Both pH meters were calibrated at a pH of 4, 7, and 10 using standard buffer solutions from Fisher Scientific. A pH strip (0-14) with a resolution of 1 pH unit was used to verify both pH meters.

Results

The Nernst equation below was used to correct for the effect of temperature, first on RHE vs NHE and then on SCE vs NHE, at each of the four temperatures. Subtracting these two values gave the theoretical, calculated OCV between RHE and SCE at the desired temperature. The activity of dissolved H_2 was assumed to be unity for each calculation.

$$2H^+ + 2e^- \leftrightarrow H_2 \tag{18}$$

$$pH = -\log[H^+] \tag{19}$$

$$E = E^o - \frac{RT}{nF} \times \ln\left(\frac{a_{H_2}}{\left(10^{-pH}\right)^2}\right) \tag{20}$$

Where E° is the standard potential for the hydrogen reduction reaction at 298.15°K and 1 atm which is by definition 0.0 V, R is the universal gas constant in J mol^{-1} K^{-1}, T is the temperature in K, n is the number of electrons (2, for the oxidation of H_2), a_{H2} is the activity of hydrogen in the electrolyte (assumed to be 1), and pH is the negative log of hydronium ion concentration measured by the pH meter. The results are tabulated below for the first and second experiments, respectively. The relative error shown is for the percent difference between the calculated and experimental SCE vs RHE values.

Table VII.A. Test 1 data.

Temp / °K	Experimental Temp / °K	Experimental pH	Correction RHE vs NHE / V	Potential SCE / V	Calculated SCE vs RHE / V	Experimental SCE vs RHE / V	Relative Error / %
293.15	293.15	1.03	-0.05991	0.2471	0.3070	0.3071	0.0
313.15	312.15	1.07	-0.06627	0.2340	0.3003	0.3015	0.4
333.15	332.15	1.03	-0.06788	0.2199	0.2878	0.2965	3.0
353.15	352.15	1.06	-0.07406	0.2047	0.2788	0.2819	1.1

Table VII.B. Test 2 data.

Temp / °K	Experimental Temp / °K	Experimental pH	Correction RHE vs NHE / V	Potential SCE / V	Calculated SCE vs RHE / V	Experimental SCE vs RHE / V	Relative Error / %
293.15	294.45	1.09	-0.06368	0.2471	0.3108	0.3080	0.9
313.15	312.65	0.96	-0.05955	0.2340	0.2936	0.3039	3.5
333.15	333.35	0.91	-0.06019	0.2199	0.2801	0.2970	6.0
353.15	352.75	0.73	-0.05109	0.2047	0.2558	0.2824	10.4

The pH values for test 1 above were suspect, as they did not monotonically decrease with increasing temperature. The purpose of the second test was to obtain another set of data for comparison and to see if the Denver Instrument's temperature compensation and hence pH values were more accurate. The main difference was the larger relative error between the calculated and experimental values at higher temperatures for the second test. For test 2, the experimental drift is shown in the table immediately below, including the percent ratio of potential drift to experimental SCE vs RHE values.

Table VII.C. Test 2 potential drift as a function of time.

Experimental Temp / °K	Experimental SCE vs RHE / V		Experimental Drift / V hr^{-1}	Experimental Drift / %
294.45	0.3080		0.0000	0.00
312.65	0.3039	+/-	0.0002	0.05
333.35	0.2970	-	0.0008	0.28
352.75	0.2824	-	0.0039	1.46

Both test 1 and test 2 gave similar results. The experimental values are summarized below, along with the average values, which are used in this thesis to convert SCE to RHE at each temperature. The relative error between the two experiments is also shown.

Table VII.D. Test 1 and 2 average.

TEST 1 Experimental SCE vs RHE / V	TEST 2 Experimental SCE vs RHE / V	Relative Error / %	Average Experimental Potential / V
0.3071	0.3080	0.31	0.3076
0.3015	0.3039	0.79	0.3027
0.2965	0.2970	0.17	0.2967
0.2819	0.2824	0.18	0.2822

Appendix VII

RDE design and modification

The custom RDE was previously built for another project and then modified in-house for this thesis. The RDE was modified to improve the alignment between the disk and the shaft, to better secure the disk to the shaft, and finally minimize the ohmic drop across the disk / shaft interface. Schematics of each shaft and disk design are shown. As only the interface between the shaft and disk changed, the schematics show the just the RDE tip section.

RDE design modification

The original RDE design consisted of a spring contacting the pyrolytic graphite disk (Bulk BPPG from Union Carbide Co. via Dr. Jiujun Zhang) to the brass shaft, with a heat shrinkable polyolefin tube, or HSPT, (HSK 3100 Heat Shrinkable Tubing, Dual Wall Adhesive Lined, from Circuit Test Electronics, a division of R.P. Electronic Components Ltd.) covering the length of the RDE. However, the spring tended to put the disk off center and the HSPT tended to melt into, and interfere with, the electrical contact.

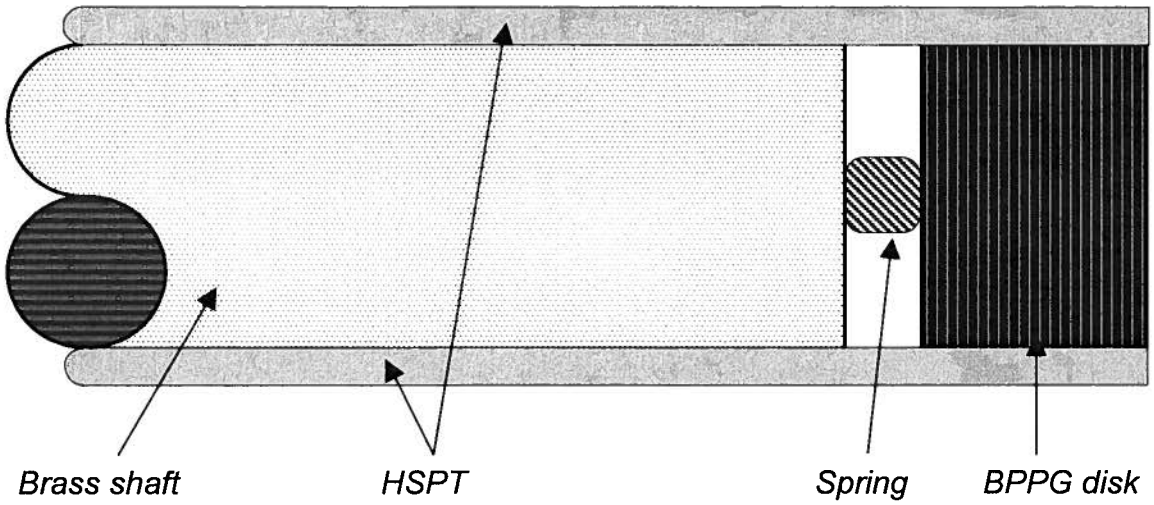

Fig. VIII.A. Cross section of original RDE tip design (not to scale).

The original RDE design was improved by removing the spring and securing the pyrolytic graphite disk flush against the brass RDE shaft tip using a high temperature electrically conductive one-part silver epoxy paste (Transene Company, http://www.transene.com/silver_epoxy.html). The silver epoxy is stable from –25°C to 200°C and has a resistance of 1×10^{-4} Ω cm^{-1}. Problems were still encountered as thermal cycling, combined with high rotation rates, tended to fracture the epoxy.

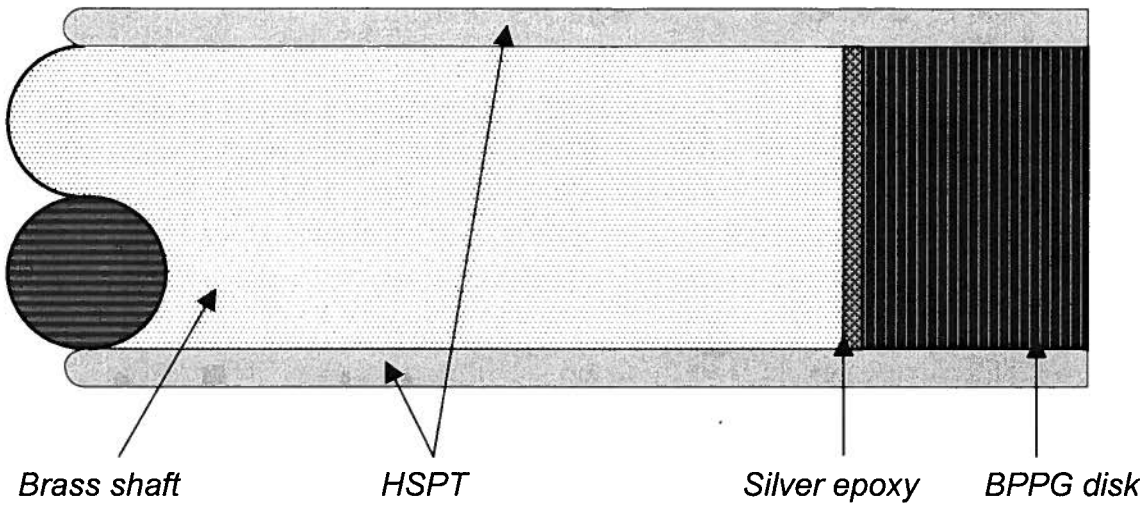

Fig. VIII.B. Cross section of first RDE tip design modification (not to scale).

The second RDE design modification incorporated a SS set screw that threaded into the centre of the brass shaft's tip, leaving a portion of the screw protruding. The entire SS set screw also had its' centre bored out. In addition, the protruding section was turned on a lathe so that the exposed threads were removed. The centre of the pyrolytic graphite disk was drilled to the same diameter and depth as the turned, protruding SS set screw. The centre of the brass shaft was drilled and tapped for the SS set screw, and had a centre bore as well as a side bore. In this way, any trapped air during assembly and epoxy curing would escape via the SS set screw and brass shaft centre bores as well as brass shaft side bore.

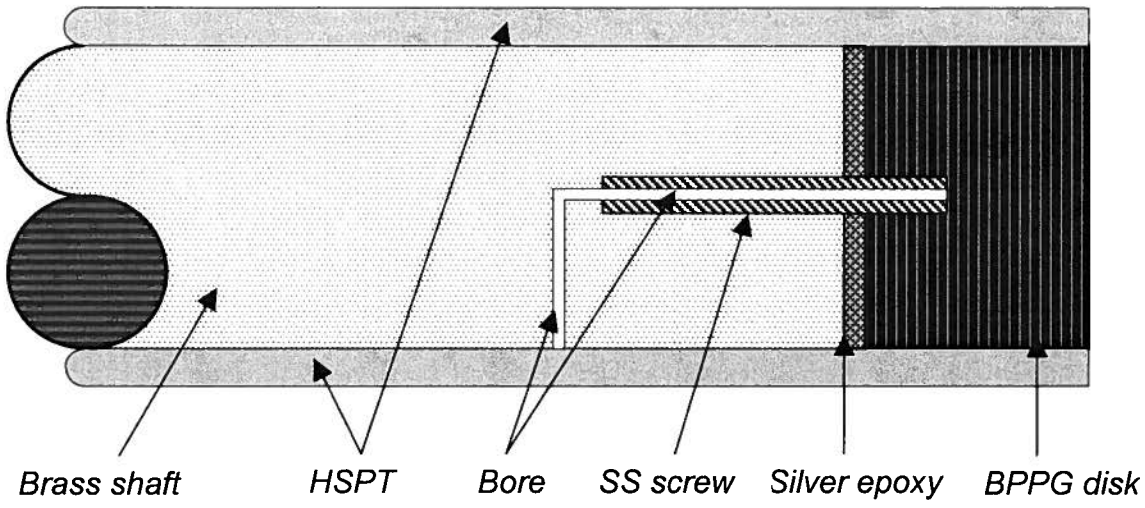

Fig. VIII.C. Cross section of second RDE tip design modification (not to scale).

RDE assembly

The brass tip was first sanded with fine grit paper. All parts (brass shaft, SS screw and pyrolytic graphite disk) were thoroughly cleaned and dried in IPA and then acetone. The SS screw was threaded into the centre of the brass shaft tip. The tip of the brass shaft was coated with a thin layer of silver epoxy and the disk was inserted. The assembled RDE was secured upside down in an Erlenmeyer flask and placed in a programmable furnace oven. The cure times and temperatures were 3 hrs at 150°C followed by 1 hr at 200°C. After the RDE cooled to room temperature inside the oven, the conductivity was checked with one of the digital multimeters described in Appendix V. The RDE brass shaft and pyrolytic graphite disk was then cleaned again before adding the HSPT. The HSPT was sealed to the entire RDE assembly using a heat gun. The excess HSPT at the disk tip was removed with a surgical blade. The disk was polished as previously described until it achieved a mirror finish. The adhesive lining on

the inner diameter of the HSPT provided a continuous, watertight seal that exposed only the disk surface. Chemical compatibility of the HSPT is further described in Appendix VIII.

Calibration check

To verify the electrical contact was sufficient, EIS was used to measure the ohmic drop between a platinized Pt CE and the RDE. The intercept at the HF end of the z' axis represents the resistance, or ohmic drop between the CE and WE leads. By using 1.0 M H_2SO_4 as the electrolyte and placing a Pt CE close to the disk of the RDE WE, the HF z' axis essentially measures only the ohmic drop across the WE. As the RDE shaft is solid brass, the only resistance will come from the pyrolytic graphite disk as well as the disk / shaft interface.

The EIS experiment used the following settings: control potential and sweep frequency, DC potential of 0.0 V vs OCV, AC amplitude of 20 mV, a frequency sweep from 10,000 Hz to 10 Hz, logarithmic and 10 steps per decade with an interval of 10. The experiment was repeated at least three times, moving the electrodes slightly each time. A HF z' axis intercept of approximately 4 Ω cm^{-2} (0.48 Ω for the 0.12 cm^2 disk) indicated the disk / shaft interface connection was good. If the values for each set of EIS experiments were either not repeatable, or were orders of magnitude larger than 4 Ω cm^{-2}, then either the disk was damaged / leaking or the contact between the disk and the shaft was poor and the RDE had to be disassembled, re-built and re-tested.

Appendix VIII

Heat shrink polyolefin tubing solvent compatibility

Work prior to this thesis using the same custom RDE has shown the HSPT to be inert in dilute aqueous acids and bases. The same work also showed HSPT was inert to ethanol, IPA and acetone as it is only has an exposure time of no more than 30 seconds. However, compatibility with other organic solvents, such as N,N-DMF, was unknown. No solvent compatibility charts were available from the manufacturer. As a quick test, three pieces of HSPT were cut and weighed on the analytical balance described in Chapter 2. The balance error is +/- 0.1 mg. They were each submerged in the same volume of N,N-DMF for 5 minutes, after which they were removed, and quickly dried.

Table VIII.A. Solvent compatibility data for HSPT in N,N-DMF.

HSPT	Initial mass / g	Final mass / g	Difference / g
1	0.2740	0.2738	-0.0002
2	0.2554	0.2550	-0.0004
3	0.2651	0.2651	0.0000

Their masses after 5 minutes exposure to N,N-DMF did not significantly increase or decrease. Both the HSPT pieces and N,N-DMF solutions were also inspected before and after the immersion test. No visible changes in any one of the three HSPT pieces or three N,N-DMF solutions were observed. It was concluded that for an exposure time of no more than 30 seconds, HSPT was compatible with N,N-DMF.

Appendix IX

Experimental determination of bare pyrolytic graphite WE active surface area

The bare pyrolytic graphite RDE WE was scanned at 25, 50, 100, 200, and 400 mV s^{-1} using CV in a 10^{-6} M solution of $K_3Fe(CN)_6$ (with 0.5 M K_2SO_4 as the supporting electrolyte) in the potential range of 0.955 to 0.110 V vs RHE at room temperature and 1 atm. The WE was held at 0.955 V vs RHE for 5 minutes before running the CV to ensure that the initial current response, positive on the reduction onset potential, was zero. The reduction current peaks were recorded as a function of scan rate. The electrochemical process measured was the Fe^{III} / Fe^{II} redox couple. The active surface area was calculated using data from the aforementioned CV's. This data is summarized below.

Table IX.A. Scan rate and peak reduction currents for 10^{-6} M $K_3Fe(CN)_6$ solution.

Scan Rate / V s^{-1}	(Scan Rate)$^{0.5}$ / $V^{0.5}$ $s^{-0.5}$	Peak Red Curr / A cm^{-2}	Peak Red Curr (μAmps)
0.000	0.000	0.000E+00	0.000
0.025	0.158	1.359E-05	13.588
0.050	0.224	1.878E-05	18.779
0.100	0.316	2.591E-05	25.912
0.200	0.447	3.552E-05	35.523
0.400	0.632	4.840E-05	48.401

A plot of peak current in μA cm^{-2} against $\upsilon^{0.5}$ gave a linear relationship through the origin, demonstrating that the electrochemical reaction at the disk surface is diffusion controlled, and that the associated reaction kinetics are rapid,

respectively. Either the slope, or each pair of associated data points can be used to solve for the active surface area. In this case, each pair of data points was used according to the Randle Sevcik relationship:

$$I_p = 2.69 \times 10^5 \times A \times n^{3/2} \times D_R^{1/2} \times C_R \times \nu^{1/2} \qquad (21)$$

where I_p is the peak (reduction) current, A is the active surface area, n is the number of electrons (1), D_R is the diffusion co-efficient of the electroactive species (6.095 x 10^{-6} cm^2 s^{-1}, determined experimentally), C_R is the concentration of the electroactive species (9.98 x 10^{-7} M), and ν is the scan rate in V s^{-1}. Solving for A, the values below were obtained.

Table IX.B. Scan rates and active surface areas for the bare pyrolytic graphite RDE disk.

Scan Rate / V s^{-1}	A / cm^2
0.025	0.12966
0.050	0.12671
0.100	0.12363
0.200	0.11985
0.400	0.11547

An average active area of 0.123 +/- 0.006 cm^{-2} was determined. This area is representative of the diffusion area of the WE surface, so an assumption is made that the diffusion area ≈ the actual disk area, and that the surface roughness of the disk is equal to unity.

Appendix X

Experimental determination of FePc species surface concentration

Peak currents and peak potentials for the anodic as well as cathodic $Fe^{III/II}$ waves for each of the five FePc species were measured at seven different scan rates (100, 200, 300, 400, 500, 750, 1000 mV s^{-1}) on the same adsorbed pyrolytic graphite WE surface. This process was repeated five times with a polished pyrolytic graphite WE and freshly adsorbed surface for each FePc species. The peak currents were measured relative to a tangent line drawn off the linear double layer charging region preceding the respective wave. This was done using CorrView's Tools/Data fitting/Line Fit function, with the "Y = m*x + B" and "Selected Data" options highlighted. Using the slope (*m*) and y-intercept (*b*) of the tangent line, its' current (*j*_line) was subtracted from the peak current (j_p), to obtain the corrected peak current (j_p_corr) which was then converted to micro amperes (j_p_corr*10^6). As an example of the one of the five fresh surfaces of one of the FePc species studies, the results and calculations for fresh surface 1, $FePcCl_{16}$ are shown. The anodic and cathodic peak potentials (V_p), from which the peak currents were measured, were averaged to verify that they were not a function of scan rate. These average values were 0.3550 +/- 0.2% and 0.3129 +/- 4% for the anodic and cathodic peak potentials, respectively.

Table X.A. Data for anodic $Fe^{II/III}$ wave, $FePcCl_{16}$ surface 1.

υ =	0.10	0.20	0.30	0.40	0.50	0.75	1.00	/ V s^{-1}
m =	1.480E-06	2.911E-06	4.082E-06	5.360E-06	6.136E-06	8.943E-06	1.354E-05	/ A cm^{-2} V^{-1}
b =	2.124E-06	4.123E-06	6.100E-06	8.070E-06	1.007E-05	1.504E-05	1.970E-05	/ A cm^{-2}
j_p =	4.211E-06	8.173E-06	1.207E-05	1.595E-05	1.986E-05	2.966E-05	3.953E-05	/ A cm^{-2}
V_p =	0.3560	0.3554	0.3555	0.3539	0.3546	0.3544	0.3554	/ V vs SCE
j_line =	2.651E-06	5.158E-06	7.550E-06	9.967E-06	1.225E-05	1.821E-05	2.451E-05	/ A cm^{-2}
j_p_corr =	1.560E-06	3.015E-06	4.520E-06	5.987E-06	7.613E-06	1.146E-05	1.502E-05	/ A cm^{-2}
j_p_corr*10^6 =	1.560	3.015	4.520	5.987	7.613	11.456	15.016	/ µA cm^{-2}

Table X.B. Data for cathodic $Fe^{III/II}$ wave, $FePcCl_{16}$ surface 1.

υ =	0.10	0.20	0.30	0.40	0.50	0.75	1.00	/ V s^{-1}
m =	-2.689E-07	-1.593E-06	-2.951E-06	-3.308E-06	-4.184E-06	-4.325E-06	-1.161E-05	/ A cm^{-2} V^{-1}
b =	-2.595E-06	-4.857E-06	-7.076E-06	-9.256E-06	-1.132E-05	-1.648E-05	-2.091E-05	/ A cm^{-2}
j_p =	-3.512E-06	-6.768E-06	-9.967E-06	-1.319E-05	-1.643E-05	-2.459E-05	-3.295E-05	/ A cm^{-2}
V_p =	0.2932	0.3038	0.3090	0.3122	0.3187	0.3246	0.3287	/ V vs SCE
j_line =	-2.674E-06	-5.341E-06	-7.988E-06	-1.029E-05	-1.266E-05	-1.788E-05	-2.473E-05	/ A cm^{-2}
j_p_corr =	8.384E-07	1.427E-06	1.979E-06	2.897E-06	3.771E-06	6.701E-06	8.227E-06	/ A cm^{-2}
j_p_corr*10^6 =	0.838	1.427	1.979	2.897	3.771	6.701	8.227	/ µA cm^{-2}

A plot of j_p against υ, shown below, is used to confirm a linear relationship through the origin. This indicates a surface controlled, and rapid, process.

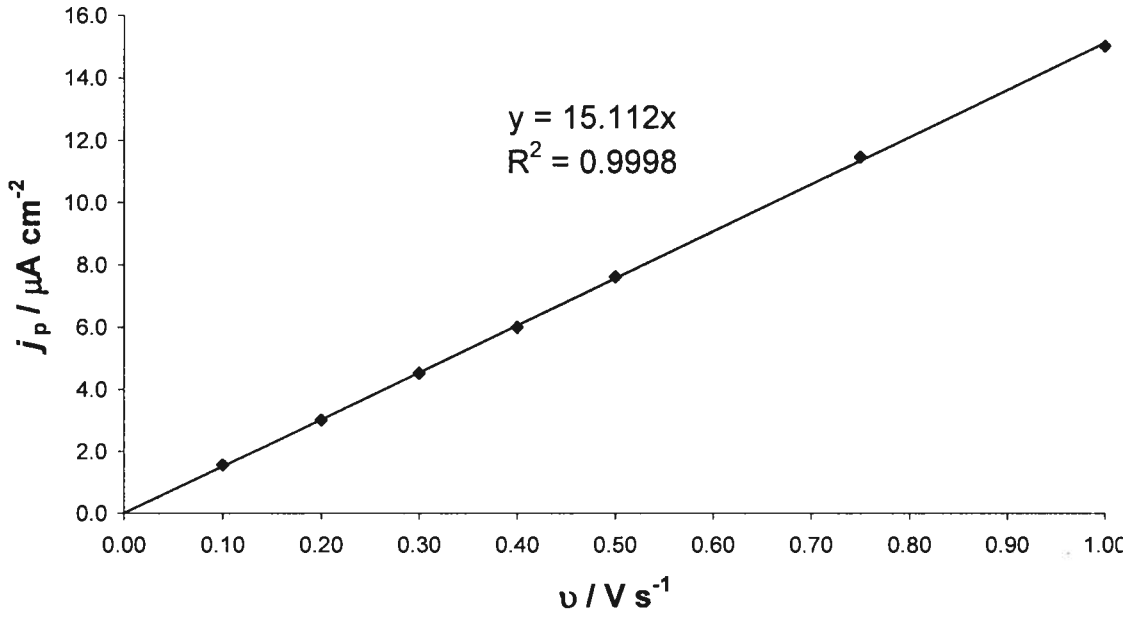

The slope from the j_p vs υ plot, and the constants shown below are used in equation (4.1), shown again below, to calculate $\Gamma_{FePcCl16}$ values at each scan rate for both the anodic and cathodic $Fe^{III/II}$ waves.

$$j_p = \frac{n_{FePc}^2 F^2}{4RT} A \upsilon \Gamma_{FePc} \qquad (22)$$

Table X.C. Constants for calculating $\Gamma_{FePcCl16}$.

$n_{FePcCl16}$ =	1
F =	96485 / C mol^{-1}
R =	8.314 / J mol^{-1} K^{-1}
T =	295.15 / °K
A =	0.12 / cm^2

Where $n_{FePcCl16}$ is the number of electrons involved in the $Fe^{III/II}$ redox couple, F, R, and T are as described before, and A is the active electrode area. The results for anodic and cathodic $\Gamma_{FePcCl16}$'s are shown below.

Table X.D. Summary of $\Gamma_{FePcCl16}$'s for all seven scan rates.

Scan Rate υ / V s^{-1}	Anodic $\Gamma_{FePcCl16}$ / mol cm^{-2}	Cathodic $\Gamma_{FePcCl16}$ / mol cm^{-2}
0.10	1.37E-10	7.37E-11
0.20	1.32E-10	6.27E-11
0.30	1.32E-10	5.80E-11
0.40	1.32E-10	6.36E-11
0.50	1.34E-10	6.63E-11
0.75	1.34E-10	7.85E-11
1.00	1.32E-10	7.23E-11

The average anodic and cathodic $\Gamma_{FePcCl16}$'s were 1.3 x 10^{-10} (+/- 1%) and 6.7 x 10^{-11} mol cm^{-2} (+/- 11%), respectively. The final step was to separately average the anodic and cathodic $\Gamma_{FePcCl16}$'s for each fresh surface as shown below.

Table X.E. Summary of anodic $\Gamma_{FePcCl16}$'s for each fresh surface.

$\Gamma_{FePcCl16}$	Anodic Wave	
1	1.333E-10	/ mol cm^{-2}
2	1.057E-10	/ mol cm^{-2}
3	1.028E-10	/ mol cm^{-2}
4	6.949E-11	/ mol cm^{-2}
5	1.170E-10	/ mol cm^{-2}
Average	1.1E-10	/ mol cm^{-2}
Std Dev	2E-11	/ mol cm^{-2}
Rel Error	22	%

Table X.F. Summary of cathodic $\Gamma_{FePcCl16}$'s for each fresh surface.

$\Gamma_{FePcCl16}$	Cathodic Wave	
1	6.689E-11	/ mol cm^{-2}
2	5.369E-11	/ mol cm^{-2}
3	5.209E-11	/ mol cm^{-2}
4	3.844E-11	/ mol cm^{-2}
5	6.134E-11	/ mol cm^{-2}
Average	5.4E-11	/ mol cm^{-2}
Std Dev	1E-11	/ mol cm^{-2}
Rel Error	20	%

Combining the two average anodic and cathodic $\Gamma_{FePcCl16}$'s gives a value of 8.0×10^{-11} mol cm^{-2} +/- 21%.

Appendix XI

Calculation of FePc species molecular plane area and monolayer coverage

Bond lengths were obtained from the CRC handbook of chemistry and physics. Bond angles (relative to the horizontal, or x-axis of the schematics shown) were measured from molecular drawings made with Chem Draw (Cambridge Software). By assuming the FePc species will occupy a square area on the disk surface, trigonometry was used to project the length of each bond, as labelled, onto one half of one horizontal length of the imaginary square. Each projected length was then summed to obtain the length of one half of one length of the square, doubled to obtain the full length, and then squared to get the calculated molecular plane area (MPA). If the FePc species was asymmetric, each half was calculated individually. The active area of the WE was then divided by the MPA to get the number of FePc species molecules on the WE surface. This number was divided by Avogadro's number (6.022×10^{23} molecules $mole^{-1}$) to obtain the calculated moles of FePc species on the WE surface, or Γ_{cal}. By dividing the Γ_{exp} by Γ_{cal} the number of monolayer equivalents was obtained. Example diagrams and calculations for all FePc species are shown below.

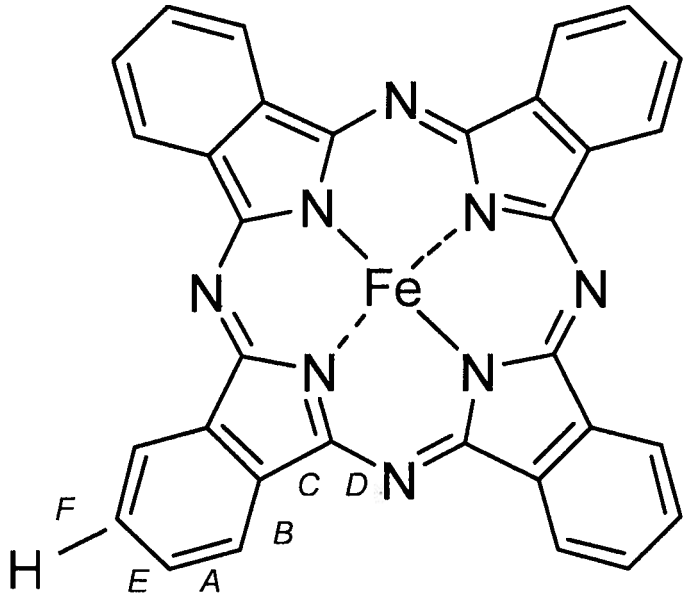

Table XI.A. Summary of FePc bond lengths and angles.

Bond	Angle / °	Bond Length / m	Projected Length / m
A	14.25	1.34E-10	1.299E-10
B	75.00	1.34E-10	3.468E-11
C	28.50	1.34E-10	1.178E-10
D	26.00	1.37E-10	1.231E-10
E	45.00	1.34E-10	9.475E-11
F	15.00	1.08E-10	1.043E-10

Table XI.B. Summary of FePc calculations.

Length of one one side	6.045E-10	/ m
Square surface area (MPA)	1.462E-18	/ m^2
Square surface area (MPA)	1.462E-14	/ cm^2
Electrode area	0.12	/ cm^2
Number of molecules on surface	8.209E+12	/ molecules
Moles of molecules on surface	1.363E-11	/ mol
Γ_{cal}	1.1E-10	/ mol cm^{-2}
Γ_{exp}	2.4E-10	/ mol cm^{-2}
Monolayer equivalents	2.1	

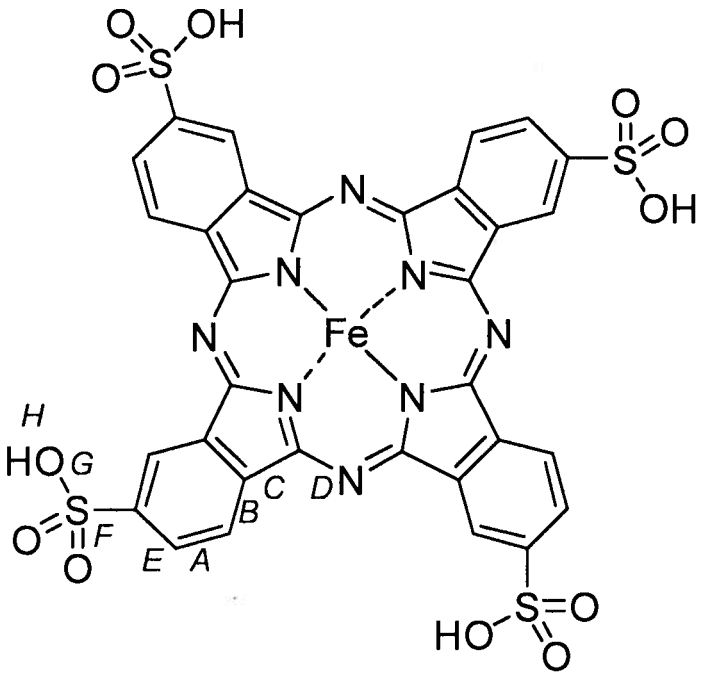

Table XI.C. Summary of $FePc(SO_3H)_4$ bond lengths and angles for one side.

Bond	Angle / °	Bond Length / m	Projected Length / m
A	14.25	1.340E-10	1.299E-10
B	75.00	1.340E-10	3.468E-11
C	28.50	1.340E-10	1.178E-10
D	26.00	1.370E-10	1.231E-10
E	45.00	1.340E-10	9.475E-11
F	14.25	1.752E-10	1.698E-10
G	64.25	1.572E-10	6.829E-11
H	7.25	9.700E-11	9.622E-11

As $FePc(SO_3H)_4$ is slightly asymmetric due to the location of the substituents, two projected length calculations were performed. The second calculation is shown below.

Table XI.D. Summary of $FePc(SO_3H)_4$ bond lengths and angles for other side.

Bond	Angle / °	Bond Length / m	Projected Length / m
A	14.25	1.340E-10	1.299E-10
B	75.00	1.340E-10	3.468E-11
C	28.50	1.340E-10	1.178E-10
D	26.00	1.370E-10	1.231E-10
E	45.00	1.340E-10	9.475E-11
F	74.25	1.752E-10	4.756E-11
G	4.25	1.572E-10	1.568E-10
H	67.25	9.700E-11	3.751E-11

Table XI.E. Summary of $FePc(SO_3H)_4$ calculations.

Length of one side	1.577E-09	/ m
Square surface area (MPA)	2.486E-18	/ m^2
Square surface area (MPA)	2.486E-14	/ cm^2
Electrode area	0.12	/ cm^2
Number of molecules on surface	4.828E+12	/ molecules
Moles of molecules on surface	8.017E-12	/ mol
Γ_{cal}	6.7E-11	/ mol cm^{-2}
Γ_{exp}	5.0E-11	/ mol cm^{-2}
Monolayer equivalents	0.8	

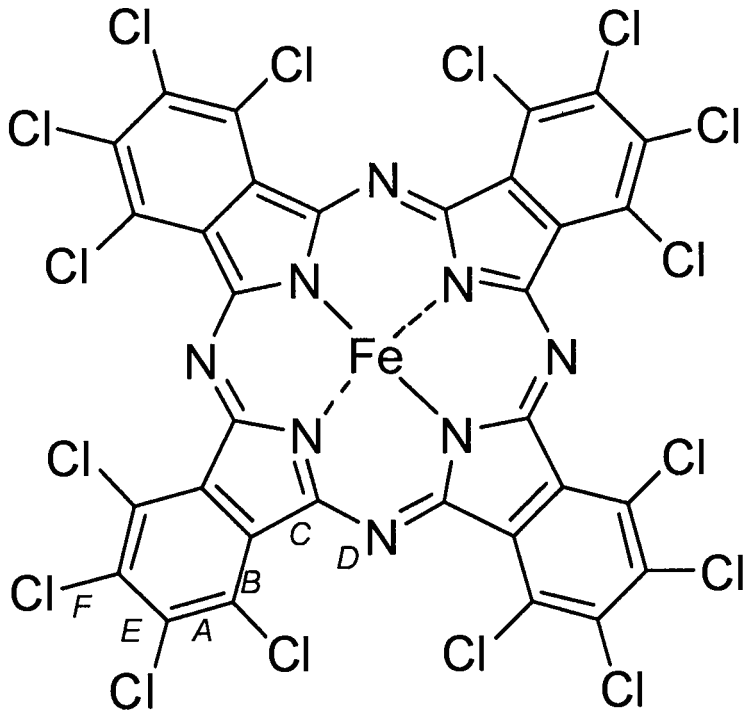

Table XI.F. Summary of $FePcCl_{16}$ bond lengths and angles.

Bond	Angle / °	Bond Length / m	Projected Length / m
A	14.25	1.340E-10	1.299E-10
B	75.00	1.340E-10	3.468E-11
C	28.50	1.340E-10	1.178E-10
D	26.00	1.370E-10	1.231E-10
E	45.00	1.340E-10	9.475E-11
F	15.00	1.739E-10	1.680E-10

Table XI.G. Summary of $FePcCl_{16}$ calculations.

Length of one one side	6.682E-10	/ m
Square surface area (MPA)	1.786E-18	/ m^2
Square surface area (MPA)	1.786E-14	/ cm^2
Electrode area	0.12	/ cm^2
Number of molecules on surface	6.719E+12	/ molecules
Moles of molecules on surface	1.116E-11	/ mol
Γ_{cal}	9.3E-11	/ mol cm^{-2}
Γ_{exp}	8.0E-11	/ mol cm^{-2}
Monolayer equivalents	0.9	

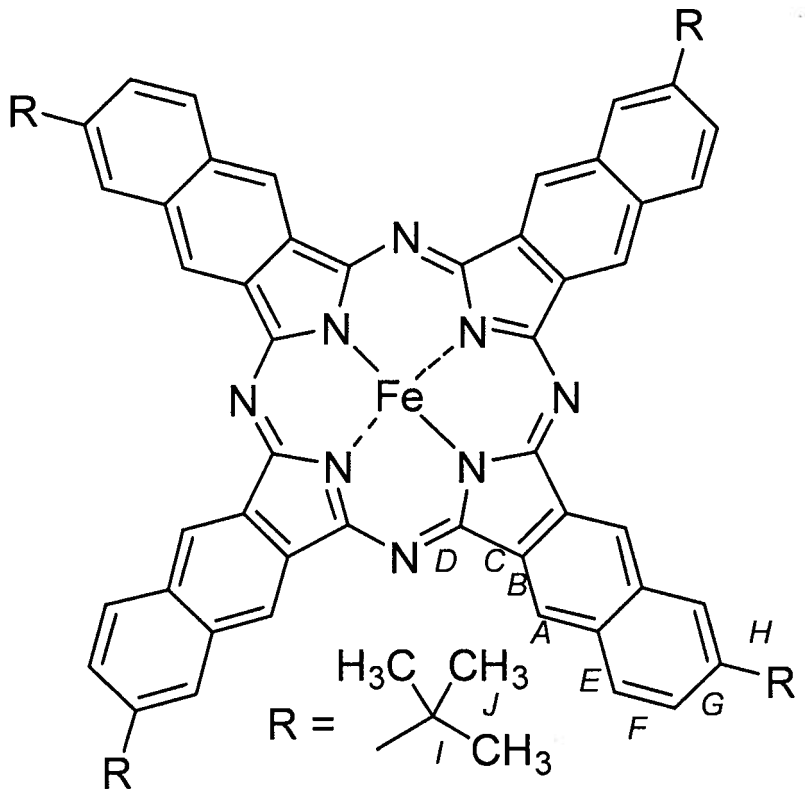

Table XI.H. Summary of FeNpPc(tBu)$_4$ bond lengths and angles for one side.

Bond	Angle / °	Bond Length / m	Projected Length / m
A	14.25	1.340E-10	1.299E-10
B	75.00	1.340E-10	3.468E-11
C	28.50	1.340E-10	1.178E-10
D	26.00	1.370E-10	1.231E-10
E	75.00	1.340E-10	3.468E-11
F	14.25	1.340E-10	1.299E-10
G	45.00	1.340E-10	9.475E-11
H	45.75	1.527E-10	1.066E-10
I	24.75	1.534E-10	1.393E-10
J	45.75	1.059E-10	7.390E-11

FeNpPc(tBu)$_4$ is also slightly asymmetric due to the location of the substituents, thus two projected length calculations were performed. The second calculation is shown below.

Table XI.I. Summary of $FeNpPc(tBu)_4$ bond lengths and angles for other side.

Bond	Angle / °	Bond Length / m	Projected Length / m
A	14.25	1.340E-10	1.299E-10
B	75.00	1.340E-10	3.468E-11
C	28.50	1.340E-10	1.178E-10
D	26.00	1.370E-10	1.231E-10
E	75.00	1.340E-10	3.468E-11
F	14.25	1.340E-10	1.299E-10
G	45.00	1.340E-10	9.475E-11
H	74.25	1.527E-10	4.145E-11
I	3.75	1.534E-10	1.531E-10
J	66.75	1.059E-10	4.180E-11

Table XI.J. Summary of $FeNpPc(tBu)_4$ calculations.

Length of one one side	1.886E-09	/ m
Square surface area (MPA)	3.556E-18	/ m^2
Square surface area (MPA)	3.556E-14	/ cm^2
Electrode area	0.12	/ cm^2
Number of molecules on surface	3.375E+12	/ molecules
Moles of molecules on surface	5.604E-12	/ mol
Γ_{cal}	4.7E-11	/ mol cm^{-2}
Γ_{exp}	1.3E-10	/ mol cm^{-2}
Monolayer equivalents	2.7	

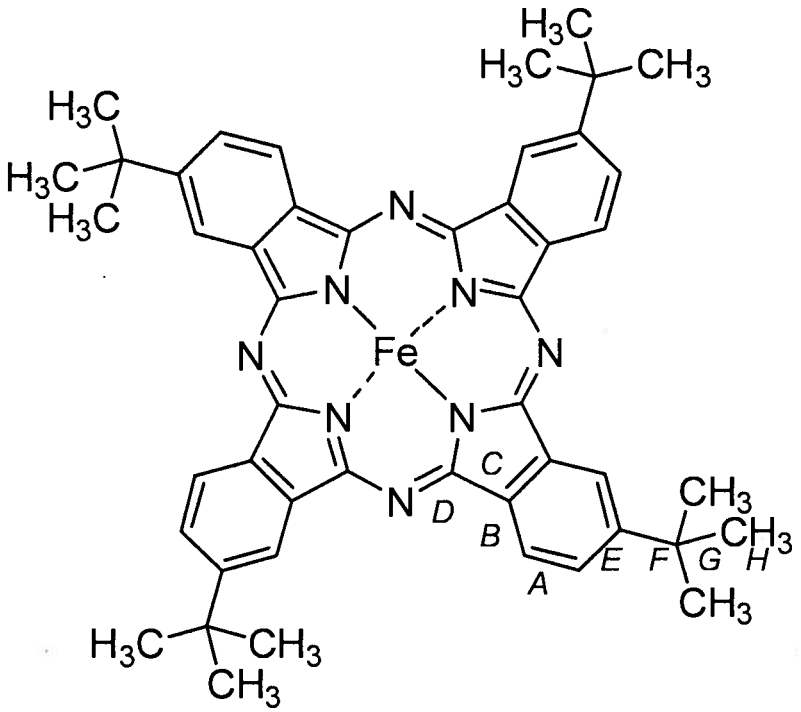

Table XI.K. Summary of $FePc(tBu)_4$ bond lengths and angles for one side.

Bond	Angle / °	Bond Length / m	Projected Length / m
A	14.25	1.340E-10	1.299E-10
B	75.00	1.340E-10	3.468E-11
C	28.50	1.340E-10	1.178E-10
D	26.00	1.370E-10	1.231E-10
E	45.00	1.340E-10	9.475E-11
F	45.75	1.527E-10	1.066E-10
G	24.75	1.534E-10	1.393E-10
H	45.75	1.059E-10	7.390E-11

In addition, $FePc(tBu)_4$ is slightly asymmetric due to the location of the substituents, thus two projected length calculations were performed. The second calculation is shown below.

Table XI.L. Summary of $FePc(tBu)_4$ bond lengths and angles for other side.

Bond	Angle / °	Bond Length / m	Projected Length / m
A	14.25	1.340E-10	1.299E-10
B	75.00	1.340E-10	3.468E-11
C	28.50	1.340E-10	1.178E-10
D	26.00	1.370E-10	1.231E-10
E	45.00	1.340E-10	9.475E-11
F	74.25	1.527E-10	4.145E-11
G	3.75	1.534E-10	1.531E-10
H	66.75	1.059E-10	4.180E-11

Table XI.M. Summary of $FePc(tBu)_4$ calculations.

Length of one one side	1.556E-09	/ m
Square surface area (MPA)	2.423E-18	/ m^2
Square surface area (MPA)	2.423E-14	/ cm^2
Electrode area	0.12	/ cm^2
Number of molecules on surface	4.953E+12	/ molecules
Moles of molecules on surface	8.225E-12	/ mol
Γ_{cal}	6.9E-11	/ mol cm^{-2}
Γ_{exp}	3.1E-10	/ mol cm^{-2}
Monolayer equivalents	4.5	

Appendix XII

Irreversible adsorption of FePc on pyrolytic graphite

Irreversible adsorption of TM macrocyclics, including FePc species, is well known from the literature. To confirm this, quick adsorption tests were performed first at 60°C for FePc and then at 80°C for the substituted FePc species.

FePc adsorption test at 60°C

CV's at room temperature of the freshly polished pyrolytic graphite RDE disk are compared to those for the freshly adsorbed baseline FePc (according to the procedures outlined in Chapters 2 and 3) after a 10 minute open circuit potential (OCP) in the 0.1 M H_2SO_4 electrolyte at 1 atm. The same FePc adsorbed WE was placed in an identical half cell with a temperature of 60°C. In comparing the FePc CV's at 20°C and 60°C, no decrease in peak currents and hence decrease in Γ, are observed.

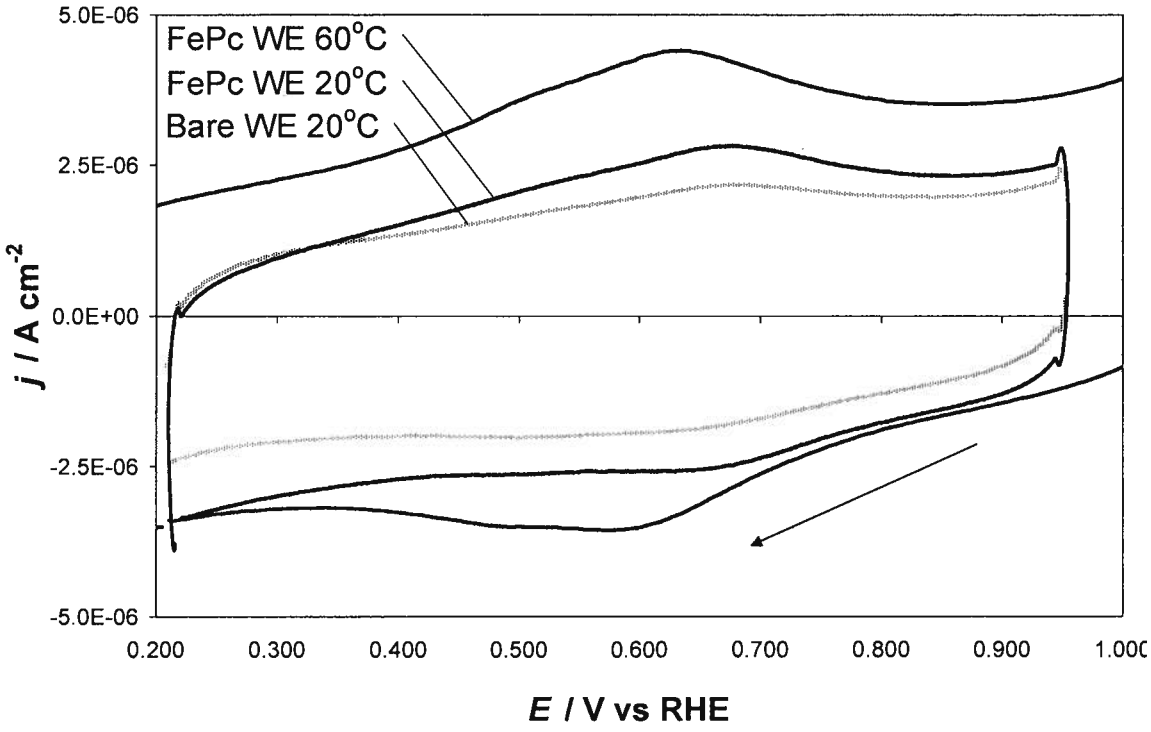

Fig. XII.A. FePc adsorption tests as marked.

Substituted FePc species adsorption tests at 80°C

In a similar fashion, tests were performed for the four substituted FePc species. Using the same experimental conditions (in the N_2 purged electrolyte), but at 80°C the procedure was modified where the CV of the bare WE was run after a 5 minute OCP. The substituted FePc species was then adsorbed and the CV immediately recorded (t = 0 min), followed by a 10 min OCP and another CV (t = 10 min), and finally a 5 minute OCP with one last CV (t = 15 min). Little change in the peak currents relative to the bare WE and to each other were observed. One observed change was the peak potentials for $FePcCl_{16}$ shifted slightly after t = 10 minutes. Another observation was the redox peak ca. 0.2 V vs RHE for $FePc(tBu)_4$ diminished slightly after t = 10 minutes.

Appendix XIII

FePc species catalyzed ORR kinetic rate constants and energies of activation

k_{O2} values

It is important to note k_{O2} values obtained from Koutecky Levich plots are inherently inaccurate. As a general rule, a difference of at least one order of magnitude must be seen to be considered significant. Even so, k_{O2} values and any calculations derived there from should be seen as qualitative and not quantitative results. The k_{O2} values reported in Chapter 3 are displayed below showing the differences between the values at 20°C and 80°C ("80-20" row) and between the substituted FePc species and the baseline FePc ("Difference k_{O2}" column). This way the relative effects of temperature, substitution, and both, on ORR kinetics can be seen.

The effect of temperature on kinetics in decreasing order is $FePc(SO_3H)_4$ >> $FePcCl_{16} \approx FeNpPc(tBu)_4 > FePc \approx FePc(tBu)_4$. The effect of substitution is more interesting, where relative to FePc, the difference in k_{O2} values shows an increase of two orders of magnitude for $FePc(SO_3H)_4$, one order of magnitude for $FePcCl_{16}$, little change, or slight decrease for $FeNpPc(tBu)_4$, and a decrease for $FePc(tBu)_4$. Thus electron withdrawing substituents increase, and electron donating substituents slightly decrease, the kinetics for the FePc species catalyzed ORR, respectively.

Table XIII.A. Summary of temperature and substituent effects on k_{O2} values for the FePc species catalyzed ORR.

Temp	FePc	$FePc(SO_3H)_4$	Difference	$FePcCl_{16}$	Difference	$FeNpPc(tBu)_4$	Difference	$FePc(tBu)_4$	Difference
	k_{O2}	k_{O2}	k_{O2}	k_{O2}	k_{O2}	k_{O2}	k_{O2}	k_{O2}	k_{O2}
/ °C	/ $cm^3\ mol^{-1}\ s^{-1}$	/ $cm^3\ mol^{-1}\ s^{-1}$	/ $cm^3\ mol^{-1}\ s^{-1}$	/ $cm^3\ mol^{-1}\ s^{-1}$	/ $cm^3\ mol^{-1}\ s^{-1}$	/ $cm^3\ mol^{-1}\ s^{-1}$	/ $cm^3\ mol^{-1}\ s^{-1}$	/ $cm^3\ mol^{-1}\ s^{-1}$	/ $cm^3\ mol^{-1}\ s^{-1}$
20	1.06E+08	9.72E+08	8.66E+08	1.86E+09	1.76E+09	5.78E+07	-4.84E+07	8.00E+07	-2.61E+07
40	1.70E+08	8.90E+08	7.20E+08	2.47E+09	2.30E+09	1.31E+08	-3.92E+07	1.07E+08	-6.37E+07
60	2.54E+08	2.18E+09	1.93E+09	1.93E+09	1.68E+09	3.12E+08	5.87E+07	1.61E+08	-9.26E+07
80	3.24E+08	5.29E+10	5.26E+10	2.76E+09	2.43E+09	8.91E+08	5.67E+08	1.86E+08	-1.38E+08
80-20	2.18E+08	5.19E+10	5.17E+10	8.93E+08	6.76E+08	8.33E+08	6.15E+08	1.06E+08	-1.12E+08

E_a calculations and results

The experimental k_{O2} values can then be used in an Arrhenius plot according to the equation:

$$\ln k_{O_2} = \ln k^{o}_{O_2} - \frac{E_a}{RT} \tag{23}$$

where k_{O2} is as described previously, k_{O2}^{o} is the kinetic reaction rate at infinite temperature in $cm^3\ mol^{-1}\ s^{-1}$, E_a is the energy of activation for the reaction in J mol^{-1}, R and T are as described previously. A plot of $\ln k_{O2}$ against T^{-1} yields a straight line of slope $-E_a / R$, and a y-intercept of $\ln k_{O2}^{o}$ from which E_a and k_{O2}^{o} can be calculated. The error inherent in the k_{O2} values obtained will be carried into the E_a and k_{O2}^{o} values as well. These values for all five substituted FePc species are shown below. Values for which there was no plateau current data are marked "n/a".

Table XIII.B. Summary of E_a and k_{O2}^{o} values for the FePc catalyzed ORR.

Phthalocyanine	E / V vs RHE	E_a / kJ mol^{-1}	k_{O2}^{o} / cm^3 mol^{-1} S^{-1}
FePc	0.015	5	9.39E+08
	0.165	9	4.87E+09
	0.315	15	4.32E+10
$FePc(SO_3)_4$	0.015	51	6.34E+17
	0.165	54	1.73E+18
	0.315	n/a	n/a
$FePcCl_{16}$	0.015	n/a	n/a
	0.165	4	9.74E+06
	0.315	26	1.77E+10
$FeNpPc(tBu)_4$	0.015	32	5.20E+13
	0.165	39	4.37E+14
	0.315	39	2.55E+14
$FePc(tBu)_4$	0.015	1	2.75E+08
	0.165	12	1.31E+10
	0.315	13	1.59E+10

The E_a values are strongly potential dependant for FePc, $FePcCl_{16}$ and $FePc(tBu)_4$ likely due to secondary redox processes occurring at these potentials. The E_a values presented are not accurate, do not show a discernable trend as a function of temperature, and do not compare well with the accepted E_a value for the Pt catalyzed ORR in acid electrolyte of approximately 52 kJ mol^{-1}. To obtain better data, either the procedure has to be modified or another technique used.

Appendix XIV

Qualitative RDE evaluation of FePc species ORR stability at 80°C

As discussed in Chapter 3, each RDE trace required a fresh surface. When the same adsorbed FePc surface was used for more than one ORR RDE trace, an increase in overpotential and decrease in current density was obvious. An example is shown below for the baseline FePc to be compared with Fig. 3.7.

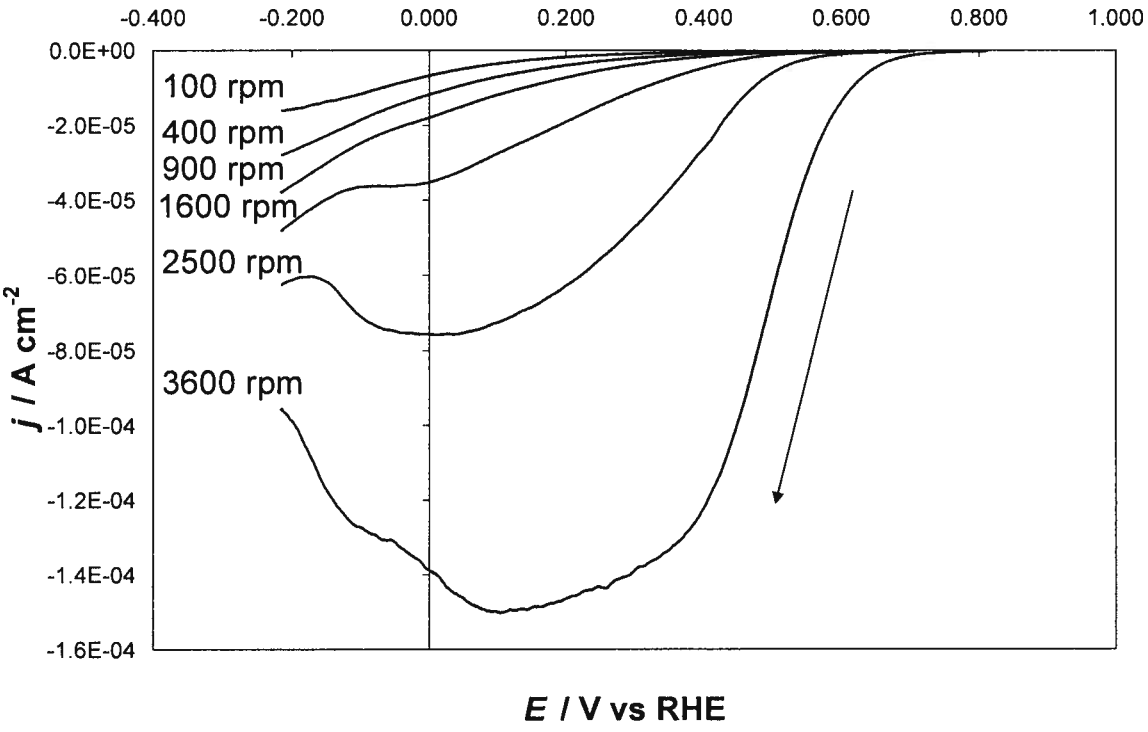

Fig. XIV.A. Plot of current-potential curves for the same FePc adsorbed surface on a rotating pyrolytic graphite disk electrode in decreasing order at different rates of rotation as marked on each trace (starting at 3600 rpm), recorded in a 0.1M H_2SO_4 air-saturated solution at 80°C and 1 atm.

As part of the experimental procedure for the ORR RDE traces using fresh surfaces for each rate of rotation, six pairs of reduction and oxidation scans were recorded for the same FePc species surface at 100, 900 and 3600 rpm to qualitatively observe relative rates of decomposition. The first and sixth reduction (black triangle) and oxidation (black triangle) scans at a rotation rate of 900 rpm are shown below for each FePc species adsorbed on a pyrolytic graphite disk in a 0.1 M H_2SO_4 air saturated electrolyte at 80°C and 1 atm. A dotted line indicates the decrease in current density at 0.165 V vs RHE between the reduction and oxidation traces of the first scan (black dots) as well as between the reduction traces of the first and sixth sequential scans (open arrows).

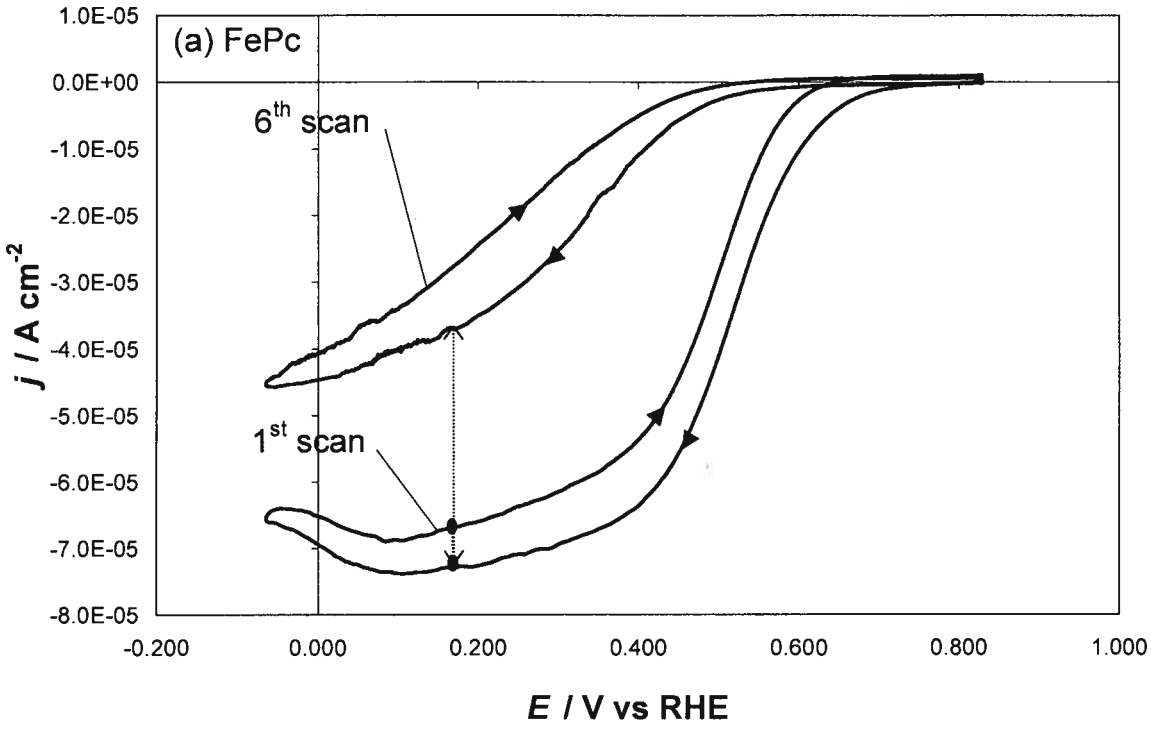

Fig. XIV.B. Plot of first and sixth current-potential curves for the same (a) FePc, (b) $FePc(SO_3H)_4$, (c) $FePcCl_{16}$, (d) $FeNpPc(tBu)_4$ and (e) $FePc(tBu)_4$ adsorbed surface on a rotating pyrolytic graphite disk electrode at 900 rpm, recorded in a 0.1M H_2SO_4 air-saturated solution at 80°C and 1 atm. Dotted line at 0.165 V vs RHE indicates the difference between reduction and oxidation trace for the first scan (black dots) as well as the difference between the reduction traces of the first and sixth scans (open arrows).

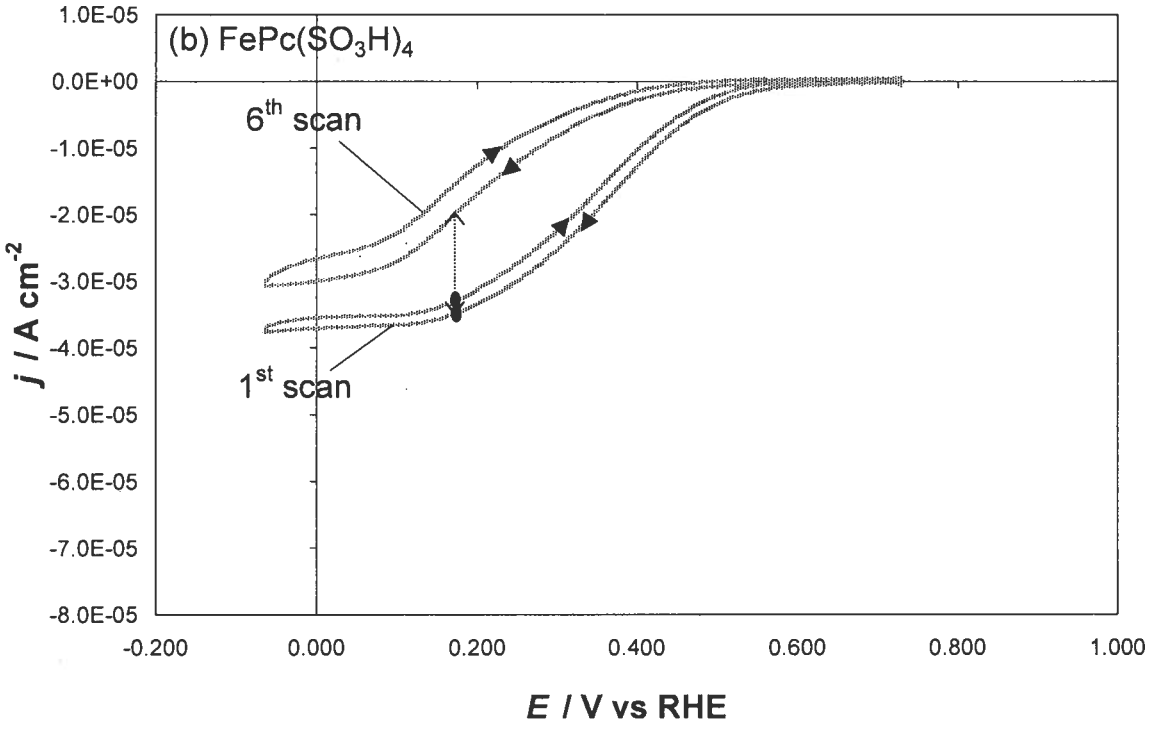
(b) FePc(SO3H)4
6th scan
1st scan
1.0E-05
0.0E+00
-1.0E-05
-2.0E-05
-3.0E-05
-4.0E-05
-5.0E-05
-6.0E-05
-7.0E-05
-8.0E-05
-0.200
0.000
0.200
0.400
0.600
0.800
1.000
j / A cm-2
E / V vs RHE

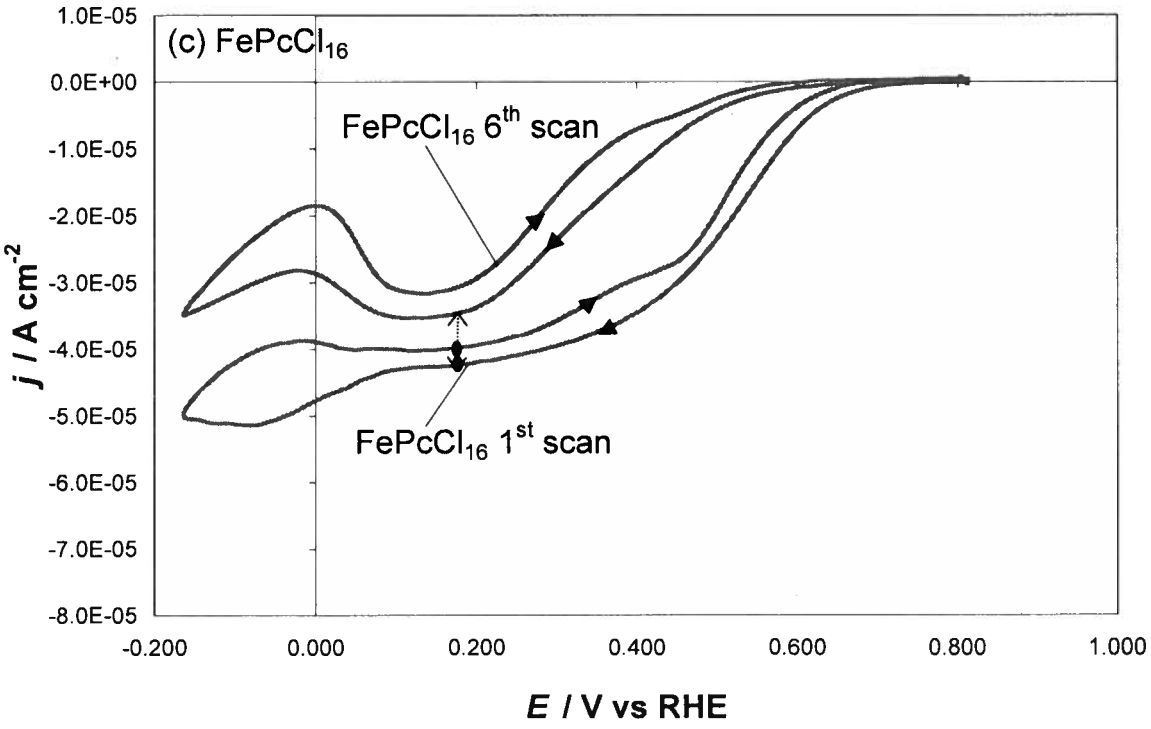
(c) FePcCl16
FePcCl16 6th scan
FePcCl16 1st scan
1.0E-05
0.0E+00
-1.0E-05
-2.0E-05
-3.0E-05
-4.0E-05
-5.0E-05
-6.0E-05
-7.0E-05
-8.0E-05
-0.200
0.000
0.200
0.400
0.600
0.800
1.000
j / A cm-2
E / V vs RHE

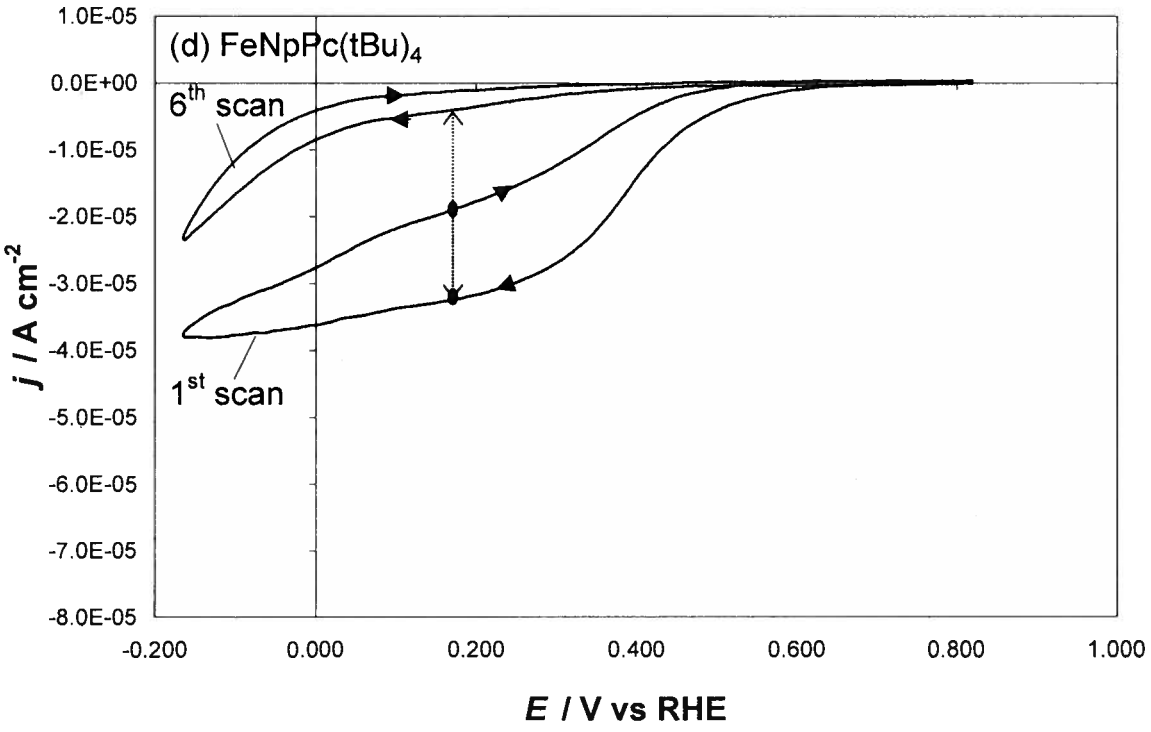
(d) FeNpPc(tBu)4
6th scan
1st scan
1.0E-05
0.0E+00
-1.0E-05
-2.0E-05
-3.0E-05
-4.0E-05
-5.0E-05
-6.0E-05
-7.0E-05
-8.0E-05
-0.200
0.000
0.200
0.400
0.600
0.800
1.000
j / A cm-2
E / V vs RHE

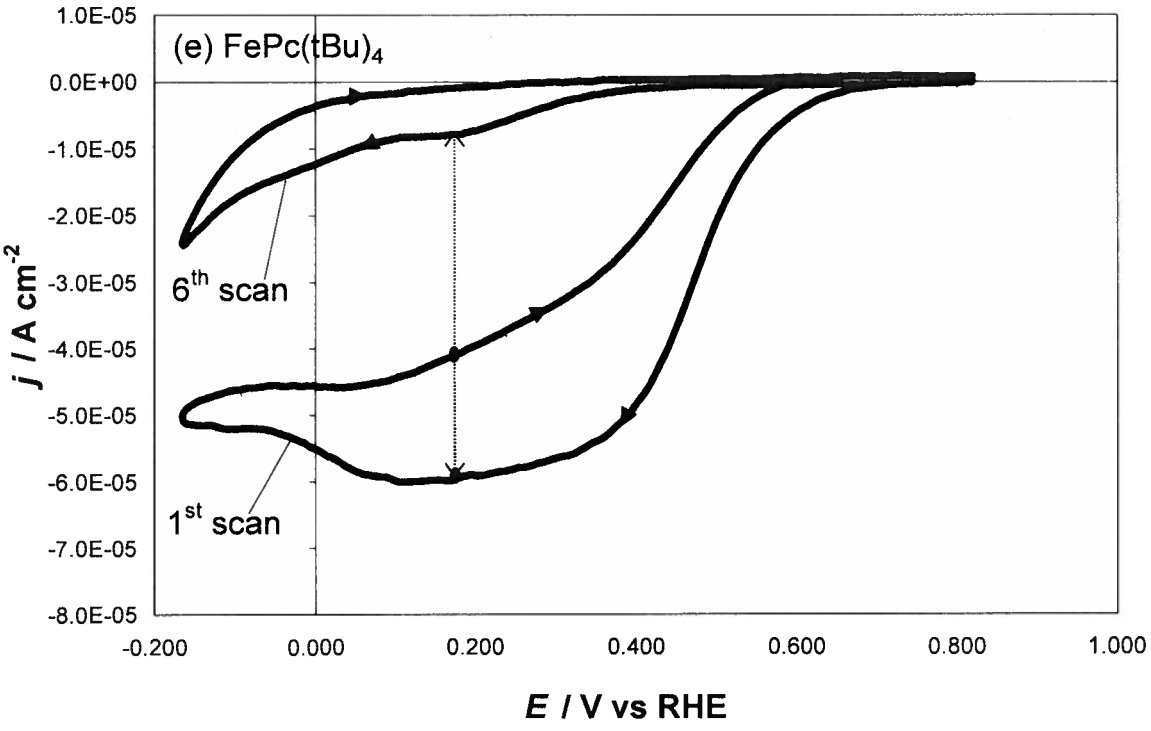
(e) FePc(tBu)4
6th scan
1st scan
1.0E-05
0.0E+00
-1.0E-05
-2.0E-05
-3.0E-05
-4.0E-05
-5.0E-05
-6.0E-05
-7.0E-05
-8.0E-05
-0.200
0.000
0.200
0.400
0.600
0.800
1.000
j / A cm-2
E / V vs RHE

It should be noted that the cathodic vertex potential for $FePcCl_{16}$, $FeNpPc(tBu)_4$ and $FePc(tBu)_4$ was much more negative than those for FePc and $FePc(SO_3H)_4$. As a result the former experience greater decomposing or deactivating conditions than the latter. The deactivation, or loss in current density in comparing the current densities of the oxidation or return scan to that of the reduction scan of the first scan of each FePc species is shown below.

Table XIV.A. Comparison of current densities at 0.165 V vs RHE for the first scan.

	j Red 1st / A cm^{-2}	j Ox 1st / A cm^{-2}	j_O / j_R
FePc	-7.29E-05	-6.70E-05	0.92
$FePc(SO_3H)_4$	-3.52E-05	-3.34E-05	0.95
$FePc(Cl)_{16}$	-4.25E-05	-3.99E-05	0.94
$FeNpPc(tBu)_4$	-3.26E-05	-1.92E-05	0.59
$FePc(tBu)_4$	-5.98E-05	-4.15E-05	0.69

The FePc species with electron withdrawing substituents showed slightly improved stability over the unsubstituted FePc, and greater stability than those with electron donating substituents. Another approach was to compare the reduction currents of the first and sixth scans, as shown below.

Table XIV.B. Comparison of current densities at 0.165 V vs RHE for first and sixth scans.

	j Red 1st / A cm^{-2}	j Red 6th / A cm^{-2}	j_6 / j_1
FePc	-7.29E-05	-3.68E-05	0.50
$FePc(SO_3H)_4$	-3.52E-05	-2.08E-05	0.59
$FePc(Cl)_{16}$	-4.25E-05	-3.49E-05	0.82
$FeNpPc(tBu)_4$	-3.26E-05	-4.06E-06	0.12
$FePc(tBu)_4$	-5.98E-05	-7.96E-06	0.13

Here the substituent effect was clear. Electron withdrawing substituents showed an obvious increase in stability, while electron donating substituents showed an obvious decrease in stability, respectively, towards the ORR. This trend was seen for all FePc species studied at all temperatures. In decreasing order the most stable FePc species were:

$$FePcCl_{16} >> FePc(SO_3H)_4 > FePc >> FePc(tBu)_4 \approx FeNpPc(tBu)_4$$

Appendix XV

Supplementary MEA fuel cell results

Fuel cell testing at room temperature

On two occasions, initial conditioning was performed at room temperature to see if changing the conditioning temperature could minimize problems with unstable performance. Even though the gas humidifier was left to cool overnight from 81°C, it never cooled to room temperature, and thus the gas humidifier and in turn fuel and oxidant streams were always near 26°C. The fuel cell was always at 21°C, so the RH for both the anode and cathode streams under these conditions was approximately 140%. Voltage versus time plots for room temperature conditioning tests are shown in Figures XV.A and XV.B.

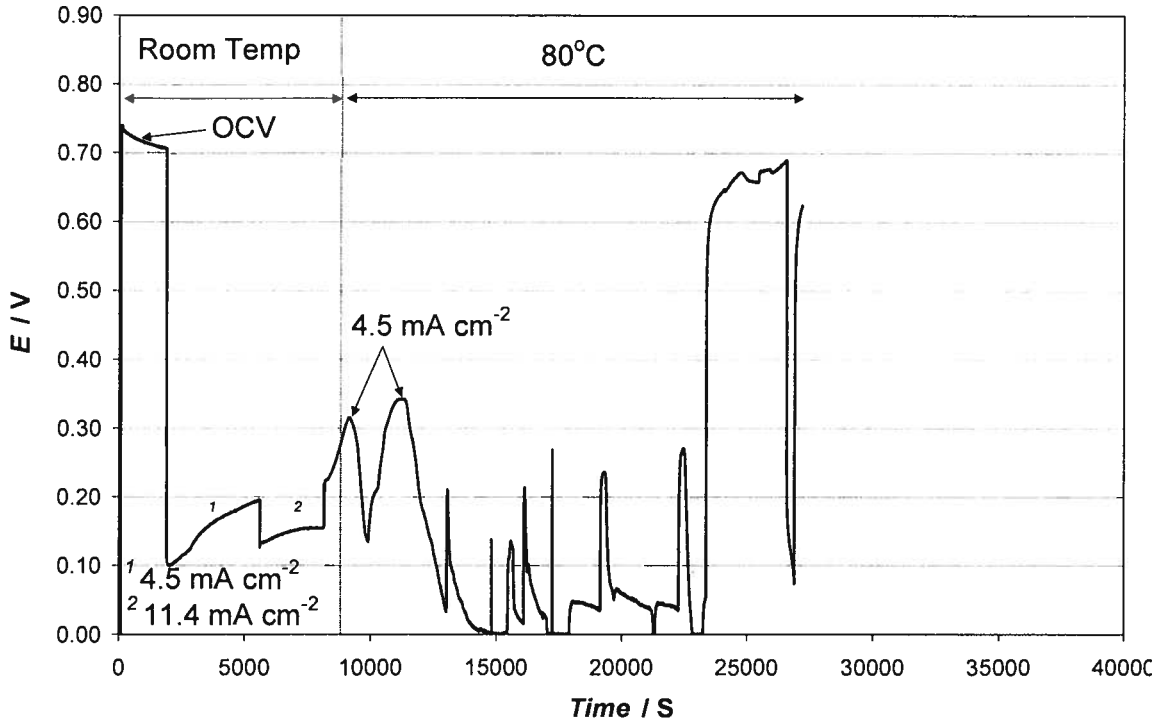

Fig. XV.A. Voltage versus time plot for the FePc catalyst ink cathode MEA fuel cell tests under galvanostatic control (first MEA testing method) at currents as marked. Data for FePc MEA #1, Mar 28 2008, operating at 20°C +/- 1°C as indicated with a hydrogen flow rate of 30 mL min^{-1} and an oxygen flow rate of 90 mL min^{-1}.

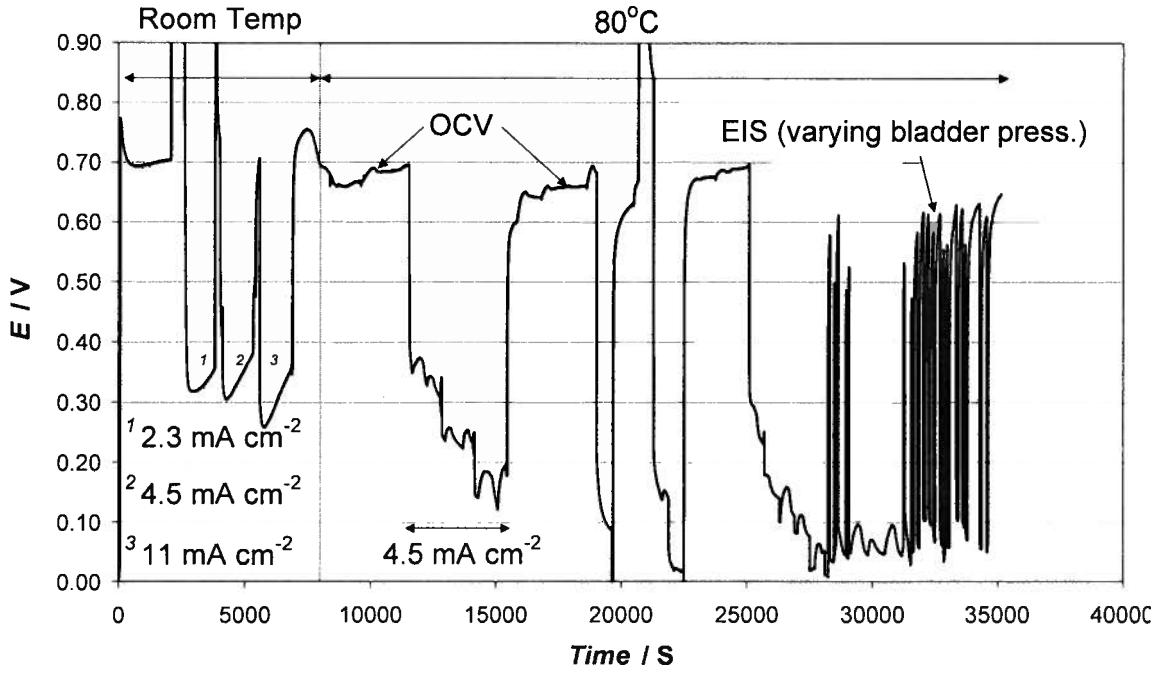

Fig. XV.B. Voltage versus time plot for the FePc catalyst ink cathode MEA fuel cell tests under galvanostatic control (first MEA testing method) at currents as marked. Data for FePc MEA #2, April 2 2008, operating at 20°C +/- 1°C as indicated with a hydrogen flow rate of 30 mL min^{-1} and an oxygen flow rate of 90 mL min^{-1}.

Voltages for the as marked constant currents were quite high, and monotonically increasing. These results were promising. However, time, equipment and material constraints reduced the number of tests performed at room temperature. With the limited number of MEA's available coupled with the risk of deactivation, it was decided to resume testing at an operating temperature of 81°C. Future MEA testing with an optimized cathode catalyst layer would include operation at room temperature.

Fuel cell testing challenges and solutions

The main issue with the fuel cell tests shown here was that the longer the cell was operated over a time scale of 30 to 60 minutes, the more seldom it reached steady state. This meant that all data had to be collected as rapidly as possible while still being considered at steady state. While operating at 81°C unstable voltages occurred frequently under galvanostatic control. This unstable performance occurred in three main modes (falling to zero, rising and bumping) that are shown in Figures XV.C, XV.D, and XV.E.

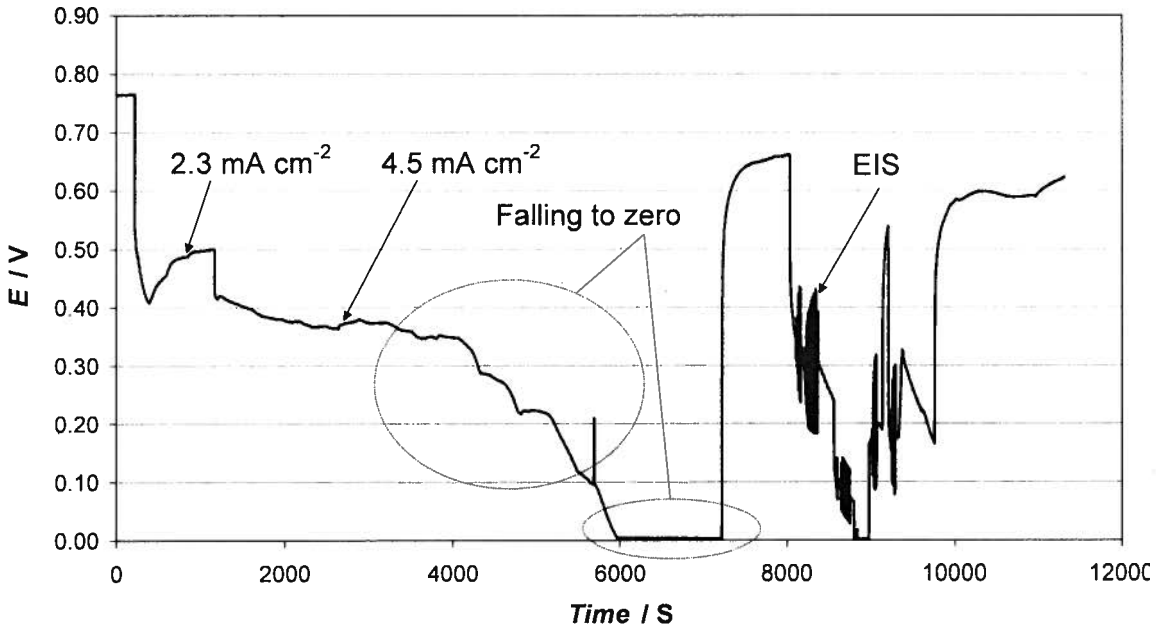

Fig. XV.C. Typical voltage versus time plot for the FePc catalyst ink cathode MEA fuel cell tests under galvanostatic control (first MEA testing method) showing a monotonically decreasing current to 0 V (falling to zero). Data from FePc MEA #1, March 21 2008, operating at 65°C with a hydrogen flow rate of 200 mL min^{-1} and an air flow rate of 500 mL min^{-1}.

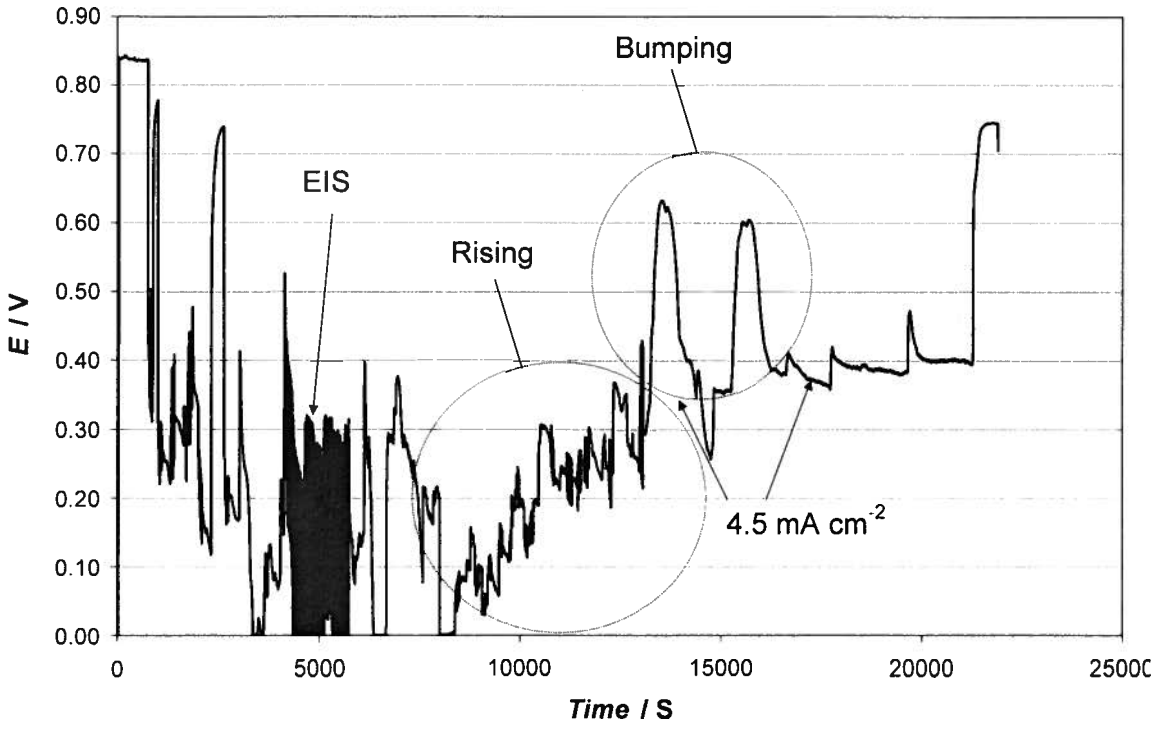

Fig. XV.D. Typical voltage versus time plot for the $FePcCl_{16}$ catalyst ink cathode MEA fuel cell tests under galvanostatic control (first MEA testing method) showing a monotonically increasing current (Rising) and oscillating current (Bumping). Data from $FePcCl_{16}$ MEA #3, March 22 2008, operating at 78°C with a hydrogen flow rate of 200 mL min^{-1} and an air flow rate of 500 mL min^{-1}.

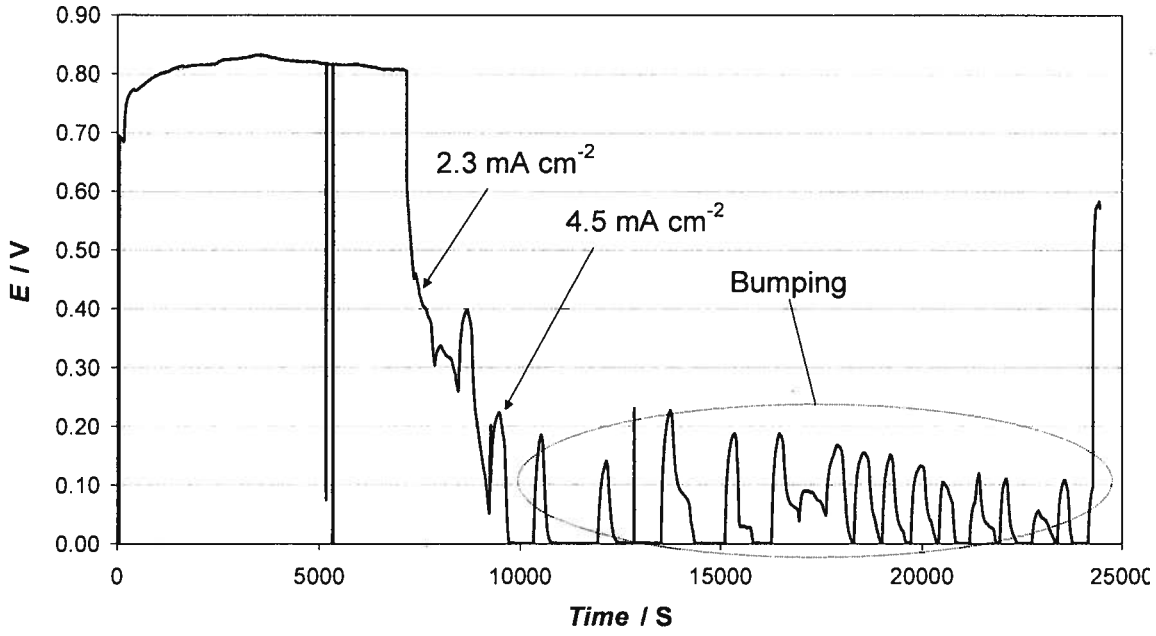

Fig. XV.E. Typical voltage versus time plot for the FePc catalyst ink cathode MEA fuel cell tests under galvanostatic control (first MEA testing method) showing an oscillating current from 0 V (Bumping). Data from FePc MEA #2, April 1 2008, operating at 81°C with a hydrogen flow rate of 30 mL min^{-1} and an oxygen flow rate of 90 mL min^{-1}.

Several attempts were made to minimize these bumping, rising, or falling to zero effects, but they were never completely eliminated. As a possible solution, several attempts were made to vary the bladder pressure and look at the effect on MEA resistance using EIS. This was to minimize any flooding as well as maximize electronic and possibly protonic conductivity. The results were inconclusive as the changes in cathode layer resistance due to the aforementioned three trends made extracting any information regarding an optimal bladder pressure impossible.

It follows the EIS and ECM techniques described in Chapter 1 and used in a related work [2] were inconclusive when applied to the FePc cathode MEA's. As the FePc cathode catalyst layers were not yet optimised, the MEA's rarely achieved steady state performance as a result. As the processes within the FePc cathode catalyst MEA were constantly changing during the EIS scan, the impedance data obtained at this stage was not usable. Again, FePc species catalyst layer optimization is beyond the scope of this thesis and could be the subject of future work.

Summary of FePc species MEA testing conditions

Finding optimal MEA testing conditions, and then performing MEA tests, all before significant cathode catalyst degradation occurs was a delicate balancing act. To better understand the different testing conditions, which MEA's were used, and under what operating conditions and times, detailed summaries for each MEA are shown in Tables XV.A and XV.B.

Table XV.A. Summary of operating conditions including experiment dates, run times, open circuit voltages (OCV's), anode and cathode flow rates, oxidant type, cathode relative humidity (RH) and MEA testing method used (FRA ldbnk = first method, or PSTAT = second method) for all FePc MEA's. Anode and cathode backpressure was 30 psig, and temperatures were equal. Anode RH was 100% unless marked otherwise.

MEA #	Date	Time	OCV		Flow Rate		Oxidant	Cathode RH	Pwr Srce
			Initial	Final	Anode	Cathode			
	/ MMM-DD	/ Hrs	/ V vs RHE	/ V vs RHE	/ L m^{-1}	/ L m^{-1}		/ % RH	
1	[a] Mar-21	3.14	0.77	0.63	0.20	0.50	Air	100	FRA ldbnk
	TOTAL	3.14	Air						
	Mar-26	7.41	0.67	0.64	0.03	0.09	O_2	100	FRA ldbnk
	Mar-26	1.80	0.66	0.63	0.03	0.09	O_2	100	FRA ldbnk
	Mar-27	10.73	0.75	0.63	0.03	0.09	O_2	60	FRA ldbnk
	[b] Mar-28	7.56	0.72	0.69	0.03	0.09	O_2	n/a	FRA ldbnk
	Mar-30	1.14	0.70	0.63	0.03	0.09	O_2	55	FRA ldbnk
	[c] Apri-06	1.14	0.68	0.66	0.03	0.09	O_2	100	PSTAT
	TOTAL	29.77	O_2						
	SUM	32.91	10 % Air 90 % O_2						
2	Apr-01	6.79	0.82	0.70	0.03	0.09	O_2	55	FRA ldbnk
	[d] Apr-02	9.76	0.70	0.65	0.03	0.09	O_2	n/a	PSTAT
	Apr-03	2.01	0.72	0.62	0.03	0.09	O_2	55	PSTAT
	[e] Apr-04	4.72	0.70	0.70	0.03	0.09	O_2	55	PSTAT
	TOTAL	23.28	O_2						
3	[f] Apr-06	1.12	0.79	0.75	0.03	0.09	O_2	100	PSTAT
	TOTAL	1.12	O_2						

[a] Operating at 65°C

[b] Started operation at 21°C 140% RH, then 81°C 55% RH followed by 100% RH cathode

[c] Good performance data

[d] Started operation at 21°C 140% RH, then 81°C 55% RH followed by 100% RH cathode

[e] Increased cathode RH from 55% to 100%

[f] Best performance data, but cathode outlet showed rust / black condensate afterwards

Table XV.B. Summary of operating conditions including experiment dates, run times, open circuit voltages (OCV's), anode and cathode flow rates, oxidant type, cathode relative humidity (RH) and MEA testing method used (FRA Idbnk = first method, or PSTAT = second method) for all $FePcCl_{16}$ MEA's. Anode and cathode backpressures were both 30 psig, and temperatures were equal. Anode RH was 100%.

MEA #	Date / MMM-DD	Time / Hrs	OCV Initial / V vs RHE	OCV Final / V vs RHE	Flow Rate Anode / L m^{-1}	Flow Rate Cathode / L m^{-1}	Oxidant	Cathode RH / % RH	Pwr Srce
1	[a] Apr-05	3.69	0.87	0.80	0.03	0.09	O_2	n/a	PSTAT
	TOTAL	3.69 O_2							
2	Apr-03	3.97	0.87	0.74	0.03	0.09	O_2	55	PSTAT
	[b] Apr-04	2.21	0.74	0.61	0.03	0.09	O_2	55	PSTAT
	[c] Apr-05	1.14	0.75	0.69	0.03	0.09	O_2	100	PSTAT
	[c] Apr-06	0.63	0.72	0.69	0.03	0.09	O_2	55	PSTAT
	TOTAL	7.95 O_2							
3	Mar-22	6.08	0.84	0.75	0.20	0.50	Air	100	FRA Idbnk
	Mar-23	5.17	0.75	0.75	0.02	0.30	Air	100	FRA Idbnk
	[d] Mar-25	5.59	0.76	0.67	0.02	0.30	Air	100	FRA Idbnk
	TOTAL	16.84 Air							
	[e] Mar 31	6.90	0.67	0.71	0.03	0.09	O_2	55	FRA Idbnk
	[e] Apr-06	1.56	0.72	0.70	0.03	0.09	O_2	100	PSTAT
	TOTAL	8.46 O_2							
	SUM	25.31	67 % Air 33 % O_2						

[a] Cathode delaminated before testing, during testing cathode RH was 55% then 100%

[b] Cathode delaminated during testing

[c] Some performance data

[d] Best performance data, but cathode outlet showed rust / black condensate afterwards

[e] Good performance data

Appendix XVI

Publication and co-authorship statement

Some of the chapters presented in this thesis are versions of manuscripts either published, in press, or submitted. As such, a full list of co-authors for each manuscript is listed below.

1. A version of Chapter 2 was submitted for publication in *Electrochimica Acta*. That manuscript was co-authored by David P. Wilkinson, and Jiujun Zhang.
2. Chapter 3 was originally based on an oral presentation at the 58th Annual Meeting of the International Society of Electrochemistry (ISE) in Banff, Alberta (September 2007). A version of Chapter 3 has been published in *Electrochimica Acta* (R. Baker, D.P. Wilkinson, J. Zhang, Electrochim. Acta 53 (2008) 6906-6919) [1].
3. Chapter 4 was based on an extended abstract, which was accepted for an oral presentation at the 214th meeting of the Electrochemical Society (ECS), PRiME 2008, in Honolulu, Hawaii (October 2008). A full paper based on Chapter 4 will be published in *ECS Transactions*. The extended abstract was co-authored by David P. Wilkinson, Jiujun Zhang and Zheng Shi.

Other related co-authored publications are as follows:

1. A conference paper, originally based on an oral presentation, was published in the proceedings (R. Baker, Z. Xie, J. Zhang, D.P. Wilkinson, Fuel Cell and Hydrogen Technologies, 44th Annual Conference of Metallurgists, Calgary, Alberta, 21st August 2005; Can. Inst. of Mining and Petroleum, (2005) 3) [2].
2. A journal paper was published on a hexa deca fluoro substituted cobalt Pc (C. Song, L. Zhang, J. Zhang, D. Wilkinson, R. Baker, Fuel Cells 7 (2007) 9) [3].